



JOHANNES GUTENBERG
UNIVERSITÄT MAINZ

**Dynamics and evaporation–driven assembly in
colloidal suspensions consisting of shape–isotropic
and shape–anisotropic particles**

written by

Yashraj Wani

geb. am 24.05.1997 in Nashik

This dissertation is submitted to the Faculty of Physics, Mathematics and Informatics of the Johannes Gutenberg University of Mainz for the degree of “Doctor of Natural Sciences”

Yashraj Wani

Dynamics and evaporation–driven assembly in colloidal suspensions consisting of shape–isotropic and shape–anisotropic particles

Doctoral Dissertation, September 19, 2024

Supervisors: Prof. Dr. Arash Nikoubashman and Prof. Dr. Hans-Jürgen Butt

Abstract

Colloidal systems are ubiquitous in nature and are found in many scientific and practical applications. Therefore, understanding their dynamical and assembly properties is key to comprehend their collective behavior and to unlock their potential in practical applications. In this thesis, we used molecular dynamics (MD) simulations to study the transport properties in colloidal suspensions and the evaporation-driven assembly of colloidal particles to form superstructures.

First, we investigated the presence of hydrodynamic interactions in colloidal suspensions using multi-particle collision dynamics coupled with a discrete particle model for the colloidal particles (MPCD). We compared the MPCD simulations with experimental data and other simulation methods such as Brownian dynamics with free-draining hydrodynamics (BD) and with far-field hydrodynamics using the Rotne-Prager-Yamakawa mobility tensor (RPY). We found that the MPCD simulations exhibited long-time self-diffusion and sedimentation coefficients that were comparable with experiments, showing that the MPCD method is a robust and simple method for modeling colloidal suspensions with hydrodynamic interactions. Additionally, we extended the discrete particle model to probe the influence of particle shape on their transport properties, examining shapes such as spheres, cubes, tetrahedra, octahedra and spherocylinders. Agreement of the simulation results with experimental data, where available, demonstrated the applicability of the discrete particle model to describe shape-anisotropic colloidal suspensions. Furthermore, we found that the self-diffusion of polyhedral shapes can be effectively estimated from its spherical analogue whose diameter is mean of the inscribed and circumscribed sphere diameters.

Second, we probed the structure formation in supraparticles fabricated from the evaporation of colloidal droplets containing elongated and/or spherical particles. We found that the orientational ordering and packing of the elongated particles in supraparticles can be controlled through the evaporation rate and aspect ratios of the rod-like particles.

Zusammenfassung

Kolloidale Systeme sind in der Natur allgegenwärtig und finden sich in vielen wissenschaftlichen und praktischen Anwendungen. Daher ist das Verständnis ihrer dynamischen Eigenschaften und ihrer Assemblierung der Schlüssel zum Verständnis ihres kollektiven Verhaltens und zur Erschließung ihres Potenzials für praktische Anwendungen. In dieser Arbeit haben wir mit Hilfe von Molekulardynamiksimulationen (MD) die Transporteigenschaften in kolloidalen Suspensionen und die verdunstungsbedingte Assemblierung von kolloidalen Partikeln zu komplexen Strukturen untersucht.

Als erstes untersuchten wir das Vorhandensein hydrodynamischer Wechselwirkungen in kolloidalen Suspensionen mit Hilfe der Mehrteilchen-Kollisionsdynamik in Verbindung mit einem diskreten Teilchenmodell für die kolloidalen Teilchen (MPCD). Wir haben die MPCD-Simulationen mit experimentellen Daten und anderen Simulationsmethoden wie Brownsche Dynamik mit frei ablaufender Hydrodynamik (BD) und mit Fernfeld-Hydrodynamik unter Verwendung des Rotne-Prager-Yamakawa-Mobilitätstensors (RPY) verglichen. Dabei stellten wir fest, dass die MPCD-Simulationen mit Experimenten vergleichbare Langzeit-Selbstdiffusions- und Sedimentationskoeffizienten aufgewiesen haben, was zeigt, dass die MPCD-Methode eine robuste und einfache Methode zur Modellierung kolloidaler Suspensionen mit hydrodynamischen Wechselwirkungen ist. Darüber hinaus haben wir das diskrete Partikelmodell erweitert, um den Einfluss der Partikelform auf ihre Transporteigenschaften zu untersuchen, wobei wir Formen wie Kugeln, Würfel, Tetraeder, Oktaeder und Kugelzylinder betrachtet haben. Die Übereinstimmung der Simulationsergebnisse mit experimentellen Daten, sofern vorhanden, zeigte die Anwendbarkeit des diskreten Partikelmodells zur Beschreibung formanisotroper kolloidaler Suspensionen. Des Weiteren haben wir festgestellt, dass die Selbstdiffusion polyedrischer Formen anhand ihres kugelförmigen Analogons, dessen Durchmesser der Mittelwert der Durchmesser der eingeschriebenen und der umschriebenen Kugel ist, effektiv abgeschätzt werden kann.

Zweitens untersuchten wir die Strukturbildung in Suprapartikeln, die aus der Verdampfung von kolloidalen Tröpfchen mit länglichen und/oder kugelförmigen Partikeln hergestellt wurden. Dabei haben wir herausgefunden, dass die orientierte Anordnung und Packung der länglichen Partikel in den Suprapartikeln durch die Verdampfungsrate und das Seitenverhältnis der stabförmigen Partikel gesteuert werden kann.

Acknowledgement

My experience in Mainz over the past three years has been incredibly special and one that I will always cherish. This memorable journey was made possible by the exceptional people who have supported and accompanied me. I would like to express my gratitude to all of them and would like to thank:

My supervisor, Arash Nikoubashman for giving me this opportunity and for his constant support and encouragement. Michael Howard for being such a wonderful collaborator and for being like a co-supervisor to me. I consider myself very lucky to have had such outstanding and ambitious supervisors, whom I will always look up to.

My experimental collaborators – Melis Yetkin, Michael Kappl, and Hans-Jürgen Butt – whose expertise and partnership was invaluable for my research. I would especially thank Melis for being such an understanding and cooperative friend and a colleague.

Friederike Schmid and Pol Besenius for their support during my research.

Daniela Reibel, Markus Haack and Mariana Cosarinsky for all their administrative support.

My friends and colleagues – Gaurav, Rodrique, Emanuele, Lucia, Janka, Marios, Ashreya, Jude, Le, Tasos, Fabian, Kritika, Yannick, Kay, Arya, Xiaofei, and Jan for the time we spent in and outside the University, and the numerous enlightening coffee break conversations we had over the years.

My friends from outside the university and from the Institute of Molecular Biology for all the good times and unforgettable moments we shared outside of the university, providing a perfect balance to my academic life.

Especially, my parents and my brother for their unwavering support during my studies over several years.

Finally, I would like to thank the Research Training Group GRK 2516 for funding my doctoral research (Deutsche Forschungsgemeinschaft – Project number 405552959).

Contents

Abstract	i
Zusammenfassung	iii
1 Background	1
1.1 Colloids	2
1.1.1 Historical context	2
1.1.2 Definition and classification	4
1.2 Particle interactions	5
1.3 Brownian motion	10
1.4 Hydrodynamic interactions	13
1.5 Diffusion	15
1.6 Sedimentation	17
1.7 Drying of colloidal suspensions	18
1.7.1 Supraparticles	19
2 Mesoscale Molecular Dynamics Simulations	23
2.1 Brownian dynamics	24
2.2 Multi-particle collision dynamics	25
2.2.1 Algorithm	25
2.2.2 Solvent mapping	27
2.2.3 Solute-solvent coupling	28
3 Paper I	31
4 Paper II	45
5 Paper III	59
6 Summary and outlook	93
Bibliography	95

Background

A cornerstone of the success of our civilization has been our ability to assemble smaller materials into functional forms. This is evident across a wide range of length scales. On the larger end of the scale, spanning from centimeters to hundreds of meters, engineers have designed practical structures like buildings, bridges, and machinery that are integral to our lives. On the other end of the scale, at the molecular level, chemists have achieved remarkable precision in synthesizing distinct molecular architectures such as drugs and catalysts[1]. The intermediate length scale, ranging from tens of nanometers to several micrometers, forms an important focus of modern scientific investigations due to the immense untapped potential in this area. Advancements in particle synthesis techniques has enabled the production of nanoparticles with diverse shapes, functionalities, and compositions, that have the potential to serve as the building blocks of future materials, if effectively assembled into functional structures[2].

Unlike macroscopic building blocks like bricks and metal columns, that can be handled easily, nanoparticles in their dry form can become easily airborne and pose health hazards[3]. Therefore, they are stored and handled in the form of solutions, also known as colloids. Many technical applications, such as coatings, inkjet printing, and adhesives, use colloids as the starting material. To utilize colloids effectively for these applications, it is essential to understand the dynamics and assembly of the constituent nanoparticles.

In this chapter, we will begin with an introductory discussion on colloids, delving into their historical context and providing a technical overview (Sec. 1.1). Then we will discuss the various interactions present in colloidal systems and their modeling for theoretical/computational studies (Sec. 1.2). Following this, we will examine the Brownian motion of colloidal particles (Sec. 1.3), and introduce the concept of hydrodynamic interactions that can additionally affect particle dynamics (Sec. 1.4). Subsequently, we will describe the transport properties in colloidal suspensions, specifically diffusion (Sec. 1.5) and sedimentation (Sec. 1.6). Lastly, we will explore a particular instance of non-equilibrium dynamics: drying of colloidal suspensions (Sec. 1.7).

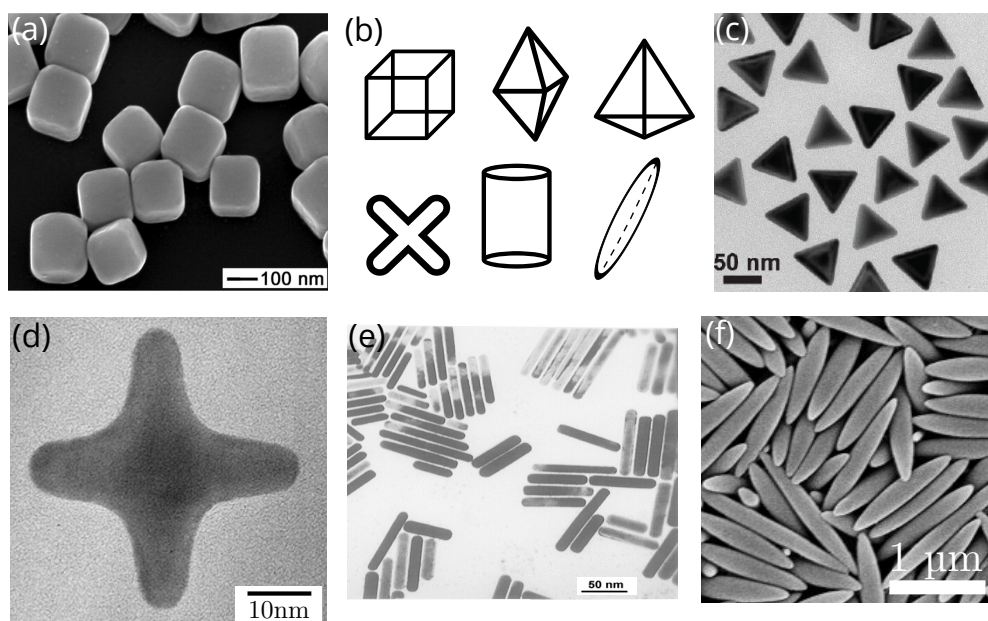


Fig. 1.1: Selected examples of colloidal particles with anisotropic shapes, made possible by advancements in synthesis techniques. The particles shown include (a) silver nanocubes[4], (c) gold nanotetrahedra[5], (d) gold tetrapod nanocrystal[6], (e) gold nanorods[7], and polystyrene ellipsoids[8]. The SEM images have been reproduced with permissions from the references indicated.

1.1 Colloids

1.1.1 Historical context

Colloids have captivated the minds of scientists and scholars for many centuries. In ancient times, colloidal gold was used for staining glass, exemplified by the 4th century Lycurgus cup[9]. During the middle ages, solutions containing gold salts held a reputation for their supposed medical properties[10].

The modern scientific phase of colloid science, marking the era when scientists began to grasp the colloidal phenomena, began in the early 19th century. Approximately, it started when Robert Brown and Adolphe Brongniart, individually in 1827, observed random and persistent motion of small pollen grains suspended in water[11, 12]. Initially, this motion was attributed to the presence of microscopic living organisms (“animalcules”). However, Brown’s subsequent observations of similar behavior in finely powdered inorganic materials immersed in water suggested a more fundamental origin for this random motion.

Not fully convinced, several conflicting hypotheses emerged, suggesting that external factors such as vibrations, capillary forces, microscopic currents, thermal variations, caused the Brownian motion of the particles. These debates continued for several decades without conclusive resolutions. Finally, in the late 1880s, through numerous experiments, Leon Guoy showed that external factors were not responsible for Brownian motion and that its origins

were indeed fundamental[13].

The molecular–kinetic theory, conceptualizing colloidal particles as very large molecules, gained popularity for describing the motion of colloidal particles. In his seminal 1905 paper, Einstein argued that if the kinetic theory were applicable to colloids, then a colloidal osmotic pressure should exist[14]. He proposed a dynamic equilibrium between a fictitious force and a “restoring” force arising from the colloidal osmotic pressure, and obtained the well-known Stokes–Einstein relation for the diffusion of a small spherical particle suspended in a medium. In addition, he showed that beyond a certain “Brownian time”, the mean squared displacement of a colloidal particle depends linearly on time and diffusion coefficient of the particle. Interestingly, this idea forms the basis of the sophisticated dynamic light scattering technique that is used to measure the hydrodynamic size of suspended particles.

Only a few years later, in 1908, Paul Langevin came to the same conclusion as Einstein through a much simpler approach[15]. He essentially applied Newton’s second law to a Brownian particle by equating it to the sum of a random force originating from collisions with surrounding fluid molecules and an opposing frictional force consistent with Stokes’ description. Then employing the equipartition theorem, he obtained a relation between particle displacements and time, which reduced to Einstein’s relation at long time. Through this method, Langevin was able to elucidate the concept of “Brownian time” as hypothesized in Einstein’s derivation. This is examined in greater detail in Sec. 1.3.

Accurately measuring particle displacements was a challenging task at the time, making it difficult to validate the theoretical hypotheses proposed by Einstein and Langevin. However, Jean Perrin adopted an alternative approach in his pioneering work. He hypothesized that if the kinetic theory applied to colloids, then at sedimentation equilibrium,¹ the distribution of the particles as a function of height in a column under the action of gravity should exhibit a similar trend as gas molecules under gravity, *i.e.*, the particle concentration should decrease exponentially with height[16, 12]. Extensive experimental studies by Perrin’s group substantiated the validity of the molecular–kinetic theory for colloids, ultimately earning him the Nobel prize in Physics in 1926. (Interestingly, almost a century after Brown had first published his observations!)

Unfortunately, just as colloid science had taken the front seat to scientific advancements, the cutting edge of physics turned to the subatomic and quantum regimes. However, with the advent and recognition of several mesoscale technologies such as foods, coatings, and cosmetics, colloid science came to the forefront once again. With significant improvement in our understanding, the scope of colloids has broadened and encompasses more than just small spheres suspended in a liquid. Materials such as foams, aerosols, emulsions, and gels also fall under the category of colloids. Therefore, over time, the definition of a colloid has

¹Sedimentation equilibrium in a colloidal suspension refers to the state where the sedimentation of particles under the action of gravity is balanced by their thermal motion (diffusion) resulting in a stable concentration gradient of the particles.

also been tweaked to cover such materials.

1.1.2 Definition and classification

A colloid can be defined as a mixture where an insoluble substance is uniformly dispersed throughout another substance, with the former referred to as the dispersed phase and the latter as the continuous phase[17]. Colloids can be categorized into various types based on the three states of matter – solid, liquid, and gas. Examples of such colloids are sols, emulsions, foams, and aerosols[18]. In this study, our focus is on the type where solid particles are dispersed in a liquid medium, commonly known as sol. Examples of such colloids include paints, inks, milk, and blood. For simplicity, we will use the term “colloid” throughout the remainder of this work, omitting the term sol.

In the previous section, we vaguely referred to colloidal particles as “small.” However, it is essential to define what constitutes “small.” A brief review of the literature tells that colloidal particles typically range in size from a few nanometers to a few micrometers in diameter, spanning a range of 3 – 4 orders of magnitude[18]. We can rationalize the statement using some reasonable arguments.

The lower limit on the size of colloidal particles can be determined by requiring that these particles interact effectively with the surrounding liquid molecules, where the properties of the latter can be defined through macroscopic observables such as viscosity and temperature[19]. Consequently, the colloidal particles should be large enough to interact with multiple liquid molecules simultaneously. Considering water as the continuous phase, with individual water molecules described as spheres with diameter of approximately 0.28 nm,² the colloidal particles should be at least an order of magnitude larger to interact with a statistically significant number of water molecules[19]. Thus, the diameter of a colloidal particle should be roughly a few nanometers.

The upper limit on the size of colloidal particles can be inferred from sedimentation equilibrium, by positing that the particle displacement due to sedimentation is not larger than its own radius, during an experiment lasting, say, one second[19]. As will be shown in Sec. 1.6, the sedimentation velocity of a single colloidal particle is,

$$\mathbf{v}_s^\infty = \frac{2}{9} \frac{a^2 \Delta \rho}{\eta_0} \mathbf{g},$$

where a is the particle radius, $\Delta \rho$ is the difference in mass density of the colloidal particle and solvent, η_0 is the solvent viscosity, and \mathbf{g} ($g = 9.8 \text{ m/s}^2$) is the acceleration due to gravity. Considering polystyrene particles suspended in water ($\eta_0 = 10^{-3} \text{ Ns/m}^2$ and $\Delta \rho = 50 \text{ kg/m}^3$)

²The length of 0.28 nm corresponds to the first peak in the radial distribution function of oxygen atoms, as determined by x-ray diffraction analysis of liquid water under ambient conditions[20].

and solving for the particle radius we get,

$$a = \frac{9\eta_0}{2\Delta\rho g}$$

which equates to $a = 9 \mu\text{m}$. Therefore, the maximum size of colloidal particles can be up to a few tens of micrometers.

1.2 Particle interactions

Depending on the application/purpose, there are various colloidal systems at one's disposal, each possessing unique physical and chemical properties. Examples include metallic nanoparticles[21] (such as gold, silver, and copper), polymeric particles[22] (including polystyrene and polymethyl methacrylate), colloidal silica[23] (comprising silicon dioxide), clay particles of both natural (such as montmorillonite, kaolinite) and synthetic origin (like laponite)[24].

The macroscopic behavior of colloids is dictated by the interplay of various interactions present in the system. In general, if colloidal particles experience a net repulsive force, they remain homogeneously dispersed, leading to the formation of a *stable suspension*. Conversely, if particles experience a net attractive force, they tend to aggregate and eventually precipitate out, resulting in an *unstable suspension*.

Classifying interactions based on opposites like attractive vs. repulsive, or long-ranged vs. short-ranged may seem logical at first glance. However, the logic fails when solvent properties come into play or when interactions originate from purely entropic effects[17]. Here, we will discuss the most common interactions present in colloidal systems.

In any colloidal system, two interactions are typically present: hard-core repulsion and van der Waals attraction. Hard-core repulsion between colloidal particles can be considered as the colloidal equivalent of Pauli's exclusion principle, which prevents direct overlap between any two colloidal particles. For two hard spherical particles with radii a , the repulsion is zero at separations larger than $2a$ and becomes infinitely large for smaller separations. In case of colloidal particles with a "softer" core, such as swollen latex particles or polymer grafted nanoparticles, the repulsion increases smoothly as particle separations decrease. In classical molecular dynamics (MD) simulations, an effective hard-sphere potential can be approximated using the core-shifted Weeks-Chandler-Andersen (WCA) potential[25],

$$\beta V_{\text{WCA}}(r) = \begin{cases} 4 \left[\left(\frac{\sigma}{r-\Delta} \right)^{12} - \left(\frac{\sigma}{r-\Delta} \right)^6 \right] + 1, & r \leq \Delta + 2^{1/6}\sigma \\ 0, & \text{otherwise} \end{cases} \quad (1.1)$$

where $\beta = 1/k_{\text{B}}T$, r is the radial distance between two particles, Δ is the distance at which the potential diverges, generally chosen to be close to the diameter of a particle, and σ is

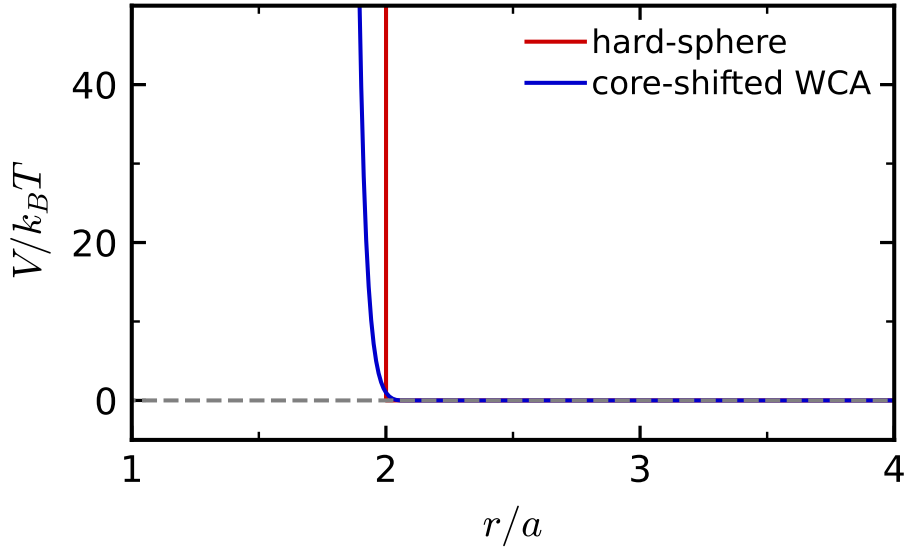


Fig. 1.2: Comparison between the hard-sphere potential (red) and core-shifted WCA potential (blue) given by Eq. (1.1).

a length parameter that sets the cutoff distance for the potential and is often used as the unit of length in MD simulations. This form of the potential ensures that the potential is purely repulsive and continuously goes to zero at the cutoff distance. Figure 1.2 shows a comparison between hard-sphere potential (shown in red) and the smoother WCA potential (shown in blue). The parameters used in the above example are $a = 3\sigma$, and $\Delta = 5\sigma$.

Van der Waals attraction, also known as dispersion force, originates from quantum mechanical principles. An intuitive understanding of this force can be illustrated using the example of a neutral molecule like helium. In a helium molecule, electrons are distributed in an electron cloud around the nucleus, resulting in an average dipole moment of zero. However, there exists a possibility that at any given instant, the electrons may be displaced in the electron cloud such that the molecule gets a finite dipole moment. This instantaneous dipole can induce attraction between other particles experiencing similar fluctuations[17]. Larger molecules have a higher likelihood of experiencing such fluctuations, thereby increasing the probability of generating instantaneous dipole moments and consequently enhancing the van der Waals attraction.

For two “mesoscale” spherical particles of radius a , whose surfaces are separated by a distance d , Hamaker derived an equation for the strength of the van der Waals interaction[17, 26],

$$V(d) = -\frac{A_H}{6} \left[\frac{2a^2}{(4a+d)d} + \frac{2a^2}{(2a+d)^2} + \ln \frac{(4a+d)d}{(2a+d)^2} \right] \quad (1.2)$$

where A_H is called the Hamaker constant. The van der Waals force can be easily calculated

as,

$$F(d) = -\frac{\partial V}{\partial d} = -\frac{A_H}{6} \left[\frac{64a^6}{d^2(2a+d)^3(4a+d)^2} \right] \quad (1.3)$$

At very small separations ($d \ll a$), the equation simplifies to,

$$F = -\frac{A_H a}{12d^2} \quad (1.4)$$

At larger separations, $d \gg a$ the van der Waals force follows a $\sim d^{-6}$ dependency. As an example, consider polystyrene spheres of radius $a = 200$ nm dispersed in water, where $A_H \sim 10^{-20}$ J (as provided in Table 13.3 in Ref. [17]). For two particles in close contact, say $d = 0.5$ nm, the attractive force between them will be $F = 0.66$ nN which corresponds to an energy of $V = -78 k_B T$ ($T = 298$ K). Now, if we increase the separation by 20x, $d = 10$ nm, the attraction strength decreases to 1.5 pN corresponding to an energy of $V = -3 k_B T$. This illustrates that even at a separation of 10 nm, which is 5% of the particle radius, the interaction energy exceeds $k_B T$. Therefore, in the absence of additional interactions, van der Waals attraction can destabilize a suspension, which is undesirable in many practical cases.

The destabilizing effect can be countered using various methods. One approach involves grafting polymer chains onto the surface of colloidal particles[19]. In *good solvent* conditions, the polymer chains preferentially interact with the solvent and therefore remain expanded, effectively masking the van der Waals attraction. However, the effect becomes reversed in *bad solvent* conditions. In addition to the van der Waals interaction, polymeric particles, such as polystyrene latex particles, are hydrophobic,³ increasing their tendency to aggregate. Experimentally, the range of hydrophobic interactions has been determined to be similar to van der Waals attraction, typically falling within the range of 0 to 10 nm[28, 29]. To counter this, polystyrene colloidal particles are often functionalized with carboxylic or sulfate groups, that tend to stick out from the colloid surface. These functional groups can readily ionize in solvents like water, resulting in the colloidal particles becoming electrostatically repulsive. This method of stabilization is commonly referred to as charge stabilization in the context of colloidal suspensions.

Ionization of the functional groups on the colloid surface leads to the formation of an electric double layer around the particles due to attraction of counterions and repulsion of coions from the surface, leading to a partial screening of the electrostatic repulsion[17]. The electric double layer consists of two main regions: the Stern layer and the diffuse layer. Closest to the surface is the Stern layer, where counterions are tightly bound to neutralize the surface charge, while in the diffuse layer, ions are more loosely bound with the colloid surface. The concentration of counterions gradually decreases as the distance from the surface increases, while it increases for the coions, until both reach the equilibrium

³The hydrophobic effect/interaction is an entropic effect that originates from the higher preference of water molecules to interact with each other and form hydrogen bonds. Therefore at small separations, nonpolar molecules experience an effective attraction which minimizes the disruption of the hydrogen bond network in water[17, 27].

bulk concentration. However, in many practical cases charged particles interact with each other in the presence of additional ions in the solution. For example, the physiological salt concentration in living cells ranges between 0.1 – 0.2 M (mainly NaCl/KCl)[30]. The presence of such ions affects the ion distribution around colloidal particles and increases the electrostatic screening.

Using the Debye–Hückel approximation, the electrostatic potential $\psi(r)$ around a spherical particle of radius a and charge Z (expressed in units of the elementary charge e) in an electrolyte solution is given as[17],

$$\psi(r) = C \frac{\exp(-\kappa r)}{r} \quad (1.5)$$

where the potential decreases exponentially with the characteristic length κ^{-1} , also known as the Debye length. Here C is a proportionality constant. In a monovalent electrolyte solution (NaCl), the Debye length is[31, 32],

$$\kappa^{-1} = \sqrt{\frac{\epsilon_r \epsilon_0 k_B T}{2 \times 10^3 N_A e^2 I}} \quad (1.6)$$

where ϵ_r is the relative permittivity of the solution, ϵ_0 is the free space permittivity, e is the elementary charge, N_A is the Avogadro number, and I is the molar strength of the electrolyte. Clearly, Debye length depends only on the property of the medium, *i.e.*, ionic strength of the electrolyte, and not on any property of the charged surface.

Using appropriate boundary conditions, we can solve for C in Eq. (1.5) to get,

$$\psi(r) = \frac{Ze}{4\pi\epsilon_r\epsilon_0} \left(\frac{1}{1 + \kappa a} \right) \frac{\exp(-\kappa r)}{r} \quad (1.7)$$

The interaction potential between two such particles can be easily solved to obtain,

$$\beta V_{\text{EL}}(r) = \lambda_B \left(\frac{Z \exp(\kappa a)}{1 + \kappa a} \right)^2 \frac{\exp(-\kappa r)}{r} \quad (1.8)$$

where $\lambda_B = e^2/(4\pi\epsilon_0\epsilon_r k_B T)$ is the Bjerrum length. Experimentally, it is difficult to measure the charge carried by the colloidal particles. However, the charge can be estimated from the (experimentally measurable) zeta potential ζ ,⁴ as given by the linear screening theory at low packing fractions[33, 34],

$$Z = \frac{\lambda_B}{a} (1 + \kappa a) \frac{e\zeta}{k_B T} \quad (1.9)$$

The DVO theory, named after the scientists Boris Derjaguin, Lev Landau, Evert Verway and Theodoor Overbeek, combines the screened electrostatic repulsion [Eq. (1.8)] and van der

⁴Within the diffuse layer there is an imaginary surface beyond which the liquid particles move freely relative to the particle. The electric potential at this imaginary surface is known as zeta potential.

Waals attraction [Eq. (1.2)] to explain the aggregation behavior in colloids[17]. The two interactions differ from each other in two ways. First, the van der Waals interaction is mostly insensitive to variations in salt concentrations and pH of the medium, while the electrostatic screening is sensitive to such variations. Second, van der Waals interaction is a power law (*i.e.*, $V \propto 1/d^6$) while the screened electrostatic repulsion decays exponentially. Therefore, at very small separations ($d \rightarrow 0$), van der Waals attraction exceeds the electrostatic repulsion. Thus, when the salt concentration is sufficiently low, the energy barrier due to electrostatic repulsion is strong enough to prevent the aggregation of the particles. However, as the salt concentration in the medium is increased, the electrostatic repulsion gets increasingly screened and after a critical concentration is passed the energy barrier becomes too small and particles can fall into potential well due to the van der Waals attraction.

Empirically, the hard-core repulsion and short ranged van-der-Waals attraction can be approximated using the core-shifted WCA potential as given in Eq. (1.1), but without the distance cutoff. The different variables can be tuned to obtain the proper features such as the position of the hard-core repulsion, width and depth of the attractive potential well. Figure 1.3 shows an illustrative example of the combined action of the screened electrostatic repulsion, van der Waals attraction and hard-core repulsion modeled using Eq. (1.8) and core-shifted WCA potential, respectively. The parameters for this example were tuned carefully from colloidal probe atomic force microscopy and dynamic light scattering measurements performed on polystyrene colloidal particles[31]. The core-shifted WCA potential is shown using a blue dashed curve that diverges at $\Delta = 440$ nm and remains unchanged with the change in salt concentration in the medium. In contrast, the screened electrostatic repulsion shown using orange dashed curves becomes weaker as salt concentration is increased in the medium. The net potential is shown with black (or gray) color. In one case the ionic strength of the medium was low enough (light orange; $[\text{NaCl}] = 10$ mM) that the electrostatic repulsion remained stronger than the van der Waals attraction. However, as the ionic strength increases (dark orange; $[\text{NaCl}] = 80$ mM), the electrostatic repulsion becomes increasingly screened, allowing the van der Waals attraction to dominate at small separations. This transition results in the particles exhibiting an attractive interaction.

When charge functionalization is insufficient to stabilize colloids, surfactants can also be employed[35, 8]. Surfactants are chemical compounds possessing both hydrophobic and hydrophilic domains. Typically, these are compounds with a hydrophilic head that is polar and may or may not carry an electrical charge and a hydrophobic tail composed of hydrocarbon chains. In case the colloidal particles have a hydrophobic domain (such as polystyrene latex particles), the hydrophobic tail readily attaches to the surface of colloids, thereby preventing the aggregation of colloidal particles.

Some interactions between colloidal particles have purely entropic origins. For instance, a short ranged, weak attractive interaction can be induced by adding depletants – nonadsorbing polymers or small colloidal particles – to the solution[36]. When two “large” colloidal

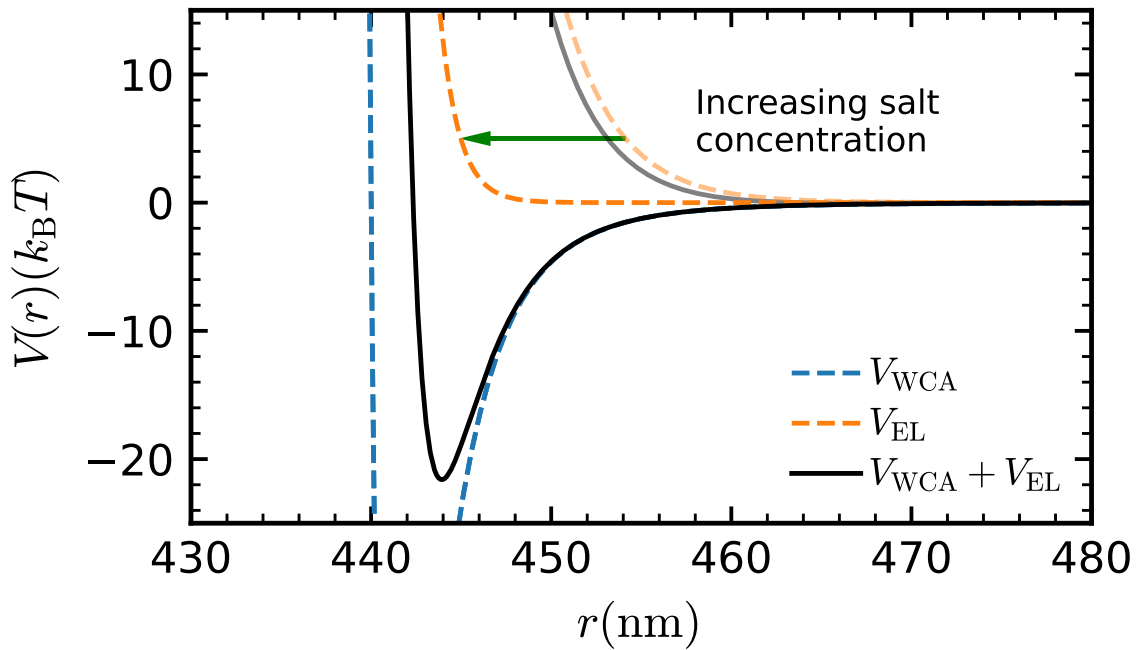


Fig. 1.3: Illustration of the combined action of screened electrostatic repulsion (orange), van der Waals attraction + hard-core repulsion (blue). The black (/gray) curve represents the net interaction potential between two particles at high (/low) salt concentrations. The arrow shows increased screening of electrostatic repulsion with increasing salt concentration in the suspension.

particles approach each other closely enough that the depletants cannot fit between them, an osmotic pressure is generated, causing the colloidal particles to come closer together [37, 38]. The range and strength of this attraction depends on the size and concentration of the depletants in the suspension.

In summary, the net interaction between colloidal particles is a combination of multiple interactions, as described above. Fortunately, for most practical applications, only a few of these interactions are present at a time.

1.3 Brownian motion

As mentioned briefly in the previous sections, colloidal particles exhibit erratic motion that stems from their rapid and random collisions with the solvent molecules. Since the colloidal particles are generally much larger than the solvent particles, the mass of a colloidal particle $m \gg m_s$, where m_s is the mass of a solvent particle.

The net force on a colloidal particle is a result of its combined interaction with the solvent \mathbf{F}_s and other colloidal particles \mathbf{F}_c . Therefore, we have

$$\mathbf{F}_{\text{total}} = \mathbf{F}_s + \mathbf{F}_c \quad (1.10)$$

For simplicity, we can assume that under very dilute conditions, a colloidal particle interacts solely with the solvent, and therefore $\mathbf{F}_c = 0$.

The interaction with the solvent particles \mathbf{F}_s , can be split in two parts:

1. As a colloidal particle moves with a velocity $\mathbf{v}(t)$, it experiences a frictional force due to the solvent molecules in its path, whose magnitude is proportional to $\mathbf{v}(t)$. This force can be written as $\mathbf{F}_{\text{drag}}(t) = -\gamma_0 \mathbf{v}$, where γ_0 is known as the friction coefficient. For a particle of radius a moving through a viscous fluid, $\gamma_0 = 6\pi\eta_0 a$, where η_0 is the dynamic viscosity of the fluid (according to Stoke's law).
2. Collisions with the solvent particles result in a stochastic force $\mathbf{F}_r(t)$ on the colloidal particles.

Therefore, the equation of motion for a colloidal particle can be expressed in Newtonian form as,

$$m \frac{d}{dt} \mathbf{v}(t) = -\gamma_0 \mathbf{v}(t) + \mathbf{F}_r(t) \quad (1.11)$$

This equation, known as the Langevin equation, was first proposed by Paul Langevin in 1908. To analyze the dynamics, we must describe the properties of $\mathbf{F}_r(t)$. Since the solvent particles can collide with the colloidal particle from any direction, we can assume that $\mathbf{F}_r(t)$ follows a normal distribution with zero mean,

$$\langle \mathbf{F}_r(t) \rangle = 0 \quad (1.12)$$

Due to the significant difference in their masses, the timescales relevant for the solvent and colloidal particles are generally separated by several orders of magnitude. For a time τ , which is longer than the mean free time of the solvent particles τ_s , but short compared to the momentum relaxation time of the colloidal particles $\tau_c = m/\gamma_0$, the stochastic force $\mathbf{F}_r(t)$ can be assumed to be delta correlated,

$$\langle \mathbf{F}_r(t) \cdot \mathbf{F}_r(t') \rangle = h \delta(t - t') \quad (1.13)$$

where $|t' - t| \approx \tau$ and h quantifies the strength of thermal fluctuations. Using this assumption along with Eq. (1.12), we can solve the Langevin equation to obtain (for simplicity we only solve for the one dimensional case),

$$v(t) = v_0 e^{-t/\tau_c} + \int_0^t ds e^{-(t-s)/\tau_c} F_r(s) \quad (1.14)$$

where v_0 is the initial velocity. Taking an ensemble average of the velocity (assuming that all the particles have initial velocity v_0), the stochastic term vanishes,

$$\langle v(t) \rangle = v_0 e^{-t/\tau_c} \quad (1.15)$$

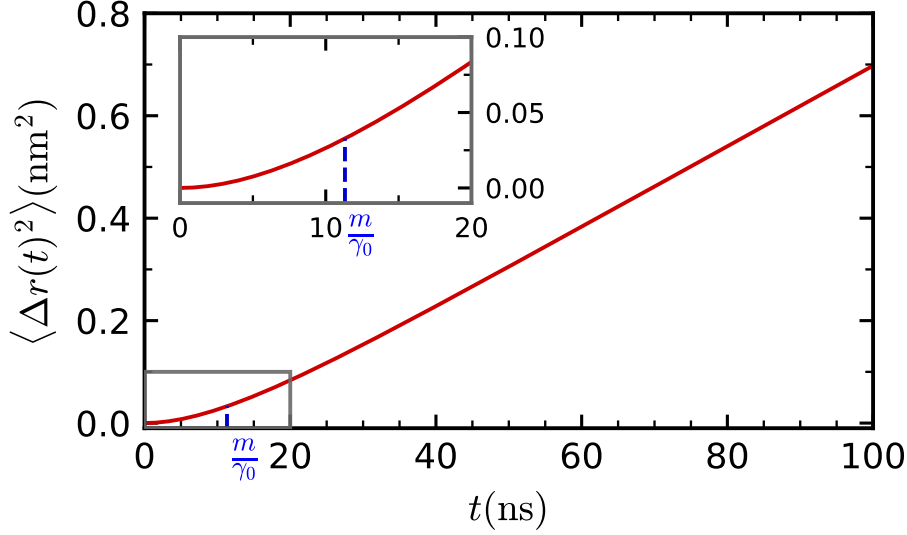


Fig. 1.4: Time dependence of the mean squared displacement of a polystyrene colloidal particle of radius $a = 200$ nm. The inset shows the time dependence at short times with the blue dashed line showing momentum relaxation timescale for the colloidal particle.

Here, the velocity decays exponentially with time, implying that information about the initial velocity is lost for $t \gg \tau_c$.

Squaring Eq. (1.14),

$$\langle v^2(t) \rangle = v_0^2 e^{-2t/\tau_c} + \int_0^t ds \int_0^t ds' e^{-(t-s)/\tau_c} e^{-(t-s')/\tau_c} F_r(s) F_r(s') + 2v_0 e^{-t/\tau_c} \int_0^t ds e^{-(t-s)/\tau_c} F_r(s)$$

and then taking an ensemble average gives us,

$$\begin{aligned} \langle v^2(t) \rangle &= v_0^2 e^{-2t/\tau_c} + \int_0^t ds \int_0^t ds' e^{-(t-s)/\tau_c} e^{-(t-s')/\tau_c} h \delta(t-t') \\ \implies \langle v^2(t) \rangle &= v_0^2 e^{-2t/\tau_c} + \frac{h\tau_c}{2} [1 - e^{-2t/\tau_c}] \end{aligned} \quad (1.16)$$

As time goes to infinity, $\langle v^2(t) \rangle = h\tau_c/2$. According to the equipartition theorem, the average kinetic energy of a particle at temperature T in one dimension is,

$$\left\langle \frac{mv^2}{2} \right\rangle = \frac{k_B T}{2} \quad (1.17)$$

Thus, $\langle v^2(t) \rangle \rightarrow k_B T/m$ at long times and

$$h = \frac{2k_B T}{m\tau_c} = \frac{2k_B T}{m^2} \gamma_0 \quad (1.18)$$

This relation is known as the *Fluctuation-dissipation theorem*, which relates the fluctuations h to the dissipation γ_0 in the system.

We can readily derive the time–dependence of the position from Eq. (1.14) by using the initial conditions: $x(0) = x_0$ and $v(0) = v_0$,

$$x(t) = x_0 + \int_0^t v(k) dk$$

$$x(t) - x_0 = v_0 \tau_c [1 - e^{-t/\tau_c}] + \tau_c \int_0^t ds [1 - e^{-(t-s)/\tau_c}] F_r(s) \quad (1.19)$$

Taking squares on both sides of Eq. (1.19) and then the ensemble average we get,

$$\langle [x(t) - x_0]^2 \rangle = \langle v_0^2 \rangle \tau_c^2 (1 - e^{-t/\tau_c})^2 + h \tau_c^2 \int_0^t ds [1 - e^{-(t-s)/\tau_c}]^2$$

Using the fluctuation–dissipation relation (Eq. (1.18)) and $\langle v_0^2 \rangle = k_B T/m$, we obtain an expression for the mean squared displacement,

$$\langle \Delta x(t)^2 \rangle \equiv \langle [x(t) - x_0]^2 \rangle = 2\tau_c^2 \frac{k_B T}{m} \left[\frac{t}{\tau_c} - 1 + e^{-t/\tau_c} \right] \quad (1.20)$$

At short times, $t \ll \tau_c$, the mean squared displacement reduces to

$$\langle \Delta x(t)^2 \rangle = \frac{k_B T}{m} t^2 \equiv \langle v_0^2 \rangle t^2 \quad (1.21)$$

showing that, at short times, colloidal particles move freely according to their thermal velocities. But at long times $t \gg \tau_c$, also known as the diffusive limit, the mean squared displacement reduces to,

$$\langle \Delta x(t)^2 \rangle = 2 \frac{k_B T}{6\pi\eta_0 a} t \equiv 2D_0 t \quad (1.22)$$

which is linear in time. The proportionality factor $D_0 = k_B T/6\pi\eta_0 a$ is known as the diffusion coefficient. In three dimensions, the relation becomes $\langle \Delta r(t)^2 \rangle = 6D_0 t$. Figure 1.4 shows the time dependence of the mean squared displacement [Eq. (1.20)] for polystyrene colloidal particles of radius $a = 200$ nm in water, with the inset showing the $\sim t^2$ dependence at short times.

1.4 Hydrodynamic interactions

An additional level of complexity to colloidal dynamics arises from hydrodynamic interactions. As colloidal particles translate or rotate, they induce a flow in the surrounding solvent molecules, which in turn transfer momentum to other colloidal particles that move in response[19]. These interactions are known as solvent–mediated hydrodynamic interactions. The significance and complexity of hydrodynamic interactions are underscored by their range and multi–body characteristics, respectively.

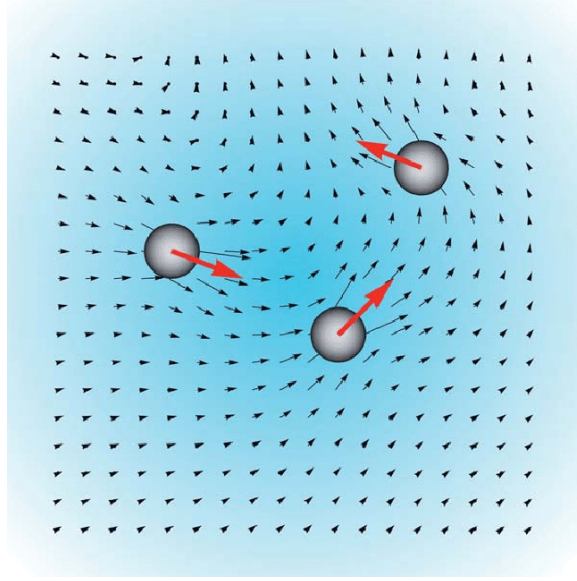


Fig. 1.5: Illustration explaining the long-ranged hydrodynamic interactions between colloidal particles due to the flow field generated in the solvent. Figure adapted from Ref. [39] with permissions.

Stokes equation for incompressible fluids at very small Reynolds number ($\text{Re} \ll 1$) are given as[19],

$$\nabla p(\mathbf{r}, t) - \eta_0 \nabla^2 \mathbf{u}(\mathbf{r}, t) = \mathbf{f}(\mathbf{r}), \quad (1.23)$$

$$\nabla \cdot \mathbf{u}(\mathbf{r}, t) = 0 \quad (1.24)$$

where $\mathbf{u}(\mathbf{r}, t)$ is the local fluid velocity, $p(\mathbf{r}, t)$ is the pressure, η_0 is the fluid shear viscosity, and $\mathbf{f}(\mathbf{r})$ is any external force acting on the fluid. Equation (1.23) is also referred to as the creeping flow equation and Eq. (1.24) is the relation for incompressibility of the fluid. An approximate solution for the fluid flow velocity, in case of a single spherical particle of radius a translating with velocity \mathbf{v} in an unbounded fluid which is at rest at infinity is,

$$\mathbf{u}(\mathbf{r}, t) = \mathbf{A}(\mathbf{r} - \mathbf{v}t) \cdot \mathbf{v},$$

where

$$\mathbf{A}(\mathbf{r}) = \frac{3a}{4r}(\mathbf{I} + \hat{\mathbf{r}}\hat{\mathbf{r}}) + \frac{1}{4} \left(\frac{a}{r}\right)^3 (\mathbf{I} - 3\hat{\mathbf{r}}\hat{\mathbf{r}}) \quad (1.25)$$

with $r = |\mathbf{r}|$, $\hat{\mathbf{r}} = \mathbf{r}/r$. Here we have assumed that the sphere is not rotating and the boundary conditions are: $\mathbf{u}(\mathbf{r}) \rightarrow 0$ for ($r \rightarrow \infty$) and $\mathbf{u}(\mathbf{r}) = \mathbf{v}$ for $r = a$, when the center of the sphere lies at the origin. This shows that perturbations in the fluid flow due to the movement of a colloidal particle decay as $1/r$, and therefore are long ranged. When multiple particles are present in the system, each particle generates a flow field that propagates through the fluid. The net fluid velocity at any point is a superposition of the flow fields generated by all particles, making the problem inherently many-body in nature.

Hydrodynamic interactions can be incorporated into MD simulations using various methods.

Brownian dynamics with the Rotne–Prager–Yamakawa mobility tensor[40, 41, 42] and Stokesian dynamics[43] are well-known implicit solvent simulation methods that account for hydrodynamic interactions between colloidal particles through the equations of motion. Other simulation techniques, such as multi-particle collision dynamics[44, 45, 46], and lattice-Boltzmann methods[47, 48], utilize simplified models of the solvent that are computationally less demanding but have properties similar to real solvent. We will discuss some of these methods in greater detail in Chapter 2.

1.5 Diffusion

The term diffusion is typically associated with the process in which particles move from a region of high concentration to a region of low concentration. While this captures part of its essence, the concept extends further. As seen from the analysis of Brownian motion, individual colloidal particles exhibit non-zero (squared) displacements due to their thermal motion, which is also a form of diffusion. Therefore, diffusion can be categorized into two types: collective diffusion and self-diffusion.

Collective diffusion involves the movement of mass in response to concentration gradients, ultimately leading to the homogenization of the system[19]. This process is driven by entropy. For instance, consider a drop of ink in water. At the ink–water interface, ink particles experience more frequent collisions with other ink particles where the concentration is higher. As a result, there is a net flow of particles toward the region of lower concentration. This gradual mixing is illustrated graphically in Fig. 1.6(a→b).

Self-diffusion refers to the motion of an individual colloidal particle, often referred to as a “tracer” particle, within a system as it interacts with its surrounding particles and is commonly studied in homogeneous systems[19]. A straightforward approach to quantify self-diffusion is to measure the mean squared displacement of the particles over an extended duration, $t \gg m/\gamma_0$.

An important assumption in the analysis of Brownian motion was that of infinite dilution. In reality, even at low finite concentrations, colloidal particles interact with each other, potentially influencing the time-dependent behavior of the mean squared displacement. To accommodate this, we replace D_0 in Eq. (1.22) with the concentration dependent self-diffusion coefficient D , yielding

$$\langle \Delta r(t)^2 \rangle = 6Dt \tag{1.26}$$

In the diffusive limit ($t \gg m/\gamma_0$), self-diffusion of colloidal particles can be categorized into: short-time D_s and long-time D_ℓ self-diffusion. During short times, the environment surrounding a tracer particle can be considered stationary, effectively forming a local cage

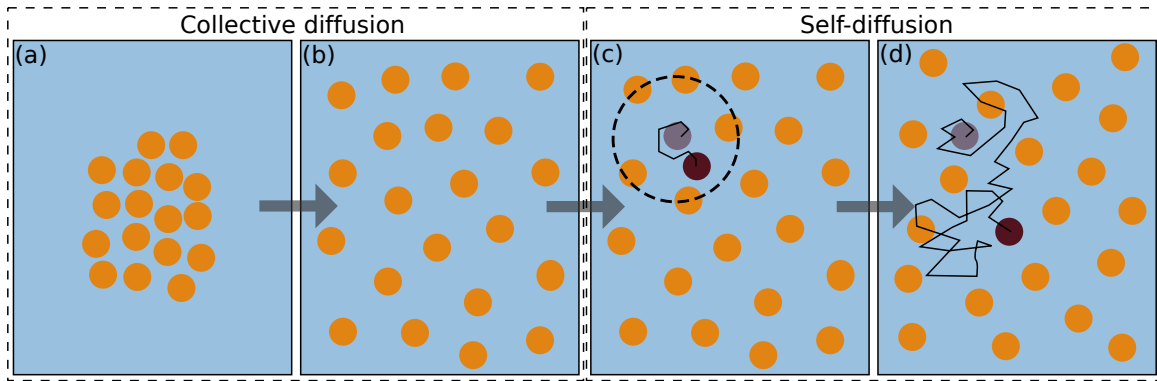


Fig. 1.6: Illustration for the different diffusive regimes in a colloidal system. (a) In response to concentration gradients in the system, colloidal particles move to region of lower concentration – collective diffusion – to form a (b) homogeneous suspension. In a homogeneous suspension particles undergo self-diffusion (c) and (d), where the tracer particle is shown in a different color. (c) illustrates the local cage dynamics of the tracer particle at short times $t \ll m/\gamma$, while (d) shows the long-time diffusion of a colloidal particle.

within which it can move. The diffusive motion within this local cage can be described by D_s . If the tracer particle does not interact with its surroundings, one would expect $D_s = D_0$. However, hydrodynamic interactions between particles affect the diffusion of the colloidal particles, leading to a different short-time diffusion $D_s < D_0$. Over longer periods, the surrounding particles also undergo displacements, allowing the tracer particle to escape from one cage to another multiple times. The diffusive dynamics over such extended duration can be characterized by D_ℓ . Figure 1.6 shows a visual representation of both short-time (c) and long-time (d) self-diffusion of colloidal particles.

The dynamics of colloidal particles is influenced by various factors, including shape, size, interactions, and volume fractions. Due to practical considerations, much of the theoretical and experimental work has predominantly focused on spherical colloidal particles. Research in this area has explored the impact of particle size, volume fractions, and hydrodynamic interactions on colloidal dynamics. Research exploring the effects of hydrodynamic interactions remains an active area of research. In Chapter 3, we present a systematic study of self-diffusion in colloidal suspensions comprising of spherical particles. Here we employ the multi-particle collision dynamics (MPCD) method coupled with a discrete particle model for colloids[49]. Through simulations spanning a wide range of volume fractions, we evaluate the effectiveness of the discrete particle model, comparing the simulation results with existing experimental data, theoretical predictions, and other simulation methods. The different simulation methods employed are described in Chapter 2.

Research investigating the influence of particle shape on colloidal dynamics has been relatively limited. Existing studies on shape-anisotropic colloidal particles primarily focus on rod-like shapes due to their practical interest. However other shapes are equally important to study. A key experimental challenge has been the limited accessibility to high quality shape-anisotropic colloidal particles. While on the theoretical front, the lack of models

capable of handling shape–anisotropic particles has posed limitations. In Chapter 4, we address this gap by extending the discrete particle model to accommodate shape–anisotropic particles[50]. We systematically examine self–diffusion in suspensions of cubes, tetrahedra, octahedra and spherocylinders, across various volume fractions.

1.6 Sedimentation

Sedimentation refers to the phenomena where colloidal particles drift with a constant velocity in response to an external force. This constant velocity is known as sedimentation velocity. An example of such an external force is gravity, which is typically not significant enough to affect colloidal particles due to their small mass. To illustrate this, we can consider the simple case of spherical colloidal particles at infinite dilution. At steady state, the sedimentation velocity \mathbf{v}_s^∞ (the infinity symbol here refers to the infinite dilution limit) is governed by a balance between the external driving force \mathbf{F}_{ext} and the frictional force $\mathbf{F}_{\text{drag}} = -6\pi\eta_0 a\mathbf{v}_s^\infty$ on the colloidal particle. Therefore,

$$\mathbf{v}_s^\infty = \frac{1}{6\pi\eta_0 a}\mathbf{F}_{\text{ext}} \equiv \gamma_0^{-1}\mathbf{F}_{\text{ext}} \quad (1.27)$$

If we assume that the gravity as the external force, then we can derive the sedimentation velocity as,

$$\mathbf{v}_s^\infty = \frac{2}{9} \frac{a^2 \Delta\rho}{\eta_0} \mathbf{g} \quad (1.28)$$

where $\Delta\rho$ is density difference between the colloidal particle and the fluid. For a polystyrene particle of radius $R = 200 \text{ nm}$ in water, the sedimentation velocity would be $\mathbf{v}_s^\infty = 6 \times 10^{-3} \text{ nm/s}$, which is too small to measure. Hence, techniques like centrifugation are needed to artificially increase the force to obtain measurable sedimentation velocities. Alternatively, the sedimentation velocity can be increased by increasing the density difference $\Delta\rho$, such as by lowering the density of the fluid or using particles with a higher density.

In incompressible suspensions, the presence of solvent backflow plays a critical role. In the laboratory frame, the flux of colloidal particles through a cross–section normal to the sedimentation velocity \mathbf{v}_s , is compensated exactly by an opposite flow of the solvent. This equilibrium can be expressed as,

$$\phi\mathbf{v}_s + (1 - \phi)\mathbf{v}_b = 0 \quad (1.29)$$

where ϕ represents the volume fraction of the suspension, and \mathbf{v}_b is the solvent backflow velocity. Solvent backflow tends to obstruct the sedimentation of colloidal particles, thus sedimentation depends on volume fraction of the colloids[32]. Moreover, the influence of hydrodynamic interactions further enhances the dependence on volume fraction.

Sedimentation can be readily characterized by the sedimentation coefficient K , defined as,

$$\mathbf{v}_s = K\gamma_0^{-1}\mathbf{F}_{\text{ext}}. \quad (1.30)$$

Comparing this with Eq. (1.27), we observe that at infinite dilution, $K = 1$.

In Chapter 3, we investigate the sedimentation in colloidal suspensions comprised of spherical particles, employing the discrete particle model for colloids. The simulations cover a wide range of volume fractions, evaluating the discrete particle model and comparing the simulation results with existing experimental data, theoretical predictions, and other simulation methods. Further, in Chapter 4, we also study sedimentation in suspensions of shape–anisotropic colloidal particles.

1.7 Drying of colloidal suspensions

Colloidal systems encountered in real life are often subjected to conditions that give rise to emergent collective behavior such as phase transitions, self–assembly, and pattern formation. Evaporation of colloidal suspensions is a representative example that plays a fundamental role in many practical applications such as coatings[51, 52, 53], ink–jet printing[54, 55], and foods[56]. A common feature across these applications is the structural organization of particles that emerges from the interplay of various factors that include evaporation rate (moving interface), confining geometry, transport properties and particle interactions.

A familiar household example of structure formation due to evaporation is when a coffee drop dries up, leaving a characteristic stain that is darker along the edges[57, 58, 59, 60]. This phenomenon occurs because the droplet’s contact line gets pinned to the substrate. As water evaporates, the pinned edge must be constantly replenished from the interior, leading to a net transport of the coffee particles to the edge.

A geometry of interest for practical applications such as paints and coatings is that of films[62, 63, 64, 65]. As opposed to the coffee–ring effect, in films there is no contact line pinning and water evaporates uniformly from the surface of the film. As water evaporates, the volume fraction of the colloidal particles increases until they get jammed. The arrangement of the colloidal particles in the dried film determines its properties, with closely packed particles forming crystalline films with interesting optical features, while randomly packed particles yield amorphous films.

The critical parameters influencing this process are the evaporation and diffusion rates of colloidal particles. When the air–water interface moves faster than the particle diffusion rate, particles accumulate at the drying interface (skin–layer formation)[62, 66, 61, 67]. Conversely, if the diffusion rate exceeds the interface movement, particles remain homogeneously distributed. The relative importance of advective (evaporation) and diffusive

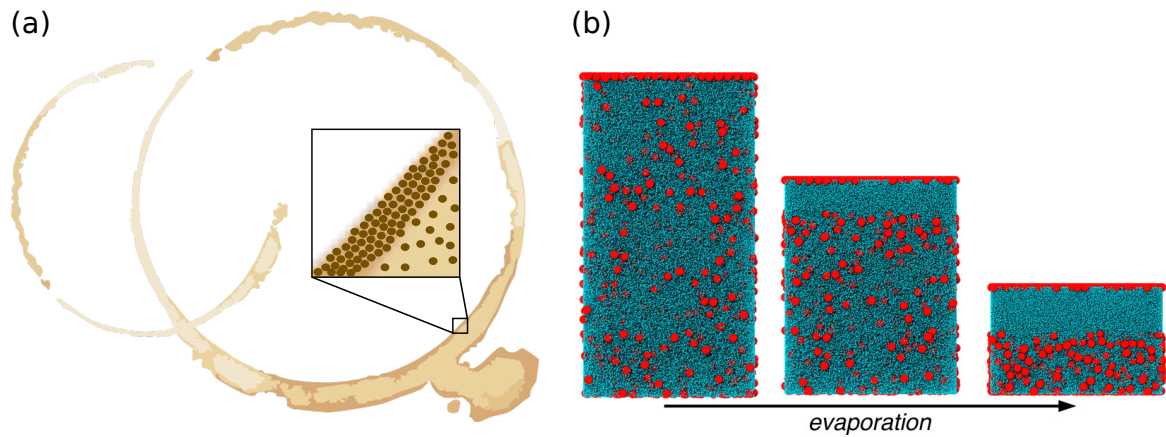


Fig. 1.7: (a) A characteristic stain produced from the evaporation of coffee spills, which is darker on the edges. The zoomed in section is an illustration of how coffee particles are distributed in the ring. (b) Snapshots of a colloidal film, composed of large (red) and small (blue) particles, drying at a constant evaporation rate. Figure adapted from Ref. [61]

transport can be quantified using the dimensionless Péclet number, which is defined as the ratio of the rate of particle advection and diffusion rate of the colloidal particles. In the case of films, Péclet number can be defined as, $Pe = H_0 v / D_0$, where H_0 is the height of the film at the beginning of evaporation, v is the speed of the drying interface, and D_0 is the particle diffusion coefficient[61, 62].

Interesting effects occur in the presence of multiple particle types (sizes), leading to varied diffusion rates and therefore different Péclet numbers. For example, drying of a binary suspension has been observed to exhibit inverted stratification [Fig. 1.7(b)], where the smaller colloids form the top layer[61, 67, 65, 68]. The extent of stratification depends on the particle size ratios, with larger size ratios leading to larger stratified layers. This phenomenon stems from the interplay between colloidal particle diffusion and accumulation at the drying interface, leading to concentration gradients that are more pronounced for larger particles. Leveraging this behavior can facilitate the creation of multilayer coatings in a single step, although it may be disadvantageous when seeking a homogeneous distribution.

1.7.1 Supraparticles

The drying of spherical droplets is another case of particular interest, where the eventually dried assembly of colloidal particles is commonly referred to as a “supraparticle”[69, 70]. Depending on the composition, chemistry, and arrangement of the constituent particles, supraparticles can exhibit emergent properties beyond those of the individual constituent particles[69]. By controlling their emergent behavior, supraparticles have the potential to find applications in various technological fields such as catalysis[71, 72, 73, 74], photonics[75, 76], drug delivery[77], and energy storage[78].

Different synthesis techniques such as spray drying[79, 80], Leidenfrost levitation[81], emul-

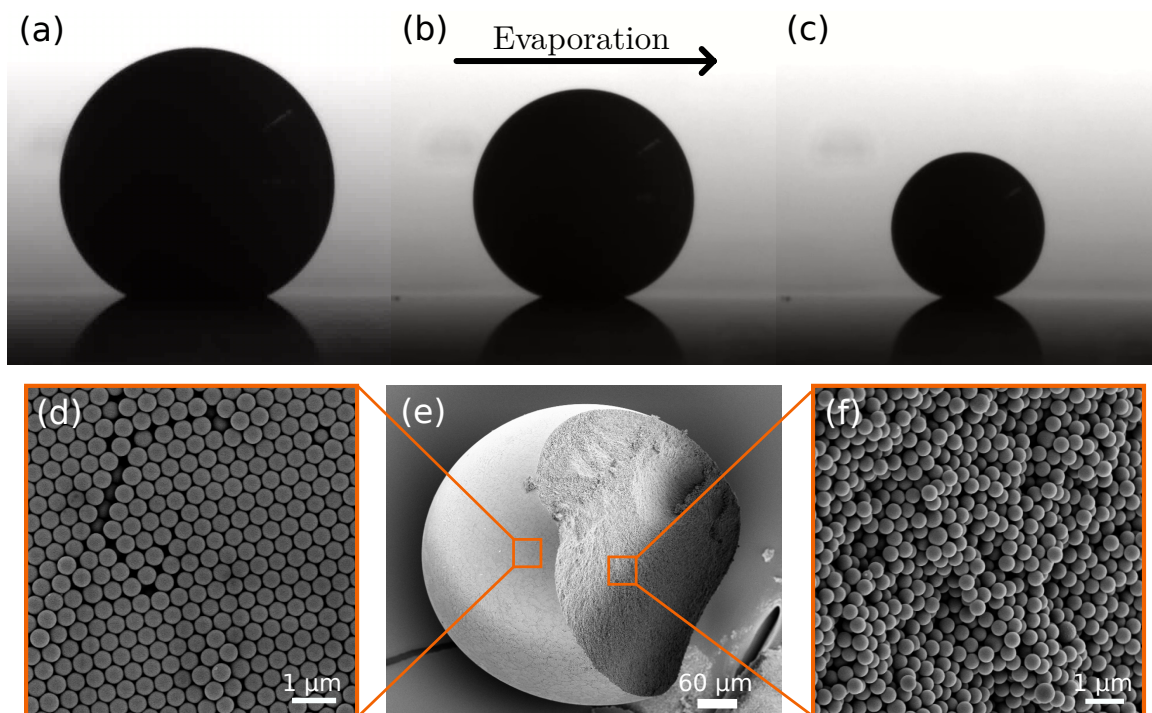


Fig. 1.8: (a–c) Time evolution of a polystyrene (PS) suspension droplet drying on a superamphiphobic surface. The bottom row shows (e) an SEM image of a supraparticle formed after drying of PS suspension droplet, with zoomed in sections of the (d) surface and (f) crosssection.

sion drying[82, 83], and drying from solid surfaces[70, 31, 71], allow for spherical drying geometries. In emulsion drying, small colloidal droplets of one liquid are contained within another immiscible liquid and stabilized by surfactants or emulsifying agents. Examples include, water–in–oil or oil–in–water emulsions. With emulsion drying, one can achieve very slow drying speeds. However, a disadvantage of the method is the need for additional processing liquids, which must be disposed of carefully. This issue is not encountered in other “dry” methods, where the droplets are dried directly through the evaporation of water into air. Spray drying and Leidenfrost levitation are well–known dry assembly methods, which are generally conducted at high temperatures, where drying occurs very quickly. Although these methods are economically attractive, conducting systematic studies to investigate the structure formation in supraparticles using these methods proves challenging[84, 85]. For example, the drying of the droplets can finish within a few seconds, and therefore performing real time experiments can be difficult, requiring sophisticated techniques such as small angle X–ray scattering[86]. The lack of control over the drying speed limits the ability to investigate drying over a range of Péclet number, defined as $Pe = R_0 v_0 / D_0$, for drying droplets. Here R_0 is the initial droplet radius, D_0 is the particle diffusion rate, and $v_0 = \alpha / 8\pi R_0$ is the initial drying speed (α is the rate of change of surface area, which is assumed to be constant)[87].

Another dry assembly method involves evaporation of droplets from solid substrates, where

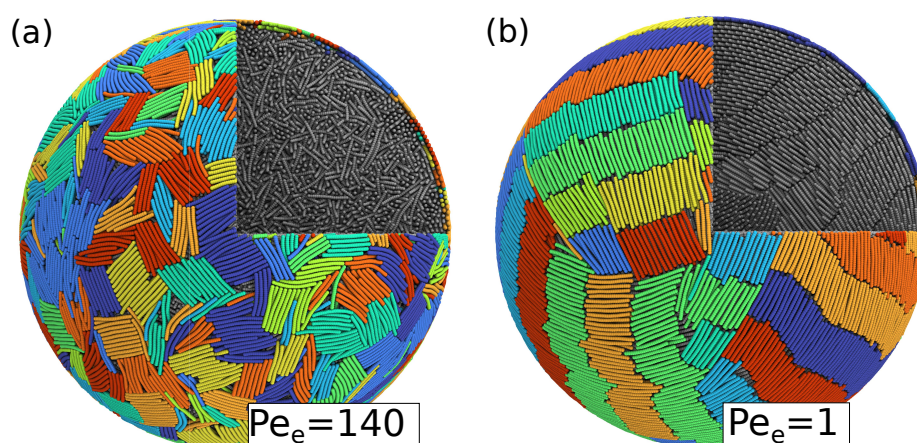


Fig. 1.9: Simulation snapshots of supraparticles (SP) composed of elongated/rod-like particles of aspect ratio 11, formed from (a) fast and (b) slow evaporation. The Péclet numbers of drying are indicated on the bottom right of the snapshots. The ordered clusters on the SP surface are indicated using different colors for visual aid. SP crosssections (first quadrant of the snapshots) show the ordering of rods in the interior – (a) random and (b) ordered bundles.

the pinning of the droplets can be prevented by using superamphiphobic surfaces⁵[88, 89]. Compared to spray drying and Leidenfrost levitation, drying on solid substrates is slower and can be easily controlled, where one can systematically study the effect of drying rates on the structure formation in supraparticles[8].

While utilizing spherical colloidal particles, supraparticles of various structures have been fabricated by controlling parameters such as the evaporation rate and particle compositions. For example, similar to film geometry, drying of binary suspension droplets results in the segregation of colloids based on their sizes, forming a core-shell morphology, with small particles forming the shell[70]. The extent of this stratification depends on the evaporation rate, with faster evaporation leading to greater stratification. Hydrodynamic interactions between suspended particles also influence the structure formation in supraparticles[70, 87].

Highly porous supraparticles have been created from binary suspensions of TiO₂ and polymeric particles, where the polymer particles serve as sacrificial components that can be removed through calcination[71]. The shape and internal structure of supraparticles can be further tuned by modulating the interactions between colloidal particles. As discussed in Sec. 1.2, in a charge stabilized suspension, interactions can be controlled by introducing salt into the medium. Experiments have shown that after the addition of salt, supraparticles transition from crystalline to amorphous structures[31]. Additionally, with increased salt concentration, the shape of supraparticles changes from spherical to non-spherical[31, 8].

In addition to evaporation rate and particle compositions, the shape of colloidal particles is

⁵Superamphiphobic surfaces repel water and non-polar liquids, allowing for droplets to have high contact angles ($> 150^\circ$) and a low contact area between the liquid and solid. Additionally, superamphiphobic surfaces have a porous structure that allows for radially symmetric evaporation.

another crucial factor that can be used to tune the properties of supraparticles. For example, supraparticles made from silica nanorods using emulsion drying showed smectic ordering of the rods on the surface, which could be adjusted by adding salt[90]. The smectic ordering of silica nanorods resulted in enhanced reflectance and scattering efficiency, offering potential applications in ultrabright coatings that could replace the environmentally burdensome TiO_2 nanoparticles traditionally used for this purpose[90]. In another study, supraparticles composed of silica-coated gold nanorods fabricated *via* emulsion drying demonstrated enhanced Raman scattering of analyte molecules when the supraparticles were porous, suggesting applications in material sensing[91].

To that end, in Chapter 5, we investigate the structure formation in supraparticles composed of elongated/rod-like and spherical particles through the evaporation of droplets on a superamphiphobic surface. Through experiments and simulations, we systematically probe the effect of varying the evaporation rate and aspect ratios of particles on the structure formation in the supraparticles. We find that the ordering of the rods can be controlled by the evaporation rate, with slow evaporation leading to more ordered structures [Fig. 1.9]. Additionally, we observe that supraparticle porosity tends to increase with higher evaporation rates and larger aspect ratios. The ability to control the ordering of rods in supraparticles makes them ideal candidates for applications in catalysis and optics.

Mesoscale Molecular Dynamics Simulations

In the modern era of high performance computing, MD simulations are invaluable tools that allow us to probe the “evolution” of molecular systems at resolutions often impossible to reach in experiments. By offering insights at the molecular level, MD simulations can complement experiments and assist in the design of novel functional materials, drug molecules and polymers.

The basic workflow of MD simulations is similar to that of experiments. It begins with the initialization of a system consisting of N particles with positions $\mathbf{r}_1, \mathbf{r}_2, \dots, \mathbf{r}_N$ and velocities $\mathbf{v}_1, \mathbf{v}_2, \dots, \mathbf{v}_N$ in a simulation box. Then, by choosing appropriate interactions in the system, we can compute forces between the particles and update their positions and velocities accordingly using the Newton’s equations of motion. When one is interested in equilibrium processes, this step is repeated until the system is equilibrated, *i.e.*, the properties of the system fluctuate around stable average values over time (energy minimization). Post equilibration, production runs are conducted where we measure the necessary quantities.

Integrating Newton’s equations of motion allows us to describe a system in the microcanonical (NVE) ensemble. However, to simulate experimental conditions, it is desirable to perform simulations at constant temperature or pressure. Several algorithms are available for controlling the temperature and pressure of the system, which are known as thermostats and barostats, respectively. Depending on which state variables are held constant, one can perform simulations in different statistical ensembles – NVE, NVT, NPT.

Depending on the time and length scales of the phenomena of interest, one must choose appropriate representations and interactions in the system. For example, atomistic simulations offer the finest resolution where each atom is treated as an individual particle. These simulations are useful to study phenomena such as chemical reactions, protein–ligand interactions, or identifying drug–target interactions. But the high level of accuracy comes at the cost of high computational resources. When the time and length scales of interest are much larger, then atomistic simulations become unfeasible. This limitation can be overcome through a process known as *coarse-graining*, where a group of atoms/molecules are represented as an individual particle and the coarse-grained interaction potentials take an effective form.

Typically, in mesoscale systems, the number of solvent particles outnumber the colloidal/polymeric particles by several orders and therefore take up a large portion of the computational power. In many cases, the actual dynamics of the solvent is not of particular interest.

Therefore, in such systems coarse-grained simulations are the preferred method that try to eliminate/reduce the degrees of freedom of the solvent through various approximations. There are several coarse-grained methods at one's disposal.

One approach is to completely eliminate the solvent and incorporate its effect through the equations of motion. Such methods are referred to as *implicit solvent* methods, which include Brownian dynamics and Langevin dynamics. The Brownian dynamics method is discussed in greater detail in Sec. 2.1.

Instead of completely eliminating the solvent, a class of mesoscale simulation methods employ a simplified description of the solvent which is computationally less demanding than the atomistic description, but retains properties resembling real solvents. Such methods include MPCD[40, 46, 44, 45, 92], and lattice Boltzmann method[40, 93, 47]. The MPCD method is discussed in greater detail in Sec. 2.2.

2.1 Brownian dynamics

Brownian dynamics (BD) simulation is a well-known method that takes advantage of the large time-scale separations of the colloidal and solvent particle dynamics and replaces the solvent-colloid interactions with a stochastic force. It describes a system in the canonical (NVT) ensemble.

At the core of Brownian dynamics lies the Langevin equation as discussed in Sec. 1.3. In the overdamped limit, the inertial term vanishes and the dynamics can be written as,

$$\frac{d\mathbf{r}}{dt} = \frac{1}{\gamma_0}(\mathbf{F}_C + \mathbf{F}_R) \equiv \frac{D_0}{k_B T}(\mathbf{F}_C + \mathbf{F}_R) \quad (2.1)$$

where D_0 and γ_0 are the diffusion coefficient and friction coefficient at infinite dilution. Here \mathbf{F}_C is the total systematic force on the particle and \mathbf{F}_R is a random force due to collisions with solvent particles.

Equation (2.1) ignores the solvent mediated hydrodynamic interactions between colloidal particles and any memory effects in the random force. To account for these interactions, a configuration-dependent diffusion coefficient is introduced, modifying the displacement equation to[94],

$$\Delta\mathbf{r} = \frac{\mathbf{D}}{k_B T} \cdot \mathbf{F}_C \Delta t + \nabla \cdot \mathbf{D} \Delta t + \mathbf{R}, \quad (2.2)$$

where \mathbf{D} is a $3N \times 3N$ diffusion tensor that depends upon the instantaneous positions of all the N particles, and \mathbf{R} is a random displacement having a Gaussian distribution with zero mean and covariance $\langle \mathbf{R}\mathbf{R} \rangle = 2\mathbf{D}\Delta t$.

In the absence of hydrodynamic interactions the diffusion tensor is diagonal and constant,

$$\mathbf{D}_{ij} = \delta_{ij} \frac{k_B T}{6\pi\eta_0 a} \quad (2.3)$$

where δ_{ij} is the Kronecker delta function. In this case, $\nabla \cdot \mathbf{D} = 0$ and therefore the average displacement of a particle depends only on the force acting on it.

In the presence of hydrodynamic interactions, the diffusion tensor can be approximated using the Rotne–Prager–Yamakawa (RPY) tensor[41, 42, 40], where the diagonal elements remain as in Eq. (2.3) and the off–diagonal elements are,

$$\mathbf{D}_{ij} = \begin{cases} \left(\frac{k_B T}{8\pi\eta r_{ij}} \right) \left[\left(1 + \frac{2a^2}{3r_{ij}^2} \right) \mathbf{I} + \left(1 - \frac{2a^2}{r_{ij}^2} \right) \hat{\mathbf{r}}_{ij} \hat{\mathbf{r}}_{ij} \right], & r_{ij} \geq 2a \\ \left(\frac{k_B T}{6\pi\eta a} \right) \left[\left(1 - \frac{9}{32} \frac{r_{ij}}{a} \right) \mathbf{I} + \frac{3}{32} \frac{r_{ij}}{a} \hat{\mathbf{r}}_{ij} \hat{\mathbf{r}}_{ij} \right], & r_{ij} < 2a \end{cases} \quad (2.4)$$

where $\hat{\mathbf{r}}_{ij} = \mathbf{r}_{ij}/r_{ij}$. This tensor also has zero divergence, $\nabla \cdot \mathbf{D} = 0$. The average displacement of a particle depends not only on the force acting on it, but also on the positions of all other particles in the system. We must keep in mind that the RPY tensor is only a leading approximation for the hydrodynamic interactions and assumes pairwise additivity (ignoring the multi–body effects involving three or more particles)[95, 40].

2.2 Multi–particle collision dynamics

MPCD is a simulation technique that coarse–grains the solvent into a functional and computationally inexpensive form, where the idea is to preserve momentum conservation and reproduce certain properties of real solvents, such as the kinematic viscosity and diffusivity, which are closely connected with the propagation of hydrodynamic interactions. The coarse–grained solvent is coupled to the solute particles using suitable models to achieve hydrodynamic coupling between the solute particles[40].

2.2.1 Algorithm

The MPCD solvent is modeled as N point–like particles of mass m that move in continuous space *via* alternating streaming and collision steps that occur at a regular time interval Δt_c . The assumption of point–like particles means that the solvent particles do not interact with each other through an interaction potential and obey an ideal gas equation of state.

During the streaming step, the solvent positions and velocities are updated as[49, 46, 44],

$$\begin{aligned} \frac{d\mathbf{r}_i}{dt} &= \mathbf{v}_i \\ m \frac{d\mathbf{v}_i}{dt} &= \mathbf{F}_i, \end{aligned} \quad (2.5)$$

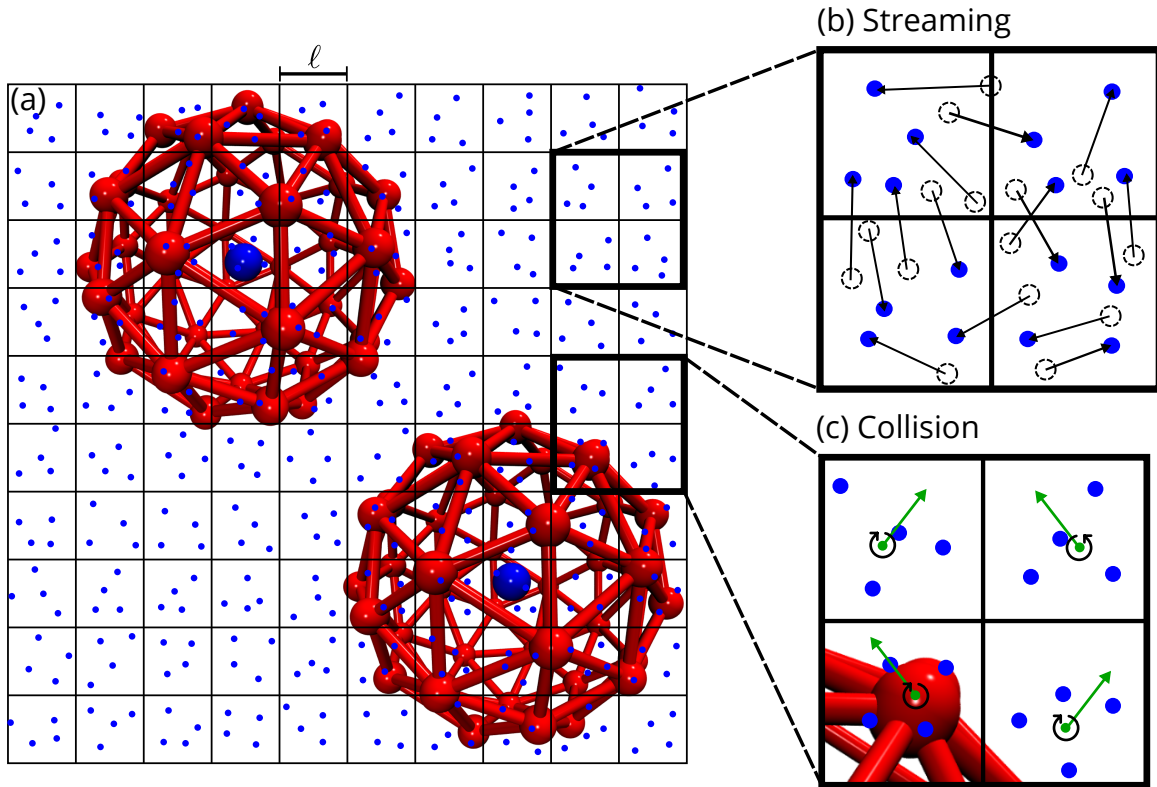


Fig. 2.1: (a) Illustration of colloids (solute) immersed in an MPCD solvent, with the colloidal particles described using the discrete particle model. The figure shows a two dimensional projection of a three dimensional system for ease of understanding. (b) During the streaming step, solvent particles move according to Eq. (2.5). The solute particles move according to the classical MD algorithm whose timestep Δt is generally at least an order smaller then the MPCD streaming timestep Δt_c . (c) In the collision step, solvent and solute particles exchange momentum locally, according to Eq. (2.6).

where $\mathbf{r}_i(t)$ is the position, $\mathbf{v}_i(t)$ is the velocity of particle i , and $\mathbf{F}_i(t)$ is any external force acting on the solvent [Fig. 2.1(b)].

After streaming, the particles undergo multi-particle collisions where they exchange momentum locally. There are multiple algorithms that have been proposed, but they have a common feature: They are spatially restricted such that their effects are “local”[40, 44]. Here we consider the widely used stochastic rotation dynamics (SRD) scheme first proposed by Malevanets and Kapral [Fig. 2.1(c)][45].

To perform collisions, particles are first sorted into smaller cubic collision cells of edge length ℓ , where they only interact with members of their own cell. The average number of particles per cell ρ_0 is fixed and is typically chosen between 3 and 20[46]. The actual number of particles in a cell can vary during the simulations. The collision step involves a stochastic rotation of the particle velocities in every collision cell,

$$\mathbf{v}_i \leftarrow \mathbf{u}_j + \boldsymbol{\Omega}_j \cdot (\mathbf{v}_i - \mathbf{u}_j), \quad (2.6)$$

where \mathbf{u}_j is the center of mass velocity of particles in cell j , and $\mathbf{\Omega}_j$ is the rotation operator for cell j . Typically, $\mathbf{\Omega}_j$ rotates the velocities by a fixed angle α around a randomly chosen axis, which is mutually independent for every cell.

Malevanets and Kapral showed that the SRD algorithm obeys an H–theorem, meaning that at equilibrium the solvent particle velocities have a Maxwellian distribution and the algorithm reproduces the correct hydrodynamic equations with an ideal–gas equation of state[45]. However, discretizing the simulation box into a cubic grid can lead to the loss of Galilean invariance, which is most pronounced when the mean free path of the solvent particles is smaller than the cell size ℓ , as the solvent particles remain correlated over multiple collisions[92, 45]. To retain Galilean invariance, the collision grid is shifted before the collision step, by a random vector whose components are drawn from a uniform distribution in the range $[-\ell/2, \ell/2]$ [96, 97]. Additionally, grid shifting also accelerates momentum transfer between cells and can influence the transport coefficients of the solvent.

2.2.2 Solvent mapping

The natural system of units sufficient to describe the properties of the MPCD solvent are the collision cell edge–length ℓ , solvent particle mass m , and the energy $k_B T$. Subsequently we can derive the unit of time as $\tau = \sqrt{m\ell^2/k_B T}$, and solvent mass density $\rho = \rho_0 m/\ell^3$.

The simplicity of the SRD algorithm allows for the analytical calculation of different transport properties of the solvent particles, which prove useful to efficiently tune the solvent without having to run additional simulations. The diffusion coefficient of a solvent particle, within the random–collision approximation is derived as[98],

$$\frac{D}{D_0} = \lambda \left[\frac{3}{2(1 - \cos \alpha)} \left(\frac{\rho_0}{\rho_0 - 1} \right) - \frac{1}{2} \right] \quad (2.7)$$

where $D_0 = \ell^2/\tau$, and $\lambda = \Delta t_c/\tau$ is the dimensionless mean free path of the solvent particles.

In addition the kinematic viscosity $\nu_0 = \eta_0/\rho$ can also be determined analytically with the means of kinetic theory[99]. The total kinetic viscosity, $\nu_0 = \nu_{\text{kin}} + \nu_{\text{coll}}$, is the sum of the kinetic and collisional contributions. In three dimensions, they are given as[99, 100, 101],

$$\begin{aligned} \frac{\nu_{\text{kin}}}{\ell^2/\tau} &= \lambda \left[\frac{1}{4 - 2 \cos \alpha - 2 \cos 2\alpha} \frac{5\rho_0}{\rho_0 - 1} - \frac{1}{2} \right], \\ \frac{\nu_{\text{coll}}}{\ell^2/\tau} &= \frac{1}{\lambda} \frac{(1 - \cos \alpha)}{18} \left(1 - \frac{1}{\rho_0} \right) \end{aligned} \quad (2.8)$$

For typical SRD parameters of $\alpha = 130^\circ$, $\rho_0 = 5 \ell^{-3}$, and $\Delta t_c = 0.1 \tau$, the analytic expressions predict solvent diffusivity $D = 0.064 \ell^2/\tau$ and total kinematic viscosity $\nu_0 = 0.79 \ell^2/\tau$, implying a dynamic viscosity $\eta_0 = 3.95 k_B T \tau/\ell^3$. The analytic prediction for kinematic

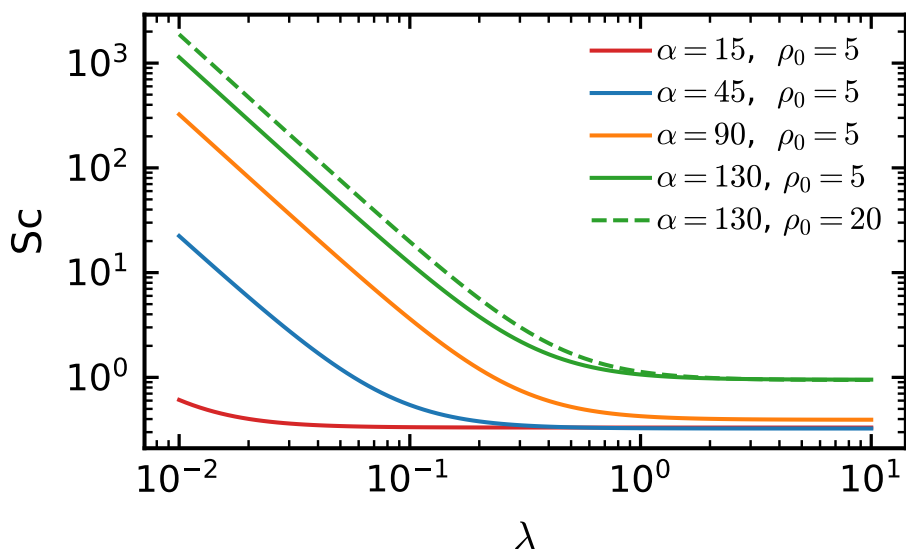


Fig. 2.2: Theoretical estimate for Schmidt number Sc versus dimensionless mean free path λ for various values of α and ρ_0 .

viscosity has been verified with measurements from simulations of Poiseuille flows[102, 99]. However, the analytic estimate for the diffusion coefficient is lower than that measured in direct simulations which is argued to originate from the lack of hydrodynamic correlations in the analytic derivations[44, 99].

We note from Eq. (2.8) that, for a large α and small λ , $\nu_{\text{coll}} > \nu_{\text{kin}}$. Conversely, for a small α and large λ , $\nu_{\text{kin}} > \nu_{\text{coll}}$. This means that kinetic transport is dominant when the mean free path is large and the rotation angle is small, implying little exchange of momentum between particles during collisions. This condition is characteristic of gases and the opposite is true in liquids. A suitable measure to characterize fluids is through the dimensionless Schmidt number $Sc = \nu_0/D$, which is defined as the ratio between momentum transport (ν_0) and mass transport (D). The Schmidt number is on the order of unity for gases, while for liquids it is between 10^2 to 10^3 . Figure 2.2 shows how the Schmidt number varies with the three parameters: λ , α , and ρ_0 . Clearly, for a given λ , the Schmidt number can be maximized by increasing the rotation angle α and ρ_0 . However, the impact of increasing ρ_0 on the Schmidt number is only marginal.

2.2.3 Solute–solvent coupling

MPCD is an attractive method for modeling soft matter systems with hydrodynamic interactions due to its flexibility and compatibility with various solutes such as polymers[103], colloids[49, 104], and membranes[105]. Typically, the solute and the MPCD solvent are coupled using a hybrid MD and MPCD scheme. In this approach, solute particles are treated as regular MD particles that exchange momentum with the MPCD solvent during the streaming

and/or collision steps.

During the streaming step, the solute–solvent coupling involves the reflection of solvent particles from the solute surface to achieve slip or no–slip boundary conditions. In the collision step, solute particles participate similarly to solvent particles, but with the distinction of being treated as “heavy” particles. This means their contribution to the center of mass velocity in a particular cell is higher[44].

Modeling of colloidal particles with MPCD using the reflection based approach has proven to be challenging[44]. Reflection of solvent particles from the solute surface often results in collision cells that are underfilled or completely devoid of solvent particles, leading to abrupt changes in local solvent properties, such as diffusion [Eq. (2.7)] and viscosity [Eq. (2.8)]. To mitigate these effects, virtual solvent particles are introduced during the collision step. Instead some studies model the solute–solvent and solute–solute interactions with short–ranged repulsive pair potentials, while the solvent–solvent interactions are mediated through the MPCD collisions[92, 98, 106, 107, 108]. In addition to the problem of partially filled cells, this method can introduce subtleties at the solvent–colloid interface, potentially leading to spurious depletion interactions, that need careful handling/parameterization[98].

These complexities were overcome by representing colloidal particles as a mesh of point (“vertex”) particles connected via harmonic springs[109]. In this model, the vertex particles are coupled to the solvent particles through momentum exchange in the collision step and allow solvent particles to move freely through the colloidal particles, thereby eliminating the need for virtual particles. This discrete-particle model simplifies the simulation and reduces computational overhead. In Chapter 3, this model is employed to characterize the transport properties of colloids, such as self–diffusion and sedimentation[49]. Chapter 4 extends the discrete–particle model to accommodate shape–anisotropic particles, further demonstrating the model’s versatility and robustness in handling complex soft matter systems[50].

Title: “Diffusion and sedimentation in colloidal suspensions using multiparticle collision dynamics with a discrete particle model.”

Contributions:

- **Simulation setup and execution:** I was responsible for setting up and executing simulations for this study. This involved writing scripts to construct colloidal particles as a spherical/cubic mesh, setting up the bulk systems consisting of the colloids and the MPCD solvent, troubleshooting issues that arose during the simulations and refining model parameters as necessary.
- **Data analysis:** I analyzed the simulation trajectories to measure the self-diffusion and sedimentation coefficients.
- **Comparative simulations:** I performed additional simulations using other well-known methods to validate and test the accuracy of our model. The simulation results were additionally compared with experimental observations which served as the exact results.
- **Figure preparation:** I created the plots shown in the paper, ensuring that they clearly communicated the key findings.
- **Manuscript contribution:** I contributed to writing and revising the manuscript.

Reprint permissions:

Reprinted from “Yashraj M. Wani, Penelope Grace Kovakas, Arash Nikoubashman, Michael P. Howard; Diffusion and sedimentation in colloidal suspensions using multiparticle collision dynamics with a discrete particle model. *J. Chem. Phys.* 14 January 2022; 156 (2): 024901. <https://doi.org/10.1063/5.0075002>,” with the permission of AIP Publishing.

Diffusion and sedimentation in colloidal suspensions using multiparticle collision dynamics with a discrete particle model

Cite as: J. Chem. Phys. 156, 024901 (2022); doi: 10.1063/5.0075002

Submitted: 12 October 2021 • Accepted: 21 December 2021 •

Published Online: 13 January 2022



View Online



Export Citation



CrossMark

Yashraj M. Wani,¹  Penelope Grace Kovakas,² Arash Nikoubashman,^{1,a)}  and Michael P. Howard^{2,a)} 

AFFILIATIONS

¹Institute of Physics, Johannes Gutenberg University Mainz, Staudingerweg 7, 55128 Mainz, Germany

²Department of Chemical Engineering, Auburn University, Auburn, Alabama 36849, USA

^{a)}Authors to whom correspondence should be addressed: anikouba@uni-mainz.de and mphoward@auburn.edu

ABSTRACT

We study self-diffusion and sedimentation in colloidal suspensions of nearly hard spheres using the multiparticle collision dynamics simulation method for the solvent with a discrete mesh model for the colloidal particles (MD+MPCD). We cover colloid volume fractions from 0.01 to 0.40 and compare the MD+MPCD simulations to experimental data and Brownian dynamics simulations with free-draining hydrodynamics (BD) as well as pairwise far-field hydrodynamics described using the Rotne–Prager–Yamakawa mobility tensor (BD+RPY). The dynamics in MD+MPCD suggest that the colloidal particles are only partially coupled to the solvent at short times. However, the long-time self-diffusion coefficient in MD+MPCD is comparable to that in experiments, and the sedimentation coefficient in MD+MPCD is in good agreement with that in experiments and BD+RPY, suggesting that MD+MPCD gives a reasonable description of hydrodynamic interactions in colloidal suspensions. The discrete-particle MD+MPCD approach is convenient and readily extended to more complex shapes, and we determine the long-time self-diffusion coefficient in suspensions of nearly hard cubes to demonstrate its generality.

Published under an exclusive license by AIP Publishing. <https://doi.org/10.1063/5.0075002>

I. INTRODUCTION

The dynamics of nanometer- or micrometer-sized colloidal particles (“colloids”) suspended in a solvent control many processes, ranging from the nanoscale assembly of functional materials¹ and transport in biological systems² to industrial-scale processes such as enhanced oil recovery.³ The motion of the colloids is dictated by not only direct interactions between the suspended particles, such as dispersion forces or electrostatics, but also fluctuating hydrodynamic forces exerted by the solvent.⁴ The many-body hydrodynamic interactions in colloidal suspensions are typically described theoretically using a low-Reynolds-number treatment of the solvent.^{5–7} These equations are challenging to solve for all but a handful of special theoretical cases, so numerical approaches are frequently required. Here, we restrict our discussion to particle-based computer simulation techniques that are well-suited for describing suspensions with thermal fluctuations and complex chemistries.

Particle-based computer simulations that fully resolve both the suspended colloids and solvents [e.g., atomistic molecular dynamics (MD)] are prohibitively expensive for reaching the long time scales and large length scales that are practically relevant, necessitating the use of coarse-grained models.⁸ In these models, the colloids are resolved explicitly, while the thermodynamic and hydrodynamic effects of the solvent are captured either implicitly or using a simplified description. Brownian dynamics (BD) is a classic implicit-solvent technique⁹ that, in its simplest form, neglects hydrodynamic forces other than single-colloid drag (the free-draining approximation). Hydrodynamic forces between colloids can be introduced to BD by an appropriate hydrodynamic tensor,¹⁰ as in the Rotne–Prager–Yamakawa^{11,12} (BD+RPY) or Stokesian dynamics approaches.^{13,14} These techniques are powerful and computationally efficient because they do not need to capture details of the solvent; however, the correct hydrodynamic tensor must be known, which can be challenging for complex particle shapes or bounded geometries.

An alternative family of “mesoscale” simulation methods, which includes multiparticle collision dynamics (MPCD),^{8,15,16} dissipative particle dynamics,^{17,18} and the lattice Boltzmann method,^{19,20} retains an explicit solvent but uses a simplified model with similar physical properties to the real solvent. The colloids are coupled to the solvent so that hydrodynamic forces between them emerge naturally within the model. Hence, these approaches are generally more compatible with complex particles and geometries; however, there are still active questions about how the solvent properties and coupling scheme affect the hydrodynamic forces and, in particular, whether they reproduce low-Reynolds-number results in appropriate limits.^{21–23} The focus of this article is on the MPCD method, which is the newest of the three mesoscale approaches listed above. In MPCD, the solvent is modeled as point particles that interact with each other through stochastic collisions in spatially localized cells.¹⁵ Depending on the collision scheme, the MPCD solvent has properties of a gas-like or liquid-like (typically Newtonian) fluid.²⁴

Numerous approaches have been proposed for coupling colloids to the MPCD solvent. Several studies modeled the colloids as smooth spheres that interact with the solvent through a short-ranged repulsive pair potential,^{25–28} however, this coupling can only give slip boundary conditions on the colloids. Inoue *et al.* proposed an alternative approach where the solvent is stochastically scattered from the colloids,²⁹ transferring both translational and rotational momentum to produce no-slip boundary conditions. The resulting dynamics of a single colloid were in good agreement with theoretical predictions,³⁰ while the colloid long-time self-diffusion coefficients in suspensions were slightly larger than those in reference simulations using fast lubrication dynamics.³¹ This coupling scheme has been used to study many processes including sedimenting³² and sheared^{33,34} suspensions. We note, however, that the stochastic reflection procedure approximates the colloid surface as an infinite plane, which limits its application to particles with a low curvature and when the mean free path of the solvent particles is small compared to the colloid diameter;³³ this assumption can be relaxed by reflecting the solvent from the surface as an elastic collision.³⁵

All of these reflection-based coupling schemes suffer from a few practical drawbacks. First, reflection may introduce spurious depletion forces between colloids that must be carefully handled.^{26,33} Second, the presence of impenetrable solid surfaces inevitably leads to partially filled collision cells; this alters the local solvent properties near the surfaces and requires the insertion of “virtual” solvent particles inside the moving colloids.^{36–38} Finally, performing the reflection requires pairwise collision detection between the solvent and colloids, which is computationally expensive due to the large number of solvent particles. These issues are exacerbated in dense suspensions.

To circumvent these problems, Poblete *et al.* recently proposed a discrete particle model³⁹ that represents a colloid as a mesh of point particles (“vertex particles”) connected by elastic springs (Fig. 1).^{40–42} Unlike in reflection-based coupling schemes, the colloid is fully penetrable to the solvent, and the vertex particles couple to the solvent only during the stochastic collision. In addition to the benefits of addressing physical and computational challenges associated with reflection-based coupling, this model is compatible with arbitrary colloid shapes, such as spherocylinders,⁴³ and with complex surface patterns.^{43,44} The hydrodynamic properties of a

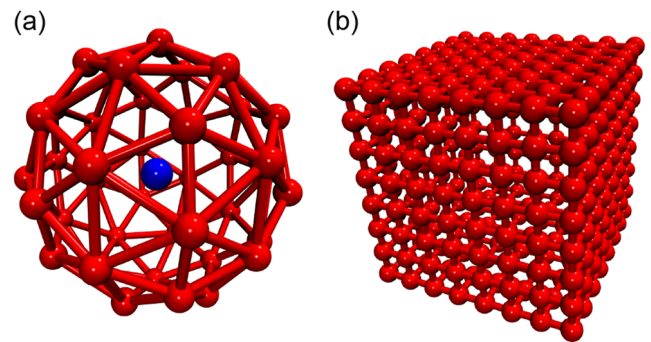


FIG. 1. Discrete particle model for (a) a spherical colloid with a radius of $a = 3\ell$ and (b) a cubic colloid with a diameter of $d = 6\ell$. The N_v vertex particles and bonds between nearest neighbors are shown in red. The central particle for the spherical colloid is shown in blue; particle sizes have been reduced for clarity. Rendered using Visual Molecular Dynamics (version 1.9.3).⁴⁹

single such colloid were studied for various degrees of discretization, finding good agreement with low-Reynolds-number theoretical predictions when one vertex particle occupied approximately one collision cell.³⁹ To our knowledge, however, the properties of suspensions represented using this colloid model in MPCD have not been studied in detail. Characterizing the transport properties of colloidal suspensions is not only of fundamental interest in its own right but also important for reliably applying similar models to more complex soft-matter systems.

Here, we perform bulk simulations of a colloidal suspension of nearly hard spheres using MPCD with a discrete particle model. We characterize the short-time and long-time self-diffusive motion from equilibrium simulations and the sedimentation coefficients from nonequilibrium simulations. We compare these simulations to BD and BD+RPY simulations as well as experimental data and low-Reynolds-number theoretical predictions as functions of volume fraction, finding good agreement for some quantities but discrepancies in others. To demonstrate the generality of the discrete particle model, we also simulate a colloidal suspension of nearly hard cubes and report the long-time self-diffusion coefficient as a function of volume fraction. Overall, we find that MPCD with a discrete particle model is convenient to implement and gives a good description of colloidal suspension dynamics.

II. MODELS

A. Multiparticle collision dynamics

The MPCD solvent consists of point particles, each having a position \mathbf{r}_i , a velocity \mathbf{v}_i , and the same mass m , whose motion is governed by alternating streaming and collision steps.^{8,16} During the streaming step, the solvent particles move according to Newton's equations of motion,

$$\begin{aligned} \frac{d\mathbf{r}_i}{dt} &= \mathbf{v}_i, \\ m_i \frac{d\mathbf{v}_i}{dt} &= \mathbf{F}_i, \end{aligned} \quad (1)$$

where m_i is the mass of particle i and \mathbf{F}_i is the force acting on it. In the case of a constant (or zero) force acting on each particle, these equations may be analytically integrated to give the equations of ballistic motion, while more complex forces require a numerical integration scheme.⁹

A stochastic multiparticle collision is performed at equal time intervals between streaming steps. During this collision step, each particle is assigned to a cubic cell of edge length ℓ to undergo a spatially localized momentum exchange. To ensure Galilean invariance,⁴⁵ the collision cells are shifted along each Cartesian axis by a random amount drawn uniformly on $[-\ell/2, +\ell/2]$. In this work, we apply the stochastic rotation dynamics (SRD) collision scheme without angular momentum conservation,¹⁵ where the particle velocities are updated during the collision by

$$\mathbf{v}_i \leftarrow \mathbf{u}_j + \mathbf{\Omega}_j \cdot (\mathbf{v}_i - \mathbf{u}_j), \quad (2)$$

where \mathbf{u}_j is the center-of-mass velocity and $\mathbf{\Omega}_j$ is the rotation operator of the cell j that contains particle i . The rotation operator is chosen to have a fixed rotation angle but a random rotation axis for each cell. During the collision, we apply a cell-level Maxwellian thermostat to maintain a constant temperature T .⁴⁶ Both the streaming and collision steps conserve linear momentum, and hydrodynamic interactions in the solvent are approximately reproduced down to the cell size.^{28,47}

The natural system of units describing the MPCD solvent is defined by the mass m of a solvent particle, the length ℓ of a collision-cell edge, and the energy scale $k_B T$ with k_B being Boltzmann's constant; the resulting unit of time is $\tau = \sqrt{m\ell^2/\beta}$ with $\beta = 1/(k_B T)$. We adopted standard SRD parameters—a collision time of 0.1τ , an average solvent number density of $\rho_0 = 5\ell^{-3}$, and a rotation angle of 130° —resulting in a liquid-like Newtonian fluid with dynamic viscosity $\eta_0 = 3.95 \pm 0.01 k_B T \tau / \ell^3$ and kinematic viscosity $\nu_0 = \eta_0 / (\rho_0 m) = 0.79 \ell^2 / \tau$.⁴⁸

B. Discrete particle model for colloids

The spherical colloids were coupled to the MPCD solvent using a discrete particle model [Fig. 1(a)].³⁹ Each colloid was represented by N_v vertex particles on the surface of a sphere of radius a . An additional particle was placed at the center of the sphere and used to compute excluded-volume interactions between colloids (see below). The positions of the vertices were generated by recursively subdividing the faces of a regular icosahedron into equilateral triangles and then radially scaling the vertices to a distance a from the center of the sphere. Note that the scaling procedure distorts the triangular faces so that the separations between neighboring vertices may no longer be equal. The resulting shape is sometimes referred to as an icosphere.

To maintain the surface-mesh shape, the vertex particles were connected with their nearest neighbors and with the central particle using a harmonic potential,

$$\beta u_b(r) = \frac{k}{2} (r - r_b)^2, \quad (3)$$

where r and r_b are the actual and desired distances between bonded particles, respectively. We set the spring constant to $k = 5000\ell^{-2}$ to ensure the (nearly) rigid shape of the colloid.³⁹ In this work, we

used a sphere radius of $a = 3\ell$ and subdivided the icosahedron once, resulting in $N_v = 42$ vertex particles and bond lengths $r_b = 1.64\ell$, 1.85ℓ , and 3ℓ . We set the mass of each vertex particle and the central particle equal to the average mass of the solvent in a collision cell ($m_v = 5m$), giving a total colloid mass of $M = (N_v + 1)m_v = 215m$.

To represent hard-sphere excluded-volume interactions between colloids, the central particles interacted through the core-shifted Weeks–Chandler–Andersen potential,⁵⁰

$$\beta u(r) = \begin{cases} 4 \left[\left(\frac{\sigma}{r - \Delta} \right)^{12} - \left(\frac{\sigma}{r - \Delta} \right)^6 \right] + 1, & r \leq r^* \\ 0, & \text{otherwise,} \end{cases} \quad (4)$$

where r is the distance between two central particles, and we used $\sigma = 1.0\ell$, $\Delta = 5.0\ell$, and $r^* = \Delta + 2^{1/6}\sigma \approx 6.12\ell$. This potential is purely repulsive and gives an effective hard-sphere diameter of 6.02ℓ upon mapping the second virial coefficient, in good agreement with the nominal diameter $d = 6\ell$.

The vertex particles (but not the central particle) were coupled to the MPCD solvent through the collision step³⁹ [Eq. (2)] with appropriate treatment of the different particle masses when computing the center-of-mass velocity of a cell and applying the thermostat. Between collisions, the positions and velocities of the vertex particles and the central particle were evolved according to Newton's equations of motion [Eq. (1)] using a velocity Verlet integration scheme with a time step of 0.005τ , as in traditional MD simulations.⁹ Accordingly, we will refer to the discrete particle model coupled to the MPCD solvent as MD+MPCD in the rest of this article.

C. Brownian dynamics

To facilitate the assessment of the MD+MPCD model, we also performed Brownian dynamics simulations using both free-draining hydrodynamics (BD) and pairwise far-field hydrodynamics (BD+RPY).^{9–12} These models are popular and have well-defined hydrodynamic interactions, so they serve as useful reference points for understanding the solvent-mediated interactions that emerge in the MD+MPCD model. A single colloid at infinite dilution in a Newtonian fluid diffuses according to the Stokes–Einstein relationship, $D_0 = k_B T / \gamma_0$, at times much longer than the inertial (Brownian) time scale $\tau_B = M / \gamma_0$. For spheres with no-slip boundary conditions, the friction coefficient is $\gamma_0 = 6\pi\eta_0 a$, so $D_0 = 4.48 \times 10^{-3} \ell^2 / \tau$ and $\tau_B = 0.96\tau$ for the MPCD solvent (Sec. II A). This inertial time is much less than the time required for a colloid to diffuse its own radius $\tau_0 = a^2 / D_0 \approx 2.0 \times 10^3 \tau$, justifying the neglect of colloid inertia that is implicit to Brownian dynamics simulations.

We represented each colloid using only the central particle, as vertex particles are not required for Brownian dynamics simulations of bulk suspensions of spheres, using the same colloid interactions given by Eq. (4). Considering only the translation of the colloids in the low-Reynolds-number limit, the vector of positions of all colloids $\mathcal{R} = (\mathbf{r}_1, \mathbf{r}_2, \dots)$ changes by $\Delta\mathcal{R}$ over a time Δt according to¹⁰

$$\Delta\mathcal{R} = [\mathcal{M} \cdot \mathcal{F} + k_B T (\nabla \cdot \mathcal{M})] \Delta t + \Delta\mathcal{W}, \quad (5)$$

where \mathcal{M} is the mobility tensor coupling the translation of each colloid to the vector of forces on all of the colloids $\mathcal{F} = (\mathbf{F}_1, \mathbf{F}_2, \dots)$ and

$\Delta\mathcal{W}$ is the vector of random displacements of all colloids having a Gaussian distribution with zero mean and covariance $\langle \Delta\mathcal{W}\Delta\mathcal{W} \rangle = 2k_B T \mathcal{M} \Delta t$. The divergence of \mathcal{M} is taken with respect to \mathcal{R} .^{10,51}

The hydrodynamic interactions that are present in the simulations are determined by the choice of \mathcal{M} . Stokesian dynamics includes both near-field (lubrication) and far-field coupling in \mathcal{M} and can also include torques and stresslets,¹⁴ but has a corresponding large computational cost. Here, we use the simpler but reasonably accurate approximation that the entries of \mathcal{M} are given pairwise,

$$\mathcal{M} = \begin{pmatrix} \mathbf{M}^{(11)} & \mathbf{M}^{(12)} & \dots \\ \mathbf{M}^{(21)} & \mathbf{M}^{(22)} & \dots \\ \vdots & \vdots & \ddots \end{pmatrix}, \quad (6)$$

where $\mathbf{M}^{(ij)}$ couples the velocity of colloid i to the force on colloid j and depends on only \mathbf{r}_i and \mathbf{r}_j . With free-draining hydrodynamics (BD), $\mathbf{M}^{(ii)} = \gamma_0^{-1} \mathbf{I}$ and $\mathbf{M}^{(ij)} = \mathbf{0}$ for $i \neq j$ so that each colloid experiences only its bare particle drag and no hydrodynamic interactions with the other colloids (\mathbf{I} is the identity tensor.) With pairwise far-field hydrodynamics (BD+RPY), we use a periodic formulation⁵² of the free-space RPY tensor,^{11,12} $\mathbf{M}^{(ii)} = \gamma_0^{-1} \mathbf{I}$ and

$$\mathbf{M}^{(ij)} = \gamma_0^{-1} \begin{cases} \left(\frac{3a}{4r} + \frac{a^3}{2r^3} \right) \mathbf{I} + \left(\frac{3a}{4r} - \frac{3a^3}{2r^3} \right) \hat{\mathbf{r}}\hat{\mathbf{r}}, & r > d, \\ \left(1 - \frac{9r}{32a} \right) \mathbf{I} + \frac{3r}{32a} \hat{\mathbf{r}}\hat{\mathbf{r}}, & r \leq d, \end{cases} \quad (7)$$

for $i \neq j$, where $\hat{\mathbf{r}} = \mathbf{r}/r$ is the unit vector from j to i ($\mathbf{r} = \mathbf{r}_i - \mathbf{r}_j$ and $r = |\mathbf{r}|$). The periodic formulation of the free-space tensor is⁵³

$$\mathbf{M}^{(ij)} = \frac{1}{\eta_0 V} \sum_{\mathbf{k} \neq \mathbf{0}} e^{i\mathbf{k} \cdot (\mathbf{r}_i - \mathbf{r}_j)} \frac{1}{k^2} \left(\frac{\sin ka}{ka} \right)^2 (\mathbf{I} - \hat{\mathbf{k}}\hat{\mathbf{k}}), \quad (8)$$

where V is the volume of the simulation box, \mathbf{k} is a wavevector commensurate with the simulation box, $k = |\mathbf{k}|$, and $\hat{\mathbf{k}} = \mathbf{k}/k$. The sum over wavevectors must be treated carefully when applying Eq. (5), so we used the efficient positively split Ewald technique of Fiore *et al.* with a splitting parameter of 0.5 and a relative error tolerance of 10^{-3} .⁵³ The mobility tensor \mathcal{M} for both the BD model and the BD+RPY model is divergence-free ($\nabla \cdot \mathcal{M} = \mathbf{0}$),^{10,51} so this term can be neglected in Eq. (5). We used a time step of $\Delta t = 10^{-5} \tau_0 \approx 0.02\tau$ in both our BD and BD+RPY simulations for numerical stability.

The natural system of units describing the colloids in Brownian dynamics is defined by the colloid radius a , the energy scale $k_B T$, and the diffusion time τ_0 . As this system of units is also useful and general for describing colloidal suspensions, we will use these units rather than the MPCD units of Sec. II A to present most of our results. It is straightforward to convert between the two if desired.

D. Langevin dynamics

In addition to MPCD and BD, we also used Langevin dynamics (LD) simulations with free-draining hydrodynamics to initially equilibrate the colloid configurations and to perform selected comparisons (Sec. III A). The standard LD equations of motion for a

particle i are⁹

$$\begin{aligned} \frac{d\mathbf{r}_i}{dt} &= \mathbf{v}_i, \\ m_i \frac{d\mathbf{v}_i}{dt} &= \mathbf{F}_i - \gamma_i \mathbf{v}_i + \mathbf{F}_{R,i}, \end{aligned} \quad (9)$$

where γ_i is the particle drag coefficient and $\mathbf{F}_{R,i}$ is a randomly fluctuating force having a Gaussian distribution with zero mean and covariance $\langle \mathbf{F}_{R,i}(t) \mathbf{F}_{R,i}(t') \rangle = 2k_B T \gamma_i \delta(t - t') \mathbf{I}$. For colloids represented by single spheres, these equations apply straightforwardly with $m_i = M$ and $\gamma_i = \gamma_0$ (BD is the overdamped limit of LD). However, they may also be applied to the discrete particle model using $m_i = m_v$ and a desired γ_i . Taking $\gamma_i = \gamma_0/(N_v + 1)$ results in the same diffusivity for an isolated colloid, but other values can be chosen, e.g., to accelerate equilibration.

E. Simulation details

We simulated bulk suspensions containing N spheres in a three-dimensional cubic simulation box of edge length L with periodic boundary conditions. For most simulations, we fixed the box size at $L = 120\ell = 40a$ and varied the number of colloids to obtain a desired volume fraction of $\phi = Nv/L^3$, where v is the volume of a single colloid ($v = 4\pi a^3/3$ for spherical colloids). We varied ϕ in the range $0.01 \leq \phi \leq 0.40$, giving between 153 and 6112 colloids. We also varied L in some simulations to test for finite-size effects (Sec. III). Equilibrium configurations were prepared by initially placing the discrete-particle colloids in the box without overlap and then simulating for $2.5 \times 10^4 \tau$ using Langevin dynamics with $\gamma_i = 1.0m/\tau$. We saved eight equilibrated configurations that we subsequently used to initialize production simulations for the various models. The simulations were performed using HOOMD-blue (version 2.9.6)^{54,55} extended with azplugins (version 0.10.2)⁵⁶ and a public version of the positively split Ewald method^{53,57} with minor modifications for compatibility with the version of HOOMD-blue that we used.

III. DIFFUSION

Neutrally buoyant colloids in a suspension move ballistically at times $t \ll \tau_B$ before their motion can become diffusive at $t \gtrsim \tau_B$. At infinite dilution, the colloid self-diffusion coefficient is D_0 for $t \gg \tau_B$; however, at finite concentration, the colloids cannot diffuse freely for an indefinite duration. They eventually come into contact with other colloids at times $t \sim \tau_0$, leading to a slowing of their dynamics while their local environment relaxes. At longer times $t \gg \tau_0$, the colloid dynamics can then be viewed as the collective motion of a colloid carrying a ‘‘cage’’ of other colloids, resulting in slower dynamics.⁵⁸ Hence, the diffusive motion of a colloid is commonly described by two diffusion coefficients: a short-time self-diffusion coefficient D_S that characterizes local diffusive motion at times $\tau_B \ll t \ll \tau_0$ and a long-time self-diffusion coefficient D_L ($\leq D_S$ for hard spheres) that characterizes the overall relaxation at $t \gg \tau_0$. Note that D_S and D_L are identical at infinite dilution and equal to D_0 .

To determine diffusion coefficients in our simulations, we measured the mean squared displacement $\langle \Delta r^2 \rangle$ of the suspended

colloids and computed its time derivative,

$$\alpha(t) = \frac{1}{6} \frac{d\langle \Delta r^2 \rangle}{dt}. \quad (10)$$

Diffusive motion is characterized by $\langle \Delta r^2 \rangle \sim 6Dt$ in three dimensions, meaning that $\alpha \sim D$ should be a constant for diffusive motion. The long-time self-diffusion coefficient D_L can be determined from the long-time plateau of α ; we averaged α over $3\tau_0 \leq t \leq 12\tau_0$ for our data. The short-time self-diffusion coefficient D_S is a little more ambiguous to characterize, and we will discuss this point further in Sec. III A.

The long-ranged nature of hydrodynamic interactions [see, e.g., Eq. (7)] can lead to significant finite-size effects in simulations with periodic boundary conditions due to the solvent-mediated interactions of the suspended particles with their periodic images.^{59–62} Dünweg and Kremer showed that the long-time self-diffusion coefficient D_L^∞ for a solute in an infinitely sized simulation box can be obtained from measurements of D_L in a cubic simulation box with edge length L using

$$D_L^\infty = D_L + \xi \frac{k_B T}{6\pi\eta_0 L}, \quad (11)$$

where $\xi \approx 2.837297$ plays a role analogous to a Madelung constant.^{52,61,62} Finite-size corrections have also been developed for noncubic periodic^{52,63} and partially confined systems,⁶⁴ but will not be discussed here.

Equation (11) can be readily applied to compute D_L^∞ in dilute suspensions ($\phi \rightarrow 0$); however, this expression becomes inaccurate even at small volume fractions. In this concentration regime, the functional form of the hydrodynamic interactions remains unchanged,⁶⁵ but the interactions must propagate through a medium with an effectively higher viscosity.^{66,67} Hence, finite-concentration effects can be accounted for in Eq. (11) by replacing the solvent viscosity η_0 by the suspension viscosity η .⁶⁶ Determining η would require additional simulations, but fortunately, we can approximately eliminate the suspension viscosity from Eq. (11) by positing a Stokes–Einstein relationship $D_L^\infty = D_0(\eta_0/\eta)$.⁶² Substituting for η and solving for D_L^∞ gives

$$D_L^\infty \approx D_L \left(1 - \xi \frac{\gamma_0}{6\pi\eta_0 L} \right)^{-1}. \quad (12)$$

To apply Eq. (12) to our simulations, we assumed that the spherical colloids had hydrodynamic radius a and no-slip boundary conditions in both the MD+MPCD and BD+RPY models, so $\gamma_0 = 6\pi\eta_0 a$ could be directly substituted. It is important to note that Eqs. (11) and (12) are based on a low-Reynolds-number description of hydrodynamics and are, therefore, also subject to the approximations discussed in Sec. II C.

To test this approach for correcting finite-size effects, we performed additional MD+MPCD and BD+RPY simulations at $\phi = 0.05$ and $\phi = 0.30$, varying the box size between $L = 20a$ and $L = 60a$, and corrected the measured D_L using Eq. (12). We found that the resulting D_L^∞ values at both ϕ were independent of L within our measurement accuracy, which provides an *a posteriori* justification for the assumptions we made. Therefore, we have corrected the long-time self-diffusion coefficients from the

MD+MPCD and BD+RPY simulations using Eq. (12) to facilitate comparison with experiments, theory, and other simulations. For simplicity, we will not distinguish D_L^∞ from D_L in the following discussion.

A. Short-time self-diffusion

Within a Brownian dynamics theoretical framework, the motion of a colloid is instantaneously diffusive due to the neglect of inertia, so D_S must relate to the displacement of a colloid over a single small time step Δt . Accordingly, D_S can be determined from the trace of the mobility tensor \mathcal{M} ,⁶⁵

$$D_S = \frac{k_B T}{3N} \text{tr} \mathcal{M}. \quad (13)$$

For pairwise hydrodynamic interactions, it immediately follows that $D_S = (k_B T/3) \text{tr} \mathbf{M}^{(ii)}$, so $D_S = D_0$ for free-draining hydrodynamics or free-space RPY hydrodynamics [Eq. (7)], and D_S can be evaluated for periodic RPY hydrodynamics using Eq. (8).⁵³ For our simulation box ($L = 40a$), we find $D_S = 0.929D_0$, which should be regarded as a finite-size effect to be corrected. For higher-order hydrodynamic interactions, D_S is expected to depend on ϕ , but determining an analytic expression is challenging. Batchelor derived the first-order correction to the short-time self-diffusion with the two-sphere mobility tensor,⁶⁸ finding $D_S(\phi) = D_0(1 - 1.83\phi)$. Beenakker and Mazur then included second-order correction terms to D_S based on approximated near-field hydrodynamic interactions and a partial resummation of the many-body contributions;⁶⁹ the predicted D_S values were in good agreement with the results from experiments and accelerated Stokesian dynamics simulations for $\phi \lesssim 0.40$,⁷⁰ despite the lack of lubrication corrections in the theory.

Given this theoretical background, we expected both the BD and BD+RPY simulations to give short-time self-diffusion coefficients $D_S \approx D_0$, independent of ϕ . To approximately extract D_S from the simulations, we considered $\alpha(t)$, which should steadily decrease from D_S at $t = 0$ to its long-time limit, D_L . We found that α approximately approached D_0 in the BD simulations and a slightly smaller value in the BD+RPY simulations as $t \rightarrow 0$ [Fig. 2(a)]. Both the values were consistent with—but slightly smaller than—those predicted by Eq. (13) at $\phi = 0.30$ due to excluded-volume interactions between the colloids during the measurement time, which effectively reduce α . We have verified that we exactly obtain theoretically expected values for D_S from our simulations at smaller ϕ or if we measure the displacement over a single simulation time step with the excluded-volume interactions disabled.

In stark contrast to the BD and BD+RPY simulations, α was not a monotonic function of t in the MD+MPCD simulations: α increased at short times, obtained a maximum α^* at time t^* , and then decreased to a long-time plateau for $t \gtrsim \tau_0$ [Fig. 2(b)]. To rule out the maximum α^* emerging due to inertial effects, which are present in MD+MPCD but not in BD or BD+RPY (Sec. II C), we performed LD simulations of single-particle colloids with $\gamma_i = \gamma_0$. We found that α in the LD simulations increased for $t \lesssim 2.5 \times 10^{-3} \tau_0 \approx 5\tau_B$, reflecting the ballistic motion of the colloids at short times, but essentially tracked α from the BD simulations after that time [Fig. 2(a)]. The maximum α^* in the MD+MPCD simulations occurs, however, at much later times $t^* \gg 5\tau_B$ [Fig. 2(b)]

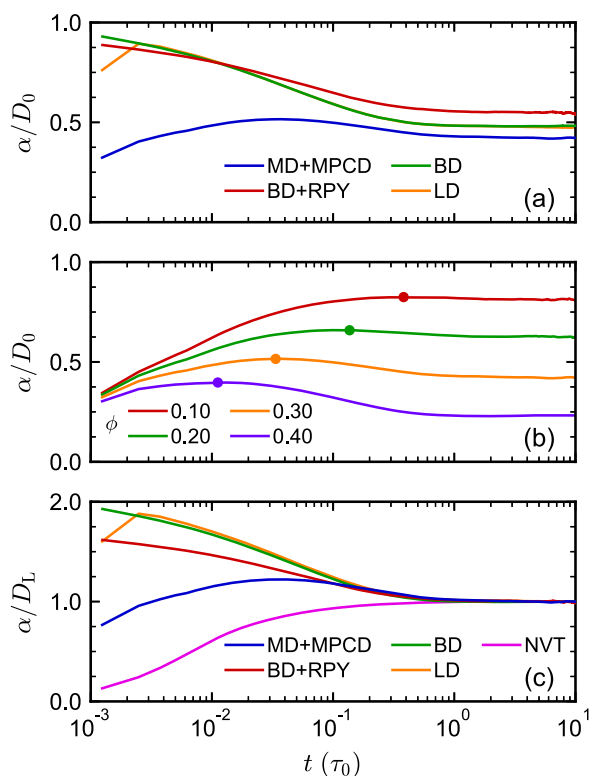


FIG. 2. Time derivative α of the colloid mean squared displacement from (a) different methods at $\phi = 0.30$ and (b) MD+MPCD at different ϕ . In (c), α is normalized by D_L without finite-size corrections to compare methods in (a) with NVT simulations.

and, therefore, cannot be due to inertia if the colloid experiences a hydrodynamic friction γ_0 .

We considered that the behavior of α in the MD+MPCD simulations might be caused by a lack of coupling between the colloids and the MPCD solvent such that the hydrodynamic friction on a colloid is less than γ_0 at short times. In the worst-case limit, the colloids would be completely decoupled from the solvent and experience no friction, as in vacuum. To compare the MD+MPCD results with this limit, we performed isothermal–isochoric (NVT) simulations⁹ of the colloids, each represented by a single particle, using a Nosé–Hoover thermostat with a time constant of 0.1τ and a time step of 0.005τ . The colloid motion was expected to become diffusive in the NVT simulations at long times because of collisions between particles. However, the corresponding long-time self-diffusion coefficient D_L was expected to be larger than that in the MD+MPCD simulations due to the lack of solvent. Indeed, at $\phi = 0.30$, α was consistently larger in the NVT simulations than that in the MD+MPCD simulations, leading to D_L being roughly 40 times larger. Accordingly, we normalized α by D_L to facilitate comparison with the MD+MPCD simulations [Fig. 2(c)]. In the NVT simulations, α/D_L increased monotonically to one. Its shape at short times is reminiscent of the MD+MPCD simulations at short times, but there was no significant maximum α^* in the NVT simulations. This comparison suggests that there may

be *partial* coupling of the colloids to the solvent in MD+MPCD at short times, but more complete hydrodynamic coupling at longer times. This contrasts with the BD and BD+RPY simulations, where the colloids experience an exactly prescribed friction at all times.

The fundamental differences between the MD+MPCD and BD+RPY simulations at short times might be understood by considering the time scales at which hydrodynamic interactions propagate.^{7,23} In BD+RPY, the solvent-mediated coupling between the colloids is instantaneous and only depends on their positions, whereas in MD+MPCD, shear and sound waves propagate with finite velocities. The speed of sound in the MPCD solvent is $c \sim \ell/\tau$, so the typical time scale of sound-wave propagation is $\tau_c \sim a/c = 1.5 \times 10^{-3}\tau_0$. The viscous time scale associated with the lifetime of a shear wave is $\tau_v \sim a^2/\nu_0 = 5.7 \times 10^{-3}\tau_0$.^{7,39} These time scales are comparable in magnitude to each other and are one order of magnitude larger than $\tau_B = 4.8 \times 10^{-4}\tau_0$. It was argued in Ref. 23 that this lack of time scale separation may cause incomplete hydrodynamic coupling at short times.

Nevertheless, it is tempting to identify α^* in the MD+MPCD simulations as the short-time self-diffusion coefficient D_S because it decreases with increasing ϕ [Fig. 3(a)] and occurs in the expected time interval $\tau_B \lesssim t^* \lesssim \tau_0$ [Fig. 2(b)]. Previous MD+MPCD simulations that used reflection-based colloid–solvent coupling adopted this definition of D_S .³¹ We note, however, that this definition is somewhat at odds with the idea that D_S should result from hydrodynamic interactions between colloids at times before the colloids physically interact. To interrogate this point, we determined t^* as a function of ϕ [Fig. 3(b)], finding that it decreased as ϕ increased. We simultaneously estimated the average surface-to-surface distance d_{cc} between nearest-neighbor colloids using a theoretical expression developed by Torquato for random hard-sphere packings⁷¹

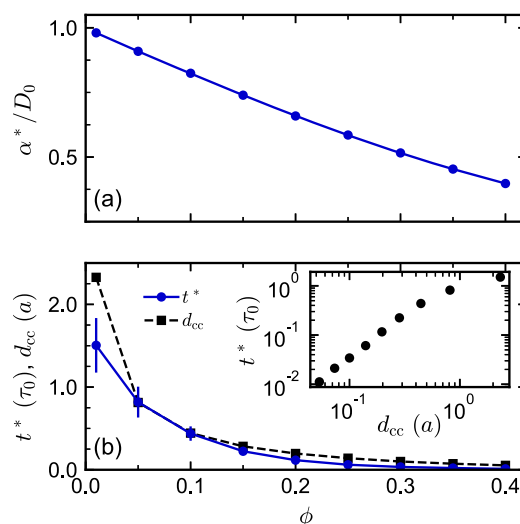


FIG. 3. (a) Maximum α^* at time t^* from the MD+MPCD simulations [Fig. 2(b)]. (b) t^* and theoretical average nearest surface-to-surface distance of colloids d_{cc} as functions of ϕ . Inset: t^* vs d_{cc} .

[Fig. 3(b)]. Note that d_{cc} is considerably smaller than the radius of a colloid at most packing fractions and also decreases with ϕ , implying that two colloids can encounter each other at times much shorter than τ_0 . This behavior is consistent with the monotonic decrease in α in the BD and BD+RPY simulations at short times, as colloids should diffuse more slowly when they are hindered or caged by nearby particles.

We found that t^* was much larger than the hydrodynamic time scales τ_c and τ_v , but correlated strongly with d_{cc} [inset of Fig. 3(b)], suggesting that the maximum in α in the MD+MPCD simulations may be due to interactions between close colloids. However, it is challenging to separate effects from direct interactions [Eq. (4)], from (possible) hydrodynamic interactions, and from lack of separation of time scales in MD+MPCD simulations. Collective cage dynamics can be characterized from the intermediate scattering function at wavevectors where the static structure factor has its first maximum,⁷ and this measurement has been carried out previously for MD+MPCD with a similar discrete particle model.⁷² However, we emphasize that short-time cage dynamics are fundamentally different than the short-time diffusion coefficient defined by Eq. (13).⁷ Given this ambiguity, we have chosen not to report α^* as D_S for the MD+MPCD simulations. The curious short-time behavior in the MD+MPCD simulations should be carefully considered when applying the model to study dynamics. We are, however, encouraged that despite differences at short times, α still has qualitatively the same behavior at intermediate and long times in MD+MPCD as in BD+RPY [Fig. 2(b)].

B. Long-time self-diffusion

The long-time self-diffusion of the colloids is strongly tied to the structure of the suspension. Brady argued that for hard spheres, D_L can be factored into hydrodynamic and structural contributions, approximately given by⁵⁸

$$D_L(\phi) = D_S(\phi) [1 + 2\phi g(d^+; \phi)]^{-1}, \quad (14)$$

where $g(d^+; \phi)$ is the contact value of the radial distribution function $g(r)$ for a given volume fraction ϕ as $r \rightarrow d$ from the right. Figure 4 shows $g(r)$ from our simulations at different ϕ , demonstrating the well-known behavior that the first peak in $g(r)$ increases with

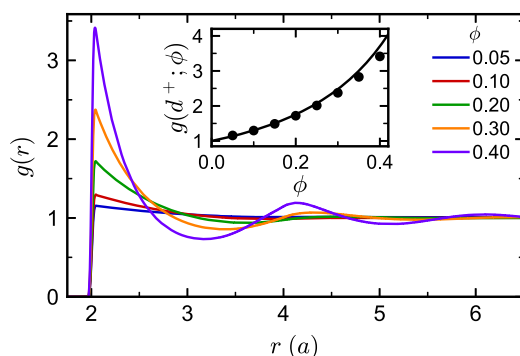


FIG. 4. Radial distribution function $g(r)$ between the colloids for selected volume fractions ϕ . Inset: Value at contact $g(d^+; \phi)$ as a function of ϕ from our simulations (symbols) and from Eq. (15) (solid line).

increasing ϕ for hard spheres as their local structure becomes more pronounced. For a hard-sphere fluid, the first peak corresponds to $g(d^+; \phi)$, and its value is related to the thermodynamic pressure. We theoretically estimate

$$g(d^+; \phi) = \frac{1 - \phi/2}{(1 - \phi)^3}, \quad (15)$$

using the Carnahan–Starling equation of state.⁷³ We simulated nearly hard spheres [Eq. (4)] rather than true hard spheres, so contact is not as precisely defined for our model: the first peak in $g(r)$ occurs at r slightly larger than d . We approximated $g(d^+; \phi)$ in the simulations by the height of the first peak, which we determined by fitting a quadratic interpolating function through the first peak of $g(r)$. The computed $g(d^+; \phi)$ is in excellent agreement with Eq. (15) (inset of Fig. 4), especially for $\phi \lesssim 0.20$. We accordingly compared D_L from our simulations to predictions of Eq. (14) using Eq. (15) and assuming $D_S = D_0$. This value of D_S is prescribed in the BD and BD+RPY simulations and is an approximation for the MD+MPCD simulations for lack of well-defined short-time diffusion (Sec. III A).

For small colloid volume fractions $\phi \lesssim 0.10$, the long-time self-diffusion coefficient D_L measured in the BD simulations (Fig. 5) was close to the theoretical prediction [Eq. (14)] using $D_S = D_0$. At larger ϕ , however, D_L was systematically larger in the BD simulations than theoretically predicted. To test whether this discrepancy originated from the soft colloid–colloid repulsion in our simulations [Eq. (4)], we compared our results with previous Monte Carlo simulations using a true hard-sphere model,⁷⁴ finding excellent agreement within the measurement accuracy. Furthermore, using the measured $g(d^+; \phi)$ value in Eq. (14) rather than Eq. (15) did not significantly change the theoretical prediction. In the BD+RPY simulations, D_L was systematically larger than that in both the BD simulations and the theoretical prediction. We were surprised to also observe a qualitatively different dependence on ϕ given that both the BD and BD+RPY simulations have $D_S = D_0$ and give the same suspension structure, so D_L should have the same dependence on ϕ in both methods according to Eq. (14). Brady pointed out in his analysis that although Eq. (14) gives the proper asymptotic behavior as ϕ approaches maximum packing, it should be regarded as a simple estimate at other ϕ .⁵⁸ Evidently, this estimate is inaccurate

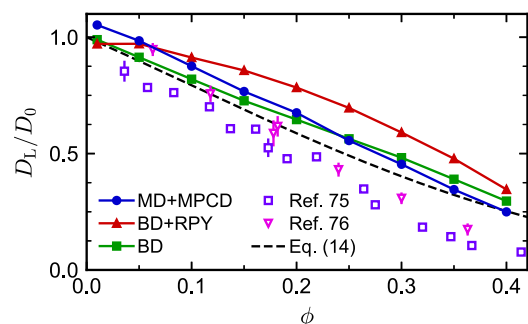


FIG. 5. Long-time self-diffusion coefficients D_L as functions of volume fraction ϕ for the different simulation methods, reference experiments,^{75,76} and as predicted by Eq. (14) with Eq. (15) and $D_S = D_0$.

for BD+RPY at the simulated volume fractions, which are far from maximum packing.

In the MD+MPCD simulations, D_L had similar values and dependence on ϕ as in the BD simulations and as predicted by Eq. (14), assuming $D_S = D_0$. These values of D_L were systematically larger than those reported in experiments with hard-sphere-like colloidal particles^{75,76} but had a similar dependence on ϕ . We note that careful inspection of Fig. 5 shows that D_L was slightly larger (about 5%) than D_0 in the MD+MPCD simulations at $\phi = 0.01$. This discrepancy might be interpreted as a slightly smaller effective friction on the colloid than expected from the Stokes–Einstein relation, which could be explained by an effective hydrodynamic radius that differs from the nominal radius a . Following this idea, Poblete *et al.* reported the effective hydrodynamic radius for their discrete particle model in MPCD based on single-colloid simulations. The specific value depended on the measurement protocol but was typically larger than a by as much as 10%. This finding contrasts with our measurement, which would lead to an effective radius about 5% smaller than a in order to make D_L larger than D_0 for $\phi = 0.01$. However, we prefer not to attribute this difference to the hydrodynamic size since it is not straightforward to separate the colloid size from other factors (e.g., viscosity), determining the friction coefficient in the MD+MPCD model. A smaller friction coefficient than expected could be related to the extent of colloid–solvent coupling discussed in Sec. III A.

IV. SEDIMENTATION

In addition to equilibrium self-diffusion, we also studied nonequilibrium sedimentation of the spherical colloids. Sedimentation is not only an important process in its own right but also helpful for understanding the analogous process of collective diffusion down a concentration gradient.^{68,77–79} During sedimentation, all colloids are subject to a constant external force \mathbf{f} that causes them to move in the direction of \mathbf{f} with average velocity \mathbf{u} . If the suspension is incompressible, the motion of the colloids implies an opposing backflow of the solvent with average velocity \mathbf{u}_0 such that the volume-average velocity $\mathbf{u}_v = \phi\mathbf{u} + (1 - \phi)\mathbf{u}_0$ is zero. Backflow tends to hinder sedimentation of the colloids, and as a result, the rate of sedimentation is experimentally known to depend on the colloid volume fraction ϕ .⁴ This dependence is enhanced by hydrodynamic interactions between colloids.

Sedimentation is conveniently characterized by the sedimentation coefficient K , defined by $\mathbf{u} = K\gamma_0^{-1}\mathbf{f}$, which relates the average velocity of a colloid in the suspension to the average velocity of a single colloid moving under the same force. Batchelor showed that⁸⁰

$$K(\phi) = 1 - 6.55\phi \quad (16)$$

for an incompressible hard-sphere suspension at dilute volume fractions using exact two-sphere mobility tensors. Batchelor's result can be extrapolated to higher volume fractions using the empirical expression⁴

$$K(\phi) \approx (1 - \phi)^{6.55}, \quad (17)$$

which has the same small- ϕ expansion. Banchio and Nägele computed the sedimentation coefficient for an incompressible hard-sphere suspension with pairwise far-field hydrodynamics given by

the RPY tensor,⁷⁰

$$K(\phi) = \frac{(1 - \phi)^3}{1 + 2\phi} + \frac{\phi^2}{5}, \quad (18)$$

correcting an earlier result from Brady and Durlofsky.^{66,81} The small- ϕ expansion of this result is $K(\phi) = 1 - 5\phi$, which has a slightly weaker dependence on ϕ than Eq. (16).

We measured K for our models using nonequilibrium simulations,⁸² where we applied a constant force $\mathbf{f} = f_x\hat{\mathbf{x}}$ to the colloids along the x -direction $\hat{\mathbf{x}}$. In the MD+MPCD simulations, this force was equally distributed to all $N_v + 1$ constituent particles of a colloid, and an opposing force was applied to the solvent particles to ensure that the entire system was force-free and did not accelerate. (These simulations were performed using double-precision floating-point arithmetic to improve numerical accuracy and momentum conservation.⁵⁴) In the BD and BD+RPY simulations, the force was applied to the single particle representing the colloid.

For all simulation methods, we applied two forces $f_x = 1.5k_B T/a$ and $3.0k_B T/a$ and measured \mathbf{u} in a stationary frame, that is, the value we observed in the simulations. We simulated $50\tau_0$ to reach a steady state and then sampled \mathbf{u} roughly every $5 \times 10^{-5}\tau_0$ during a $25\tau_0$ simulation. We noted that the colloids in the MD+MPCD simulations accelerated between stochastic collisions because the colloids follow Newton's equations of motion [Eq. (1)] during this time and experience a net force. We also found that the central and vertex particles oscillated out of phase with each other due to their bonded interactions, which are not damped between collisions. We accordingly computed \mathbf{u} in the MD+MPCD simulations using the average velocity of all particles comprising a colloid and sampled \mathbf{u} uniformly over time steps between collisions to obtain a representative average. In the BD and BD+RPY simulations, we simply computed \mathbf{u} from the displacement of the colloids during a single time step. We then fit $u_x = \mathbf{u} \cdot \hat{\mathbf{x}}$ as a linear function of f_x , which is the expected relationship for small f_x , and determined K from the slope of the fit. Figure 6 shows u_x as a function of f_x for the MD+MPCD simulations, and the data are well-fit by a line for all investigated ϕ .

Similarly to self-diffusion coefficients, sedimentation coefficients measured in simulations with periodic boundary conditions

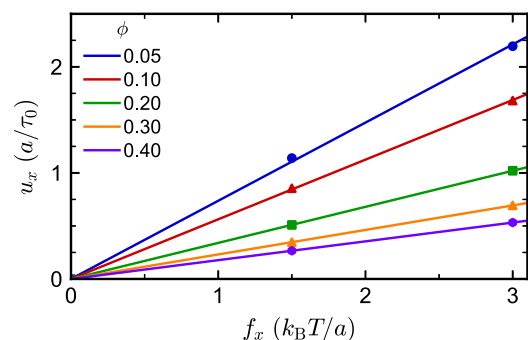


FIG. 6. Average colloid velocities u_x in the stationary frame as functions of applied force f_x from the MD+MPCD simulations for all investigated colloid volume fractions ϕ . The estimated measurement uncertainty is smaller than the symbol size.

should be corrected for finite-size effects.^{66,83,84} We determined the sedimentation coefficient in an infinite-size box K^∞ from measurements of K in a finite-size box using the correction^{83,84}

$$K^\infty \approx K \left(1 - \xi S(0) \frac{\eta_0 a}{\eta L} \right)^{-1}, \quad (19)$$

where $S(0)$ is the static structure factor of the suspension extrapolated to zero wavevector. To eliminate the suspension-viscosity dependence in this correction, we made an assumption consistent with Eq. (12) that $\eta_0/\eta = D_L^\infty/D_0$, so

$$K^\infty \approx K \left(1 - \xi S(0) \frac{D_L^\infty a}{D_0 L} \right)^{-1}. \quad (20)$$

Given the consistency of the measured $g(d^+; \phi)$ (Fig. 4) with Eq. (15), we estimated $S(0)$ from the isothermal compressibility of the Carnahan–Starling equation of state,^{73,83}

$$S(0) = \frac{(1 - \phi)^4}{1 + 4\phi + 4\phi^2 - 4\phi^3 + \phi^4}. \quad (21)$$

We applied this finite-size correction to our measurements, but as for D_L , we will not retain the notation K^∞ in the discussion that follows.

Figure 7(a) shows the sedimentation coefficient K as a function of ϕ for the MD+MPCD, BD, and BD+RPY simulations. For the BD simulations, K can be analytically determined to be $K = 1$ independent of ϕ using a simple argument: The sum of all pairwise forces between colloids must be zero and the time average of the random displacements is also zero, so averaging the displacements in Eq. (5) over all colloids for BD hydrodynamics leaves only the

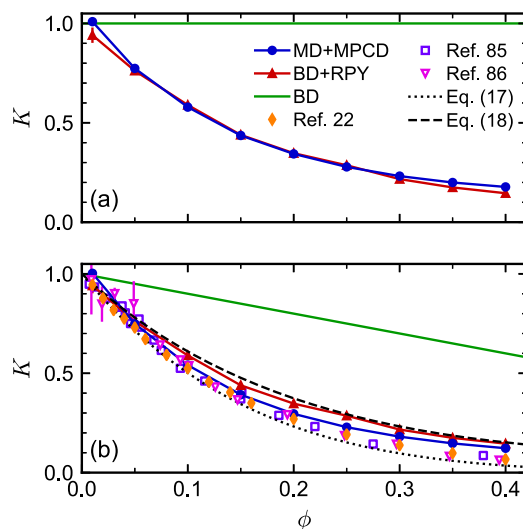


FIG. 7. Sedimentation coefficients K as functions of colloid volume fraction ϕ for the different simulation methods in (a) the stationary frame observed in the simulations and (b) the frame where the volume-averaged velocity is zero. (Note that the BD+RPY data are the same in both panels.) Theoretical predictions, reference experiments,^{85,86} and reference simulations using BD+RPY with a discrete particle model²² are also shown in (b).

displacement from the external force $\langle \Delta \mathbf{r} \rangle = \langle N^{-1} \sum_{i=1}^N \Delta \mathbf{r}_i \rangle = \gamma_0^{-1} \mathbf{f} \Delta t$ and $K = 1$. Accordingly, we have plotted only this theoretical value, but we verified that this result was also obtained in BD simulations. In contrast, K decreased strongly as ϕ increased in the BD+RPY and MD+MPCD simulations and was nearly the same for both methods at all ϕ investigated. As expected, $K \rightarrow 1$ as $\phi \rightarrow 0$ in the BD+RPY simulations, but in the MD+MPCD simulations, K was slightly larger than one at $\phi = 0.01$. This discrepancy is consistent with D_L being somewhat larger than D_0 at the same concentration (Fig. 5).

In order to compare these results with each other and with theoretical predictions, it is important to note that K depends on the reference frame chosen to measure \mathbf{u} .^{87,88} In the theoretical analyses leading to Eqs. (16) and (18), the sedimentation velocities are defined relative to \mathbf{u}_v ,^{80,81} which is zero for an incompressible suspension because there is no volume flux. The MD+MPCD simulations, however, were effectively performed in a reference frame where the mass-averaged velocity $\mathbf{u}_m = w\mathbf{u} + (1-w)\mathbf{u}_0$, with w being the colloid mass fraction, is zero due to conservation of linear momentum. Having $\mathbf{u}_m = \mathbf{0}$ does not also give $\mathbf{u}_v = \mathbf{0}$ for our MD+MPCD model, so the colloid velocities were effectively measured relative to \mathbf{u}_m rather than \mathbf{u}_v . The BD equations of motion imply a stationary solvent, so the colloid velocities were measured relative to the solvent velocity \mathbf{u}_0 rather than \mathbf{u}_v . The BD+RPY simulations have a backflow of solvent that results from discarding the $\mathbf{k} = \mathbf{0}$ wavevector in Eq. (8) such that $\mathbf{u}_v = \mathbf{0}$,¹³ so these simulations have the same reference frame as the theoretical calculations.

Accordingly, we shifted \mathbf{u} and \mathbf{u}_0 measured in the MD+MPCD and BD simulations to $\mathbf{u}' = \mathbf{u} - \mathbf{u}_v$ and $\mathbf{u}'_0 = \mathbf{u}_0 - \mathbf{u}_v$ so that $\mathbf{u}'_v = \mathbf{0}$ in the shifted reference frame. For the MD+MPCD simulations, $\mathbf{u}' = (1 - \phi)[1 + w/(1 - w)]\mathbf{u}$, with $w = MN/(MN + m\rho_0 L^3)$, because $\mathbf{u}_0 = -[w/(1 - w)]\mathbf{u}$ in the frame where $\mathbf{u}_m = \mathbf{0}$. In performing this shift, we note that there is some ambiguity in defining the colloid and solvent volume fractions in the MD+MPCD model because the colloids do not exclude volume to the solvent; we used the nominal values ϕ and $1 - \phi$ for consistency with the other simulations. For the BD simulations, $\mathbf{u}' = (1 - \phi)\mathbf{u}$ because $\mathbf{u}_0 = \mathbf{0}$ in the frame that moves with the solvent. These scaling factors between \mathbf{u} and \mathbf{u}' can be straightforwardly applied to transform the measured K .

After applying the shift to a common reference frame [Fig. 7(b)], K remained consistently smaller in the MD+MPCD and BD+RPY simulations than in the BD simulations due to the presence of hydrodynamic interactions between colloids. As expected, K for the BD+RPY simulations was in nearly perfect agreement with Eq. (18). The values of K in the MD+MPCD simulations were typically larger than Eq. (17) but smaller than Eq. (18). For $\phi \lesssim 0.25$, K was similar to Eq. (17), experimental measurements,^{85,86} and simulations conducted using BD+RPY with a discrete particle model for the colloids.²² At larger ϕ , K more closely resembled the results of the BD+RPY simulations.

Overall, the MD+MPCD simulations showed sedimentation behavior that was consistent with the presence of hydrodynamic interactions between colloids. This observation is somewhat at odds with a recent report²³ that found essentially no long-ranged hydrodynamic interactions between two mutually diffusing colloids modeled using MD+MPCD with a reflection scheme for the solvent–colloid coupling; their conclusion was that MD+MPCD

was not suitable for modeling colloidal suspensions. Given the fundamentally different nature of their measurements and ours, it is challenging to make a conclusive comparison but this discrepancy surely deserves further consideration.

V. DIFFUSION OF CUBIC COLLOIDS

Having shown that MD+MPCD with a discrete particle model largely reproduces the experimentally observed and theoretically expected dynamics of spherical colloids, we extended the model to cubic colloids to demonstrate the generality and flexibility of the approach. The diameter (edge length) of the cubes was set to $d = 6\ell$, and vertex particles were placed on their surface in a square lattice with a spacing of $6/7\ell$, i.e., seven vertex particles per edge and $N_v = 296$ vertex particles per colloid [Fig. 1(b)]. Each vertex particle was connected to its nearest neighbor and its diametrically opposed vertex particle using a harmonic potential [Eq. (3)]. Unlike the spherical colloids, we did not include a central particle to model the excluded-volume interactions between cubes because these interactions do not have a simple mathematical form. Instead, all nonbonded vertex particles interacted with each other through the Weeks–Chandler–Andersen pair potential⁵⁰ [Eq. (4) with $\sigma = 1.0\ell$ and $\Delta = 0.0\ell$]. We confirmed that the vertex–particle spacing was small enough that the cubes did not penetrate each other. As a side effect of this model for the interactions, each cube had a slightly corrugated texture and excluded a larger volume $v_{\text{ex}} \approx (d + \sigma)^3$ than expected from its hydrodynamic diameter, $v = d^3$. In dilute suspensions where colloid–colloid interactions are predominantly solvent-mediated, the hydrodynamic volume fraction $\phi = Nv/L^3$ may dictate the behavior, whereas in concentrated suspensions where excluded-volume interactions dominate, the thermodynamic volume fraction $\phi_{\text{ex}} = Nv_{\text{ex}}/L^3$ ($\approx 1.6\phi$ for the chosen parameters) may be more relevant. We restricted our simulations to $\phi_{\text{ex}} < 0.40$ to stay well below the freezing transition of hard cubes.⁸⁹ The size of the simulation box was set to $L = 120\ell$, and we performed four independent simulations per volume fraction using the same MPCD parameters as for the spherical colloids (Sec. II A).

Okada and Satoh numerically determined the translational diffusion coefficient of a cube at infinite dilution by measuring the drag force under a uniform low-Reynolds-number flow.⁹¹ They found that the translational friction coefficient γ_0 was independent of orientation.⁹² The resulting colloid diffusion coefficient D_0 was reduced by a factor of 1.384 compared to a sphere with the same diameter. Interestingly, this factor is comparable to the mean diameter of the spheres that inscribe and circumscribe the cube, $(1 + \sqrt{3})/2 d \approx 1.366 d$. Thus, cubes are predicted to diffuse much slower than spheres with the same diameter d . Even if one adjusts the cube diameter to match the sphere volume, the resulting D_0 of a cube would be about 10% smaller than that of a sphere. In the simulations, we can determine D_0 from D_L in the dilute regime $\phi \rightarrow 0$. We applied the same finite-size correction [Eq. (12)] as for the spheres, but using a friction coefficient of $\gamma_0 \approx 13.04\eta_0 d$ for the cubes.⁹¹ Figure 8 shows the adjusted D_L as functions of ϕ and ϕ_{ex} . At $\phi = 0.01$, we find $D_L = (3.17 \pm 0.06) \times 10^{-3} \ell^2/\tau$, which is close to the theoretically expected value of $D_0 = 3.23 \times 10^{-3} \ell^2/\tau$. The diffusivity decreases with increasing colloid volume fraction, as expected, and D_L approaches zero as ϕ_{ex} comes close to the freezing transition.⁸⁹ We

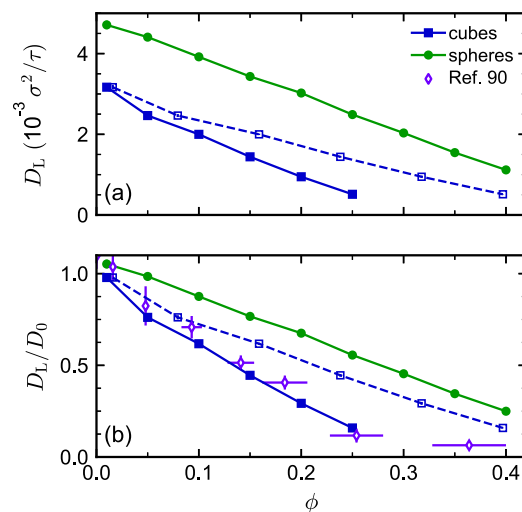


FIG. 8. Long-time self-diffusion coefficients D_L of cubic and spherical colloids as functions of their volume fraction ϕ . Filled and open squares indicate definition of ϕ using the hydrodynamic size (v) and the excluded volume (v_{ex}) of the cubes, respectively. The results are shown (a) in MD+MPCD units and (b) reduced by the theoretically expected self-diffusion coefficient at infinite dilution, D_0 . Reference experiments for pseudo-cubic colloidal superballs⁹⁰ are also shown in (b).

also remark that D_L has a similar dependence on volume fraction as reported in experiments of pseudo-cubic silica superballs⁹⁰ when ϕ is defined using the hydrodynamic size. This agreement is further indication that MD+MPCD gives a good approximation of the long-time diffusive suspension dynamics.

VI. CONCLUSIONS

We studied the diffusion and sedimentation of colloidal particles suspended in a Newtonian solvent using various computer simulation techniques. We focused, in particular, on a discrete particle model for the colloids coupled to the multiparticle collision dynamics model for the solvent (MD+MPCD). We characterized the short-time and long-time motion of spherical colloids and determined the long-time self-diffusion coefficient and sedimentation coefficient spanning a range of colloid volume fractions from $\phi = 0.01$ to $\phi = 0.40$. We compared the MD+MPCD model to experiments, theoretical predictions based on low-Reynolds-number hydrodynamics, and additional Brownian dynamics simulations using both free-draining hydrodynamics (BD) and pairwise far-field hydrodynamics (BD+RPY).

Overall, we found that the MD+MPCD model for spherical colloids gave satisfactory results that were generally similar to experimental measurements, the theoretical predictions, and BD+RPY simulations. The largest discrepancy was found for the short-time motion of the colloids: a maximum was observed in the time derivative α of the colloid mean squared displacement in the MD+MPCD model that was absent from the BD and BD+RPY models. As ϕ increased, this maximum decreased and occurred at earlier times; we found that this time correlated with the average distance between nearest colloids. By a careful comparison with additional simulations, we posited that this maximum should not

be identified as a short-time self-diffusion coefficient, but rather might be due to partial hydrodynamic coupling of the colloids to the solvent in MD+MPCD at short times. However, at longer times, the MD+MPCD model showed many expected features for colloidal suspensions, including a decrease in α to a long-time plateau that gave a long-time self-diffusion coefficient that depended on ϕ and was largely consistent with experimental data. Furthermore, the sedimentation coefficients measured in MD+MPCD were almost identical to BD+RPY in the stationary frame, were similar to experimental data in the frame where the volume-averaged velocity was zero, and differed significantly from BD simulations with free-draining hydrodynamics. Together, these data suggest the presence of hydrodynamic interactions in the MD+MPCD simulations.

One major benefit of the discrete particle model we used is its extensibility to particle shapes other than spheres. To demonstrate this flexibility, we also studied the long-time self-diffusion of cubic colloidal particles using MD+MPCD. Compared to a spherical colloid of the same diameter, the long-time self-diffusion coefficient of a cube at nearly infinite dilution ($\phi = 0.01$) was reduced by a factor of roughly 1.5, in reasonable agreement with theoretical predictions.⁹¹ At all investigated colloid volume fractions ϕ , the cubes diffused slower than spheres of equal diameter and were in good agreement with experiments using pseudo-cubic colloidal superballs.⁹⁰ Altogether, we found MD+MPCD to be a convenient and reasonable approach to study colloidal suspensions, especially for particles with complex shapes.

ACKNOWLEDGMENTS

The authors thank Zachary Sherman for many helpful discussions on this topic. This work was completed, in part, with resources provided by the Auburn University Easley Cluster. Computing time was also granted on the supercomputer Mogon at the Johannes Gutenberg University Mainz (www.hpc.uni-mainz.de). This work was funded by the Deutsche Forschungsgemeinschaft (DFG, German Research Foundation) (Project Nos. 274340645, 405552959, and NI 1487/7-1).

AUTHOR DECLARATIONS

Conflict of Interest

The authors have no conflicts of interest to disclose.

DATA AVAILABILITY

The data that support the findings of this study are available from the corresponding authors upon reasonable request.

REFERENCES

- ¹M. A. Boles, M. Engel, and D. V. Talapin, "Self-assembly of colloidal nanocrystals: From intricate structures to functional materials," *Chem. Rev.* **116**, 11220–11289 (2016).
- ²R. P. Sear, "Diffusiophoresis in cells: A general nonequilibrium, nonmotor mechanism for the metabolism-dependent transport of particles in cells," *Phys. Rev. Lett.* **122**, 128101 (2019).
- ³H. Shamsijazeyi, C. A. Miller, M. S. Wong, J. M. Tour, and R. Verduzco, "Polymer-coated nanoparticles for enhanced oil recovery," *J. Appl. Polym. Sci.* **131**, 40576 (2014).
- ⁴W. B. Russel, D. A. Saville, and W. R. Schowalter, *Colloidal Dispersions* (Cambridge University Press, New York, 1989).
- ⁵J. Happel and H. Brenner, *Low Reynolds Number Hydrodynamics: With Special Applications to Particulate Media* (Martinus Nijhoff, Hingham, MA, 1983).
- ⁶S. Kim and S. J. Karrila, *Microhydrodynamics: Principles and Selected Applications* (Dover, Mineola, NY, 2005).
- ⁷G. Nägele, "On the dynamics and structure of charge-stabilized suspensions," *Phys. Rep.* **272**, 215–372 (1996).
- ⁸M. P. Howard, A. Nikoubashman, and J. C. Palmer, "Modeling hydrodynamic interactions in soft materials with multiparticle collision dynamics," *Curr. Opin. Chem. Eng.* **23**, 34–43 (2019).
- ⁹M. P. Allen and D. J. Tildesley, *Computer Simulation of Liquids*, 2nd ed. (Oxford University Press, Oxford, 2017).
- ¹⁰D. L. Ermak and J. A. McCammon, "Brownian dynamics with hydrodynamic interactions," *J. Chem. Phys.* **69**, 1352–1360 (1978).
- ¹¹J. Rotne and S. Prager, "Variational treatment of hydrodynamic interactions in polymers," *J. Chem. Phys.* **50**, 4831–4837 (1969).
- ¹²H. Yamakawa, "Transport properties of polymer chains in dilute solution: Hydrodynamic interactions," *J. Chem. Phys.* **53**, 436–443 (1970).
- ¹³J. F. Brady, R. J. Phillips, J. C. Lester, and G. Bossis, "Dynamic simulation of hydrodynamically interacting suspensions," *J. Fluid Mech.* **195**, 257–280 (1988).
- ¹⁴J. F. Brady and G. Bossis, "Stokesian dynamics," *Annu. Rev. Fluid Mech.* **20**, 111–157 (1988).
- ¹⁵A. Malevanets and R. Kapral, "Mesoscopic model for solvent dynamics," *J. Chem. Phys.* **110**, 8605–8613 (1999).
- ¹⁶G. Gompper, T. Ihle, D. Kroll, and R. G. Winkler, "Multi-particle collision dynamics: A particle-based mesoscale simulation approach to the hydrodynamics of complex fluids," *Adv. Polym. Sci.* **221**, 1–87 (2009).
- ¹⁷P. J. Hoogerbrugge and J. M. V. A. Koelman, "Simulating microscopic hydrodynamic phenomena with dissipative particle dynamics," *Europhys. Lett.* **19**, 155–160 (1992).
- ¹⁸R. D. Groot and P. B. Warren, "Dissipative particle dynamics: Bridging the gap between atomistic and mesoscopic simulation," *J. Chem. Phys.* **107**, 4423–4435 (1997).
- ¹⁹G. R. McNamara and G. Zanetti, "Use of the Boltzmann equation to simulate lattice-gas automata," *Phys. Rev. Lett.* **61**, 2332–2335 (1988).
- ²⁰A. J. C. Ladd and R. Verberg, "Lattice-Boltzmann simulations of particle-fluid suspensions," *J. Stat. Phys.* **104**, 1191–1251 (2001).
- ²¹R. L. Marson, Y. Huang, M. Huang, T. Fu, and R. G. Larson, "Inertio-capillary cross-streamline drift of droplets in Poiseuille flow using dissipative particle dynamics simulations," *Soft Matter* **14**, 2267–2280 (2018).
- ²²A. M. Fiore, G. Wang, and J. W. Swan, "From hindered to promoted settling in dispersions of attractive colloids: Simulation, modeling, and application to macromolecular characterization," *Phys. Rev. Fluids* **3**, 063302 (2018).
- ²³A. Shakeri, K.-W. Lee, and T. Pöschel, "Limitation of stochastic rotation dynamics to represent hydrodynamic interaction between colloidal particles," *Phys. Fluids* **30**, 013603 (2018).
- ²⁴M. Ripoll, K. Mussawisade, R. G. Winkler, and G. Gompper, "Dynamic regimes of fluids simulated by multiparticle-collision dynamics," *Phys. Rev. E* **72**, 016701 (2005).
- ²⁵A. Malevanets and R. Kapral, "Solute molecular dynamics in a mesoscale solvent," *J. Chem. Phys.* **112**, 7260–7269 (2000).
- ²⁶J. T. Padding and A. A. Louis, "Hydrodynamic interactions and Brownian forces in colloidal suspensions: Coarse-graining over time and length scales," *Phys. Rev. E* **74**, 031402 (2006).
- ²⁷G. Batôt, V. Dahirel, G. Mériguet, A. A. Louis, and M. Jardat, "Dynamics of solutes with hydrodynamic interactions: Comparison between Brownian dynamics and stochastic rotation dynamics simulations," *Phys. Rev. E* **88**, 043304 (2013).
- ²⁸V. Dahirel, X. Zhao, B. Couet, G. Batôt, and M. Jardat, "Hydrodynamic interactions between solutes in multiparticle collision dynamics," *Phys. Rev. E* **98**, 053301 (2018).
- ²⁹Y. Inoue, Y. Chen, and H. Ohashi, "Development of a simulation model for solid objects suspended in a fluctuating fluid," *J. Stat. Phys.* **107**, 85–100 (2002).

- ³⁰J. T. Padding, A. Wysocki, H. Löwen, and A. A. Louis, "Stick boundary conditions and rotational velocity auto-correlation functions for colloidal particles in a coarse-grained representation of the solvent," *J. Phys.: Condens. Matter* **17**, S3393–S3399 (2005).
- ³¹D. S. Bolintineanu, G. S. Grest, J. B. Lechman, F. Pierce, S. J. Plimpton, and P. R. Schunk, "Particle dynamics modeling methods for colloid suspensions," *Comput. Part. Mech.* **1**, 321–356 (2014).
- ³²A. Wysocki, C. P. Royall, R. G. Winkler, G. Gompper, H. Tanaka, A. van Blaaderen, and H. Löwen, "Multi-particle collision dynamics simulations of sedimenting colloidal dispersions in confinement," *Faraday Discuss.* **144**, 245–252 (2010).
- ³³M. Hecht, J. Harting, T. Ihle, and H. Herrmann, "Hydrodynamic correlations in multiparticle collision dynamics fluids," *Phys. Rev. E* **72**, 011408 (2005).
- ³⁴E. Bianchi, A. Nikoubashman, and A. Z. Panagiotopoulos, "Self-assembly of Janus particles under shear," *Soft Matter* **11**, 3767–3771 (2015).
- ³⁵M. Yang, A. Wysocki, and M. Ripoll, "Hydrodynamic simulations of self-phoretic microswimmers," *Soft Matter* **10**, 6208–6218 (2014).
- ³⁶A. Lamura, G. Gompper, T. Ihle, and D. M. Kroll, "Multi-particle collision dynamics: Flow around a circular and a square cylinder," *Europhys. Lett.* **56**, 319–325 (2001).
- ³⁷D. S. Bolintineanu, J. B. Lechman, S. J. Plimpton, and G. S. Grest, "Particle dynamics modeling methods for colloid suspensions," *Phys. Rev. E* **86**, 066703 (2012).
- ³⁸J. K. Whitmer and E. Luijten, "Fluid–solid boundary conditions for multiparticle collision dynamics," *J. Phys.: Condens. Matter* **22**, 104106 (2010).
- ³⁹S. Poblete, A. Wysocki, G. Gompper, and R. G. Winkler, "Hydrodynamics of discrete–particle models of spherical colloids: A multiparticle collision dynamics simulation study," *Phys. Rev. E* **90**, 033314 (2014).
- ⁴⁰V. Lobaskin and B. Dünweg, "A new model for simulating colloidal dynamics," *New J. Phys.* **6**, 54 (2004).
- ⁴¹L. P. Fischer, T. Peter, C. Holm, and J. de Graaf, "The raspberry model for hydrodynamic interactions revisited. I. Periodic arrays of spheres and dumbbells," *J. Chem. Phys.* **143**, 084107 (2015).
- ⁴²J. W. Swan and G. Wang, "Rapid calculation of hydrodynamic and transport properties in concentrated solutions of colloidal particles and macromolecules," *Phys. Fluids* **28**, 011902 (2016).
- ⁴³Y. Kobayashi, N. Arai, and A. Nikoubashman, "Structure and dynamics of amphiphilic Janus spheres and spherocylinders under shear," *Soft Matter* **16**, 476–486 (2020).
- ⁴⁴Y. Kobayashi, N. Arai, and A. Nikoubashman, "Structure and shear response of Janus colloid–polymer mixtures in solution," *Langmuir* **36**, 14214–14223 (2020).
- ⁴⁵T. Ihle and D. M. Kroll, "Stochastic rotation dynamics: A Galilean-invariant mesoscopic model for fluid flow," *Phys. Rev. E* **63**, 020201(R) (2001).
- ⁴⁶C.-C. Huang, A. Chatterji, G. Sutmann, G. Gompper, and R. G. Winkler, "Cell-level canonical sampling by velocity scaling for multiparticle collision dynamics simulations," *J. Comput. Phys.* **229**, 168 (2010).
- ⁴⁷C.-C. Huang, G. Gompper, and R. G. Winkler, "Hydrodynamic correlations in multiparticle collision dynamics fluids," *Phys. Rev. E* **86**, 056711 (2012).
- ⁴⁸A. Statt, M. P. Howard, and A. Z. Panagiotopoulos, "Unexpected secondary flows in reverse nonequilibrium shear flow simulations," *Phys. Rev. Fluids* **4**, 043905 (2019).
- ⁴⁹W. Humphrey, A. Dalke, and K. Schulten, "VMD—Visual molecular dynamics," *J. Mol. Graphics* **14**, 33–38 (1996).
- ⁵⁰J. D. Weeks, D. Chandler, and H. C. Andersen, "Role of repulsive forces in determining the equilibrium structure of simple liquids," *J. Chem. Phys.* **54**, 5237–5247 (1971).
- ⁵¹E. Wajnryb, P. Szymczak, and B. Cichocki, "Brownian dynamics: Divergence of mobility tensor," *Physica A* **335**, 339–358 (2004).
- ⁵²H. Hasimoto, "On the periodic fundamental solutions of the Stokes equations and their application to viscous flow past a cubic array of spheres," *J. Fluid Mech.* **5**, 317–328 (1959).
- ⁵³A. M. Fiore, F. Balboa Usabiaga, A. Donev, and J. W. Swan, "Rapid sampling of stochastic displacements in Brownian dynamics simulations," *J. Chem. Phys.* **146**, 124116 (2017).
- ⁵⁴M. P. Howard, A. Z. Panagiotopoulos, and A. Nikoubashman, "Efficient mesoscale hydrodynamics: Multiparticle collision dynamics with massively parallel GPU acceleration," *Comput. Phys. Commun.* **230**, 10–20 (2018).
- ⁵⁵J. A. Anderson, J. Glaser, and S. C. Glotzer, "HOOMD-blue: A Python package for high-performance molecular dynamics and hard particle Monte Carlo simulations," *Comput. Mater. Sci.* **173**, 109363 (2020).
- ⁵⁶See <https://github.com/mphowardlab/azplugins> for source code for the software.
- ⁵⁷See <https://github.com/stochasticHydroTools/PSE> for source code for the software.
- ⁵⁸J. F. Brady, "The long-time self-diffusivity in concentrated colloidal dispersions," *J. Fluid Mech.* **272**, 109–134 (1994).
- ⁵⁹C. W. J. Beenakker, "Ewald sum of the Rotne–Prager tensor," *J. Chem. Phys.* **85**, 1581–1582 (1986).
- ⁶⁰B. Dünweg and K. Kremer, "Microscopic verification of dynamic scaling in dilute polymer solutions: A molecular-dynamics simulation," *Phys. Rev. Lett.* **66**, 2996 (1991).
- ⁶¹B. Dünweg and K. Kremer, "Molecular dynamics simulation of a polymer chain in solution," *J. Chem. Phys.* **99**, 6983–6997 (1993).
- ⁶²I.-C. Ye and G. Hummer, "System-size dependence of diffusion coefficients and viscosities from molecular dynamics simulations with periodic boundary conditions," *J. Phys. Chem. B* **108**, 15873–15879 (2004).
- ⁶³A. Botan, V. Marry, and B. Rotenberg, "Diffusion under confinement: Hydrodynamic finite-size effects in simulation," *Mol. Phys.* **113**, 2674–2679 (2015).
- ⁶⁴P. Simonnin, B. Noetinger, C. Nieto-Draghi, V. Marry, and B. Rotenberg, "Diffusion under confinement: Hydrodynamic finite-size effects in simulation," *J. Chem. Theory Comput.* **13**, 2881–2889 (2017).
- ⁶⁵C. W. J. Beenakker and P. Mazur, "Self-diffusion of spheres in a concentrated suspension," *Physica A* **120**, 388–410 (1983).
- ⁶⁶A. J. C. Ladd, "Hydrodynamic transport coefficients of random dispersions of hard spheres," *J. Chem. Phys.* **93**, 3484–3494 (1990).
- ⁶⁷C. I. Mendoza and I. Santamaría-Holek, "The rheology of hard sphere suspensions at arbitrary volume fractions: An improved differential viscosity model," *J. Chem. Phys.* **130**, 044904 (2009).
- ⁶⁸G. K. Batchelor, "Brownian diffusion of particles with hydrodynamic interaction," *J. Fluid Mech.* **74**, 1–29 (1976).
- ⁶⁹C. W. J. Beenakker and P. Mazur, "Diffusion of spheres in a concentrated suspension II," *Physica A* **126**, 349–370 (1984).
- ⁷⁰A. J. Banchio and G. Nägele, "Short-time transport properties in dense suspensions: From neutral to charge-stabilized colloidal spheres," *J. Chem. Phys.* **128**, 104903 (2008).
- ⁷¹S. Torquato, "Nearest-neighbor statistics for packings of hard spheres and disks," *Phys. Rev. E* **51**, 3170–3182 (1995).
- ⁷²S. Bucciarelli, J. S. Myung, B. Farago, S. Das, G. A. Vliegthart, O. Holderer, R. G. Winkler, P. Schurtenberger, G. Gompper, and A. Stradner, "Dramatic influence of patchy attractions on short-time protein diffusion under crowded conditions," *Sci. Adv.* **2**, e1601432 (2016).
- ⁷³N. F. Carnahan and K. E. Starling, "Equation of state for nonattracting rigid spheres," *J. Chem. Phys.* **51**, 635–636 (1969).
- ⁷⁴B. Cichocki and K. Hinsen, "Self and collective diffusion coefficients of hard sphere suspensions," *Ber. Bunsenges. Phys. Chem.* **94**, 243–246 (1990).
- ⁷⁵W. van Meegen and S. M. Underwood, "Tracer diffusion in concentrated colloidal dispersions. III. Mean squared displacements and self-diffusion coefficients," *J. Chem. Phys.* **91**, 552–559 (1989).
- ⁷⁶A. van Blaaderen, J. Peetermans, G. Maret, and J. K. G. Dhont, "Long-time self-diffusion of spherical colloidal particles measured with fluorescence recovery after photobleaching," *J. Chem. Phys.* **96**, 4591–4603 (1992).
- ⁷⁷G. K. Batchelor, "Diffusion in a dilute polydisperse system of interacting spheres," *J. Fluid Mech.* **131**, 155–175 (1983).
- ⁷⁸A. Fortini, I. Martin-Fabiani, J. Lesage De La Haye, P.-Y. Dugas, M. Lansalot, F. D'Agosto, E. Bourgeat-Lami, J. L. Keddie, and R. P. Sear, "Dynamic stratification in drying films of colloidal mixtures," *Phys. Rev. Lett.* **116**, 118301 (2016).
- ⁷⁹M. P. Howard, A. Nikoubashman, and A. Z. Panagiotopoulos, "Stratification dynamics in drying colloidal mixtures," *Langmuir* **33**, 3685–3693 (2017).

Title: “Mesoscale simulations of diffusion and sedimentation in shape-anisotropic nanoparticle suspensions.”

Contributions:

- **Simulation setup and execution:** I was responsible for setting up the simulations for this study and constructing of colloids with spherocylindrical and cubic shapes.
- **Data analysis:** I contributed to the analysis of the simulation trajectories to measure the self-diffusion and sedimentation coefficients from bulk simulations.
- **Figure preparation:** I contributed to the creation of figures and tables in the paper, ensuring that they clearly illustrated the comparison between different shapes and experimental observations.
- **Manuscript contribution:** I was responsible for writing the original draft of the manuscript and its revision based on the feedback from co-authors and reviewers.

Reprint permissions:

Reprinted from “Y. M. Wani, P. G. Kovakas, A. Nikoubashman and M. P. Howard; Mesoscale simulations of diffusion and sedimentation in shape-anisotropic nanoparticle suspensions, *Soft Matter*, 2024, 20, 3942 DOI: 10.1039/D4SM00271G,” with the permission from the Royal Society of Chemistry.



Cite this: *Soft Matter*, 2024, 20, 3942

Mesoscale simulations of diffusion and sedimentation in shape-anisotropic nanoparticle suspensions

Yashraj M. Wani, ^{†a} Penelope Grace Kovakas, ^{†b} Arash Nikoubashman ^{*cd} and Michael P. Howard ^{*d}

We determine the long-time self-diffusion coefficient and sedimentation coefficient for suspensions of nanoparticles with anisotropic shapes (octahedra, cubes, tetrahedra, and spherocylinders) as a function of nanoparticle concentration using mesoscale simulations. We use a discrete particle model for the nanoparticles, and we account for solvent-mediated hydrodynamic interactions between nanoparticles using the multiparticle collision dynamics method. Our simulations are compared to theoretical predictions and experimental data from existing literature, demonstrating good agreement in the majority of cases. Further, we find that the self-diffusion coefficient of the regular polyhedral shapes can be estimated from that of a sphere whose diameter is the average of their inscribed and circumscribed sphere diameters.

Received 29th February 2024,
Accepted 15th April 2024

DOI: 10.1039/d4sm00271g

rsc.li/soft-matter-journal

I Introduction

The dynamics of nanoparticles (NPs) in suspensions play an important role in numerous applications, ranging from cellular transport¹ to the fabrication of functional nanomaterials.² For example, therapeutic agents can be encapsulated inside or attached to NPs for targeted drug delivery, and differences in NP dynamics in the body can affect their uptake and efficacy.^{3–5} Many factors impact the motion of NPs, including their size, interactions with each other, and interactions with their surroundings.⁶ This work focuses specifically on the effect of shape, which has emerged as an important factor for modulating the properties and function of NPs in many practical applications.^{7,8} For example, shape-anisotropic iron-oxide-based magnetic NPs were shown to enhance contrast for magnetic resonance imaging compared to spherical NPs,⁸ while quantum rods were shown to have enhanced diffusion compared to quantum dots in confined networks.⁹ Given that NPs with a variety of shapes can be readily synthesized^{10–12} and that many naturally occurring NPs (*e.g.*, the rod-like tobacco

mosaic virus^{13,14} and gibbsite platelets¹⁵) also exhibit pronounced shape anisotropy, it is important to develop a fundamental understanding of the relationship between shape and transport properties, such as diffusion coefficients, in order to engineer NPs for practical applications.

Experimentally characterizing how NP dynamics depend on shape and concentration can be challenging. For example, dynamic light scattering is a common technique for measuring NP diffusion from fluctuations in scattered light intensity.¹⁶ However, knowledge about the distribution of NP sizes and/or shapes is needed to extract the diffusion coefficient from the raw measurement data,^{17,18} and it is difficult to perform this analysis for non-dilute solutions.¹⁹ Camera-based tracking of tagged NPs is an alternative approach that allows for the direct measurement of the NP diffusion coefficient,^{9,20} but this method has limited spatial and temporal resolution.²⁰ NP properties may also be affected if labeling agents, such as fluorescent markers, are used.²¹ Further, it can be difficult to prepare NP suspensions with sufficiently low polydispersity and at high enough concentrations to accurately assess how the diffusion coefficient varies with both NP characteristics and concentration.

As a result, theory and simulations have proven to be useful approaches for studying the dynamics of NP suspensions. Early theories predominantly focused on spherical NPs, for which the single-particle translational and rotational diffusion coefficients can be calculated using the classical Stokes–Einstein and Stokes–Einstein–Debye relations, respectively. Theoretical predictions for the first-order concentration dependence of the

^a *Institute of Physics, Johannes Gutenberg University Mainz, Staudingerweg 7, 55128, Mainz, Germany*

^b *Department of Chemical Engineering, Auburn University, Auburn, Alabama 36849, USA. E-mail: mphoward@auburn.edu*

^c *Leibniz-Institut für Polymerforschung Dresden e.V., Hohe Straße 6, 01069 Dresden, Germany. E-mail: anikouba@ipfdd.de*

^d *Institut für Theoretische Physik, Technische Universität Dresden, 01069 Dresden, Germany*

[†] These authors contributed equally.



long-time self-diffusion coefficient for suspensions of spherical NPs have also been derived.^{22,23} Beyond spherical NPs, pioneering works by Kuhn, Kirkwood, and others have led to estimates for the single-particle translational and rotational diffusion coefficients of rod-like particles.^{24–29} At finite concentration, the diffusive motion of the rods becomes more complex but can be split qualitatively into three regimes: at dilute concentrations, rods have essentially unrestricted motion in all directions; at semi-dilute concentrations, their motion is slightly hindered perpendicular to the long axis of the rod; and at high concentrations, the perpendicular diffusive motion is entirely suppressed.³⁰ However, predicting the dynamics of rod-like NPs with quantitative accuracy still remains challenging because their anisotropic shape can lead to complex flow patterns around individual NPs and to non-trivial collective behavior such as nematic or smectic ordering. For more complicated NP shapes than rods, predicting even single-particle diffusion coefficients becomes challenging, and numerical approaches are often required.^{31,32} In general, fully analytic descriptions of NP dynamics in suspensions are challenging to construct due to the many-body hydrodynamic interactions (HIs) between NPs that are mediated by the solvent.

Computer simulations are highly useful tools for numerically investigating NP dynamics in suspensions. The main challenge is to construct models that capture the relevant physics while remaining computationally tractable. Explicitly resolving both the NPs and the solvent molecules they are suspended in using, *e.g.*, classical molecular dynamics (MD) approaches, quickly becomes infeasible because NPs are typically much larger than solvent molecules. However, given the corresponding separation of time scales between the solvent dynamics and NP dynamics, it is often possible to overcome this difficulty using coarse-grained models having simplified or implicit treatments of the solvent.³³ For example, Brownian dynamics (BD) is a well-known implicit-solvent technique that accounts for solvent-induced drag and fluctuating forces on the NPs,³⁴ but which neglects HIs between the NPs in its most basic form. HIs can be introduced to BD through appropriate mobility tensors,³⁵ such as the pairwise far-field Rotne–Prager–Yamakawa tensor for spherical particles.^{36,37} Stokesian dynamics, a gold-standard approach for simulating colloidal suspensions, additionally accounts for short-range lubrication forces between NPs within the BD framework.^{38,39} However, BD approaches that include HIs are often still computationally demanding to implement and require expressions for the mobility tensor, which may be difficult to obtain for complex NP shapes.

To circumvent issues determining inputs needed for a fully implicit treatment of the solvent, several mesoscale simulation methods, including multiparticle collision dynamics (MPCD),^{33,40,41} dissipative particle dynamics,^{42,43} and the lattice Boltzmann method,^{44,45} use simplified particle-based solvent models that are less demanding to simulate than an atomistic model but still have properties resembling that of real solvents. In this work, we will use MPCD because we have recently shown that MPCD can reasonably reproduce expected results for the long-time self-diffusion coefficient and sedimentation coefficient for

suspensions of spherical NPs over a range of NP concentrations,⁴⁶ and the same approach used to model the spherical NPs can be extended to NPs with other shapes. In MPCD, NPs are modeled as conventional MD particles that can be coupled to the solvent through different schemes to ensure HIs develop.^{46–52} The current state-of-the-art coupling scheme, first proposed by Poblete *et al.*, uses a discrete particle model that represents an NP as a mesh of “vertex” particles interconnected *via* elastic springs.⁴⁷ The solvent particles interact with the NPs only through stochastic collisions that are straightforward to compute. We used a discrete particle model to study the long-time self-diffusion of cubes,⁴⁶ and similar models have been used to simulate the self-assembly of colloids with shape and/or interaction anisotropy.^{53–58} However, we are unaware of a systematic study using MPCD to characterize the long-time self-diffusion coefficients and sedimentation coefficients for suspensions of shape-anisotropic NPs at varying concentrations.

In this work, we use MPCD with a discrete particle model to study the long-time self-diffusion and sedimentation coefficients of octahedra, cubes, tetrahedra, and spherocylinders as a function of NP concentration. We investigate the effect of shape by comparing the results for the different NP shapes with each other and with spheres. We also assess the influence of solvent-mediated HIs by comparing the MPCD simulations with implicit-solvent Langevin dynamics (LD) simulations.

II Models

A. Multiparticle collision dynamics

In MPCD, the solvent consists of point particles that are propagated in alternating streaming and collision steps that occur at a regular time interval Δt . During the streaming step, the solvent particles move according to Newton’s equations of motion,

$$\begin{aligned} \frac{d\mathbf{r}_i}{dt} &= \mathbf{v}_i \\ m_i \frac{d\mathbf{v}_i}{dt} &= \mathbf{F}_i, \end{aligned} \quad (1)$$

where \mathbf{r}_i is the position, \mathbf{v}_i is the velocity, and m_i is the mass of particle i , while \mathbf{F}_i is the force acting on particle i . All solvent particles have the same mass m . Unlike standard MD particles, MPCD particles do not interact with each other by pairwise forces, but each particle may be acted on by a body force. For a constant \mathbf{F}_i , eqn (1) can be integrated analytically to give the standard equations of ballistic motion.

In the collision step, the solvent particles are sorted into cubic cells of edge length ℓ , then exchange momentum with particles in the same cell according to a collision scheme. Here, we use the stochastic rotation dynamics (SRD) scheme without angular momentum conservation.^{40,41} SRD updates the velocity of particle i in cell j according to:

$$\mathbf{v}_i \leftarrow \mathbf{u}_j + \mathbf{\Omega}_j (\mathbf{v}_i - \mathbf{u}_j), \quad (2)$$

where \mathbf{u}_j is the mass-averaged velocity of the particles in cell j and $\mathbf{\Omega}_j$ is the rotation matrix for cell j . The matrix $\mathbf{\Omega}_j$ rotates about an axis randomly selected for cell j by a fixed angle α . At



each collision step, the collision cells are shifted along each Cartesian direction by a random amount drawn uniformly from $[-\ell/2, +\ell/2]$ to ensure Galilean invariance,^{59,60} and a cell-level Maxwellian thermostat is used to maintain a constant temperature T .⁶¹

The natural units for MPCD simulations are the length ℓ of the collision cells, the mass m of the solvent particles, and the thermal energy $k_B T$, where k_B is the Boltzmann constant. The corresponding unit of time is $\tau = \sqrt{m\ell^2\beta}$, where $\beta = 1/(k_B T)$. We adopted the standard SRD parameters $\Delta t = 0.1\tau$, $\alpha = 130^\circ$, and average solvent number density $5\ell^{-3}$, which give a liquid-like Newtonian fluid with dynamic viscosity $\eta_0 = 3.95k_B T\tau/\ell^3$.⁶²

B. Discrete particle model

A discrete particle model was used to represent the NPs and couple them to the solvent.^{46,47} The NP shapes we modeled were a sphere, an octahedron, a cube, a tetrahedron, and two spherocylinders with different aspect ratios (Fig. 1). Each NP consisted of N_v vertex particles on the surface of the shape, and each vertex particle had mass $5m$. The vertex particles were bonded to their nearest neighbors with a harmonic potential,

$$\beta u_b(r) = \frac{k_b}{2}(r - r_b)^2, \quad (3)$$

where r is the distance between two particles, r_b is the distance required for the bond by the shape, and k_b is the spring constant. To ensure that the NPs maintained their shapes, the vertex particles were also bonded to either an additional particle in the center of the NP (sphere, octahedron, cube, & tetrahedron) or their diametrically opposed vertex particle (spherocylinders). Excluded-volume interactions between NPs were modeled by applying the Weeks–Chandler–Andersen repulsive potential⁶³ between vertex particles

$$\beta u(r) = \begin{cases} 4 \left[\left(\frac{\sigma}{r} \right)^{12} - \left(\frac{\sigma}{r} \right)^6 \right] + 1, & r \leq 2^{1/6}\sigma \\ 0, & \text{otherwise} \end{cases} \quad (4)$$

All vertex particles (but not the central particle) were coupled to the MPCD solvent through the collision step eqn (2).⁴⁷ Between collision steps, the central and vertex particles moved according to eqn (1). Based on our prior work,⁴⁶ we used $k_b = 5000\ell^{-2}$ to make stiff bonds and $\sigma = \ell$, and we integrated eqn (1) using

the velocity Verlet algorithm with time step 0.005τ . We visually confirmed that all NPs maintained a nearly rigid shape and that no NPs penetrated each other for the vertex-particle configurations chosen as described next.

Sphere.—We modeled a sphere having diameter $d = 6\ell$ [Fig. 1(a)] as a reference point. To create the vertex particles, we subdivided the triangular faces of a regular icosahedron twice and scaled the positions of all vertices to lie on the surface of the sphere. This process resulted in $N_v = 162$ vertex particles with a typical nearest-neighbor distance between 0.83ℓ and 0.97ℓ . Note that this model differs from the one we used in ref. 46 in two ways: (1) the number of vertex particles is larger and (2) the excluded volume is handled through the vertex particles rather than through the central particle. These choices were made in this work so that the spheres would have a comparable surface density of vertex particles and the same style of excluded-volume interactions as the anisotropic NPs we studied.

Octahedron and tetrahedron.—We modeled a regular octahedron and a regular tetrahedron, both having edge length $a = 6\ell$ [Fig. 1(b) and (d)]. Because the faces of these polyhedra are equilateral triangles, we first created a three-dimensional triangulated model of each shape using computer-aided design software, then subdivided the faces 3 times to create a triangular mesh of vertex particles. This process resulted in 9 vertex particles per edge and distance $a/8 = 0.75\ell$ between all nearest-neighbor vertex particles for both shapes. The total number of vertex particles was $N_v = 258$ for the octahedron and $N_v = 130$ for the tetrahedron.

Cube.—We modeled a cube with edge length $a = 6\ell$ [Fig. 1(c)] using a square mesh with 8 vertex particles per edge. The total number of vertex particles was $N_v = 296$, and the distance between nearest-neighbor vertex particles was $a/7 \approx 0.86\ell$. This is the same vertex particle configuration as in ref. 46, and the description here corrects a typographical error for the number of vertex particles per edge. Unlike in ref. 46, though, a central particle was used to maintain rigidity to keep consistency with the sphere, octahedron, and tetrahedron.

Spherocylinder.—We modeled two types of spherocylinders: both had two hemispheres with diameter $d = 6\ell$, but one had a cylinder of length $h = 6\ell$ while the other cylinder had the length $h = 12\ell$ [Fig. 1(e)]. Thus, the spherocylinders had aspect ratios $\lambda \equiv d/h = 1$ and 2 , respectively. This degree of anisotropy is

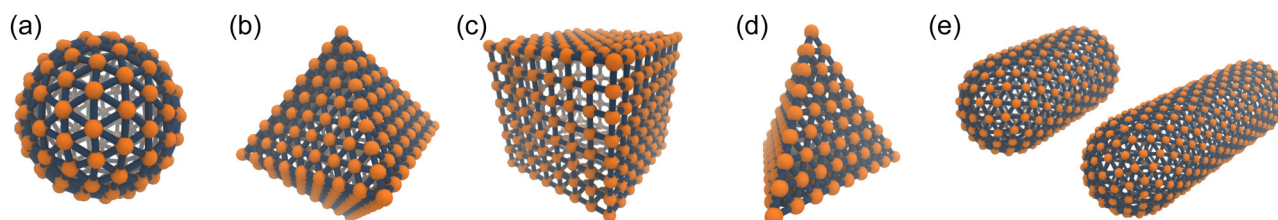


Fig. 1 Discrete particle model for (a) sphere, (b) octahedron, (c) cube, (d) tetrahedron and (e) two spherocylinders (aspect ratios $\lambda = 1$ and 2). The N_v vertex particles are shown in orange, and the bonds to their nearest neighbors are shown in blue. To improve the clarity of these renderings, the size of the vertex particles has been decreased, and central particles and additional bonds used to maintain the shape have been omitted. These snapshots were rendered using visual molecular dynamics (version 1.9.3).⁶⁴



much smaller than that of many rod-like particles, such as those of biological origin like the fd virus^{65,66} and tobacco mosaic virus,¹³ that is often in the range $\lambda \gtrsim 10$. Nanorods with smaller aspect ratios can be synthesized,^{67–69} but we found surprisingly little data on their transport coefficients. Hence, we chose to study spherocylinders with these smaller aspect ratios to begin to bridge the knowledge gap between spheres and long rod-like NPs. Discrete particle models for the spherocylinders were constructed through a multi-step process: First, a mesh of vertex particles for the hemispheres was created by slicing our discrete sphere model in half along a plane that exposed 20 evenly spaced vertex particles around its circumference and had 91 vertex particles in total. Then, vertex particles for the cylinder were generated from the ring of 20 exposed vertex particles by translating the ring by 0.75ℓ and rotating it around the axis of the cylinder by 9° to stagger the particles on consecutive rings. This process was repeated until the entire cylinder surface was covered with vertex particles. The total number of vertex particles per spherocylinder was $N_v = 322$ for $\lambda = 1$ and $N_v = 482$ for $\lambda = 2$, with the nearest-neighbor distance between vertex particles ranging from 0.83ℓ to 0.97ℓ .

C. Simulation details

We performed bulk simulations containing N NPs in a cubic simulation box with edge length $L = 120\ell$ and periodic boundary conditions. We simulated a range of nominal NP volume fractions $\phi = Nv/L^3$, where v is the nominal volume of each NP (Table 1), by varying N . We created equilibrated configurations of NPs at the different volume fractions using LD simulations. LD simulations are faster to perform than MPCD simulations because they do not include HI, and we also chose the friction coefficient for the LD simulations to give faster NP dynamics than in the MPCD simulations in order to accelerate equilibration. Starting from these configurations, we measured the long-time self-diffusion coefficient as a function of ϕ using equilibrium simulations (Section IIIA) and the sedimentation coefficient as a function of ϕ using nonequilibrium simulations (Section IIIB). All simulations were conducted using HOOMD-blue^{70,71} (version 2.9.7) extended with azplugins⁷² (version 0.12.0).

For the spheres and regular polyhedra, we performed one equilibrium simulation of length $2 \times 10^5\tau$ and recorded the position of all central particles every 10τ . We performed one nonequilibrium simulation consisting of a warmup period of

$0.5 \times 10^5\tau$ to reach steady state followed by a production period of length $1.5 \times 10^5\tau$ in which we recorded the average velocity of the NPs every 0.105τ and the average velocity of the solvent every 0.1τ . The different sampling frequencies for the NPs and solvent were chosen to account for acceleration of the NPs between solvent collisions.⁴⁶ To estimate error bars, we subdivided these trajectories into three blocks and computed the standard error between blocks.

For the spherocylinders, we performed eight equilibrium simulations of length $10^5\tau$ and recorded the position of enough vertex particles to reconstruct the center of mass of each NP every 2.5τ . We performed three nonequilibrium simulations consisting of a $0.5 \times 10^5\tau$ warmup period and $1 \times 10^5\tau$ production period with the velocities sampled in the same way as for the other shapes. Error bars were estimated as the standard error of the independent simulations.

III Results and discussion

A. Long-time self-diffusion coefficient

We computed the long-time self-diffusion coefficient D of the NPs from the time derivative of the average mean squared displacement $\langle \Delta r^2 \rangle$ of each NP,³⁴

$$D = \lim_{t \rightarrow \infty} \frac{1}{6} \frac{d\langle \Delta r^2 \rangle}{dt}. \quad (5)$$

To improve statistics, we averaged $\langle \Delta r^2 \rangle$ over NPs and time origins, and we extracted D from the time average of the long-time plateau of $d\langle \Delta r^2 \rangle/dt$, which we fit in the time range $10^4\tau \leq t < 2 \times 10^4\tau$ for the spheres and regular polyhedra and in the range $3 \times 10^4\tau \leq t < 5 \times 10^4\tau$ for the spherocylinders. Note that in defining D in this way, the long-time self-diffusion coefficient is a scalar quantity. For anisotropic NPs, the short-time motion is characterized by a diffusion tensor; this tensor is isotropic for the regular polyhedra we have studied,⁷³ but it is anisotropic for the spherocylinders.⁷⁴ Hence, D reported in this work implies an orientational average at long times for the spherocylinders.

Due to the long-ranged nature of solvent-mediated HIs, self-diffusion coefficients measured in simulations with periodic boundary conditions can suffer from noticeable finite-size effects.^{75–77} For a cubic simulation box such as ours, the self-diffusion coefficient in an infinitely large box D^∞ is related to D

Table 1 Geometric properties of the regular polyhedra investigated. General formulae are given in terms of the edge length a , with the specific value for $a = 6\ell$ (the edge length for all our polyhedral NPs) quoted in parentheses. The properties are the volume v , surface area A , sphericity ψ , inscribed-sphere diameter d_i , circumscribed-sphere diameter d_c , and mean of inscribed-sphere and circumscribed-sphere diameters \bar{d}

	v	(ℓ^3)	A	(ℓ^2)	ψ	d_i	(ℓ)	d_c	(ℓ)	\bar{d}	(ℓ)
Octahedron	$\frac{\sqrt{2}}{3}a^3$	(101.8)	$2\sqrt{3}a^2$	(124.7)	0.846	$\frac{\sqrt{2}}{\sqrt{3}}a$	(4.9)	$\sqrt{2}a$	(8.5)	$\frac{\sqrt{2} + \sqrt{3}}{\sqrt{6}}a$	(6.7)
Cube	a^3	(216.0)	$6a^2$	(216.0)	0.806	a	(6.0)	$\sqrt{3}a$	(10.4)	$\frac{1 + \sqrt{3}}{2}a$	(8.2)
Tetrahedron	$\frac{a^3}{6\sqrt{2}}$	(25.5)	$\sqrt{3}a^2$	(62.4)	0.671	$\frac{a}{\sqrt{6}}$	(2.4)	$\frac{\sqrt{3}}{\sqrt{2}}a$	(7.3)	$\frac{\sqrt{2}}{\sqrt{3}}a$	(4.9)



in a finite box with edge length L by^{76,77}

$$D^\infty = D + \xi \frac{k_B T}{6\pi\eta L}, \quad (6)$$

where $\xi \approx 2.837297$ and η is the suspension viscosity. Applying eqn (6) can be challenging in practice because it requires knowledge of η , which depends on the shape and volume fraction of the NPs. Analytic expressions for η exist for some NP shapes,^{78,79} but they are typically only valid for small NP volume fractions.⁸⁰ Hence, additional costly simulations are usually needed to accurately determine η . To avoid this step, we approximated η with a Stokes–Einstein-like proportionality, $\eta/\eta_0 = D_0/D^\infty$,^{46,77} where $D_0 = k_B T/\gamma_0$ is the long-time self-diffusion coefficient at infinite dilution (*i.e.*, the single-particle limit) and γ_0 is the corresponding hydrodynamic friction coefficient for the NP (again, orientationally averaged for the spherocylinders). Substituting for η in eqn (6) and solving for D^∞ yields

$$D^\infty \approx D \left(1 - \xi \frac{\gamma_0}{6\pi\eta_0 L} \right)^{-1}. \quad (7)$$

We previously tested this approximate correction by computing D for spherical NPs in different box sizes L and confirming that D^∞ was independent of L within our measurement accuracy.⁴⁶

To apply eqn (7), γ_0 must be determined for each NP shape. Experimental correlations⁸¹ for γ_0 exist [*e.g.*, eqn (9) below]; however, it is not guaranteed that the MPCD simulations are consistent with these. Instead, we noted that all diffusivities are corrected by the same factor in eqn (7) regardless of ϕ and that eqn (6) can be used directly when ϕ is sufficiently small that $\eta \approx \eta_0$. Accordingly, we linearly extrapolated our measured D to $\phi = 0$, using the data from the smallest two values of ϕ that we simulated, to obtain a measured D_0 with finite-size effects. We then applied eqn (6) with $\eta = \eta_0$ to calculate D_0^∞ from D_0 and used the ratio D_0^∞/D_0 as the finite-size correction factor for all D . In the rest of the paper, all diffusion coefficients have been corrected for finite-size effects in this way, but we will still refer to them as D and D_0 for notational simplicity.

1. Regular polyhedra. We first investigated the shape-dependence of the long-time self-diffusion coefficient extrapolated to infinite dilution D_0 for the regular polyhedra we simulated (octahedron, cube, and tetrahedron). Pettyjohn and Christiansen experimentally measured the settling rates of particles with these shapes at low Reynolds number.^{73,81} They found that the settling rate could be correlated with particle shape using the sphericity ψ , defined as the ratio of the surface area of a sphere having the same volume as the shape to the actual surface area A of the shape,

$$\psi = \frac{\pi^{1/3}(6v)^{2/3}}{A}. \quad (8)$$

The sphericities of our regular polyhedra are listed in Table 1. Using the correlation for the settling velocity from ref. 81, a correlation for the hydrodynamic friction coefficient γ_0 is

$$\gamma_0 = 3\pi\eta_0 \left(\frac{6v}{\pi} \right)^{1/3} \left[0.843 \log_{10} \left(\frac{\psi}{0.065} \right) \right]^{-1}. \quad (9)$$

Table 2 Diffusion coefficient at infinite dilution D_0 for the sphere and regular polyhedra calculated from our simulations, using eqn (9), and using the Stokes–Einstein relationship for a sphere with mean diameter \bar{d} given in Table 1. All values are in units of $10^{-3} \ell^2/\tau$

	Simulation	Using eqn (9)	Using \bar{d}
Sphere	4.32	4.48	
Octahedron	3.95	4.36	4.01
Cube	3.31	3.33	3.28
Tetrahedron	5.14	6.29	5.48

Note that the first term in parentheses is the diameter of an equivalent-volume sphere to the shape, so eqn (9) gives $\gamma_0 = 3\pi\eta_0 d$ for a sphere with diameter d as expected.

Based on eqn (9), a cube should diffuse more slowly than an octahedron, while an octahedron should diffuse more slowly than a tetrahedron when all have the same edge length a ; a sphere with diameter $d = a$ is predicted to have D_0 between that of the octahedron and the tetrahedron (Table 2). Indeed, our simulation results for D_0 were qualitatively consistent with these predictions. Quantitatively, D_0 from the cube simulations was in excellent agreement with the value predicted using eqn (9), but D_0 from the octahedron and tetrahedron simulations was 9% and 18% smaller, respectively. We calculated a similar deviation between the measured and predicted D_0 for tetrahedra in recent experiments by Hoffmann and coworkers, who fabricated tetrahedral clusters from four spherical polystyrene NPs with diameter 154 nm; they measured a self-diffusion coefficient of $D_0 = 1.72 \times 10^{-12} \text{ m}^2 \text{ s}^{-1}$ in water,^{82,83} which is 22% smaller than the predicted value of $D_0 = 2.2 \times 10^{-12} \text{ m}^2 \text{ s}^{-1}$ when using an edge length of $a = 308 \text{ nm}$ in eqn (9). These clusters are, however, not true tetrahedra so it is unclear whether this deviation from eqn (9) should be expected in the MPCD simulations too.

We and others previously found that D_0 for a cube can also be reasonably well-approximated by D_0 for a sphere with diameter $\bar{d} = (d_1 + d_c)/2$, the arithmetic mean of the diameters d_1 and d_c of the spheres that inscribe and circumscribe it, respectively.^{32,46} We carried out the same calculation for the octahedron and tetrahedron, and we again found good agreement with our simulations (Table 2). Thus, using \bar{d} seems to provide a quick and reasonable estimate of D_0 for regular polyhedra as an alternative to eqn (9).

We next investigated the volume-fraction dependence of D [Fig. 2(a)]. Given that the different NP shapes had different D_0 , we report D/D_0 to facilitate comparison between shapes [Fig. 2(b)]. The tetrahedra exhibited the strongest dependence on ϕ , the spheres exhibited the weakest dependence on ϕ , while both the cubes and octahedra exhibited a similar dependence on ϕ that was intermediate between the spheres and tetrahedra. In general, we expected D to decrease when ϕ increased because increased interactions between NPs usually slow their motion. At low NP volume fractions, long-ranged solvent-mediated HIs are important because short-ranged interactions are infrequent. Differences in the dependence of D/D_0 on ϕ seen in Fig. 2 when ϕ is small are then likely caused by differences in HIs between shapes.

At higher NP volume fractions, direct interactions between NPs become more frequent and significant, particularly those



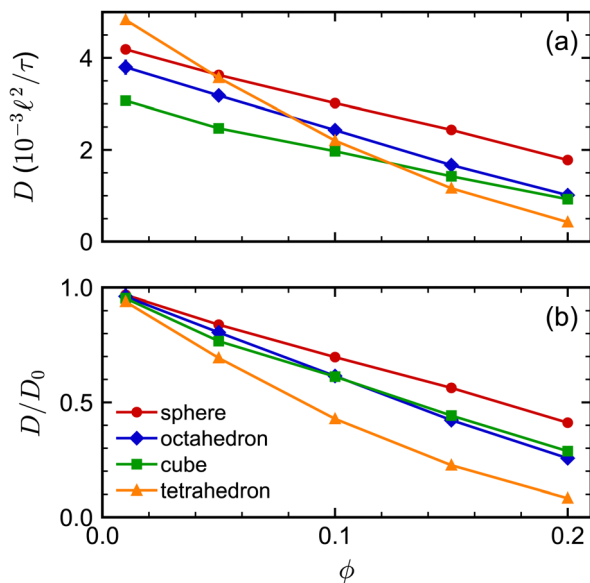


Fig. 2 (a) Long-time self-diffusion coefficient D of spheres, octahedra, cubes, and tetrahedra as a function of nominal volume fraction ϕ . (b) D normalized by its value linearly extrapolated to infinite dilution D_0 .

due to excluded-volume between NPs. Indeed, we expect that eventually $D/D_0 \rightarrow 0$ when the NPs reach a freezing or jamming transition that essentially traps each NP in a local cage of surrounding NPs. Based on ϕ , the regular polyhedra we simulated were all expected to be fluids even at our largest concentration ($\phi = 0.20$).^{84–87} However, we noted that the actual excluded volume v_{ex} of the NPs (and hence excluded-volume fraction ϕ_{ex}) differs from the nominal volume v (and nominal volume fraction ϕ) because the vertex particles in our discrete model have a finite size. For example, the vertex particles on the surface of the cube [Fig. 1(c)] protrude roughly $\sigma/2$, so the edge length of the volume excluded by the cube is roughly σ longer than the nominal edge length. In general, we define the excluded volume as that of the regular polyhedron that contains the spheres with diameter σ on the surface of the nominal regular polyhedron. Geometric considerations give the edge length a_{ex} of our excluded-volume regular polyhedra as $a_{\text{ex}} = a(1 + \sigma/d_i)$. The ratio of the excluded volume to nominal volume is then $v_{\text{ex}}/v \approx (1 + \sigma/d_i)^3$ and ϕ_{ex} is proportionally larger than ϕ by the same factor. This larger excluded size a_{ex} is evident in the radial distribution function $g(r)$ (Fig. 3) for all shapes.

We attempted to assess the effect of this difference in nominal and excluded volume using the spherical NPs. We performed additional simulations where we implemented the excluded-volume interaction between spheres through a core-shifted Weeks–Chandler–Andersen potential between only their central particles, like in ref. 46. As expected, we found that there was less structuring in the fluid, measured through $g(r)$, at a given nominal volume fraction ϕ due to the smaller excluded volume of each sphere [Fig. 4(a)]. However, we found little difference in the diffusivity over the range of volume fractions investigated [Fig. 4(b)]. Moreover, the simulation data for D/D_0 agreed well with experimental data when plotted using ϕ .

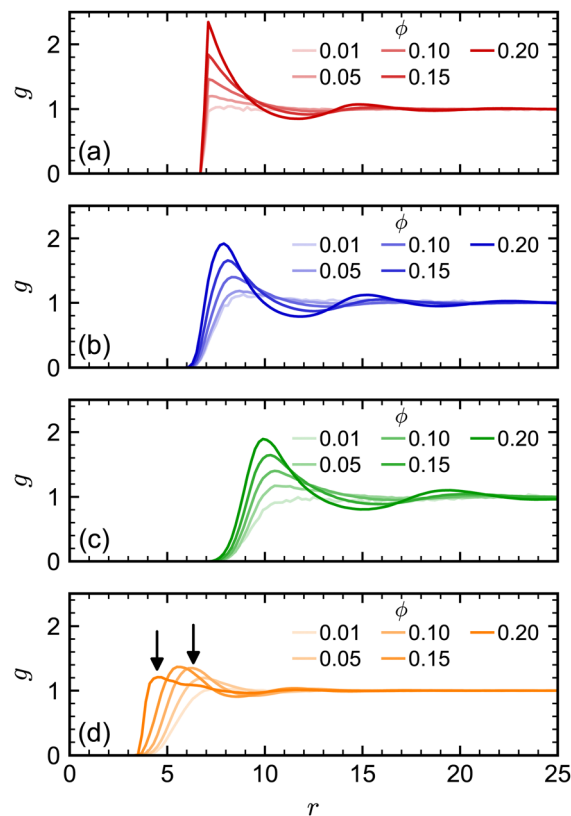


Fig. 3 Radial distribution function for (a) spheres, (b) octahedra, (c) cubes, and (d) tetrahedra at different nominal volume fractions ϕ . The arrows in (d) denote signature peaks for the transition to pentagonal dipyrramids at $0.55a_{\text{ex}}$ and $0.75a_{\text{ex}}$.^{84,85}

We observed similar agreement between MPCD simulations and experiments for cubes using the nominal volume fraction ϕ in our

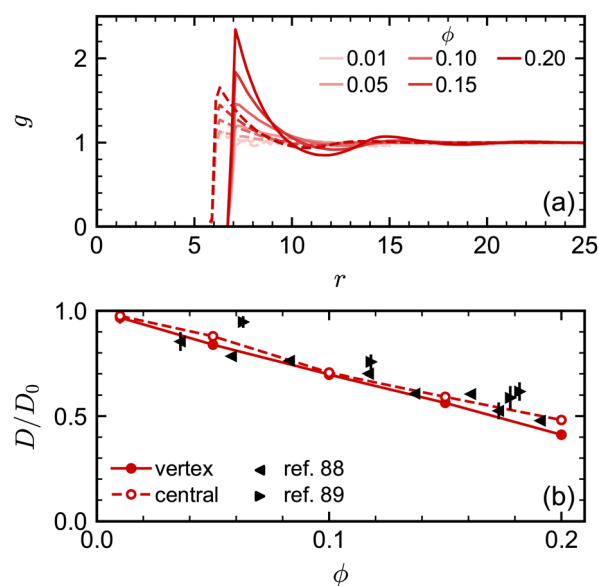


Fig. 4 (a) Radial distribution function for spheres with excluded volume handled through either vertex particles (solid lines) or a central particle (dashed lines). (b) Long-time self-diffusion coefficient D (normalized by D_0) for the same systems compared with experimental data.^{88,89}



prior work⁴⁶ [see also Fig. 5(c)]. Hence, at least over the range of volume fractions considered for the spheres, the nominal volume fraction ϕ seems to be a good description of the concentration.

We note, though, that structural effects caused by differences in nominal and excluded volume may still become significant at sufficiently high excluded volume fractions, particularly if a phase transition is approached. The tetrahedron, which has the largest v_{ex}/v ratio of our regular polyhedra, is an excellent example of this point. Previous simulations of hard tetrahedra^{84,85} revealed a transition to a fluid consisting of pentagonal dipyramids when the volume fraction was 0.47. That study found that $g(r)$ showed a distinct signature of this transition: at low volume fractions where dipyramids did not form, $g(r)$ had its first peak at $r = 0.75a$; whereas, at higher volume fractions where dipyramids formed, this original peak disappeared, and the first peak shifted to a much smaller distance $r = 0.55a$. Our largest nominal volume fraction $\phi = 0.20$ is well below the reported transition to dipyramids, but if we instead consider the excluded volume fraction ($\phi_{\text{ex}} = 0.56$), then the system should have surpassed this transition. When we computed $g(r)$ for the tetrahedra [Fig. 3(d)], we observed these signature peaks emerging at the reported r if a_{ex} was used rather than a . Thus, the tetrahedra appear to undergo a transition to dipyramids that is not expected using only ϕ . The more dramatic slowing down of the tetrahedra dynamics with ϕ compared to the other shapes could be partially due to this transition.

Finally, we assessed the influence of HIs between the NPs on their long-time self-diffusion by performing complementary LD

simulations that do not have these interactions (Fig. 5). Due to the lack of long-ranged solvent-mediated HIs, we did not perform any finite-size corrections for the LD diffusion coefficients. Qualitatively, D/D_0 had a similar dependence on ϕ both with and without HIs, with differences for the tetrahedra being most pronounced and differences for the cubes being least pronounced. However, there were clear quantitative differences between the MPCD simulations with HIs and the LD simulations without HIs. For all shapes, D/D_0 was smaller for a given ϕ (had a stronger ϕ dependence) in the LD simulations compared to the MPCD simulations. Taken together, these differences support the established picture that solvent-mediated HIs and excluded-volume interactions between NPs that determine their fluid structure both play a role in determining the NP dynamics.

As an aside, we remark that the agreement between our MPCD simulations and experiments^{88,89} significantly improved for the spherical NPs compared to our previous study,⁴⁶ which is likely due to the higher surface density of vertex particles used in this work. The accuracy of discrete particle models typically improves with increasing surface density,⁹¹ and the surface density of vertex particles on the sphere was roughly four times that of ref. 46. We note that Poblete *et al.* recommended a surface density of $0.53/\ell^2$ in their study of spherical NPs to balance discretization and inertia effects,⁴⁷ which lies between the value of $0.37/\ell^2$ used in ref. 46 and $1.43/\ell^2$ used here. The surface density of vertex particles used for the other regular polyhedra was comparable to that of our spheres.

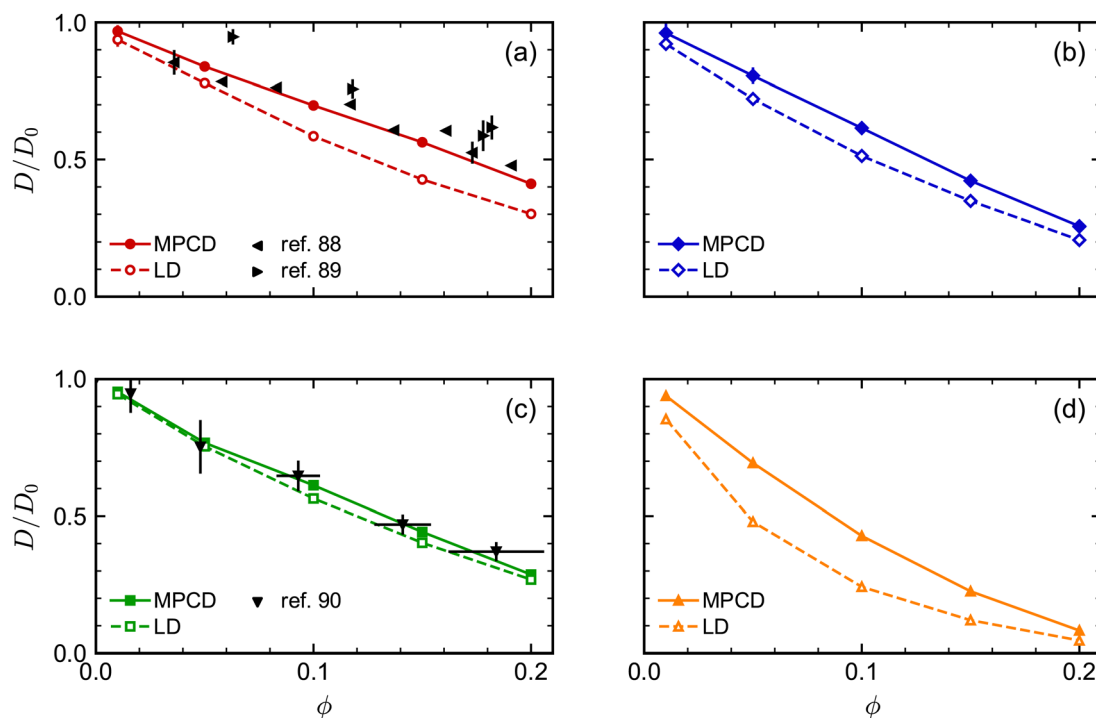


Fig. 5 Comparison of long-time self-diffusion coefficient D (normalized by D_0) of (a) spheres, (b) octahedra, (c) cubes, and (d) tetrahedra as a function of volume fraction ϕ from MPCD and LD simulations. Experimental data is included in (a) and (c) from multiple sources. The experimental values of D for the spheres^{88,89} were scaled by the Stokes–Einstein prediction for D_0 , while the experimental values of D for the cubes⁹⁰ were scaled such that $D/D_0 = 1$ for the lowest-concentration point in that data set ($\phi \approx 0$).



2. Spherocylinders. Having studied the self-diffusion of these regular polyhedra, we next investigated the long-time self-diffusion of spherocylinders. Bolhuis and Frenkel numerically studied the phase diagram of hard spherocylinders for a range of aspect ratios λ .⁹² For $\lambda \leq 2$, the spherocylinders exhibited only two phases—a low-density isotropic phase and a high-density crystal phase—with the transition between these occurring at volume fraction 0.58 and 0.53 for $\lambda = 1$ and 2, respectively. We therefore restricted our simulations to $\phi \leq 0.30$, which corresponds to $\phi_{\text{ex}} < 0.44$ for our spherocylinders ($v_{\text{ex}}/v = 1.45$ and 1.41 for $\lambda = 1$ and 2), in order to focus our calculations on the isotropic phase. We confirmed this was the case by computing a global nematic order parameter,^{93,94} finding it to be close to zero (0.02 and 0.03 for $\lambda = 1$ and 2 when $\phi = 0.30$) as expected for an isotropic phase.

In the isotropic phase, the translational diffusion of rod-like objects is the orientational average of their parallel and normal components. The self-diffusion coefficient of rods in the infinite dilution limit can be estimated as⁹⁵

$$D_0 = \frac{k_B T}{3\pi\eta(\lambda+1)d} \left[\ln(\lambda+1) + 0.316 + \frac{0.5825}{(\lambda+1)} + \frac{0.050}{(\lambda+1)^2} \right], \quad (10)$$

where the last three terms in the parenthesis correct for end effects.^{28,29,96} This equation gives $D_0 = 2.94 \times 10^{-3} \ell^2/\tau$ and $2.41 \times 10^{-3} \ell^2/\tau$ for rods with $\lambda = 1$ and 2 in our MPCD solvent, respectively. Our simulated values $D_0 = 3.09 \times 10^{-3} \ell^2/\tau$ and $2.57 \times 10^{-3} \ell^2/\tau$ were within 5% of eqn (10), showing the expected decrease of D_0 with λ . We also note that eqn (10) underpredicts the diffusivity of a sphere ($\lambda = 0$) by about 5% compared to the classical Stokes–Einstein relation.

The concentration dependence of D/D_0 with ϕ was similar for both spherocylinders (Fig. 6). Indeed, D/D_0 for the spherocylinders with $\lambda = 1$ was nearly indistinguishable from that for the spheres ($\lambda = 0$). The longer spherocylinders with $\lambda = 2$ showed some systematic differences, consistently having a slightly smaller value than for $\lambda = 1$ at a given ϕ . This result indicates that even a small amount of anisotropy may begin to have an effect on the diffusive dynamics, but the magnitude of this effect seems to be small. We also compared our simulation data to the parametric fit of ref. 97. Our simulations qualitatively agreed with the prediction that D/D_0 should be smaller for a larger λ at a given ϕ , but the simulations consistently had smaller values of D/D_0 than predicted. We note that ref. 97 used BD simulations that lacked HIs to develop this fit, so it is unclear to what extent we should expect agreement to simulations with HIs.

B. Sedimentation

After investigating the long-time self-diffusion coefficients of our shape-anisotropic NPs, we characterized their sedimentation coefficients. This complementary dynamic property of a suspension is important for understanding, *e.g.*, how NPs settle under gravity. We defined the sedimentation coefficient K from the linear proportionality between the average velocity \mathbf{u} of an NP under a sufficiently small applied force \mathbf{F} ,

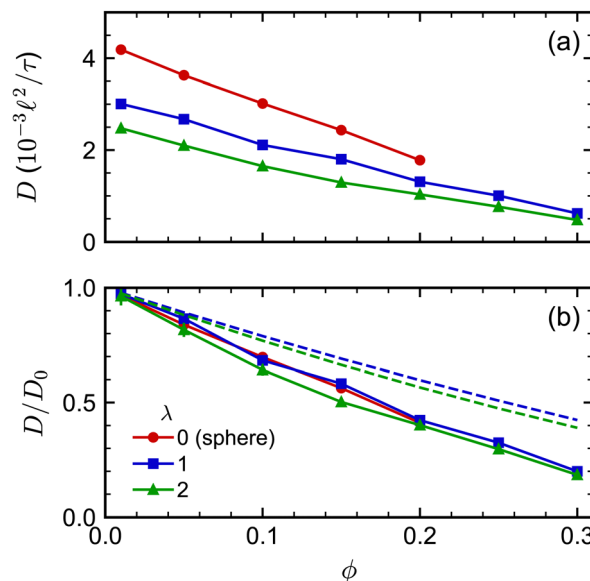


Fig. 6 (a) Long-time self-diffusion coefficient D for spherocylinders with aspect ratios $\lambda = 1$ and 2 as a function of volume fraction ϕ . The sphere data from Fig. 2 is included as a reference point with $\lambda = 0$. (b) D normalized by its value extrapolated to infinite dilution D_0 . The dashed curves in (b) are D/D_0 predicted from the fit of ref. 97.

$$\mathbf{u} = K\gamma_0^{-1}\mathbf{F}. \quad (11)$$

To measure K in our simulations, we imposed a constant force $\mathbf{F} = f_x \hat{\mathbf{x}}$ on all NPs, where $\hat{\mathbf{x}}$ is the unit vector in the x direction, and measured their average velocity $u_x = \mathbf{u} \cdot \hat{\mathbf{x}}$. The applied forces were $f_x = 0.5k_B T/\ell$ and $1.0k_B T/\ell$ per NP, which we distributed evenly among all the vertex and central particles in each NP. A balancing force was applied to the MPCD particles to ensure that the total force on the system was zero. We allowed the system to reach a steady state under the imposed forces, performed a production run where we measured u_x , and extracted K from a linear regression of u_x and f_x .

As for diffusion coefficients, the sedimentation coefficients from our MPCD simulations must be corrected for finite-size effects from periodic boundary conditions. The sedimentation coefficient measured in an infinitely large box K^∞ is related to the one measured in a finite box by⁹⁸

$$K^\infty = K + \zeta S(0) \frac{\gamma_0}{6\pi\eta L}, \quad (12)$$

where $S(0)$ is the static structure factor at zero wavevector. This structure factor is related to the isothermal compressibility and so can be computed from an equation of state. Here, we used the virial expansion of the pressure, which gives

$$S(0) = \left(1 + \sum_{n=2} n \hat{B}_n \phi_{\text{ex}}^{n-1} \right)^{-1}, \quad (13)$$

where $\hat{B}_n = B_n/v^{n-1}$ and B_n is the n -th virial coefficient. We used ϕ_{ex} in eqn (13) because it should characterize the structure of the suspension better than ϕ (see discussion of Fig. 3). We used up to the 8th virial coefficient for the regular polyhedra⁹⁹ and



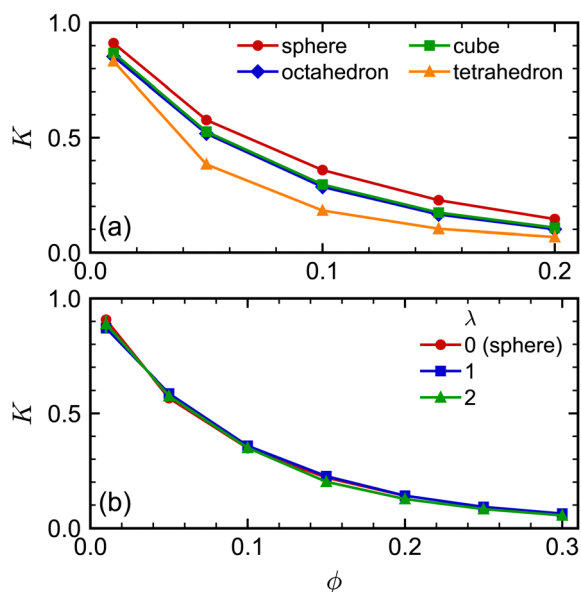


Fig. 7 Sedimentation coefficient K of (a) spheres, octahedra, cubes, and tetrahedra and (b) spherocylinders as a function of volume fraction ϕ . The frame of reference used to define K is the one where the volume-averaged velocity is zero.

up to the 5th virial coefficient for the spherocylinders.^{100,101} Like eqn (6), eqn (12) also includes the suspension viscosity η so we made the same Stokes–Einstein-like approximation to eliminate this dependency,

$$K^\infty \approx K + \zeta S(0) \frac{D}{D_0} \frac{\gamma_0}{6\pi\eta_0 L}. \quad (14)$$

We used the finite-size-corrected D/D_0 and computed $\gamma_0 = k_B T/D_0$ from the finite-size-corrected D_0 . Note that eqn (12) and (14) fix an error in eqn (19) and (20) of ref. 46. All sedimentation coefficients are corrected in this way, but for notational simplicity, we will refer to them as K in the remaining discussion.

MPCD conserves linear momentum, so the sedimentation coefficients calculated directly from the simulation are in a frame of reference where the mass-averaged velocity of the NPs and solvent is zero. However, it is a common practice to consider suspensions in the frame of reference where the volume-averaged velocity is zero, *i.e.*, $\langle \mathbf{u} \rangle = \phi \mathbf{u} + (1 - \phi) \mathbf{u}_0 = \mathbf{0}$ where \mathbf{u}_0 is the solvent velocity. Shifting from the mass-averaged to volume-averaged frame of reference amounts to a rescaling of K , which we implemented as in our previous work.⁴⁶ All values of K are presented in the frame of reference where the volume-averaged velocity is zero.

The sedimentation coefficients of the regular polyhedra [Fig. 7(a)] exhibited a qualitatively similar dependence on shape and concentration as the self-diffusion coefficients did. We consistently found that the spheres had the largest K , the tetrahedra had the smallest K , while the octahedra and cubes had an intermediate K . Moreover, all sedimentation coefficients decreased with increasing concentration, as expected, with the tetrahedra having the strongest concentration dependence. The sedimentation coefficients of both spherocylinders were highly

similar to each other and to that of the sphere [Fig. 7(b)]. These behaviors are qualitatively similar to the self-diffusion coefficients, so we will not repeat that discussion here for brevity.

IV Conclusions

We investigated the long-time self-diffusion and sedimentation of NPs with anisotropic shapes. The anisotropic shapes we studied were an octahedron, a cube, a tetrahedron, and a spherocylinder. The NPs were represented with a discrete particle model and were hydrodynamically coupled to each other using the multiparticle collision dynamics method. Simulations were conducted across a range of volume fractions for each shape where the NPs remained in a fluid/isotropic phase. Our modeling approach can be easily extended to explore the dynamics of other NP shapes, *e.g.*, irregular polyhedra and non-convex shapes.¹⁰²

For regular polyhedra having equal edge lengths, shape had a clear influence on their transport properties. Octahedra and cubes were slower diffusing than spheres with diameter equal to their edge length for all investigated volume fractions [Fig. 2(a)]. Tetrahedra diffused the fastest at small volume fractions but the slowest at larger volume fractions, which we partially attributed to the formation of pentagonal dipyrramids. The simulated self-diffusion coefficients of all investigated NP shapes at infinite dilution were in good agreement with a correlation based on sphericity and also with an approximation using the mean diameter of the spheres that inscribed and circumscribed the shapes. After accounting for differences due to shape at infinite dilution [Fig. 2(b)], the self-diffusion coefficient of the spheres showed the weakest volume-fraction dependence, that of the tetrahedra showed the strongest volume-fraction dependence, while the octahedra and cubes showed intermediate behavior. Similar trends were found for the dependence of the sedimentation coefficients on volume fraction [Fig. 7(a)].

For small-aspect-ratio spherocylinders ($\lambda = 1$ and 2), the diffusion coefficients at infinite dilution showed a dependence on aspect ratio that was consistent with theoretical expectation, meaning that the spherocylinders diffused more slowly as aspect ratio increased [Fig. 6(a)]. However, after accounting for shape effects at infinite dilution, the self-diffusion coefficient [Fig. 6(b)] had a volume-fraction dependence that closely followed that of spheres having diameter equal to the spherocylinders, with only minor differences for the spherocylinder with $\lambda = 2$. The sedimentation coefficient [Fig. 7(b)] had essentially the same volume-fraction dependence for the spheres and both spherocylinders. We expect that the dynamics of spherocylinders should deviate more significantly from spheres as λ increases, and in principle, we can extend our spherocylinder model to study this regime. However, doing so incurs higher computational cost due to a substantial increase in the number of vertex particles per spherocylinder. Further, we would need larger simulation boxes to accommodate these spherocylinders and gather good statistics, thereby also



increasing the number of solvent particles required. To mitigate these computational challenges, an alternative approach is to represent the spherocylinders as linear rods comprised of partially overlapping particles.¹⁰³ However, establishing a connection between this model, our spherocylinder model, and experiments is still an open question, which we plan to explore.

Author contributions

Yashraj M. Wani: conceptualization, formal analysis, investigation, methodology, visualization, writing – original draft. Penelope Grace Kovakas: conceptualization, formal analysis, investigation, methodology, writing – review & editing. Arash Nikoubashman: conceptualization, funding acquisition, methodology, project administration, writing – review & editing. Michael P. Howard: conceptualization, data curation, formal analysis, funding acquisition, investigation, methodology, project administration, visualization, writing – review & editing.

Data availability

The data that support the findings of this study are available from the authors upon reasonable request.

Conflicts of interest

The authors have no conflicts to disclose.

Acknowledgements

This material is based upon work supported by the National Science Foundation under Award No. 2223084 and by the Deutsche Forschungsgemeinschaft (DFG, German Research Foundation) through Project No. 233630050, 405552959, 470113688, and 509039598. This work was completed with resources provided by the Auburn University Easley Cluster, the supercomputer Mogon at Johannes Gutenberg University Mainz (www.hpc.uni-mainz.de), and the Texas Advanced Computing Center (TACC) at The University of Texas at Austin.

References

- R. P. Sear, *Phys. Rev. Lett.*, 2019, **122**, 128101.
- M. A. Boles, M. Engel and D. V. Talapin, *Chem. Rev.*, 2016, **116**, 11220–11289.
- C. Ding and Z. Li, *Mater. Sci. Eng.: C*, 2017, **76**, 1440–1453.
- P. T. Wong and S. K. Choi, *Chem. Rev.*, 2015, **115**, 3388–3432.
- R. Toy, P. M. Peiris, K. B. Ghaghada and E. Karathanasis, *Nanomedicine*, 2014, **9**, 121–134.
- Dynamic Properties of Nanoparticles*, ed. Z. L. Wang, Y. Liu and Z. Zhang, Springer, US, 2003, pp. 562–594.
- L. Yang, Z. Zhou, J. Song and X. Chen, *Chem. Soc. Rev.*, 2019, **48**, 5140–5176.
- R. G. D. Andrade, S. R. S. Veloso and E. M. S. Castanheira, *Int. J. Mol. Sci.*, 2020, **21**, 2455.
- K. A. Rose, N. Gogotsi, J. H. Galarraga, J. A. Burdick, C. B. Murray, D. Lee and R. J. Composto, *Macromolecules*, 2022, **55**, 8514–8523.
- Y. Sun and Y. Xia, *Science*, 2002, **298**, 2176–2179.
- L. Gou and C. J. Murphy, *Nano Lett.*, 2002, **3**, 231–234.
- E. C. Greyson, J. E. Barton and T. W. Odom, *Small*, 2006, **2**, 368–371.
- F. C. Bawden, N. W. Pirie, J. D. Bernal and I. Fankuchen, *Nature*, 1936, **138**, 1051–1052.
- M. W. Beijerinck, *Verhandelingen der Koninklijke Akademie van Wetenschappen te Amsterdam, Afd. Natuurkd.*, 1898, **5**, 3–21.
- F. M. van der Kooij, K. Kassapidou and H. N. W. Lekkerkerker, *Nature*, 2000, **406**, 868–871.
- B. J. Berne and R. Pecora, *Dynamic Light Scattering With Applications to Chemistry, Biology and Physics*, Dover publications, 2000.
- W. Schärftl, *Sample Preparation*, Springer Berlin Heidelberg, 2007, pp. 43–50.
- P. A. Hassan, S. Rana and G. Verma, *Langmuir*, 2015, **31**, 3–12.
- J. Stetefeld, S. A. McKenna and T. R. Patel, *Biophys. Rev.*, 2016, **8**, 409–427.
- M. P. Lettinga, E. Barry and Z. Dogic, *Europhys. Lett.*, 2005, **71**, 692–698.
- B. Kundukad, J. Yan and P. S. Doyle, *Soft Matter*, 2014, **10**, 9721–9728.
- J. F. Brady, *J. Fluid Mech.*, 1994, **272**, 109–134.
- M. Tokuyama and I. Oppenheim, *Phys. Rev. E*, 1994, **50**, R16–R19.
- W. Kuhn, *Z. Phys. Chem.*, 1932, **161A**, 1–32.
- W. Kuhn, *Kolloid-Z.*, 1933, **62**, 269–285.
- W. Kuhn and H. Kuhn, *Helv. Chim. Acta*, 1945, **28**, 1533–1579.
- J. Riseman and J. G. Kirkwood, *J. Chem. Phys.*, 1950, **18**, 512–516.
- M. M. Tirado and J. G. de la Torre, *J. Chem. Phys.*, 1979, **71**, 2581–2587.
- M. M. Tirado and J. G. de la Torre, *J. Chem. Phys.*, 1980, **73**, 1986–1993.
- M. P. B. van Bruggen, H. N. W. Lekkerkerker, G. Maret and J. K. G. Dhont, *Phys. Rev. E*, 1998, **58**, 7668–7677.
- G. K. Youngren and A. Acrivos, *J. Fluid Mech.*, 1975, **69**, 377–403.
- K. Okada and A. Satoh, *Mol. Phys.*, 2020, **118**, e1631498.
- M. P. Howard, A. Nikoubashman and J. C. Palmer, *Curr. Opin. Chem. Eng.*, 2019, **23**, 34–43.
- M. P. Allen and D. J. Tildesley, *Computer Simulation of Liquids*, Oxford University Press, 2017.
- D. L. Ermak and J. A. McCammon, *J. Chem. Phys.*, 1978, **69**, 1352–1360.
- J. Rotne and S. Prager, *J. Chem. Phys.*, 1969, **50**, 4831–4837.
- H. Yamakawa, *J. Chem. Phys.*, 1970, **53**, 436–443.
- J. F. Brady, R. J. Phillips, J. C. Lester and G. Bossis, *J. Fluid Mech.*, 1988, **195**, 257–280.



- 39 J. F. Brady and G. Bossis, *Annu. Rev. Fluid Mech.*, 1988, **20**, 111–157.
- 40 A. Malevanets and R. Kapral, *J. Chem. Phys.*, 1999, **110**, 8605–8613.
- 41 G. Gompper, T. Ihle, D. M. Kroll and R. G. Winkler, in *Multi-Particle Collision Dynamics: A Particle-Based Mesoscale Simulation Approach to the Hydrodynamics of Complex Fluids*, Springer Berlin Heidelberg, 2009, pp. 1–87.
- 42 P. J. Hoogerbrugge and J. M. V. A. Koelman, *Europhys. Lett.*, 1992, **19**, 155–160.
- 43 M. B. Liu, G. R. Liu, L. W. Zhou and J. Z. Chang, *Arch. Comput. Methods Eng.*, 2015, **22**, 529–556.
- 44 B. Dünweg and A. J. C. Ladd, *Lattice Boltzmann Simulations of Soft Matter Systems*, Springer Berlin Heidelberg, 2009, pp. 89–166.
- 45 A. J. C. Ladd and R. Verberg, *J. Stat. Phys.*, 2001, **104**, 1191–1251.
- 46 Y. M. Wani, P. G. Kovakas, A. Nikoubashman and M. P. Howard, *J. Chem. Phys.*, 2022, **156**, 024901.
- 47 S. Poblete, A. Wysocki, G. Gompper and R. G. Winkler, *Phys. Rev. E*, 2014, **90**, 033314.
- 48 A. Malevanets and R. Kapral, *J. Chem. Phys.*, 2000, **112**, 7260–7269.
- 49 A. Nikoubashman, C. N. Likos and G. Kahl, *Soft Matter*, 2013, **9**, 2603–2613.
- 50 G. Batôt, V. Dahirel, G. Méridet, A. A. Louis and M. Jardat, *Phys. Rev. E*, 2013, **88**, 043304.
- 51 V. Dahirel, X. Zhao, B. Couet, G. Batôt and M. Jardat, *Phys. Rev. E*, 2018, **98**, 053301.
- 52 J. T. Padding and A. A. Louis, *Phys. Rev. E*, 2006, **74**, 031402.
- 53 Y. Kobayashi, N. Arai and A. Nikoubashman, *Langmuir*, 2020, **36**, 14214–14223.
- 54 Y. Kobayashi, N. Arai and A. Nikoubashman, *Soft Matter*, 2020, **16**, 476–486.
- 55 T. Yokoyama, Y. Kobayashi, N. Arai and A. Nikoubashman, *Soft Matter*, 2023, **19**, 6480–6489.
- 56 Y. Kobayashi and A. Nikoubashman, *Langmuir*, 2022, **38**, 10642–10648.
- 57 B. R. Argun and A. Statt, *Soft Matter*, 2023, **19**, 8081–8090.
- 58 T. Ikeda, Y. Kobayashi and M. Yamakawa, *Mol. Syst. Des. Eng.*, 2024, **9**, 254–263.
- 59 T. Ihle and D. M. Kroll, *Phys. Rev. E*, 2001, **63**, 020201.
- 60 T. Ihle and D. M. Kroll, *Phys. Rev. E*, 2003, **67**, 066705.
- 61 C. Huang, A. Chatterji, G. Sutmann, G. Gompper and R. Winkler, *J. Comput. Phys.*, 2010, **229**, 168–177.
- 62 A. Statt, M. P. Howard and A. Z. Panagiotopoulos, *Phys. Rev. Fluids*, 2019, **4**, 043905.
- 63 J. D. Weeks, D. Chandler and H. C. Andersen, *J. Chem. Phys.*, 1971, **54**, 5237–5247.
- 64 W. Humphrey, A. Dalke and K. Schulten, *J. Mol. Graphics*, 1996, **14**, 33–38.
- 65 J. Newman, H. L. Swinney and L. A. Day, *J. Mol. Biol.*, 1977, **116**, 593–603.
- 66 M. P. Lettinga, J. K. G. Dhont, Z. Zhang, S. Messlinger and G. Gompper, *Soft Matter*, 2010, **6**, 4556–4562.
- 67 L. Scarabelli, M. Grzelczak and L. M. Liz-Marzán, *Chem. Mater.*, 2013, **25**, 4232–4238.
- 68 X. Ye, L. Jin, H. Caglayan, J. Chen, G. Xing, C. Zheng, V. Doan-Nguyen, Y. Kang, N. Engheta and C. R. Kagan, *et al.*, *ACS Nano*, 2012, **6**, 2804–2817.
- 69 S. Seibt, J. Pearson, R. Nixon-Luke, H. Zhang, P. R. Lang, G. Bryant, H. Cölfen and P. Mulvaney, *J. Phys. Chem. C*, 2023, **127**, 22336–22346.
- 70 J. A. Anderson, J. Glaser and S. C. Glotzer, *Comput. Mater. Sci.*, 2020, **173**, 109363.
- 71 M. P. Howard, A. Z. Panagiotopoulos and A. Nikoubashman, *Comput. Phys. Commun.*, 2018, **230**, 10–20.
- 72 <https://github.com/mphowardlab/azplugins>.
- 73 J. Happel and H. Brenner, in *The Motion of a Rigid Particle of Arbitrary Shape in an Unbounded Fluid*, Springer, Netherlands, 1983, pp. 159–234.
- 74 M. Doi and S. F. Edwards, *The Theory of Polymer Dynamics*, Oxford University Press, 1988.
- 75 B. Dünweg and K. Kremer, *Phys. Rev. Lett.*, 1991, **66**, 2996–2999.
- 76 B. Dünweg and K. Kremer, *J. Chem. Phys.*, 1993, **99**, 6983–6997.
- 77 I.-C. Yeh and G. Hummer, *J. Phys. Chem. B*, 2004, **108**, 15873–15879.
- 78 A. Einstein, *Ann. Phys.*, 1906, **324**, 289.
- 79 A. Einstein, *Ann. Phys.*, 1911, **339**, 591.
- 80 D. S. Bolintineanu, G. S. Grest, J. B. Lechman, F. Pierce, S. J. Plimpton and P. R. Schunk, *Comput. Part. Mech.*, 2014, **1**, 321–356.
- 81 E. A. Pettyjohn and E. B. Christiansen, *Chem. Eng. Prog.*, 1948, **44**, 157–172.
- 82 M. Hoffmann, C. S. Wagner, L. Harnau and A. Wittemann, *ACS Nano*, 2009, **3**, 3326–3334.
- 83 R. Stuckert, C. S. Plüsch and A. Wittemann, *Langmuir*, 2018, **34**, 13339–13351.
- 84 A. Haji-Akbari, M. Engel, A. S. Keys, X. Zheng, R. G. Petschek, P. Palfy-Muhoray and S. C. Glotzer, *Nature*, 2009, **462**, 773–777.
- 85 A. Haji-Akbari, M. Engel and S. C. Glotzer, *J. Chem. Phys.*, 2011, **135**, 194101.
- 86 U. Agarwal and F. A. Escobedo, *Nat. Mater.*, 2011, **10**, 230–235.
- 87 A. P. Gantapara, J. de Graaf, R. van Roij and M. Dijkstra, *Phys. Rev. Lett.*, 2013, **111**, 015501.
- 88 W. van Meegen and S. M. Underwood, *J. Chem. Phys.*, 1989, **91**, 552–559.
- 89 A. van Blaaderen, J. Peetermans, G. Maret and J. K. G. Dhont, *J. Chem. Phys.*, 1992, **96**, 4591–4603.
- 90 J. R. Royer, G. L. Burton, D. L. Blair and S. D. Hudson, *Soft Matter*, 2015, **11**, 5656–5665.
- 91 J. W. Swan and G. Wang, *Phys. Fluids*, 2016, **28**, 011902.
- 92 P. Bolhuis and D. Frenkel, *J. Chem. Phys.*, 1997, **106**, 666–687.
- 93 A. Milchev, S. A. Egorov, K. Binder and A. Nikoubashman, *J. Chem. Phys.*, 2018, **149**, 174909.
- 94 M. Yetkin, Y. M. Wani, K. Kritika, M. P. Howard, M. Kappl, H.-J. Butt and A. Nikoubashman, *Langmuir*, 2024, **40**, 1096–1108.



- 95 M. P. B. van Bruggen, H. N. W. Lekkerkerker and J. K. G. Dhont, *Phys. Rev. E*, 1997, **56**, 4394–4403.
- 96 M. M. Tirado, C. L. Martínez and J. G. de la Torre, *J. Chem. Phys.*, 1984, **81**, 2047–2052.
- 97 H. Löwen, *Phys. Rev. E*, 1994, **50**, 1232–1242.
- 98 G. Mo and A. S. Sangani, *Phys. Fluids*, 1994, **6**, 1637–1652.
- 99 M. E. Irrgang, M. Engel, A. J. Schultz, D. A. Kofke and S. C. Glotzer, *Langmuir*, 2017, **33**, 11788–11796.
- 100 P. Monson and M. Rigby, *Chem. Phys. Lett.*, 1978, **58**, 122–126.
- 101 B. Barboy and W. M. Gelbart, *J. Chem. Phys.*, 1979, **71**, 3053–3062.
- 102 C. Avendaño and F. A. Escobedo, *Curr. Opin. Colloid Interface Sci.*, 2017, **30**, 62–69.
- 103 R. G. Winkler, K. Mussawisade, M. Ripoll and G. Gompper, *J. Phys.: Condens. Matter*, 2004, **16**, S3941.



Title: “Structure formation in supraparticles composed of spherical and elongated particles.”

Contributions:

- **Simulations and experiments:** I was responsible for the conducting the droplet drying simulations in this study and contributed to the bulk simulations of rod-like particles. Additionally, I participated in the synthesis of ellipsoidal particles from polystyrene spheres.
- **Data analysis:** I performed the formal analysis of the drying simulations and computing the orientational ordering of the ellipsoids from the SEM images.
- **Figure preparation:** I generated figures in the paper that show simulation results, while ensuring that they clearly illustrate the observations.
- **Manuscript contribution:** I contributed equally in the writing of the original draft of the paper and its revisions based on the feedback from co-authors and reviewers.

Reprint permissions:

Reprinted (adapted) with permission from “Yetkin, M., Wani, Y.M., Kritika, K., Howard, M.P., Kappl, M., Butt, H.J. and Nikoubashman, A.; Structure Formation in Supraparticles Composed of Spherical and Elongated Particles. *Langmuir*, 2024, 40(1), pp.1096-1108.”
Copyright 2024 American Chemical Society.

Structure Formation in Supraparticles Composed of Spherical and Elongated Particles

Melis Yetkin,⁺ Yashraj M. Wani,⁺ Kritika Kritika, Michael P. Howard, Michael Kappi,^{*} Hans-Jürgen Butt, and Arash Nikoubashman^{*}



Cite This: *Langmuir* 2024, 40, 1096–1108



Read Online

ACCESS |



Metrics & More

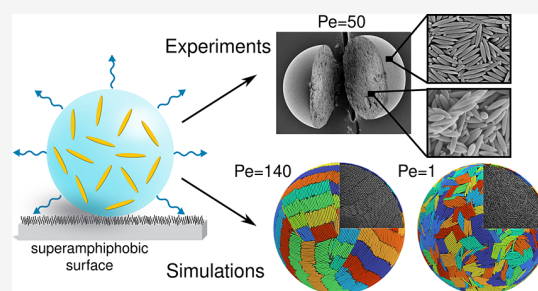


Article Recommendations



Supporting Information

ABSTRACT: We studied the evaporation-induced formation of supraparticles from dispersions of elongated colloidal particles using experiments and computer simulations. Aqueous droplets containing a dispersion of ellipsoidal and spherical polystyrene particles were dried on superamphiphobic surfaces at different humidity values that led to varying evaporation rates. Supraparticles made from only ellipsoidal particles showed short-range lateral ordering at the supraparticle surface and random orientations in the interior regardless of the evaporation rate. Particle-based simulations corroborated the experimental observations in the evaporation-limited regime and showed an increase in the local nematic ordering as the diffusion-limited regime was reached. A thin shell of ellipsoids was observed at the surface when supraparticles were made from binary mixtures of ellipsoids and spheres. Image analysis revealed that the supraparticle porosity increased with an increasing aspect ratio of the ellipsoids.



INTRODUCTION

Colloidal particles can assemble into supraparticles of various sizes, architectures, and compositions.^{1,2} The material properties of supraparticles can be engineered through the choice of the colloidal “building blocks” as well as their composition and arrangement within the supraparticle. Multiple types of materials, ranging from nanometer-sized quantum dots³ or metal organic frameworks⁴ to micrometer-sized polystyrene (PS) particles,⁵ with different shapes and chemistries can be used as building blocks to create supraparticles. The supraparticles may have emergent properties that surpass the mere sum of their parts, arising from the interactions between different types of building blocks.^{1,2} Therefore, supraparticles are versatile materials with potential applications in many fields of science and technology, including catalysis,^{1,6–8} gas adsorption and sensing,^{4,9} drug encapsulation and delivery,^{10,11} photonics,^{12–14} and energy production and storage.^{15,16}

Wet self-assembly methods have been commonly used to fabricate supraparticles by forming them inside or around droplet templates, such as emulsion droplets suspended in liquid media.^{12,17–20} However, these methods have certain drawbacks, including the need for additional processing liquids that require proper disposal as well as only limited control over the final supraparticle morphology. Dry self-assembly methods offer an alternative approach where supraparticles are obtained by evaporating droplets into air.^{1,5,21} These techniques do not need additional processing liquids and simplify the collection of the assembled supraparticles.²¹ Commonly used dry self-assembly methods include Leidenfrost levitation^{22,23} and

spray-drying,^{24–29} in which droplets dry in a contact free environment. These methods are typically performed at high temperatures, where evaporation takes only a few seconds. Therefore, studying structure formation with these techniques in real time is difficult and requires complex instruments, such as rotating anode-based X-ray sources or small-angle X-ray scattering.^{30,31} Further, the fast evaporation conditions make it quite difficult to control the final supraparticle shape and the distribution of the colloidal particles inside the supraparticle.³² For levitated droplets, additional parameters such as the thermal conductivity of the substrate can introduce challenges in controlling the resulting supraparticle shapes.^{30,32}

Alternatively, supraparticles can be fabricated by evaporating droplets supported on solid substrates. The wetting property of the substrate is important, as it directly determines the deposition characteristics in the contact region. Superamphiphobic surfaces repel water and also nonpolar liquids, surfactants, and protein solutions. Droplets on such surfaces acquire high contact angles ($> 150^\circ$) and roll off easily (tilting angle $< 10^\circ$), while the interfacial area between the liquid and solid is extremely small ($\ll V^{2/3}$, where V is the droplet volume).^{33–36} Further, superamphiphobic surfaces typically

Received: November 7, 2023
Revised: December 7, 2023
Accepted: December 8, 2023
Published: December 28, 2023



have a highly porous structure, which allows the liquid to evaporate through the substrate, leading to almost radially symmetric evaporation. As a result, the method suppresses contact line pinning and hence the coffee-ring effect,^{37–39} as well as temperature-induced Marangoni flow inside the droplet.⁴⁰ In contrast to Leidenfrost levitation and spray-drying, evaporation from superamphiphobic surfaces occurs at much longer time scales, which also makes studying the structure formation of supraparticles more convenient.⁴¹

Conventionally, spherical particles have been used to fabricate supraparticles of various structures and compositions by tuning the particle concentrations and processing parameters such as the evaporation rate.^{1,5,11,41–43} Examples include supraparticles having a core–shell morphology of larger (core) and smaller (shell) PS spheres,⁵ poly(lactic-co-glycolic acid)/ciprofloxacin supraparticles prepared in solvents of various polarity,¹¹ multicomponent spherical mesoporous supraparticles of metal oxides such as TiO₂/SnO₂ and TiO₂/ZnO,⁴² and supraparticles with nonspherical shape induced by the addition of salt.⁴¹ The shape of the colloidal particles themselves is a powerful but still largely unexplored handle for controlling supraparticle structure.^{44–46} Experiments⁴⁷ and simulations⁴⁸ of bulk systems have shown that rod-like particles tend to pack into more open random structures compared to their spherical counterparts. Simulations of sphere–rod mixtures in the bulk also revealed demixing transitions under the right conditions⁴⁹ and decreasing packing with increasing rod aspect ratios.⁵⁰ Recently, Jacucci et al. fabricated spherical supraparticles from silica nanorods via emulsion evaporation and obtained a core–shell morphology, with a disordered core and an ordered shell.⁵¹ The surface ordering of the nanorods was tuned from smectic to isotropic by adding salt into the dispersion, which resulted in a decrease of reflectance. It was noted that the light scattering efficiency could be further improved upon increasing the range of nanorod ordering.⁵¹ Van der Hoeven et al. assembled silica-coated gold nanorod supraparticles to enhance the Raman scattering of analyte molecules. Gold nanorods exhibited superior and highly tunable plasmonic properties compared to spheres due to their longitudinal surface plasmon resonance in the visible and near-infrared spectrum.⁵² Wang et al. showed that drying droplets containing lanthanide fluoride nanoplatelets could be utilized to fabricate supraparticles with tailored optoelectronic properties.⁵³

Although these prior works have hinted at the possibilities of using anisotropic building blocks for creating supraparticles, systematic studies investigating the influence of the aspect ratio of the colloidal particles, mixing colloidal particles with different aspect ratios, and evaporation rate on structure formation are still lacking. To better understand these aspects and to develop design strategies, we performed experiments and simulations on the formation of supraparticles composed of ellipsoidal particles and mixtures of spherical and ellipsoidal particles. In the experiments, we used PS colloidal particles to differentiate the effect of particle geometry from the effect of the materials properties. As the density of an aqueous PS dispersion is close to that of water, and ellipsoidal particles, having similar interaction potentials and surface chemistry, can be prepared from PS, we were able to focus on the physics of supraparticle formation. We found that (i) the ordering of the ellipsoids could be tuned by changing the evaporation rate, (ii) ellipsoids tended to form a thin shell with short-range orientational order on the surface, and (iii) supraparticle

porosity tended to increase with an increasing ellipsoid aspect ratio due to random packing in the interior.

■ EXPERIMENTAL METHODS

Materials. Methyl trichlorosilane (TCMS, 99%) and hexadecane (Reagent Plus, 99%) were purchased from Sigma-Aldrich. 1H,1H,2H,2H-Perfluorodecyltrichlorosilane (PFDTs, 96%) was purchased from Alfa Aesar. n-Hexane ($\geq 95\%$), toluene ($\geq 99.8\%$), acetone ($\geq 99.8\%$), and isopropyl alcohol (IPA, $\geq 99.8\%$) were purchased from Fisher Chemical. Ethanol ($\geq 99.8\%$) was provided by Honeywell Research Chemicals. Ultrapure water with a resistivity of 18.2 M Ω -cm was obtained using a Sartorius Arium 611 VF water purification system. Glass slides 25 \times 75 mm² in size were provided by Menzel-Gläser, Germany. PS particles (zeta potential ≈ -56 mV, with –COOH groups on the surface) with a diameter of 408 nm (polydispersity index 0.034) were synthesized by the copolymerization of styrene and acrylic acid using surfactant-free emulsion polymerization.⁵⁴ The synthesized particles were purified by several centrifugation cycles and finally redispersed in ultrapure water. Poly(vinyl alcohol) (PVA, $M_w = 115000$ g/mol, degree of hydrolysis 86.5–89%) was purchased from VWR Chemicals. Anionic surfactant sodium dodecyl sulfate (SDS) was purchased from MP Biomedicals.

Preparation of superamphiphobic surfaces. The silicone nanofilaments-based superamphiphobic surfaces were prepared as described before.^{35,55} Glass slides were sonicated in toluene, acetone, and ethanol and dried by a nitrogen flow. Then, glass slides were oxygen plasma treated at 30 W for 2 min (Diener Electronic Femto). The activated glass slides were immersed in 360 mL of toluene with 166 ppm water content in a Teflon box. The water content of toluene was measured with a Karl Fischer coulometer (Mettler Toledo C20 Compact KF coulometer). 250 μ L of TCMS was injected into the Teflon box to initiate the growth of silicone nanofilaments from the glass slides. The chamber was kept sealed for 14 h. After the reaction, the silicone nanofilament-grafted glass slides were rinsed with hexane to remove any unreacted TCMS. To fluorinate the nanofilaments, the grafted glass slides were annealed in a furnace at 200 $^{\circ}$ C for 2 h to obtain a more stable silicone network. Then, the glass slides were again activated with oxygen plasma at 120 W for 2 min and immersed in 120 mL of hexane with 0.1 mL of PFDTs. After 30 min of reaction, the substrates were rinsed with hexane to remove any unreacted fluorosilanes. The resultant nanofilament-coated glass substrates were homogeneous over a large area [Figure S1].

Preparation of polystyrene ellipsoids. PS ellipsoids were prepared from monodisperse spherical PS particles following the film-stretching method.⁵⁶ The preparation procedure is depicted schematically in Figure S2. Five grams of PVA were dissolved in 139 mL distilled water to obtain a 3.5 wt % aqueous PVA solution. The system was stirred at 375 rpm overnight by keeping the temperature at 80 $^{\circ}$ C. After obtaining a clear PVA solution, about 4 g of 10 wt % PS particle dispersion was added and stirred at 375 rpm for 5 h to obtain a homogeneous PVA/particle dispersion. The weight ratio of PS to PVA in the final mixture was 0.08. The PVA/particle dispersion was then poured into a flat Teflon mold (15 \times 28 cm²) and was air-dried for 1 day. After evaporation, a particle-embedded PVA film was formed. This film was cut into small film strips (3 \times 8 cm² or 3 \times 4 cm², depending on the desired draw ratio). These film strips were stretched in an oven at 140 $^{\circ}$ C. The stretching was done by applying uniaxial tension with a tensile test apparatus (Zwick/Roell Z005 Universal Testing Machine) to the desired length at a speed of 300 mm/min. The films were stretched at draw ratios of 100, 200 and 400% to obtain ellipsoids with varying aspect ratios of about 4, 6, and 11, respectively. The particle size and aspect ratio were calculated by counting 40 particles in a scanning electron microscopy (SEM) image of each batch [Table 1]. Several washing steps were required to recover the ellipsoidal particles from the film. After stretching, the PVA/particle film strips were cooled to room temperature while still being clamped in their stretched state and then cut into small pieces (1 \times 1 cm²). The original edges of the stretched films were rejected as there could be nonuniform stretching near the metal clamps. The

Table 1. Dimensions of the ellipsoids obtained by stretching a film embedded with 408 nm PS spheres at different draw ratios^a

Draw ratio (%)	L (μm)	d_e (μm)	$\lambda = L/d_e$
100	0.92 ± 0.05	0.26 ± 0.01	3.5 ± 0.3
200	1.30 ± 0.11	0.21 ± 0.02	6.1 ± 0.8
400	1.95 ± 0.21	0.18 ± 0.02	11 ± 2

^aThe dimensions (length L and diameter d_e) were determined by analyzing 40 particles each.

small film pieces were soaked in an IPA-water mixture (3:7) (v:v) overnight under magnetic stirring. Then, this mixture was heated to 85 °C for 1 h to dissolve the PVA matrix completely. The dispersion was centrifuged at 10000 rpm for 1 h to sediment the particles, and the viscous PVA-rich supernatant was decanted. The sediment was dissolved again in an IPA–water mixture (3:7) (v:v) and was centrifuged at 10000 rpm for 1 h. This washing procedure was repeated two times. In the final washing step, the particles were dispersed in water at 90 °C under magnetic stirring for 1 h to remove the traces of PVA. Then, the dispersion was centrifuged one last time to recover the PS ellipsoids. The resultant particles were redispersed in an appropriate amount of distilled water, depending on the required particle concentration.

Evaporation of PS dispersion droplets on superamphiphobic surfaces. The aqueous PS dispersions were prepared prior to the evaporation experiments. The volume concentration of PS ellipsoids or spheres in the dispersions was kept around 1%, whereas the total volume concentration of sphere–ellipsoid mixture dispersions was around 0.6% with a volume ratio of ellipsoids to spheres 1:1 (v:v). Each system contained a 1 mM aqueous SDS solution to stabilize the dispersions. Approximately 1 μL of these dispersions were dispensed onto the superamphiphobic surfaces with the help of an Eppendorf Research Plus pipet, which was equipped with epT.I.P.S. LoRetention Reloads tips. To conduct the evaporation experiments in a controlled manner, a humidity chamber was built in-house. The humidity chamber was equipped with an inlet, which allowed nitrogen gas to flow, and a window through which the evaporation process was monitored by a camera (Blackfly S Color 5.0 MP USB3 Camera). The humidity during evaporation of the dispersion drops was recorded with the help of a humidity sensor inside the chamber. Once the desired humidity was reached, the droplets were dispensed through the holes on top of the chamber and the holes remained closed throughout the evaporation. The dispersion droplets evaporated at 23 °C, either under ambient conditions (relative humidity of 30%) or at a relative humidity of 75%. The supraparticles formed after evaporation were released by slightly inclining the surfaces and were collected in small vials.

Characterization. The morphology of the superamphiphobic surfaces and the supraparticles were imaged by SEM (low voltage LEO 1530 Gemini, Germany). Prior to imaging, the samples were sputter coated with a 7 nm layer of Pt using a Safematic Compact Coating Unit-010 to avoid charging. The water concentration in toluene was evaluated by using a Karl Fischer coulometer (Mettler Toledo C20 Compact KF coulometer). To determine the size and polydispersity of the PS particles, dynamic light scattering (DLS) measurements were carried out on an ALV spectrometer consisting of a goniometer and an ALV-5004 multiple-tau full-digital correlator (320 channels, angular range from 30° to 150°). A He–Ne laser (wavelength of 632.8 nm) was used as the light source. Measurements were performed at 20 °C at 9 angles ranging from 30° to 150°. The zeta potential of the PS particles was measured by a Malvern Zetasizer Nano Z. Using ImageJ software, we performed image analysis with the evaporation videos of the droplets and recorded the change in droplet volume as a function of time. The volume of the droplets was estimated first by determining an arc through the circumference of the 2D image of one half of the droplet, and then by integrating dis-shaped slices (which are passing through this arc and cutting the

central axis of the droplet perpendicularly) around the central axis [Figure S3]. The method assumed no predefined droplet shape.

NUMERICAL METHODS

Explicit-solvent simulations of drying colloidal systems are computationally taxing since they require large numbers of particles and small time steps to capture the fast motion of the solvent particles. As a consequence, such explicit-solvent simulations are typically limited to systems containing a few thousand colloidal particles,^{57–59} which is usually too small to fully capture structural variations that occur during drying. However, it is often not needed to resolve individual solvent particles but rather only the solvent's effect on the solute. Therefore, implicit-solvent simulation methods have been used to model drying colloidal systems and have shown good agreement with experiments in some cases.^{60,61} However, at times there are certain qualitative and quantitative discrepancies, which are thought to originate from the lack of solvent effects that exist in real systems such as solvent backflow and hydrodynamic interactions (HI) between the particles.^{5,62–64} Therefore, in this study, we performed simulations with two methods – (a) Langevin dynamics without HI [-HI] and (b) multiparticle collision dynamics with HI [+HI].

Langevin dynamics (LD) is a widely used implicit solvent technique that incorporates the Stokes friction and Brownian motion of particles in the equations of motion,

$$m\ddot{\mathbf{x}}_i = \mathbf{F}_C - \gamma\dot{\mathbf{x}}_i + \mathbf{F}_R \quad (1)$$

where \mathbf{F}_C is the force on particle i due to all the conservative interactions in our system, γ is the friction coefficient and \mathbf{F}_R is a uniform random force acting on the particle. The magnitude of the random force is chosen in accordance with the fluctuation–dissipation theorem $\langle \mathbf{F}_R \rangle = 0$ and $\langle |\mathbf{F}_R|^2 \rangle = 6k_B T \gamma / \delta t$. The friction coefficients γ for the different colloidal particles are taken as input parameters that we determined via bulk +HI simulations of very dilute ($\phi = 0.0001$) dispersions of the elongated and spherical particles.

Multiparticle collision dynamics (MPCD) uses a simplified particle-based solvent model, which undergoes successive free-streaming and stochastic collision steps.^{65–67} The solvent is modeled as a set of point particles of number density ρ , having positions \mathbf{r}_i^s , velocities \mathbf{v}_i^s , and mass m_0 . In the free streaming step, solvent particles move ballistically,

$$\mathbf{r}_i^s(t + \Delta t) = \mathbf{r}_i^s(t) + \mathbf{v}_i^s(t)\Delta t \quad (2)$$

where Δt , is the collision time step, which effectively sets the mean free path of the particles.

The variants of MPCD algorithms differ in their implementation of the collision step. In our study, we use the widely implemented stochastic rotation dynamics algorithm, introduced by Malevanets and Kapral.⁶⁵ Particles are first binned into cubic collision cells of length l , where they undergo stochastic rotations of their velocities as,

$$\mathbf{v}_i^s(t + \Delta t) = \mathbf{u}_c^s(t) + \mathbf{Q}_c \cdot [\mathbf{v}_i^s(t) - \mathbf{u}_c^s(t)] \quad (3)$$

where $\mathbf{u}_c^s(t)$ is the average velocity of the particles in a collision cell and \mathbf{Q}_c is the rotation operator of the cell in which particle i resides at time t . The rotation operator is chosen to have a fixed angle of rotation of 130° around a random axis in each cell. To ensure Galilean invariance, the collision cells are shifted along each direction by a distance uniformly drawn from $[-l/2, l/2]$.⁶⁶ A Maxwell–Boltzmann thermostat is applied on the cell level to maintain isothermal conditions. These stochastic collisions build up HI between the particles. Solute particles are coupled to the solvent through momentum exchange in the collision step, as described further below.

In our MPCD droplet simulations, the solvent can flow through the droplet interface, which likely overpredicts solute entrapment, but still is a significant improvement over complete neglect of hydrodynamic interactions.⁶⁸ To minimize unphysical hydrodynamic interactions due to periodic boundary conditions, the simulation box is padded along all directions by the droplet's initial radius.

Spherical colloidal particles were modeled as nearly hard spheres with diameter $d_s = 3l$ via the purely repulsive Weeks–Chandler–Andersen (WCA) potential,

$$U_{\text{WCA}}(r) = \begin{cases} 4\epsilon \left[\left(\frac{\sigma}{r - \Delta} \right)^{12} - \left(\frac{\sigma}{r - \Delta} \right)^6 \right], & r < r_{\text{cut}} + \Delta \\ 0, & r \geq r_{\text{cut}} + \Delta \end{cases} \quad (4)$$

where r is the distance between two interacting particles, and we used $\sigma = l$, $\Delta = 2l$, and $r_{\text{cut}} = 2^{1/6}\sigma$. Coupling of the spherical particles with the MPCD solvent requires careful treatment. In this study we used a discrete mesh model to couple the spheres to the solvent.^{69,70} In this model, each sphere is represented as a mesh of $N_v = 12$ vertex point particles placed on the surface of the sphere with an additional particle placed in the center of the mesh to impart the nearly hard sphere excluded volume as given above [Figure 1(a)]. The mesh is created by

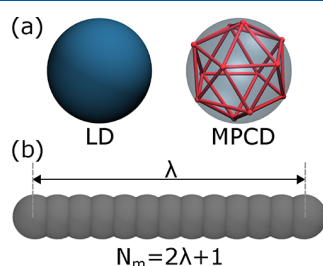


Figure 1. (a) Schematic of spherical particles in the LD and MPCD simulations, respectively. The diffuse sphere in the MPCD schematic imparts the excluded volume. (b) Schematic of rod-shaped particles in simulations.

using the vertices of an icosahedron that are scaled up such that they lie on the surface of the sphere. The vertex particles are bonded to their nearest neighbors and to the central particle via harmonic bonds which ensures that the mesh shape is conserved. The strength of the harmonic bonds was set to $k_{\text{ico}} = 5000\epsilon l^{-2}$.

Elongated colloidal particles could, in principle, be described as ellipsoids using anisotropic pair potentials such as the Gay–Berne model; however, it is challenging to couple such a model to the MPCD solvent given the rather large number of vertex particles needed for covering the ellipsoid surface. Instead, we approximate the ellipsoids of aspect ratio $\lambda = 4, 6,$ and 11 using a rod-like (“shish-kebab”) model [Figure 1(b)], with every colloidal particle consisting of $N_m = 2\lambda + 1$ monomers of diameter $d_e = l$ bonded via a harmonic potential,

$$U_{\text{bond}}(r) = \frac{1}{2}k_{\text{rod}}(r - r_0)^2 \quad (5)$$

with equilibrium length $r_0 = d_e/2$ and strength $k_{\text{rod}} = 1000 \epsilon d_e^{-2}$. This choice ensured that the excluded volume closely resembled that of a smooth rod. A bending potential between consecutive bond vectors was introduced to make the rods stiff,

$$U_{\text{bend}}(\theta) = \frac{1}{2}k_{\text{bend}}(\theta - \theta_0)^2 \quad (6)$$

with an equilibrium angle, $\theta_0 = \pi$ and strength $k_{\text{bend}} = 1000 \epsilon \text{rad}^{-2}$. Such a model for rods in conjunction with MPCD has been studied previously and shown to reproduce the expected diffusion behavior in the bulk.⁷¹ Excluded volume interactions between rods are realized through WCA interactions between the constituent monomers, as described above.

The air–droplet interface in the simulations was modeled using a harmonic potential, located at a distance of R from the center of droplet, acting radially inward on the central particles of the spheres and on all particles in the rods,

$$U_{\text{drop}}(r) = \begin{cases} 0, & r < R + \Delta_{\text{drop}} \\ \frac{k_{\text{drop}}}{2}(r - R - \Delta_{\text{drop}})^2, & r > R \end{cases} \quad (7)$$

Here, r is the distance of the particle from the center of the droplet, and $\Delta_{\text{drop}} = -d_s/2$ for the central particles of the spheres and $-d_e/2$ for the rod particles. The interaction strength is analogous to the surface tension of the droplet and was set to $k_{\text{drop}} = 200\epsilon/d_e^2$. Evaporation of the droplet was simulated by reducing the size of the droplet using the following relation,⁶⁴

$$R^2 = R_0^2 - \frac{\alpha}{4\pi}t \quad (8)$$

where α is the rate of change of surface area which is assumed to be a constant. From the above relation, we can deduce the speed of the receding interface by taking the time derivative,

$$v = -\frac{dR}{dt} = \frac{\alpha}{8\pi R} \quad (9)$$

Simulation details. MPCD simulations were performed with an initial droplet radius $R_0 = 50d_e$, whereas LD simulations were performed with droplets of size $R_0 = 50d_e$ & $100d_e$. The initial volume fraction of colloidal particles in the droplet was chosen as $\phi_0 = 0.08$ and the droplet was dried until it reached half of its original diameter, corresponding to a final volume fraction of $\phi_f = 0.64$.

The system of units for the MPCD solvent were the collision cell edge length l , mass m_0 of the solvent particles and the energy scale $\epsilon = k_B T$. The simulation time step was set to 0.001τ and the MPCD collision time step was set to $\Delta t = 0.1\tau$ where $\tau = \sqrt{m_0 l^2 / \epsilon}$. The solvent number density was set to $\rho = 5l^{-3}$. The mass of the rod monomers and sphere vertex particles in the MPCD simulations was set to $m = 5m_0$. The solute (rods/spheres) was coupled with the MPCD solvent through the collision step.

Simulations were performed using HOOMD-blue version 2.9.7^{72–75} with azplugins version 0.11.0.⁷⁶

Volume fraction profiles of the colloidal particles were computed by convolving the number density profile, ρ_i , of particle of type i with the Heaviside function, θ , that represents the volume of the sphere of radius r_i , i.e.,⁷⁷

$$\phi_i(\mathbf{r}) = \int d\mathbf{r}' \rho_i(|\mathbf{r}'|) \theta(\mathbf{r}_i - |\mathbf{r} - \mathbf{r}'|) \quad (10)$$

This integral can be simplified using the radial symmetry of the droplet as,

$$\phi_i(r) = \frac{1}{r} \int d\mathbf{r}' \rho(r') r' \pi [r_i^2 - (\mathbf{r} - \mathbf{r}')^2] \theta(r_i - |\mathbf{r} - \mathbf{r}'|) r_i, \quad r \geq r_i \quad (11)$$

Since our model for the rods consists of consecutive overlapping monomers, the overlap volume had to be accounted for while computing the volume fractions. For two overlapping spheres of radius R' , whose centers are separated by a distance R' , the overlap volume is $V' = 5\pi R'^3/12$. To approximately account for the overlap, we multiplied the Heaviside function by a constant $b = 1 - \frac{(5/16)(N_m - 1)}{N_m}$ where N_m is the number of monomers making up a rod and the prefactor $(5/16)$ is the ratio of the overlap volume to the volume of a monomer.

RESULTS AND DISCUSSION

1. Formation of supraparticles composed of ellipsoids. The evaporation-induced self-assembly of particles can be described as an advection–diffusion process in confinement. Inside the spherical droplet, the colloidal particles diffuse due to Brownian motion, while the evaporating air–solvent interface creates an effective advection⁷⁸ that can accumulate the colloidal particles and create a concentration gradient,

provided the drying is fast enough. The relative contributions of advection and diffusion can be characterized by a dimensionless quantity known as the Péclet number Pe , defined in this context as the ratio of the typical diffusion time, $\tau_d = R_0^2/D_0$, and the evaporation time, $\tau_{ev} = R_0/v_{ev}$, at the beginning of drying. Here, R_0 is the initial droplet radius, D_0 is the diffusion coefficient of the colloidal particles at infinite dilution, and v_{ev} is the initial speed of the receding droplet interface. The expression for the Péclet number then reduces to $Pe = \tau_d/\tau_{ev} = v_{ev}R_0/D_0$. We define $Pe \gg 1$ as the evaporation-limited regime and $Pe \leq 1$ as the diffusion-limited regime. In the following, Pe_e and Pe_s refer to the Péclet numbers for the elongated and spherical particles, respectively.

One μL droplets containing PS ellipsoids ($\sim 1\%$ initial volume fraction) with varying aspect ratios ($\lambda = 4, 6$, and 11 , corresponding to approximate lengths $0.92 \mu\text{m}$, $1.30 \mu\text{m}$, and $1.95 \mu\text{m}$) were evaporated from superamphiphobic surfaces at different humidity conditions that led to different evaporation rates. The PS particles have $-\text{COOH}$ groups on their surface, which lead to an electrostatic double-layer repulsion between them.^{41,79} To improve the stability of the dispersions at late stages of drying with elevated salt concentrations, 1 mM of the anionic surfactant SDS was added to each dispersion. Due to the repulsive nature of this interaction, the colloidal particles were modeled as nearly hard particles in the simulations (see the **Numerical Methods** section for details). At high relative humidity (RH = 75%, $40 \leq Pe_e \leq 70$), the complete drying of the droplets took about 90 min. Each dispersion droplet formed an almost spherical supraparticle at the end of drying [Figures 2(a), S4]. At low relative humidity (RH = 30%, $170 \leq$

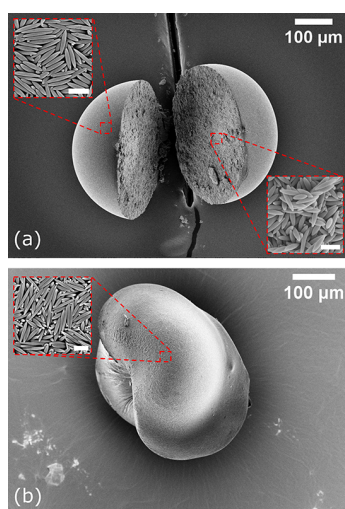


Figure 2. SEM images of supraparticles obtained from evaporation-limited drying with (a) $Pe_e = 50$ and (b) $Pe_e = 170$ for dispersion droplets containing ellipsoids with $\lambda = 6$. Insets show the surface and cross sections of the supraparticles at higher magnification. Scale bar in the insets corresponds to $1 \mu\text{m}$.

$Pe_e \leq 200$), the final supraparticles were not spherical anymore due to buckling near the end of evaporation, which typically occurred from the top [Figures 2(b), S5]. Buckling is a common phenomenon caused by mechanical instabilities.²³ The ordering of the ellipsoids on the buckled supraparticle surface resembled that of high humidity, although more ellipsoids were oriented out of plane on the supraparticle surfaces.

Examination of the supraparticle surfaces under SEM showed a short-range lateral ordering of ellipsoids upon drying at a high relative humidity [Figure 3(a-c)]. Most of the ellipsoids were oriented in plane on the supraparticle surface. The supraparticle surface with the most out of plane ellipsoids appeared to be the one with the highest aspect ratio of ellipsoids ($\lambda = 11$). To quantify ordering of the ellipsoids on the supraparticle surfaces, we computed an orientational order parameter, defined as

$$S^\dagger(\mathbf{r}_i, \mathbf{r}_j) = \langle 2\cos^2\theta_{ij} - 1 \rangle \quad (12)$$

Here, θ_{ij} is the angle between the long axes of two ellipsoids i and j , whose center of masses are separated by distance $r = |\mathbf{r}_j - \mathbf{r}_i|$ with \mathbf{r}_i being the position of ellipsoid i . By construction, a parallel alignment of particles would result in $S^\dagger = 1$, while isotropic configurations would yield $S^\dagger = 0$. The lateral and longitudinal ordering of the ellipsoids can be best understood when S^\dagger is plotted on a spatially resolved two-dimensional heatmap with the width and height of the cells set approximately equal to the single ellipsoid diameter (d_e) and length (L), respectively [Figure 3(d)], so that adjacent cells represent adjacent ellipsoids. From this plot, we find that, for $\lambda = 11$ ($Pe_e = 70$), the ellipsoids were ordered along the short axis direction up to about four ellipsoid diameters [Figure 3(d)]. For $\lambda = 6$ ($Pe_e = 50$), the ordering along the short axis reduced to three ellipsoid diameters, while no ordering was found for $\lambda = 4$ ($Pe_e = 40$) [Figure S6]. In all cases, the ellipsoids did not exhibit any ordering along their long axis direction. The experiments at low humidity were not used for analyzing the order parameter of the ellipsoids as many ellipsoids were aligned out of plane on the supraparticle surface.

To understand the extent to which the evaporation rate influenced the surface structure, we performed computer simulations in both the evaporation- and diffusion-limited drying regimes. We first performed simulations with and without hydrodynamic interactions, using droplets with an initial radius of $R_0 = 50d_e$, and found nearly identical structures from both approaches [Figure S7]. This agreement suggests that hydrodynamic interactions play only a negligible role in these systems. Therefore, we primarily performed simulations without hydrodynamic interactions, which allowed us to access larger droplets of radius $R_0 = 100d_e$. Subsequent discussion refers to these simulations.

The Péclet numbers in simulations and experiments are not exactly identical but are on the same order of magnitude, which makes the results comparable. In general, the experimental and simulation results are in good agreement [cf. Figures 3 and 4], with some minor differences: The surface SEM images for $\lambda = 11$ [Figure 3(c)] showed some ellipsoids oriented out-of-plane in the experiments, which were absent in the simulation snapshots. This difference might arise from the fact that the simulations treat the ellipsoids as (nearly) hard rods, which might affect their packing. Further, in the simulations, droplet confinement is modeled by a purely repulsive harmonic potential at the droplet–air interface [eq 7], which could suppress an out-of-plane alignment of the colloidal particles.

In the diffusion-limited regime ($Pe_e \leq 1$), the rods showed long-ranged ordering along their short and long axis directions [Figure 4(d-f)], suggesting that the range of surface ordering highly depends on the Péclet numbers. Figure 4(g) shows the

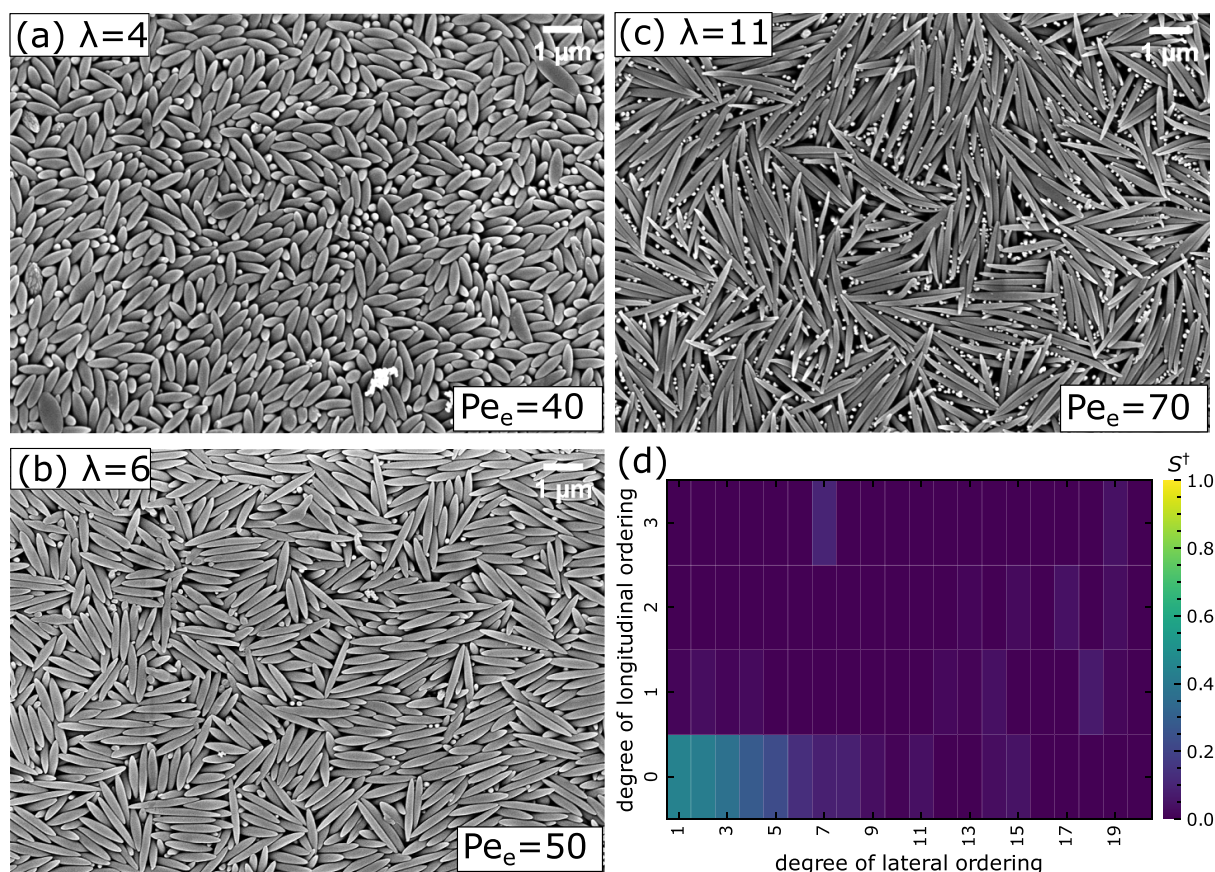


Figure 3. SEM images of supraparticle surface composed of ellipsoids with (a) $\lambda = 4$, (b) $\lambda = 6$ and (c) $\lambda = 11$. Péclet numbers for each case are shown on the bottom right of each panel. (d) 2D heat map for the order parameter S^\dagger , computed from the SEM image of the supraparticle surface shown in (c).

radially averaged S^\dagger for the $\lambda = 11$ rods on the supraparticle surface with varying Péclet numbers. The rods exhibited long-range ordering that decayed as the Péclet number increased. The largest Péclet number in our simulations was comparable to that of the experiment at high relative humidity [shown as a dashed line in Figure 4(g)], for which we obtained a similar trend of S^\dagger . We observed that the range of ordering reduced very quickly with decreasing aspect ratio λ [Figure S6]. For $\lambda = 4$ there was, on average, no lateral ordering of rods.

To characterize the ordering of the colloidal particles in the supraparticle interior, the supraparticles were cut in half with a scalpel and imaged using SEM. The images revealed randomly packed ellipsoids regardless of particle aspect ratio [see insets in Figure 2(a) and Figure S8]. Since, the packing efficiency of randomly oriented elongated particles is known to decrease with increasing aspect ratio,^{48,80–84} we expected an increase in porosity of our supraparticles as we increased λ .

The packing volume fraction ϕ of the colloidal particles was determined as a measure of porosity for the experimental supraparticles by computing the volume of the initial and final droplet via image analysis. This was achieved by first determining an arc through the circumference of the 2D image of one half of the droplet, then using the solid of revolution method to compute the volume [Figure S3]. Apart from rotational symmetry, this method does not assume a specific droplet shape and thus avoids systematic errors due to deviation from a perfect sphere. The final particle volume fraction was then calculated as $\phi_f = \phi_0 V_0 / V_f$ where, ϕ_0 is the

known initial particle volume fraction and V_0 and V_f are the initial and final droplet volumes, respectively. We computed ϕ_f for all three ellipsoid aspect ratios as well as for spherical particles that served as a reference point (Table 2). The final particle volume fraction tended to decrease with increasing ellipsoid aspect ratio λ , which is consistent with simulation studies of randomly packed rods in the bulk.^{48,80,84,85} The decrease in random packing efficiency of ellipsoids inside the supraparticles can be attributed to the increase of orientationally averaged excluded volume for particles with higher aspect ratios.^{47,48,86} Our results suggest that the supraparticle porosity might then be further increased (ϕ_f decreased) using ellipsoids with higher aspect ratios.

Likewise, the supraparticle cross sections from simulations in the evaporation-limited regime ($70 \leq Pe_e \leq 140$) showed that the rods were randomly packed in the interior [Figure 4(a–c)]. In contrast, the simulations in the diffusion-limited regime ($Pe_e \leq 1$) exhibited local nematic ordering [Figure 4(d–f)], which can be explained via entropic arguments: At sufficiently high concentrations, rods prefer to align nematic to increase the translational entropy at the expense of orientational entropy.⁸⁷ The isotropic–nematic transition shifts to lower concentrations with increasing aspect ratios.^{88,89} This transition requires the reorientation of individual rods and nematic bundles, which could be suppressed when the droplet is dried quickly ($Pe_e \gg 1$).

Since the simulation cross sections indicated the formation of orientationally ordered bundles of rods under certain

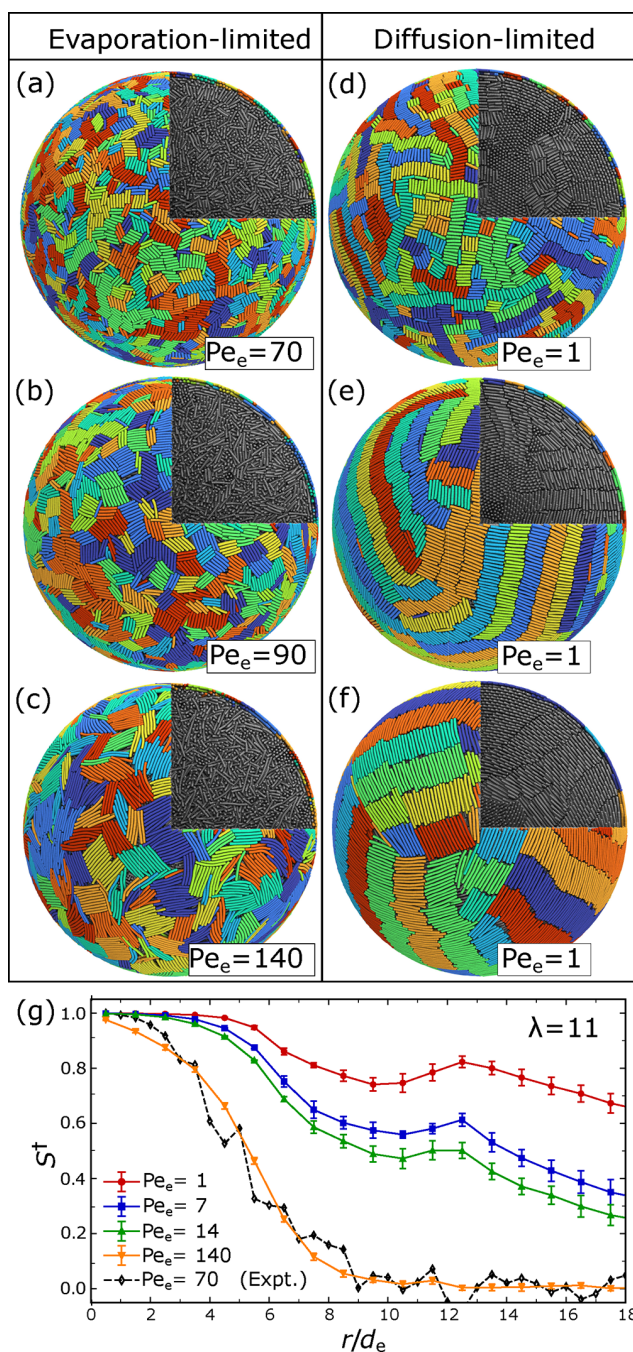


Figure 4. Simulation snapshots showing the supraparticle surface and cross sections (upper right corner of each snapshot) obtained in the (a–c) evaporation-limited ($Pe_e \gg 1$) and (d–f) diffusion-limited ($Pe_e \leq 1$) drying regimes for $\lambda = 4, 6,$ and 11 . Orientationally ordered clusters of rods on the surface are indicated via different colors for visual aid. (g) S^\dagger for $\lambda = 11$ as a function of the radial distance on the supraparticle surface for experiments and simulations.

conditions, we computed the global nematic order parameter in the droplets at various stages of the drying process. To establish a reference for the global nematic ordering of the rods, we performed additional bulk simulations at packing fractions ranging from 0.10 to 0.60 [Figure S9]. To ensure proper equilibration, two different approaches were taken when performing the bulk simulations. In the first, we started with a dilute system of randomly oriented rods and

Table 2. Final volume fractions of colloidal particles in supraparticles at high relative humidity ($10 \leq Pe_e \leq 70$). The last column shows the theoretically expected values for random packing in bulk dispersions

λ	ϕ_0	ϕ_f	Theoretically expected ϕ_f
1	0.011 ± 0.001	0.61 ± 0.06	$0.66^{48}, 0.68^{84,86}, 0.69^{85}$
4	0.011 ± 0.001	0.59 ± 0.03	$0.53^{48}, 0.55^{84}, 0.59^{80}, 0.61^{85}$
6	0.013 ± 0.002	0.57 ± 0.08	$0.51^{86}, 0.55^{85}$
11	0.081 ± 0.001	0.52 ± 0.04	$0.40^{86}, 0.43^{84}, 0.44^{80}, 0.48^{85}$

compressed the simulation box slowly to reach the desired packing fraction. In the second, we started with an ordered system at a high packing fraction and expanded the simulation box slowly. The final ordering in the bulk systems was virtually identical for both approaches, which confirms that the systems were properly equilibrated [Figure S10].

The bulk and confined systems were then analyzed for nematic order using the orientational bond order parameter,⁹⁰

$$Q_{ni}^{\alpha\beta} = \frac{1}{2}(3\mathbf{u}_{ni}^\alpha \mathbf{u}_{ni}^\beta - \delta_{\alpha\beta}) \quad (14)$$

Here, \mathbf{u}_{ni}^α is the unit bond vector connecting monomer i and $i + 1$ in the n^{th} rod, and $\alpha, \beta \in (x, y, z)$ denote the Cartesian coordinates. The largest eigenvalue S of this tensor, averaged over all bonds, gives information on the global nematic order in the system.

We compared the global nematic order in the bulk and drying simulations at low Péclet numbers ($Pe_e \sim 1$) [Figure 5(a)]. In the bulk systems, we observed an isotropic–nematic transition for all aspect ratios λ , where the volume fraction ϕ_{IN} of the transition decreased with increasing λ , as expected. The approximate volume fractions at which the isotropic–nematic transition occurred were $\phi_{\text{IN}} = 0.475, 0.375,$ and 0.225 for rods of aspect ratios 4, 6, and 11, respectively. In the case of drying droplets, the long-range nematic ordering of the rods was suppressed due to the confinement, in agreement with previous studies of nematic systems in various confinements.^{91–94} However, some smaller nematic bundles formed at volume fractions near ϕ_{IN} of the bulk systems. Since drying of a droplet is essentially a nonequilibrium process, we studied the influence of Péclet number on the long-range nematic ordering of rods in the droplet. Figure 5(b) shows for $\lambda = 11$ that the nematic order became even more suppressed with increasing Péclet numbers (data for other λ shown in Figure S11).

2. Formation of supraparticles composed of sphere–ellipsoid mixtures. When evaporating droplets containing PS sphere–ellipsoid mixtures from superamphiphobic surfaces, we obtained almost spherical supraparticles at both low and high relative humidity conditions [Figure S4]. The surface SEM images were analyzed by selecting small regions and counting the number of ellipsoids and spheres in those regions. Since particle sizes were known, we could estimate the relative area fractions of the constituent particles, denoted as σ_e and σ_s for ellipsoids and spheres, respectively [Figure 6].

We characterize the drying conditions of these binary mixtures using two Péclet numbers, namely, Pe_s for the spherical particles and Pe_e for the elongated particles, since the two particle types have different long-time self-diffusion coefficients. Supraparticles made under high-humidity conditions ($40 \leq Pe_e \leq 50$ and $Pe_s = 10$) had a surface predominantly occupied by the ellipsoids for all aspect ratios [Figure 6(a, c)]. Under low-humidity conditions ($130 \leq Pe_e \leq$

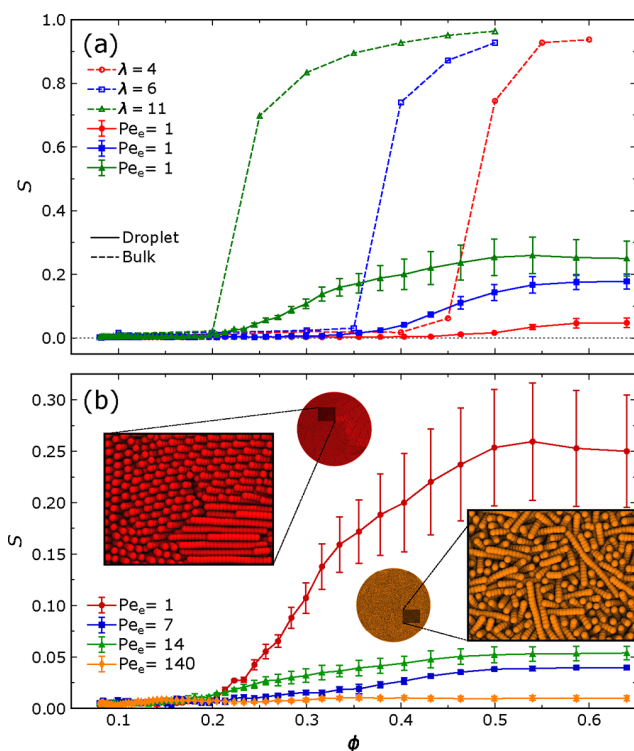


Figure 5. (a) Global nematic order parameter, S , for bulk (empty symbols with dashed lines) and diffusion-limited simulations of droplets (filled symbols with solid lines). (b) Péclet number dependence of global nematic order parameter in drying droplet for $\lambda = 11$. Simulation cross-section snapshots of final supraparticles are shown for $Pe_e = 1$ (red) and $Pe_e = 140$ (orange). Lines are guides for the eye only.

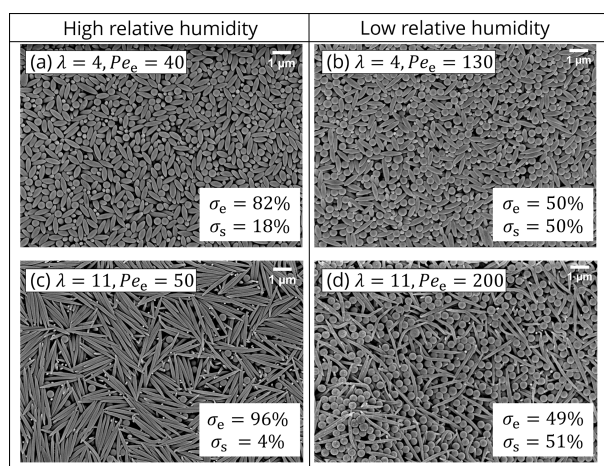


Figure 6. SEM images of the surface of supraparticles composed of sphere–ellipsoid mixtures, with ellipsoids having (a, b) $\lambda = 4$ and (c, d) $\lambda = 11$. (a) & (c) correspond to high relative humidity experiments ($40 \leq Pe_e \leq 50$ and $Pe_s = 10$), while (b) & (d) correspond to low relative humidity ($130 \leq Pe_e \leq 200$ and $30 \leq Pe_s \leq 50$). Figure S12 shows the supraparticle surfaces for $\lambda = 6$ at low and high relative humidity.

200 and $30 \leq Pe_s \leq 50$), however, the supraparticle surface was occupied by a mixture of ellipsoids and spheres [Figures 6(b, d), S12].

The cross-sectional SEM images indicated a single layer of ellipsoids oriented parallel to the interface under high relative

humidity conditions [Figure 7]. It was followed by a homogeneous mixture of the ellipsoids and spheres inside

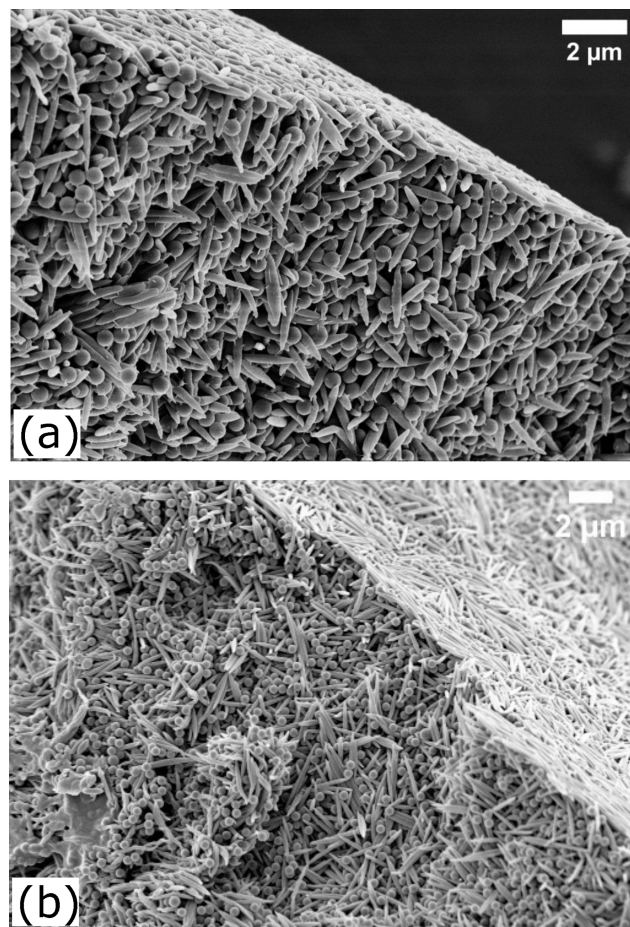


Figure 7. Cross-section SEM images near the surface of the supraparticles which were composed of sphere–ellipsoid mixtures. (a) $\lambda = 6$ at low relative humidity ($Pe_e = 120$ and $Pe_s = 30$) and (b) $\lambda = 11$ at high relative humidity ($Pe_e = 50$ and $Pe_s = 10$).

the supraparticle, irrespective of the ellipsoid aspect ratio and evaporation rate [Figures S13 and S14]. To elucidate the effect of mixing spheres and ellipsoids on the final volume fraction of colloidal particles in the supraparticles, we computed ϕ_f using image analysis of the evaporation videos as described previously. Here, we observed again a decrease in ϕ_f with increasing aspect ratio of the ellipsoids [Table 3]. This decrease in ϕ_f can be rationalized by the random packing of ellipsoids in our supraparticles, which introduces additional constraints on the packing of spheres. The final particle volume fractions obtained at low relative humidity were slightly smaller than those at high relative humidity. These findings support

Table 3. Final volume fractions of colloidal particles in supraparticles composed of sphere–ellipsoid mixtures at high relative humidity ($40 \leq Pe_e \leq 50$ and $Pe_s = 10$) and at low relative humidity ($130 \leq Pe_e \leq 200$ and $30 \leq Pe_s \leq 50$)

λ	ϕ_0	ϕ_f high RH	ϕ_f low RH
4	0.0066 ± 0.0002	0.59 ± 0.02	0.54 ± 0.02
6	0.0066 ± 0.0004	0.52 ± 0.03	0.50 ± 0.03
11	0.0066 ± 0.0004	0.48 ± 0.03	0.45 ± 0.03

our hypothesis that fast drying can be leveraged to prevent the systems from relaxing into a close-packed configuration.

Complementary drying simulations of sphere–rod mixtures were performed starting with a total initial volume fraction $\phi_0 = 0.08$, with equal initial volume fractions of rods ($\phi_{0,r}$) and spheres ($\phi_{0,s}$), i.e., $\phi_{0,r} = \phi_{0,s} = 0.04$. As with the pure rod systems, simulations with and without hydrodynamic interactions did not show any significant differences [Figure S15], suggesting that hydrodynamic interactions between the particles again play a negligible role in these systems. Accordingly, we also performed simulations without hydrodynamics for larger droplets with $R_0 = 100d_e$ to improve statistics.

The sphere and rod volume fractions were computed as a function of radial position in the supraparticle from their respective number density profiles [Figures 8 and S16]. Figure

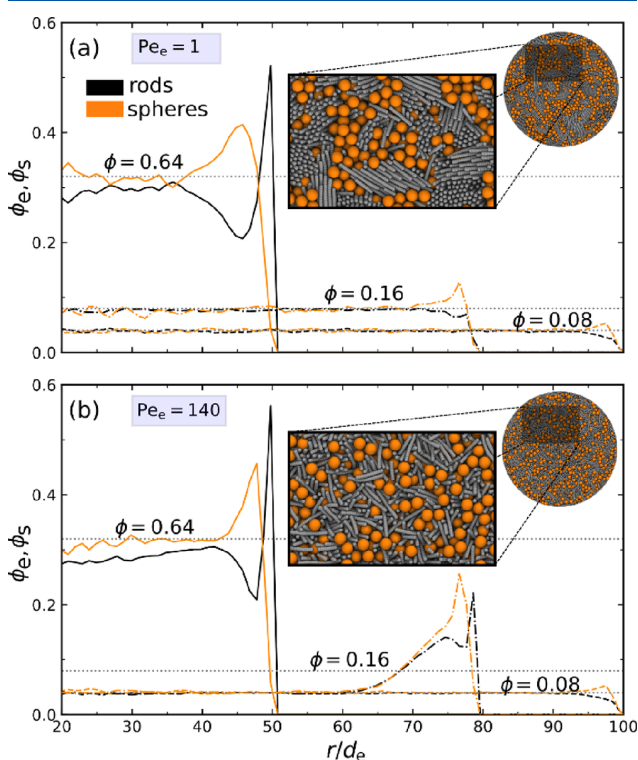


Figure 8. Volume-fraction profiles for mixtures of spheres (ϕ_s , orange) and rods (ϕ_r , black) with $\lambda = 11$, computed from drying simulations with (a) $Pe_e = 1$ (b) $Pe_e = 140$. Dotted gray lines in the plots indicate the total particle volume fraction in the droplet when the volume fraction profiles were computed ($\phi = 0.08, 0.16, 0.64$). Insets show cross-sectional snapshots at $\phi = 0.64$.

8 shows the volume-fraction profiles at initial, intermediate, and final stages of drying for rods with $\lambda = 11$, in the case of the (a) diffusion-limited drying regime ($Pe_e = 1$) and (b) evaporation-limited drying regime ($Pe_e = 140$). For both regimes, a thin shell of rods formed at the supraparticle surface, followed by a region predominantly occupied by spheres. This segregation was observed consistently for all aspect ratios of rods and all drying speeds. This behavior was in contrast with the experiments, where we observed a homogeneous distribution of ellipsoids and spheres on the surface at low relative humidity. Similar differences in the surface structure have been reported previously for supraparticles composed of bidisperse sphere mixtures,⁵ which have been attributed to the

lack of hydrodynamic interactions in most simulation models.^{62,63} However, we were able to rule out this effect for our systems, by performing simulations with and without hydrodynamic interactions, which yielded virtually identical results [Figures S15 and S16]. Another source for the discrepancy between experiments and simulations could be finite-size effects, given that the ratio between the characteristic size of the supraparticle and the colloidal particles is about 10 for the longest rods in the simulations, whereas it is close to 150 in the experiments. Even with our coarse-grained approach, it is currently impossible for us to reach such large size ratios in the simulations, so we cannot rule out this point entirely. However, we note that our simulations with half initial droplet diameter (and half final supraparticle diameter) showed the same qualitative behavior as the larger droplets [Figure S16]. The difference in surface structure might also stem from the stabilization of the dispersions with SDS, which might lead to interfacial effects that are not captured by the simulation model.

Visual inspection of the cross-section snapshots in the evaporation-limited drying simulations showed that the interior of the supraparticles consisted of randomly packed rods, with spheres filling the interstitial spaces. In contrast, in the diffusion-limited drying regime, the cross sections showed small nematic bundles of rods along with some randomly packed rods and spheres for aspect ratios 6 and 11. To better understand this behavior, we performed additional bulk simulations of the sphere–rod mixtures with volume fractions ranging from 0.10 to 0.60 using the same equilibration procedure as for the pure rod systems. For the largest aspect ratio, $\lambda = 11$, the mixture started to phase separate at $\phi = 0.4$ and at higher packing fraction, $\phi = 0.5$, the mixture was demixed and the rods were nematically aligned. For the other two cases, $\lambda = 4$ and 6, the system remained in a mixed phase throughout [Figure S17]. We compared the global nematic order in the two bulk simulations (pure rods and sphere–rod mixtures) and observed that the global nematic ordering of the rods was almost completely suppressed in the presence of spheres for $\lambda = 4$ and 6 [Figure S18]. In accordance with the observations from the bulk simulations, the drying simulations showed the formation of nematic bundles of rods for $\lambda = 11$ in the diffusion-limited drying regime. In comparison with the pure rod systems, global nematic order in the droplets was completely suppressed in the presence of spheres [Figures 5(a), S19].

CONCLUSIONS

We demonstrated that spherical supraparticles could be fabricated by using ellipsoidal particles or mixtures of spherical and ellipsoidal particles. We systematically investigated the effect of drying speed on the structure formation and characterized the different drying regimes through the dimensionless Péclet number Pe . In the evaporation-limited drying regime, experiments ($40 \leq Pe_e \leq 70$) and simulations ($70 \leq Pe_e \leq 140$) showed short-range ordering of the ellipsoidal particles on the supraparticle surface and random packing in the interior. In the diffusion-limited regime ($Pe_e \leq 1$), which we could only explore by simulations for practical reasons, we found increased ordering of rods on the supraparticle surface and the formation of nematically ordered bundles of rods in the interior. Our findings demonstrate the potential to control the degree of ordering of elongated particles by adjusting their aspect ratio and/or the evaporation

rate. The good agreement between experiments and simulations underlines the broad applicability of our strategy. Similar drying experiments can be conducted with, e.g., silica or gold rods for creating supraparticles for various applications, such as sensing or light scattering. Furthermore, the volume fraction of colloidal particles in the final supraparticles decreased with increasing aspect ratio, thus showing a pathway for creating porous supraparticles for catalytic applications.¹

When forming supraparticles from a sphere–ellipsoid mixture at high relative humidity conditions, the supraparticles exhibited an ellipsoid-rich surface monolayer. Simulations indicated an additional sphere-rich region just beneath the surface. This finding hints at the possibility of creating supraparticles with a core–shell morphology by finely tuning the ellipsoid aspect ratio and sphere diameter. Supraparticles made from sphere–ellipsoid mixtures also showed an increase in porosity with increasing ellipsoid aspect ratio. Porosity of these supraparticles could be further increased by subsequently sacrificing the spherical particles, as previously reported for bidisperse sphere mixtures.^{1,95} Based on our observations, one could also fabricate smaller supraparticles that can be used as nanocarriers in specialized applications, such as targeted drug delivery, where the drug itself forms one of the components.

■ ASSOCIATED CONTENT

SI Supporting Information

The Supporting Information is available free of charge at <https://pubs.acs.org/doi/10.1021/acs.langmuir.3c03410>.

Additional SEM images of supraparticles; orientational order parameter plots; schematic explaining solid of revolution method; simulation snapshots of droplets and bulk systems; volume fraction profiles; SEM images of superamphiphobic surfaces and schematic explaining the preparation of PS ellipsoids (PDF)

Video tracking the morphology of a droplet containing ellipsoids during evaporation at high relative humidity conditions (MP4)

■ AUTHOR INFORMATION

Corresponding Authors

Michael Kappl – Department of Physics at Interfaces, Max-Planck Institute for Polymer Research, Mainz 55128, Germany; orcid.org/0000-0001-7335-1707; Email: kappl@mpip-mainz.mpg.de

Arash Nikoubashman – Institute of Physics, Johannes Gutenberg University of Mainz, Mainz 55128, Germany; Leibniz-Institut für Polymerforschung Dresden e.V., Dresden 01069, Germany; Institut für Theoretische Physik, Technische Universität Dresden, Dresden 01069, Germany; orcid.org/0000-0003-0563-825X; Email: anikouba@ipfdd.de

Authors

Melis Yetkin – Department of Physics at Interfaces, Max-Planck Institute for Polymer Research, Mainz 55128, Germany

Yashraj M. Wani – Institute of Physics, Johannes Gutenberg University of Mainz, Mainz 55128, Germany; orcid.org/0000-0002-1158-1889

Kritika Kritika – Institute of Physics, Johannes Gutenberg University of Mainz, Mainz 55128, Germany; Leibniz-Institut für Polymerforschung Dresden e.V., Dresden 01069,

Germany; Institut für Theoretische Physik, Technische Universität Dresden, Dresden 01069, Germany;

orcid.org/0009-0005-8242-9736

Michael P. Howard – Department of Chemical Engineering, Auburn University, Auburn, Alabama 36849, United States; orcid.org/0000-0002-9561-4165

Hans-Jürgen Butt – Department of Physics at Interfaces, Max-Planck Institute for Polymer Research, Mainz 55128, Germany; orcid.org/0000-0001-5391-2618

Complete contact information is available at:

<https://pubs.acs.org/10.1021/acs.langmuir.3c03410>

Author Contributions

[†]M.Y. and Y.M.W. contributed equally to this work.

Notes

The authors declare no competing financial interest.

■ ACKNOWLEDGMENTS

This work was funded by the Deutsche Forschungsgemeinschaft (DFG, German Research Foundation) through project numbers 402234552, 405552959, 470113688, 509039598 and the National Science Foundation under Award No. 2223084. Computing time was granted on the supercomputer Mogon at the Johannes Gutenberg University Mainz (<https://hpc.uni-mainz.de>). We gratefully acknowledge Gabriele Schäfer for synthesizing the colloidal particles, Andreas Hanewald for performing the stretching experiments, and Christine Rosenauer for performing the DLS measurements.

■ REFERENCES

- (1) Liu, W.; Kappl, M.; Butt, H. J. Tuning the Porosity of Supraparticles. *ACS Nano* **2019**, *13* (12), 13949–13956.
- (2) Wintzheimer, S.; Granath, T.; Oppmann, M.; Kister, T.; Thai, T.; Kraus, T.; Vogel, N.; Mandel, K. Supraparticles: Functionality from Uniform Structural Motifs. *ACS Nano* **2018**, *12* (6), 5093–5120.
- (3) Xia, Y.; Nguyen, T. D.; Yang, M.; Lee, B.; Santos, A.; Podsiadlo, P.; Tang, Z.; Glotzer, S. C.; Kotov, N. A. Self-Assembly of Self-Limiting Monodisperse Supraparticles from Polydisperse Nanoparticles. *Nat. Nanotechnol* **2011**, *6* (9), 580–587.
- (4) Fujiwara, A.; Wang, J.; Hiraide, S.; Götz, A.; Miyahara, M. T.; Hartmann, M.; Apeleo Zubiri, B.; Spiecker, E.; Vogel, N.; Watanabe, S. Fast Gas Adsorption Kinetics in Supraparticle-Based MOF Packings with Hierarchical Porosity. *Adv. Mater.* **2023**, *35*, No. 2305980.
- (5) Liu, W.; Midya, J.; Kappl, M.; Butt, H. J.; Nikoubashman, A. Segregation in Drying Binary Colloidal Droplets. *ACS Nano* **2019**, *13* (5), 4972–4979.
- (6) Hou, K.; Han, J.; Tang, Z. Formation of Supraparticles and Their Application in Catalysis. *ACS Materials Letters* **2020**, *2* (1), 95–106.
- (7) Li, X.; Visaveliya, N.; Hafermann, L.; Gross, G. A.; Knauer, A.; Köhler, J. M. Hierarchically Structured Particles for Micro Flow Catalysis. *Chemical Engineering Journal* **2017**, *326*, 1058–1065.
- (8) Oguztürk, H. E.; Bauer, L. J.; Mantouvalou, I.; Kanngieß er, B.; Velez, O. D.; Gradzielski, M. Preparation of Reinforced Anisometric Patchy Supraparticles for Self-Propulsion. *Part. Part. Syst. Charact.* **2021**, *38* (6), No. 2000328.
- (9) Fang, X. L.; Chen, C.; Jin, M. S.; Kuang, Q.; Xie, Z. X.; Xie, S. Y.; Huang, R. B.; Zheng, L. S. Single-Crystal-like Hematite Colloidal Nanocrystal Clusters: Synthesis and Applications in Gas Sensors, Photocatalysis and Water Treatment. *J. Mater. Chem.* **2009**, *19* (34), 6154–6160.
- (10) Zhao, Y.; Cheng, Y.; Shang, L.; Wang, J.; Xie, Z.; Gu, Z. Microfluidic Synthesis of Barcode Particles for Multiplex Assays. *Small* **2015**, *11* (2), 151–174.

- (11) Rial-Hermida, M. I.; Oliveira, N. M.; Concheiro, A.; Alvarez-Lorenzo, C.; Mano, J. F. Bioinspired Superamphiphobic Surfaces as a Tool for Polymer- and Solvent-Independent Preparation of Drug-Loaded Spherical Particles. *Acta Biomater* **2014**, *10* (10), 4314–4322.
- (12) Manoharan, V. N.; Imhof, A.; Thorne, J. D.; Pine, D. J. Photonic Crystals from Emulsion Templates. *Adv. Mater.* **2001**, *13* (6), 447–450.
- (13) Park, J. G.; Kim, S. H.; Magkiriadou, S.; Choi, T. M.; Kim, Y. S.; Manoharan, V. N. Full-Spectrum Photonic Pigments with Non-Iridescent Structural Colors through Colloidal Assembly. *Angewandte Chemie - International Edition* **2014**, *53* (11), 2899–2903.
- (14) Vogel, N.; Utech, S.; England, G. T.; Shirman, T.; Phillips, K. R.; Koay, N.; Burgess, I. B.; Kolle, M.; Weitz, D. A.; Aizenberg, J. Color from Hierarchy: Diverse Optical Properties of Micron-Sized Spherical Colloidal Assemblies. *Proc. Natl. Acad. Sci. U. S. A.* **2015**, *112* (35), 10845–10850.
- (15) Koo, H. J.; Kim, Y. J.; Lee, Y. H.; Lee, W. I.; Kim, K.; Park, N. G. Nano-Embossed Hollow Spherical TiO₂ as Bifunctional Material for High-Efficiency Dye-Sensitized Solar Cells. *Adv. Mater.* **2008**, *20* (1), 195–199.
- (16) Li, X.; Gu, M.; Hu, S.; Kennard, R.; Yan, P.; Chen, X.; Wang, C.; Sailor, M. J.; Zhang, J. G.; Liu, J. Mesoporous Silicon Sponge as an Anti-Pulverization Structure for High-Performance Lithium-Ion Battery Anodes. *Nat. Commun.* **2014**, *5*, 1–7.
- (17) Han, J.; Zhang, X.; Zhou, Y.; Ning, Y.; Wu, J.; Liang, S.; Sun, H.; Zhang, H.; Yang, B. Fabrication of CdTe Nanoparticles-Based Superparticles for an Improved Detection of Cu²⁺ and Ag⁺. *J. Mater. Chem.* **2012**, *22* (6), 2679–2686.
- (18) Dinsmore, A. D.; Hsu, M. F.; Nikolaidis, M. G.; Marquez, M.; Bausch, A. R.; Weitz, D. A. Colloidosomes: Selectively Permeable Capsules Composed of Colloidal Particles. *Science* **2002**, *298* (5595), 1006–1009.
- (19) Velev, O. D.; Furusawa, K.; Nagayama, K. Assembly of Latex Particles by Using Emulsion Droplets as Templates. 1. Microstructured Hollow Spheres. *Langmuir* **1996**, *12* (10), 2374–2384.
- (20) Hsu, M. F.; Nikolaidis, M. G.; Dinsmore, A. D.; Bausch, A. R.; Gordon, V. D.; Chen, X.; Hutchinson, J. W.; Weitz, D. A.; Marquez, M. Self-Assembled Shells Composed of Colloidal Particles: Fabrication and Characterization. *Langmuir* **2005**, *21* (7), 2963–2970.
- (21) Rastogi, V.; Melle, S.; Calderón, O. G.; García, A. A.; Marquez, M.; Velev, O. D. Synthesis of Light-Diffracting Assemblies from Microspheres and Nanoparticles in Droplets on a Superhydrophobic Surface. *Adv. Mater.* **2008**, *20* (22), 4263–4268.
- (22) Lintingre, E.; Ducouret, G.; Lequeux, F.; Olanier, L.; Périé, T.; Talini, L. Controlling the Buckling Instability of Drying Droplets of Suspensions through Colloidal Interactions. *Soft Matter* **2015**, *11* (18), 3660–3665.
- (23) Tsapis, N.; Dufresne, E. R.; Sinha, S. S.; Riera, C. S.; Hutchinson, J. W.; Mahadevan, L.; Weitz, D. A. Onset of Buckling in Drying Droplets of Colloidal Suspensions. *Phys. Rev. Lett.* **2005**, *94* (1), No. 018302.
- (24) Bahadur, J.; Sen, D.; Mazumder, S.; Paul, B.; Bhatt, H.; Singh, S. G. Control of Buckling in Colloidal Droplets during Evaporation-Induced Assembly of Nanoparticles. *Langmuir* **2012**, *28* (3), 1914–1923.
- (25) Sen, D.; Mazumder, S.; Melo, J. S.; Khan, A.; Bhattacharya, S.; D'Souza, S. F. Evaporation Driven Self-Assembly of a Colloidal Dispersion during Spray Drying: Volume Fraction Dependent Morphological Transition. *Langmuir* **2009**, *25* (12), 6690–6695.
- (26) Bahadur, J.; Sen, D.; Mazumder, S.; Bhattacharya, S.; Frielinghaus, H.; Goerigk, G. Origin of Buckling Phenomenon during Drying of Micrometer-Sized Colloidal Droplets. *Langmuir* **2011**, *27* (13), 8404–8414.
- (27) Mondal, R.; Das, A.; Sen, D.; Satapathy, D. K.; Basavaraj, M. G. Spray Drying of Colloidal Dispersions Containing Ellipsoids. *J. Colloid Interface Sci.* **2019**, *551*, 242–250.
- (28) Biswas, P.; Sen, D.; Mazumder, S.; Basak, C. B.; Doshi, P. Temperature Mediated Morphological Transition during Drying of Spray Colloidal Droplets. *Langmuir* **2016**, *32* (10), 2464–2473.
- (29) Gharsallaoui, A.; Roudaut, G.; Chambin, O.; Voilley, A.; Saurel, R. Applications of Spray-Drying in Microencapsulation of Food Ingredients: An Overview. *Food Research International* **2007**, *40* (9), 1107–1121.
- (30) Sen, D.; Spalla, O.; Taché, O.; Haltebourg, P.; Thill, A. Slow Drying of a Spray of Nanoparticles Dispersion. *Situ SAXS Investigation. Langmuir* **2007**, *23* (8), 4296–4302.
- (31) Agthe, M.; Plivelic, T. S.; Labrador, A.; Bergström, L.; Salazar-Alvarez, G. Following in Real Time the Two-Step Assembly of Nanoparticles into Mesocrystals in Levitating Drops. *Nano Lett.* **2016**, *16* (11), 6838–6843.
- (32) Liu, Z.; Liu, Y.; Yang, J.; Li, S.; Peng, C.; Cui, X.; Sheng, L.; Wu, B. Highly Efficient and Controlled Fabrication of Supraparticles by Leidenfrost Phenomenon. *Langmuir* **2022**, *38* (30), 9157–9165.
- (33) Chu, Z.; Seeger, S. Superamphiphobic Surfaces. *Chem. Soc. Rev.* **2014**, *43* (8), 2784–2798.
- (34) Kota, A. K.; Choi, W.; Tuteja, A. Superomniphobic Surfaces: Design and Durability. *MRS Bull.* **2013**, *38* (5), 383–390.
- (35) Zhang, J.; Seeger, S. Superoleophobic Coatings with Ultralow Sliding Angles Based on Silicone Nanofilaments. *Angewandte Chemie - International Edition* **2011**, *50* (29), 6652–6656.
- (36) Butt, H. J.; Semperebon, C.; Papadopoulos, P.; Vollmer, D.; Brinkmann, M.; Ciccotti, M. Design Principles for Superamphiphobic Surfaces. *Soft Matter* **2013**, *9* (2), 418–428.
- (37) Deegan, R. D.; Bakajin, O.; Dupont, T. F.; Huber, G.; Nagel, S. R.; Witten, T. A. Capillary flow as the cause of ring stains from dried liquid drops. *Nature* **1997**, *389*, 827–829.
- (38) Pan, Z.; Dash, S.; Weibel, J. A.; Garimella, S. V. Assessment of Water Droplet Evaporation Mechanisms on Hydrophobic and Superhydrophobic Substrates. *Langmuir* **2013**, *29* (51), 15831–15841.
- (39) Pham, T.; Kumar, S. Drying of Droplets of Colloidal Suspensions on Rough Substrates. *Langmuir* **2017**, *33* (38), 10061–10076.
- (40) Tan, H.; Diddens, C.; Versluis, M.; Butt, H. J.; Lohse, D.; Zhang, X. Self-Wrapping of an Ouzo Drop Induced by Evaporation on a Superamphiphobic Surface. *Soft Matter* **2017**, *13* (15), 2749–2759.
- (41) Liu, W.; Kappl, M.; Steffen, W.; Butt, H. J. Controlling Supraparticle Shape and Structure by Tuning Colloidal Interactions. *J. Colloid Interface Sci.* **2022**, *607*, 1661–1670.
- (42) Wooh, S.; Huesmann, H.; Tahir, M. N.; Paven, M.; Wichmann, K.; Vollmer, D.; Tremel, W.; Papadopoulos, P.; Butt, H. J. Synthesis of Mesoporous Supraparticles on Superamphiphobic Surfaces. *Adv. Mater.* **2015**, *27* (45), 7338–7343.
- (43) Deng, X.; Paven, M.; Papadopoulos, P.; Ye, M.; Wu, S.; Schuster, T.; Klapper, M.; Vollmer, D.; Butt, H. J. Solvent-Free Synthesis of Microparticles on Superamphiphobic Surfaces. *Angewandte Chemie - International Edition* **2013**, *52* (43), 11286–11289.
- (44) Glotzer, S. C.; Solomon, M. J. Anisotropy of Building Blocks and Their Assembly into Complex Structures. *Nat. Mater.* **2007**, *6*, 557–562.
- (45) Schyck, S.; Meijer, J. M.; Baldauf, L.; Schall, P.; Petukhov, A. V.; Rossi, L. Self-Assembly of Colloidal Superballs under Spherical Confinement of a Drying Droplet. *JCIS Open* **2022**, *5*, No. 100037.
- (46) Marino, E.; Van Dongen, S. W.; Neuhaus, S. J.; Li, W.; Keller, A. W.; Kagan, C. R.; Kodger, T. E.; Murray, C. B. Monodisperse Nanocrystal Superparticles Through a Source-Sink Emulsion System. *Chem. Mater.* **2022**, *34* (6), 2779–2789.
- (47) Philipse, A. P. The Random Contact Equation and Its Implications for (Colloidal) Rods in Packings, Suspensions, and Anisotropic Powders. *Langmuir* **1996**, *12* (5), 1127–1133.
- (48) Williams, S. R.; Philipse, A. P. Random Packings of Spheres and Spherocylinders Simulated by Mechanical Contraction. *Phys. Rev. E* **2003**, *67* (5), 9.

- (49) Jungblut, S.; Binder, K.; Schilling, T. Isotropic-Isotropic Phase Separation in Mixtures of Rods and Spheres: Some Aspects of Monte Carlo Simulation in the Grand Canonical Ensemble. *Comput. Phys. Commun.* **2008**, *179* (1–3), 13–16.
- (50) Kyrlyuk, A. V.; Anne Van De Haar, M.; Rossi, L.; Wouterse, A.; Philipse, A. P. Isochoric Ideality in Jammed Random Packings of Non-Spherical Granular Matter. *Soft Matter* **2011**, *7* (5), 1671–1674.
- (51) Jacucci, G.; Longbottom, B. W.; Parkins, C. C.; Bon, S. A. F.; Vignolini, S. Anisotropic Silica Colloids for Light Scattering. *J. Mater. Chem. C Mater.* **2021**, *9* (8), 2695–2700.
- (52) van der Hoeven, J. E. S.; Gurunaryanan, H.; Bransen, M.; de Winter, D. A. M.; de Jongh, P. E.; van Blaaderen, A. Silica-Coated Gold Nanorod Supraparticles: A Tunable Platform for Surface Enhanced Raman Spectroscopy. *Adv. Funct. Mater.* **2022**, *32* (27), 2200148.
- (53) Wang, D.; Hermes, M.; Najmr, S.; Tasios, N.; Grau-Carbonell, A.; Liu, Y.; Bals, S.; Dijkstra, M.; Murray, C. B.; van Blaaderen, A. Structural Diversity in Three-Dimensional Self-Assembly of Nanoplatelets by Spherical Confinement. *Nat. Commun.* **2022**, *13* (1), 6001.
- (54) Shouldice, G. T. D.; Vandezande, G. A.; Rudin, A. Practical Aspects of the Emulsifier-Free Emulsion Polymerization of Styrene. *Eur. Polym. J.* **1994**, *30* (2), 179–183.
- (55) Geyer, F.; Schönecker, C.; Butt, H. J.; Vollmer, D. Enhancing CO₂ Capture Using Robust Superomphobic Membranes. *Adv. Mater.* **2017**, *29* (5), 1603524.
- (56) Ho, C. C.; Keller, A.; Odell, J. A.; Ottewill, R. H. Preparation of Monodisperse Ellipsoidal Polystyrene Particles. *Colloid Polym. Sci.* **1993**, *271* (5), 469–479.
- (57) Howard, M. P.; Reinhart, W. F.; Sanyal, T.; Shell, M. S.; Nikoubashman, A.; Panagiotopoulos, A. Z. Evaporation-Induced Assembly of Colloidal Crystals. *J. Chem. Phys.* **2018**, *149* (9), No. 094901.
- (58) Tang, Y.; Grest, G. S.; Cheng, S. Stratification of Drying Particle Suspensions: Comparison of Implicit and Explicit Solvent Simulations. *J. Chem. Phys.* **2019**, *150* (22), No. 224901.
- (59) Tang, Y.; Grest, G. S.; Cheng, S. Stratification in Drying Films Containing Bidisperse Mixtures of Nanoparticles. *Langmuir* **2018**, *34* (24), 7161–7170.
- (60) Fortini, A.; Martin-Fabiani, I.; De La Haye, J. L.; Dugas, P.-Y.; Lanslot, M.; D'Agosto, F.; Bourgeat-Lami, E.; Keddie, J. L.; Sear, R. P. Dynamic Stratification in Drying Films of Colloidal Mixtures. *Phys. Rev. Lett.* **2016**, *116* (11), No. 118301.
- (61) Makepeace, D. K.; Fortini, A.; Markov, A.; Locatelli, P.; Lindsay, C.; Moorhouse, S.; Lind, R.; Sear, R. P.; Keddie, J. L. Stratification in Binary Colloidal Polymer Films: Experiment and Simulations. *Soft Matter* **2017**, *13* (39), 6969–6980.
- (62) Statt, A.; Howard, M. P.; Panagiotopoulos, A. Z. Influence of Hydrodynamic Interactions on Stratification in Drying Mixtures. *J. Chem. Phys.* **2018**, *149* (2), No. 024902.
- (63) Sear, R. P.; Warren, P. B. Diffusiophoresis in Nonadsorbing Polymer Solutions: The Asakura-Oosawa Model and Stratification in Drying Films. *Phys. Rev. E* **2017**, *96* (6), No. 062602.
- (64) Howard, M. P.; Nikoubashman, A. Stratification of Polymer Mixtures in Drying Droplets: Hydrodynamics and Diffusion. *J. Chem. Phys.* **2020**, *153* (5), No. 054901.
- (65) Malevanets, A.; Kapral, R. Mesoscopic Model for Solvent Dynamics. *J. Chem. Phys.* **1999**, *110* (17), 8605–8613.
- (66) Ihle, T.; Kroll, D. M. Stochastic Rotation Dynamics: A Galilean-Invariant Mesoscopic Model for Fluid Flow. *Phys. Rev. E* **2001**, *63* (2), No. 020201.
- (67) Gompper, G.; Ihle, T.; Kroll, D. M.; Winkler, R. G. Multi-Particle Collision Dynamics: A Particle-Based Mesoscale Simulation Approach to the Hydrodynamics of Complex Fluids. In *Advanced Computer Simulation Approaches for Soft Matter Sciences III*; Springer: Berlin Heidelberg, 2009; pp 1–87 DOI: 10.1007/978-3-540-87706-6_1.
- (68) Aponte-Rivera, C.; Zia, R. N. Simulation of Hydrodynamically Interacting Particles Confined by a Spherical Cavity. *Phys. Rev. Fluids* **2016**, *1* (2), No. 023301.
- (69) Wani, Y. M.; Kovakas, P. G.; Nikoubashman, A.; Howard, M. P. Diffusion and Sedimentation in Colloidal Suspensions Using Multiparticle Collision Dynamics with a Discrete Particle Model. *J. Chem. Phys.* **2022**, *156* (2), No. 024901.
- (70) Poblete, S.; Wysocki, A.; Gompper, G.; Winkler, R. G. Hydrodynamics of Discrete-Particle Models of Spherical Colloids: A Multiparticle Collision Dynamics Simulation Study. *Phys. Rev. E* **2014**, *90* (3), No. 033314.
- (71) Winkler, R. G.; Mussawisade, K.; Ripoll, M.; Gompper, G. Rod-like Colloids and Polymers in Shear Flow: A Multi-Particle-Collision Dynamics Study. *J. Phys.: Condens. Matter* **2004**, *16* (38), 3941–3954.
- (72) Howard, M. P.; Panagiotopoulos, A. Z.; Nikoubashman, A. Efficient Mesoscale Hydrodynamics: Multiparticle Collision Dynamics with Massively Parallel GPU Acceleration. *Comput. Phys. Commun.* **2018**, *230*, 10–20.
- (73) Anderson, J. A.; Glaser, J.; Glotzer, S. C. HOOMD-Blue: A Python Package for High-Performance Molecular Dynamics and Hard Particle Monte Carlo Simulations. *Comput. Mater. Sci.* **2020**, *173*, No. 109363.
- (74) Howard, M. P.; Anderson, J. A.; Nikoubashman, A.; Glotzer, S. C.; Panagiotopoulos, A. Z. Efficient Neighbor List Calculation for Molecular Simulation of Colloidal Systems Using Graphics Processing Units. *Comput. Phys. Commun.* **2016**, *203*, 45–52.
- (75) Howard, M. P.; Statt, A.; Madutsa, F.; Truskett, T. M.; Panagiotopoulos, A. Z. Quantized Bounding Volume Hierarchies for Neighbor Search in Molecular Simulations on Graphics Processing Units. *Comput. Mater. Sci.* **2019**, *164*, 139–146.
- (76) Howard, M. A HOOMD-blue component for soft matter simulations <https://github.com/mphowardlab/azplugins> 2022.
- (77) Roth, R. Fundamental Measure Theory for Hard-Sphere Mixtures: A Review. *J. Phys.: Condens. Matter* **2010**, *22* (6), No. 063102.
- (78) Routh, A. F.; Zimmerman, W. B. Distribution of Particles during Solvent Evaporation from Films. *Chem. Eng. Sci.* **2004**, *59* (14), 2961–2968.
- (79) Israelachvili, J. N. *Intermolecular and Surface Forces*, 3rd ed.; Elsevier: Amsterdam, 2011 DOI: 10.1016/C2009-0-21560-1.
- (80) Ferreiro-Córdova, C.; Van Duijneveldt, J. S. Random Packing of Hard Spherocylinders. *J. Chem. Eng. Data* **2014**, *59* (10), 3055–3060.
- (81) Man, W.; Donev, A.; Stillinger, F. H.; Sullivan, M. T.; Russel, W. B.; Heeger, D.; Inati, S.; Torquato, S.; Chaikin, P. M. Experiments on Random Packings of Ellipsoids. *Phys. Rev. Lett.* **2005**, *94* (19), No. 198001.
- (82) Young, D. A.; Thomsen, C.; Grahm, H. T.; Maris, H. J.; Donev, A.; Cisse, I.; Sachs, D.; Variano, E. A.; Stillinger, F. H.; Connelly, R.; Torquato, S.; Chaikin, P. M. Improving the Density of Jammed Disordered Packings Using Ellipsoids. *Science* **2004**, *303* (5660), 990–993.
- (83) Mukhija, D.; Solomon, M. J. Nematic Order in Suspensions of Colloidal Rods by Application of a Centrifugal Field. *Soft Matter* **2011**, *7* (2), 540–545.
- (84) Wouterse, A.; Williams, S. R.; Philipse, A. P. Effect of Particle Shape on the Density and Microstructure of Random Packings. *J. Phys.: Condens. Matter* **2007**, *19* (40), No. 406215.
- (85) Zhao, J.; Li, S.; Zou, R.; Yu, A. Dense Random Packings of Spherocylinders. *Soft Matter* **2012**, *8* (4), 1003–1009.
- (86) Kyrlyuk, A. V.; Philipse, A. P. Effect of Particle Shape on the Random Packing Density of Amorphous Solids. *Physica Status Solidi (A) Applications and Materials Science* **2011**, *208* (10), 2299–2302.
- (87) Priestley, E. B.; Wojtowicz, P. J.; Sheng, P. *Introduction to Liquid Crystals*; Springer: New York, NY, 1975 DOI: 10.1007/978-1-4684-2175-0.
- (88) Bolhuis, P.; Frenkel, D. Tracing the Phase Boundaries of Hard Spherocylinders. *J. Chem. Phys.* **1997**, *106* (2), 666–687.

(89) Gschwind, A.; Klopotek, M.; Ai, Y.; Oettel, M. Isotropic-Nematic Transition for Hard Rods on a Three-Dimensional Cubic Lattice. *Phys. Rev. E* **2017**, *96* (1), No. 012104.

(90) Khadilkar, M. R.; Nikoubashman, A. Self-Assembly of Semiflexible Polymers Confined to Thin Spherical Shells. *Soft Matter* **2018**, *14* (33), 6903–6911.

(91) Trukhina, Y.; Schilling, T. Computer Simulation Study of a Liquid Crystal Confined to a Spherical Cavity. *Phys. Rev. E Stat Nonlin Soft Matter Phys.* **2008**, *77* (1), No. 011701.

(92) Monderkamp, P. A.; Wittmann, R.; te Vrugt, M.; Voigt, A.; Wittkowski, R.; Löwen, H. Topological Fine Structure of Smectic Grain Boundaries and Tetratic Disclination Lines within Three-Dimensional Smectic Liquid Crystals. *Phys. Chem. Chem. Phys.* **2022**, *24* (26), 15691–15704.

(93) Gârlea, I. C.; Mulder, P.; Alvarado, J.; Dammone, O.; Aarts, D. G. A. L.; Lettinga, M. P.; Koenderink, G. H.; Mulder, B. M. Finite Particle Size Drives Defect-Mediated Domain Structures in Strongly Confined Colloidal Liquid Crystals. *Nat. Commun.* **2016**, *7*, 12112.

(94) Yao, X.; Chen, J. Z. Y. Rodlike Molecules in Extreme Confinement. *Phys. Rev. E* **2020**, *101* (6), No. 062706.

(95) Egly, S.; Fröhlich, C.; Vogel, S.; Gruenewald, A.; Wang, J.; Detsch, R.; Boccaccini, A. R.; Vogel, N. Bottom-Up Assembly of Silica and Bioactive Glass Supraparticles with Tunable Hierarchical Porosity. *Langmuir* **2018**, *34* (5), 2063–2072.

Recommended by ACS

Characterization of Particle Transport and Deposition Due to Heterogeneous Dewetting on Low-Cost Inkjet-Printed Devices

Xi Li, Michael J. Schertzer, *et al.*

NOVEMBER 14, 2023

LANGMUIR

READ 

Kinetically Controlled Site-Specific Self-assembly of Hairy Colloids

Shayan Vazirieh Lenjani, Christian Rossner, *et al.*

JANUARY 05, 2024

LANGMUIR

READ 

Optical Anisotropy and Dimple Formation on Films Formed after Drying of Gelatinized Starch Solution Droplets

Subhadip Ghosh and Arun Roy

MAY 22, 2023

ACS OMEGA

READ 

Three-Dimensional Deposits from Drying Particle-Laden Drops

Beihan Zhao, Siddhartha Das, *et al.*

JUNE 30, 2023

LANGMUIR

READ 

[Get More Suggestions >](#)

Supporting Information

Structure Formation in Supraparticles Composed of Spherical and Elongated Particles

Melis Yetkin¹⁺, Yashraj M. Wani²⁺, Kritika Kritika^{2,3,4}, Michael P. Howard⁵, Michael Kappl¹, Hans-Jürgen Butt^{1*}, Arash Nikoubashman^{2,3,4*}

¹Department of Physics at Interfaces, Max-Planck Institute for Polymer Research,
Ackermannweg 10, 55128 Mainz, Germany

²Institute of Physics, Johannes Gutenberg University of Mainz, Staudingerweg 7, 55128
Mainz, Germany

³Leibniz-Institut für Polymerforschung Dresden e.V., Hohe Straße 6, 01069 Dresden,
Germany

⁴Institut für Theoretische Physik, Technische Universität Dresden, 01069 Dresden,
Germany

⁵Department of Chemical Engineering, Auburn University, Auburn, Alabama 36849,
USA

+These authors contributed equally to this work.

* Corresponding authors: butt@mpip-mainz.mpg.de & anikouba@ipfdd.de

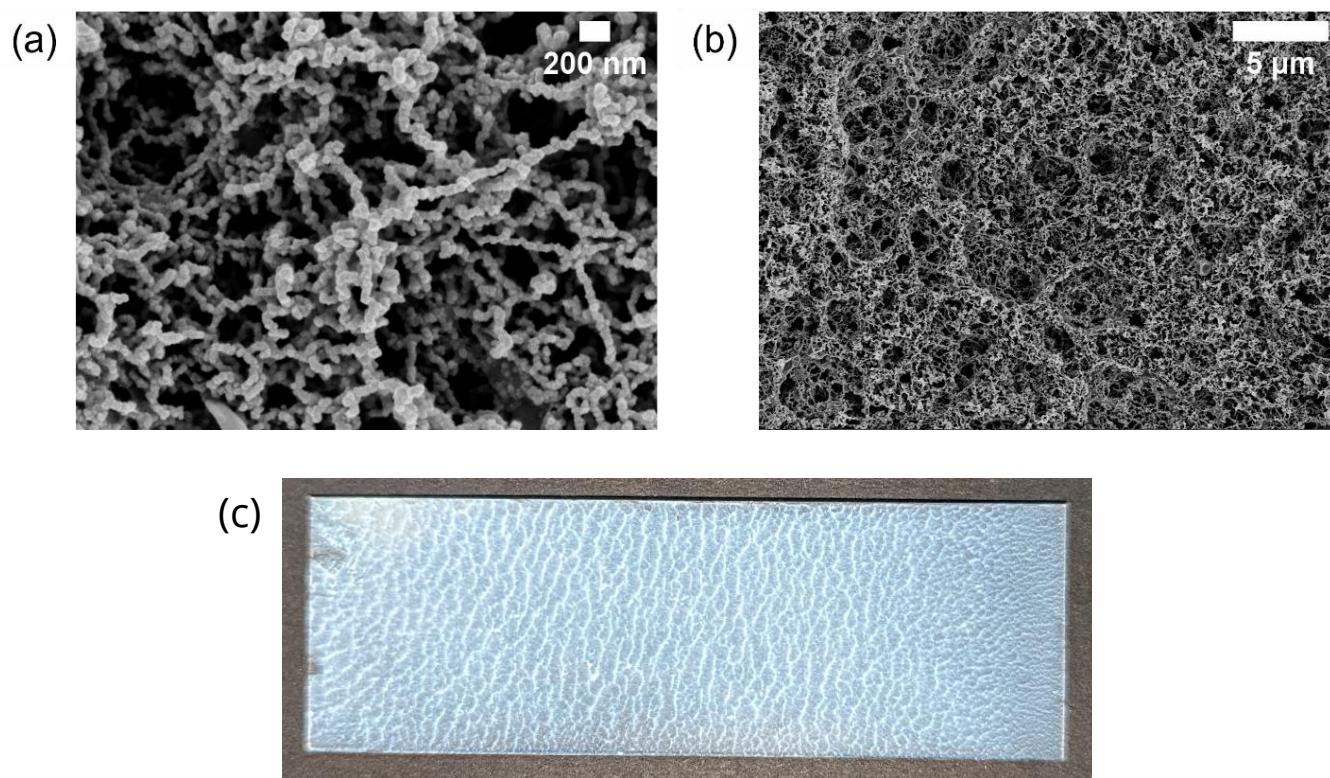


Fig. S1: (a) zoom-in and (b) zoom-out SEM images showing the surface morphology of silicone nanofilament-coated glass substrates (c) photo of the substrate.

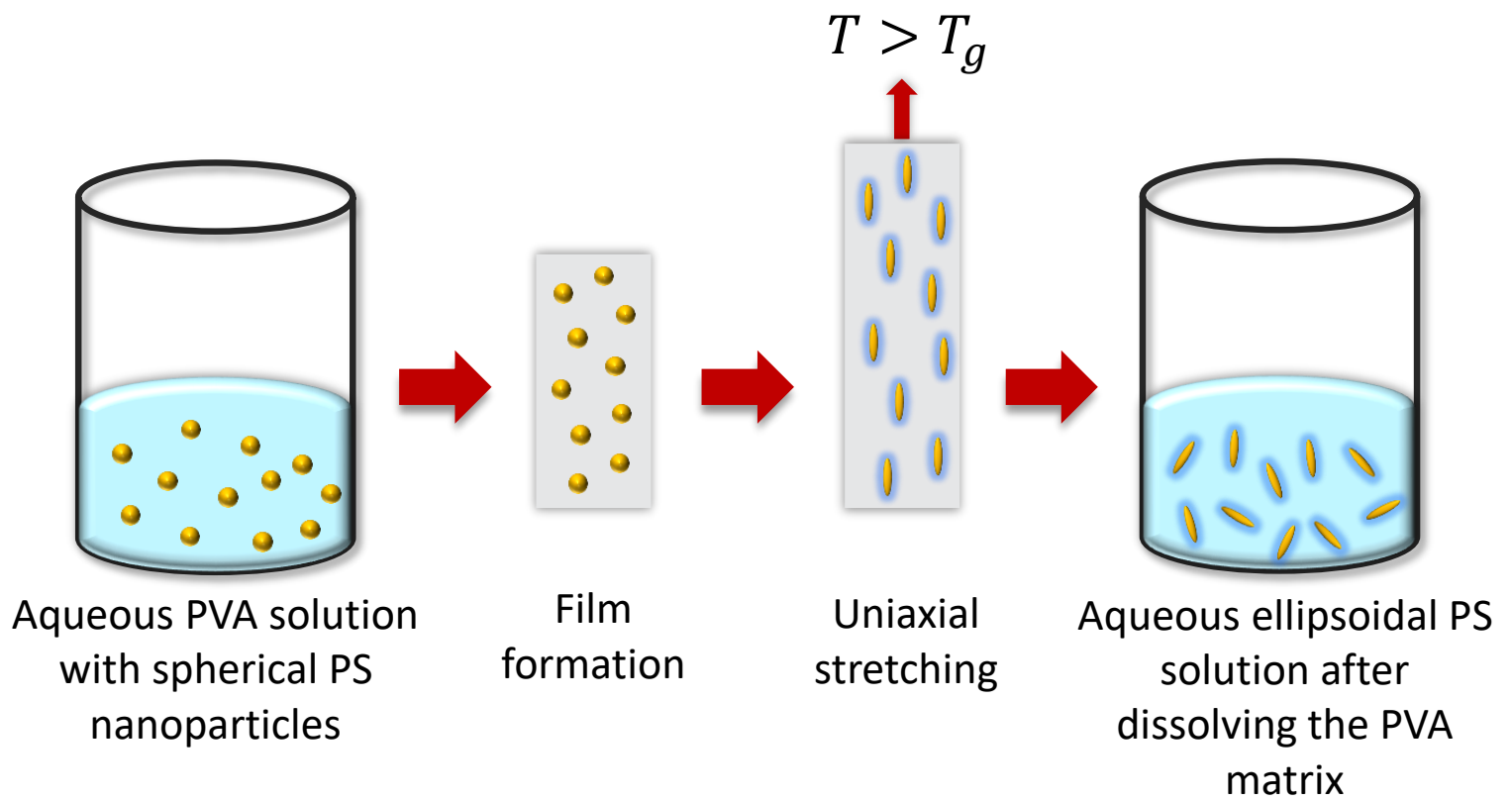


Fig. S2: Schematic depicting the preparation of polystyrene (PS) ellipsoids.

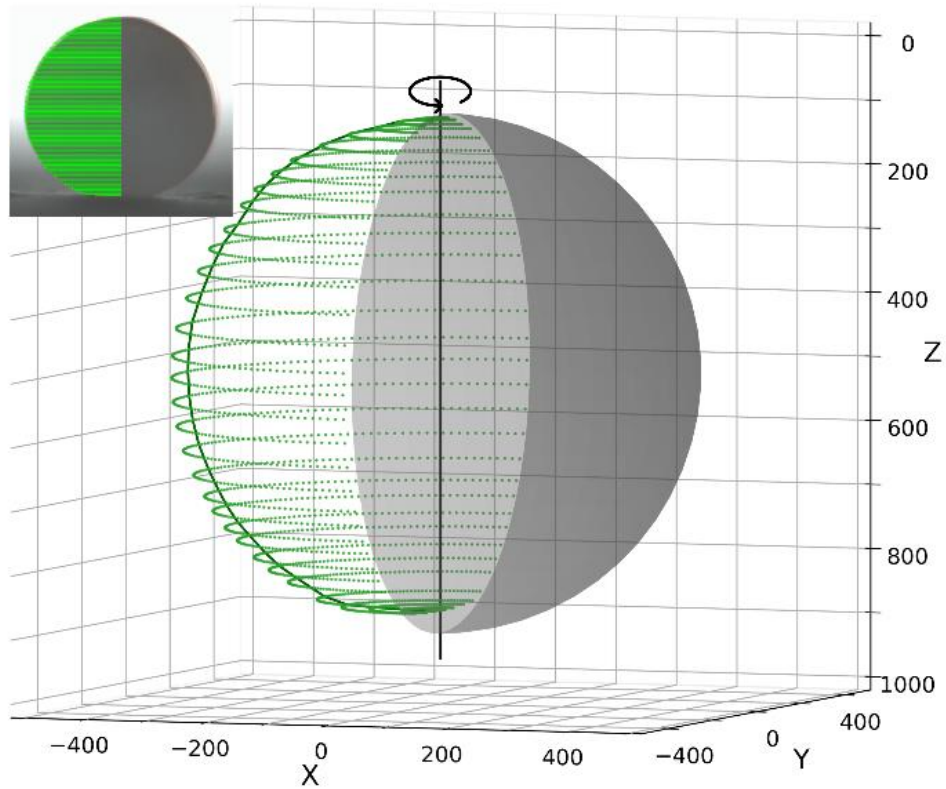


Fig. S3: 3D reconstruction of droplet using solid of revolution (green) compared with a sphere (gray). The inset shows an image of a droplet, in which disc-shape slices are determined for performing solid of revolution.

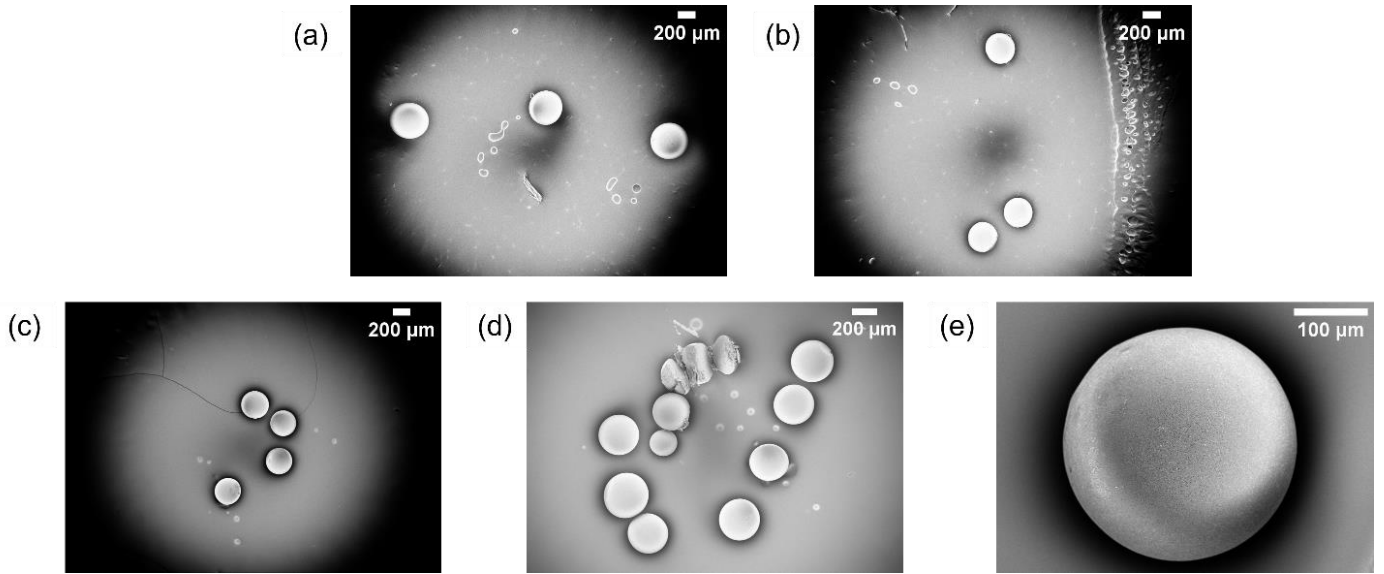


Fig. S4: SEM images showing the spherical final morphology of supraparticles composed of ellipsoids of (a) $\lambda = 6$ at $Pe_e = 50$ (b) $\lambda = 11$ at $Pe_e = 70$ and sphere-ellipsoid mixtures with ellipsoids of (c) $\lambda = 4$ at $Pe_s = 10$ and $Pe_e = 40$ (d) $\lambda = 4$ at $Pe_s = 30$ and $Pe_e = 130$ (e) $\lambda = 11$ at $Pe_s = 10$ and $Pe_e = 50$.

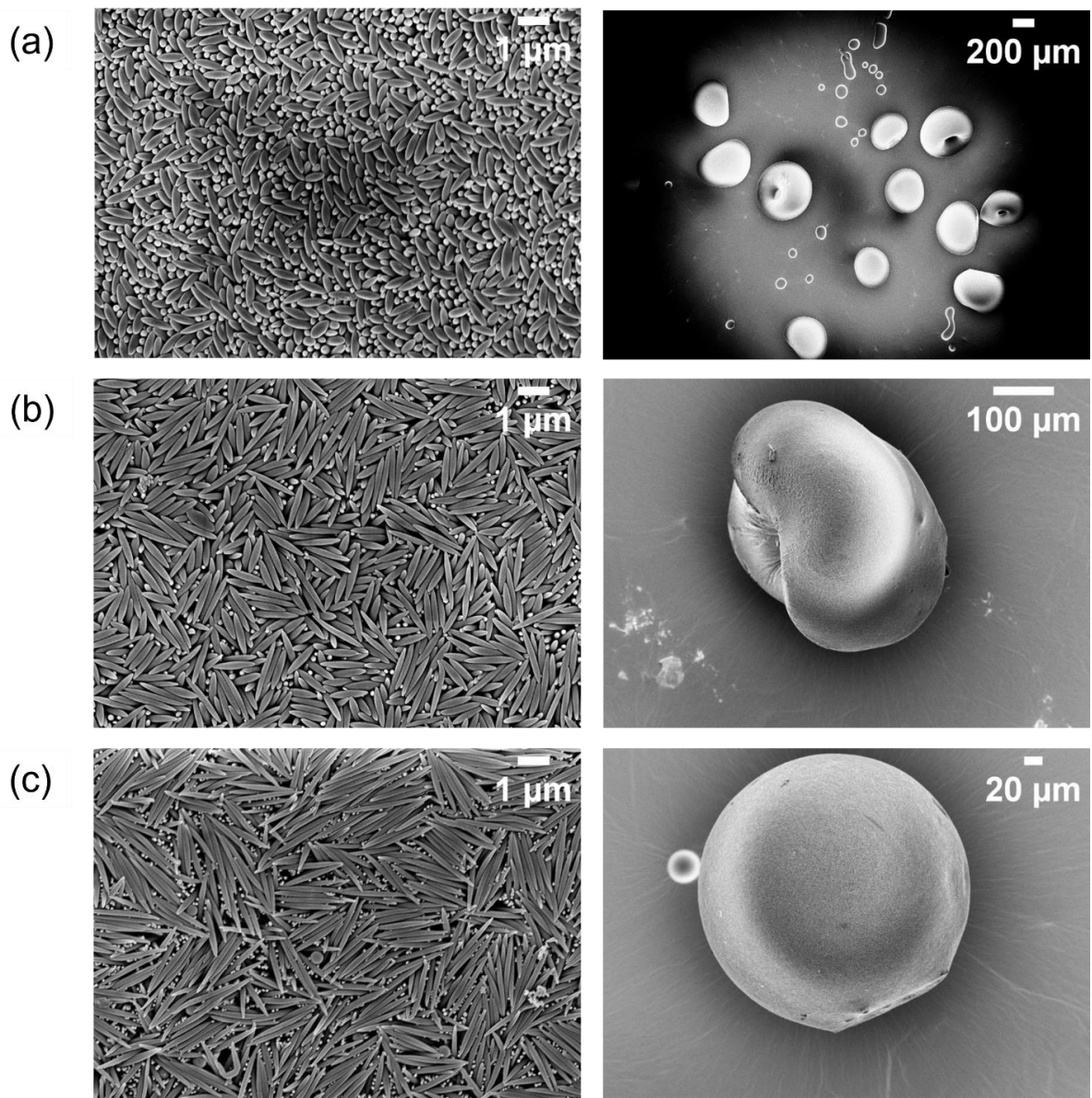


Fig. S5: SEM images of supraparticle surfaces, composed of ellipsoids of $\lambda =$ (a) 4, (b) 6, and (c) 11 at $170 \leq Pe_e \leq 200$ (left column). The corresponding supraparticles showed buckling (right column).

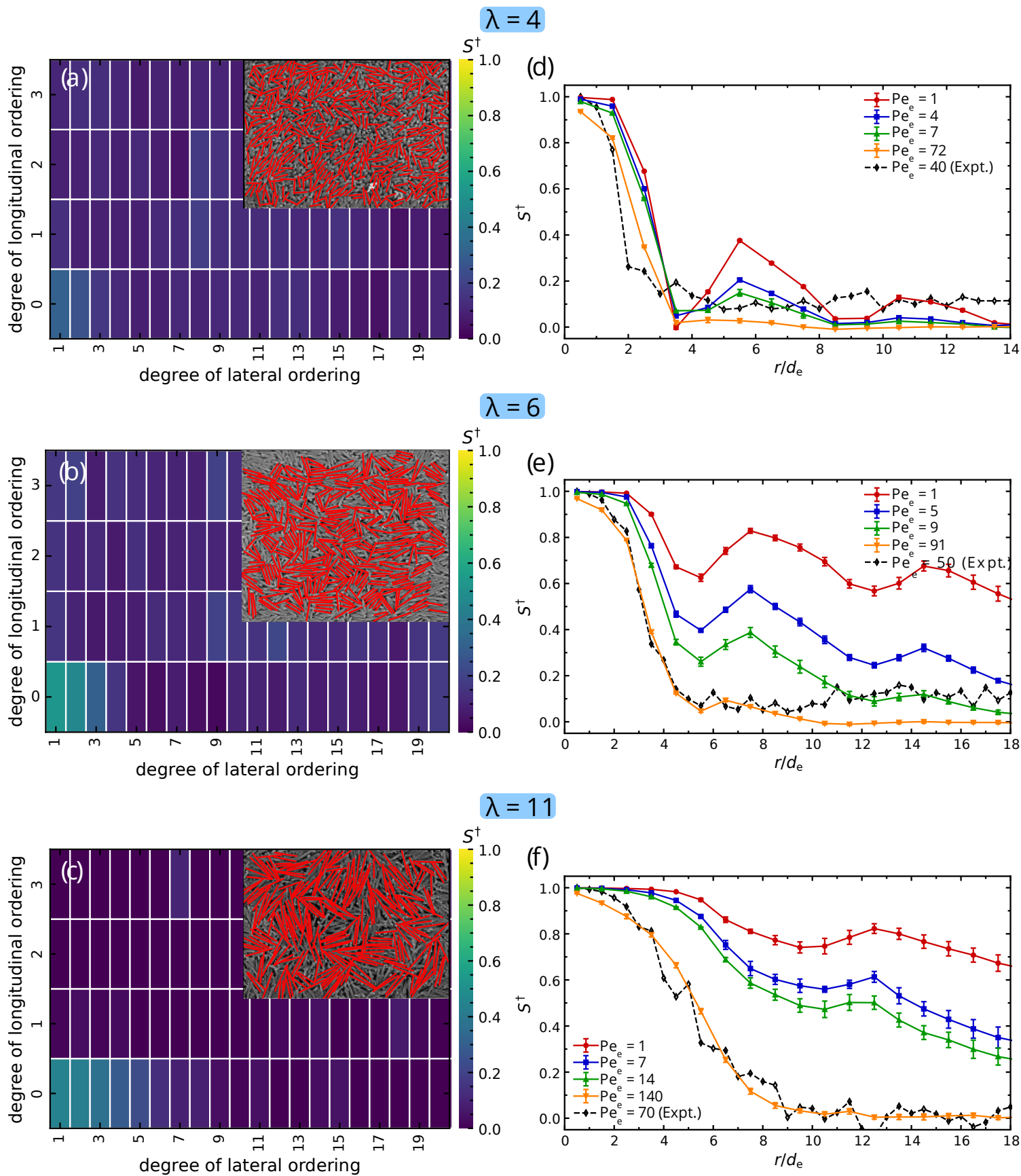


Fig. S6: (a-c) Orientational order parameter calculated from the surface SEM images. (d-f) show the Péclet number dependence of orientational order parameter.

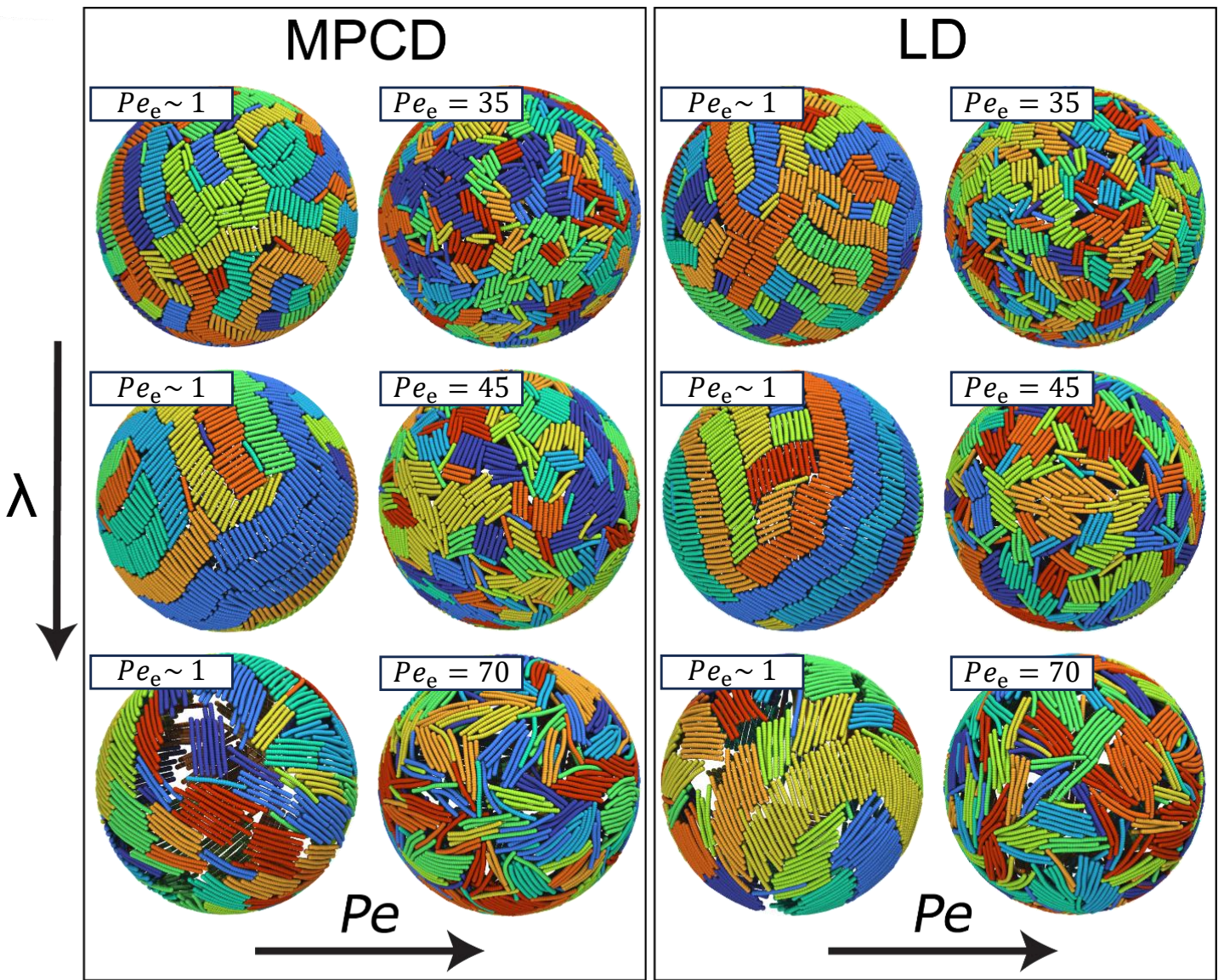


Fig. S7: Simulation snapshots showing the surface morphology of the supraparticles obtained from multi-particle collision dynamics (MPCD) and Langevin dynamics (LD) simulations for varying aspect ratios λ and Péclet numbers Pe_e .

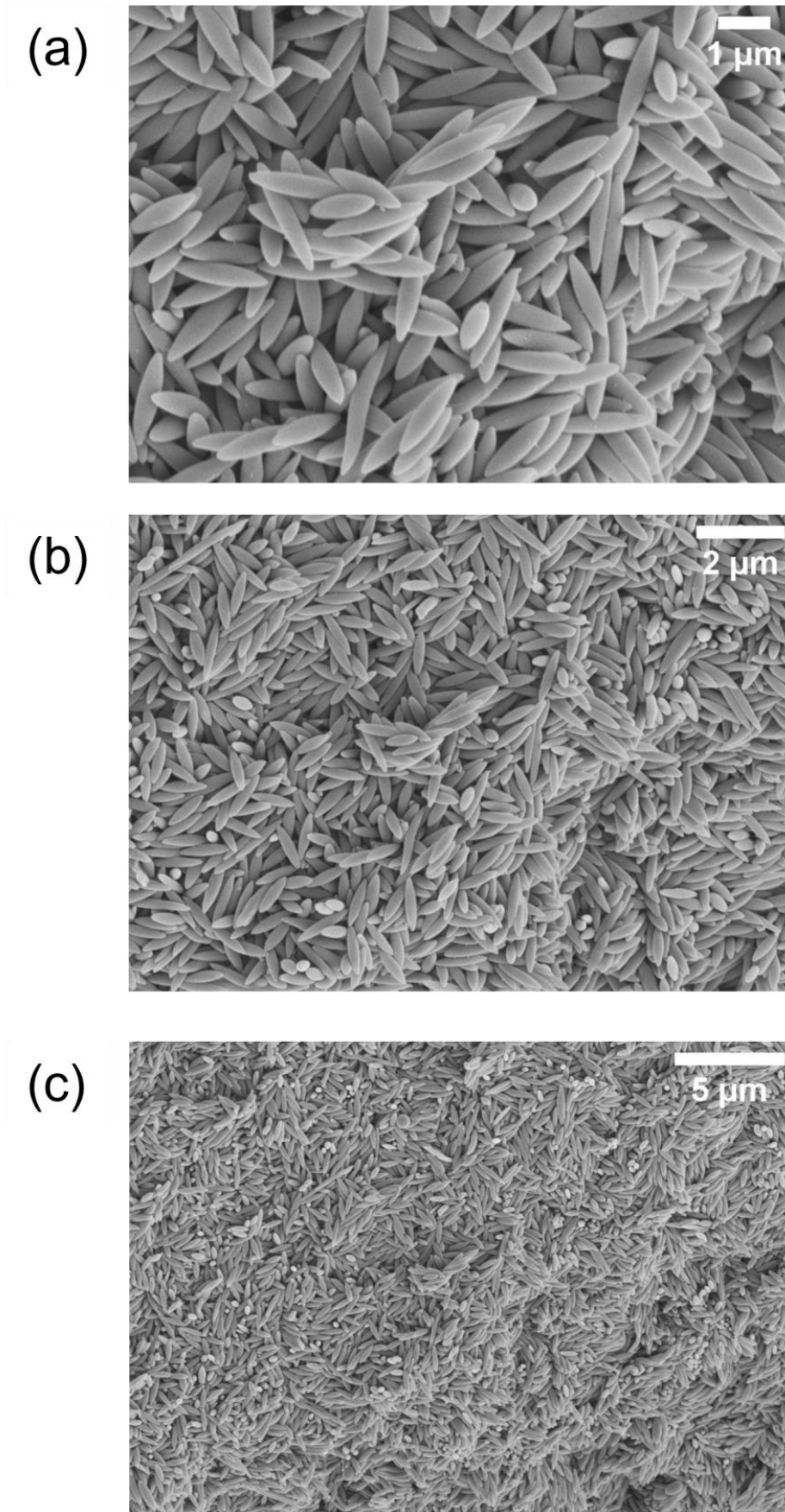


Fig. S8: The cross-section SEM images of supraparticles composed of $\lambda = 6$ ellipsoids at $Pe_e = 50$. Images were obtained by zooming out from the same region of interest (from (a-c)).

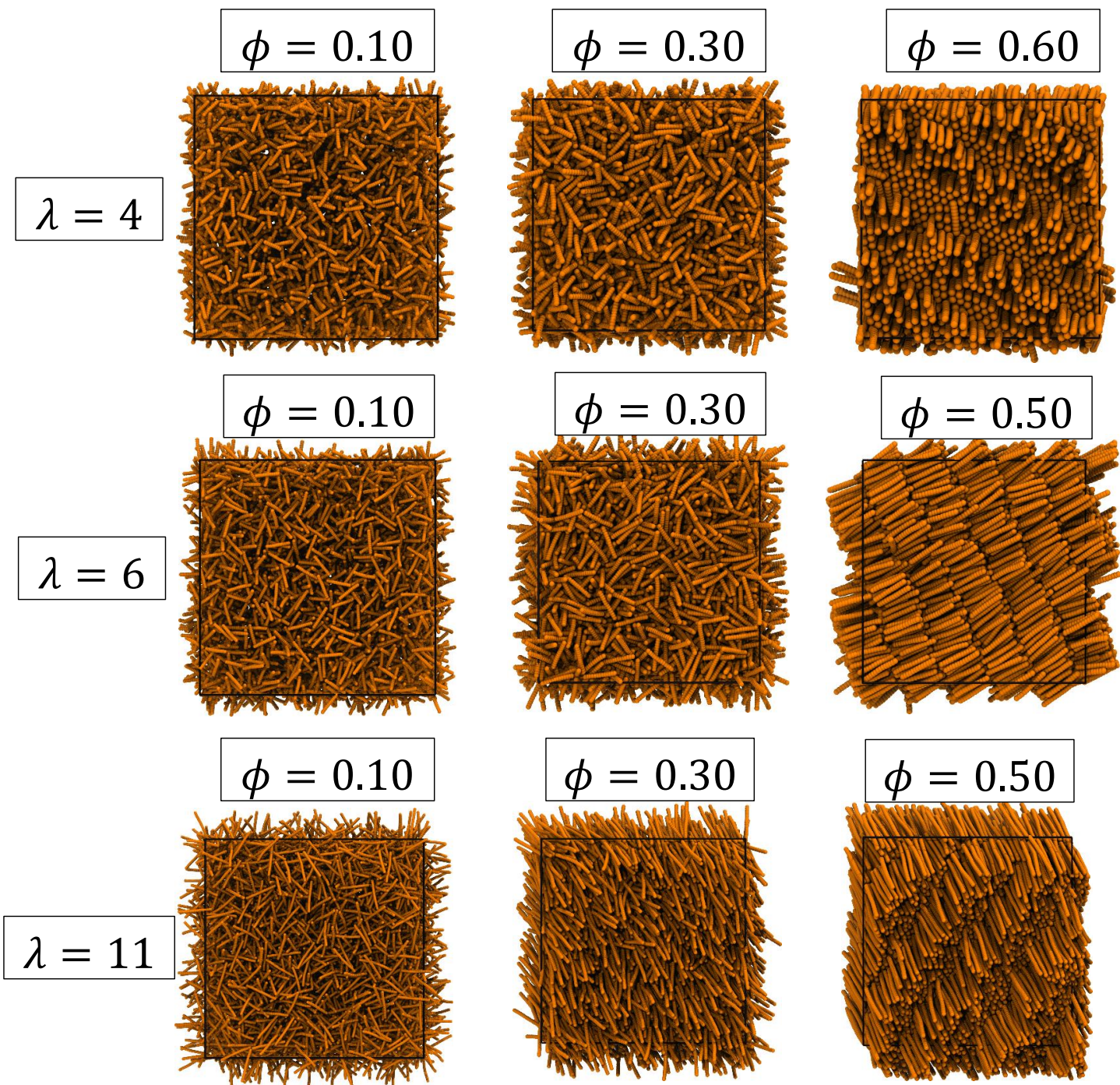


Fig. S9: Bulk simulations of pure-rod suspensions of varying aspect ratios (rows) and varying packing fractions (columns).

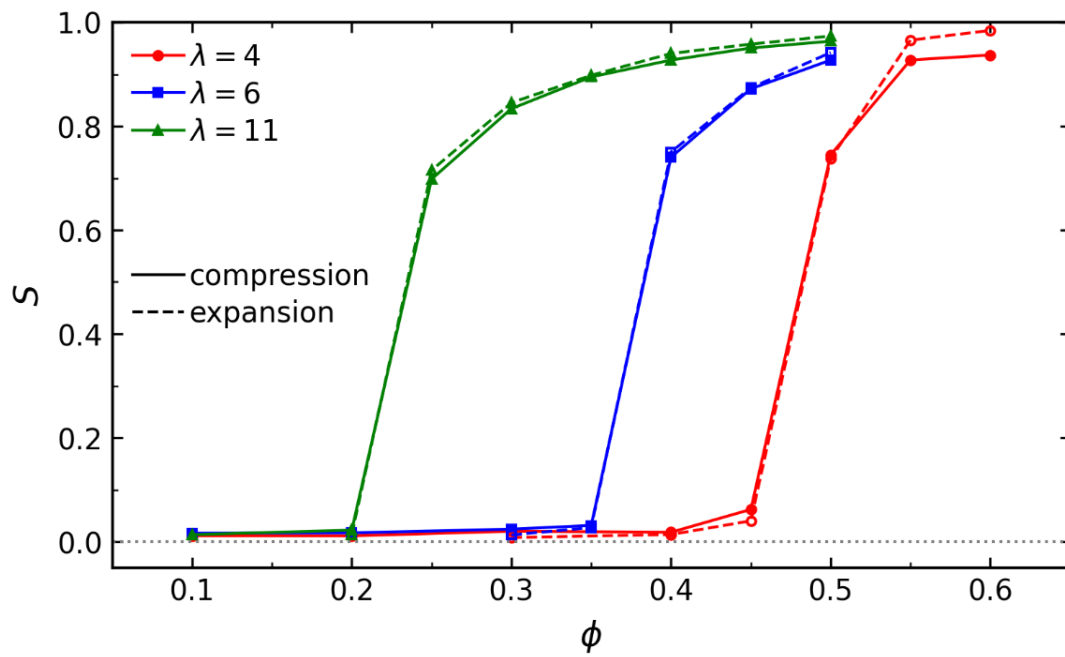


Fig. S10: Global order parameter obtained from bond order parameter in the bulk systems consisting of rods of varying aspect ratios.

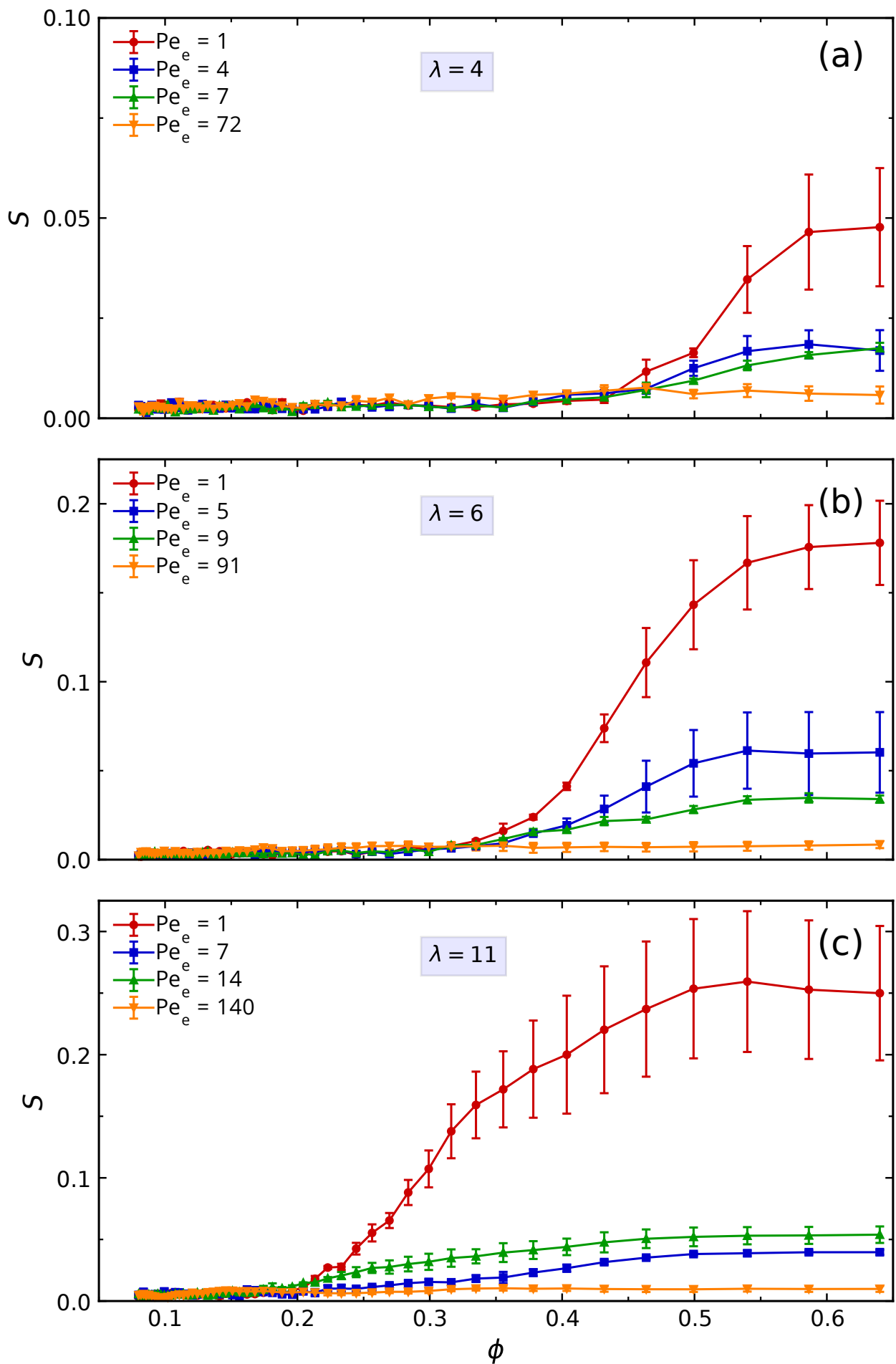
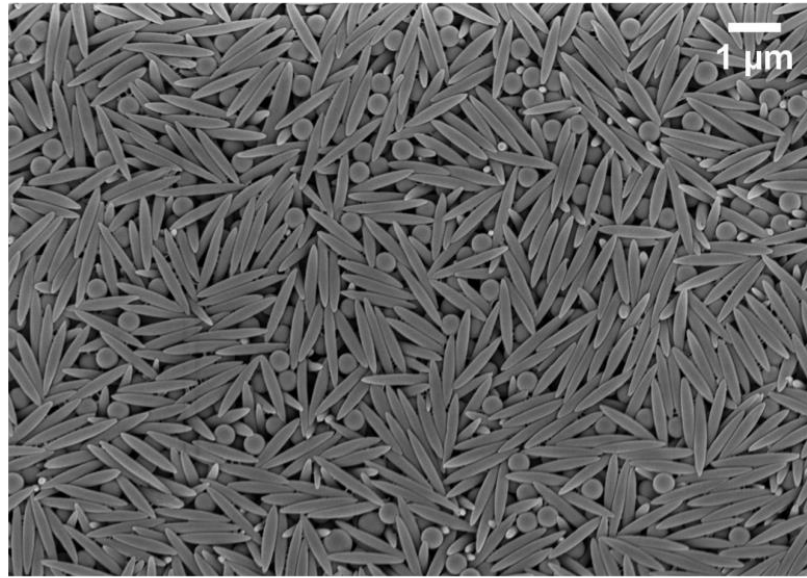


Fig. S11: Order parameter for drying droplet simulations with varying aspect ratios of rods, (a) 4, (b) 6, and (c) 11.

(a)



(b)

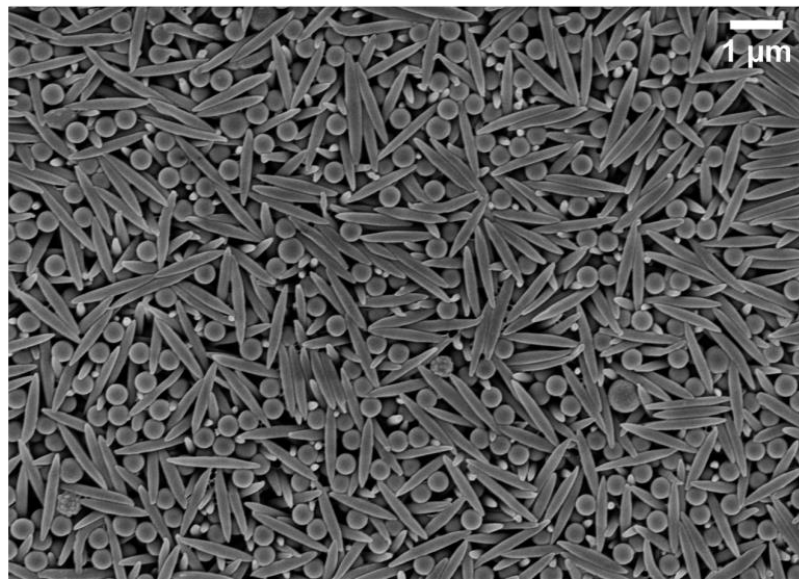
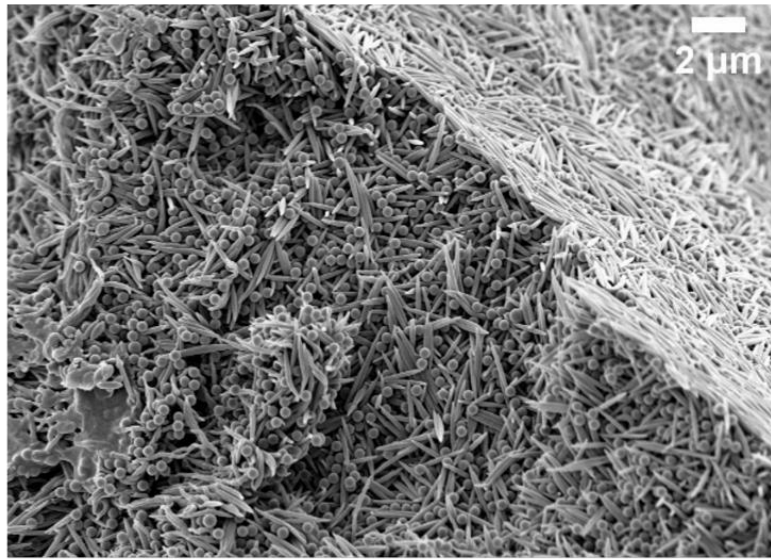
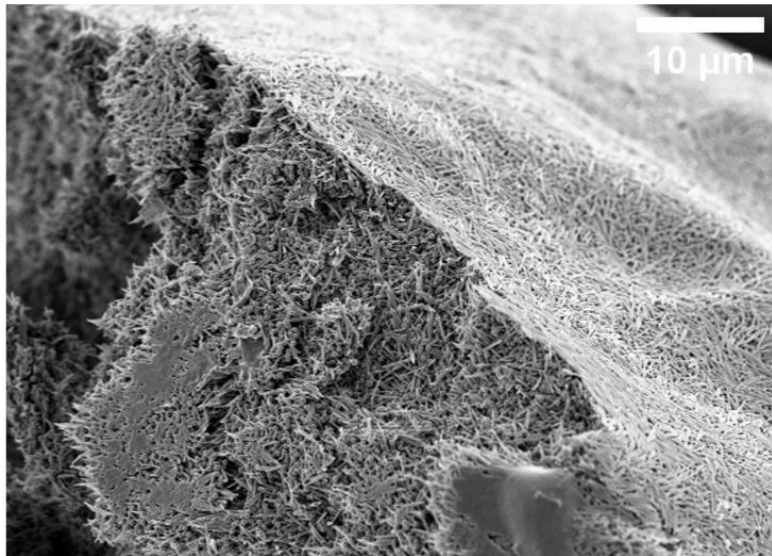


Fig. S12: SEM images showing the supraparticle surfaces composed of sphere-ellipsoid mixtures with ellipsoids of $\lambda = 6$ at (a) $Pe_e = 50$ and $Pe_s = 10$, (b) $Pe_e = 120$ and $Pe_s = 30$.

(a)



(b)



(c)

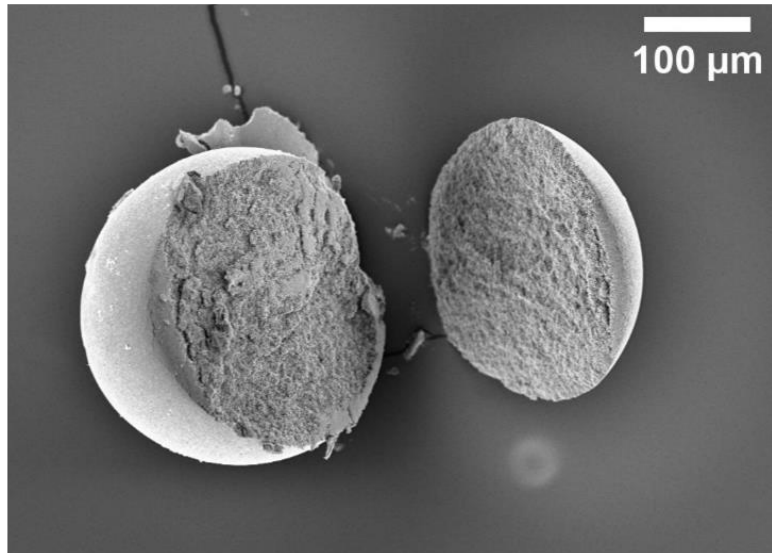


Fig. S13: The cross-section SEM images of supraparticles composed of sphere-ellipsoid mixtures with ellipsoids of $\lambda = 11$ at $Pe_e = 50$ and $Pe_s = 10$. Images were obtained by zooming out from the same region of interest (from (a-c)). The cross-section images indicated a thin crust of ellipsoids on the surface followed by a random distribution of the ellipsoids and spheres inside the supraparticle.

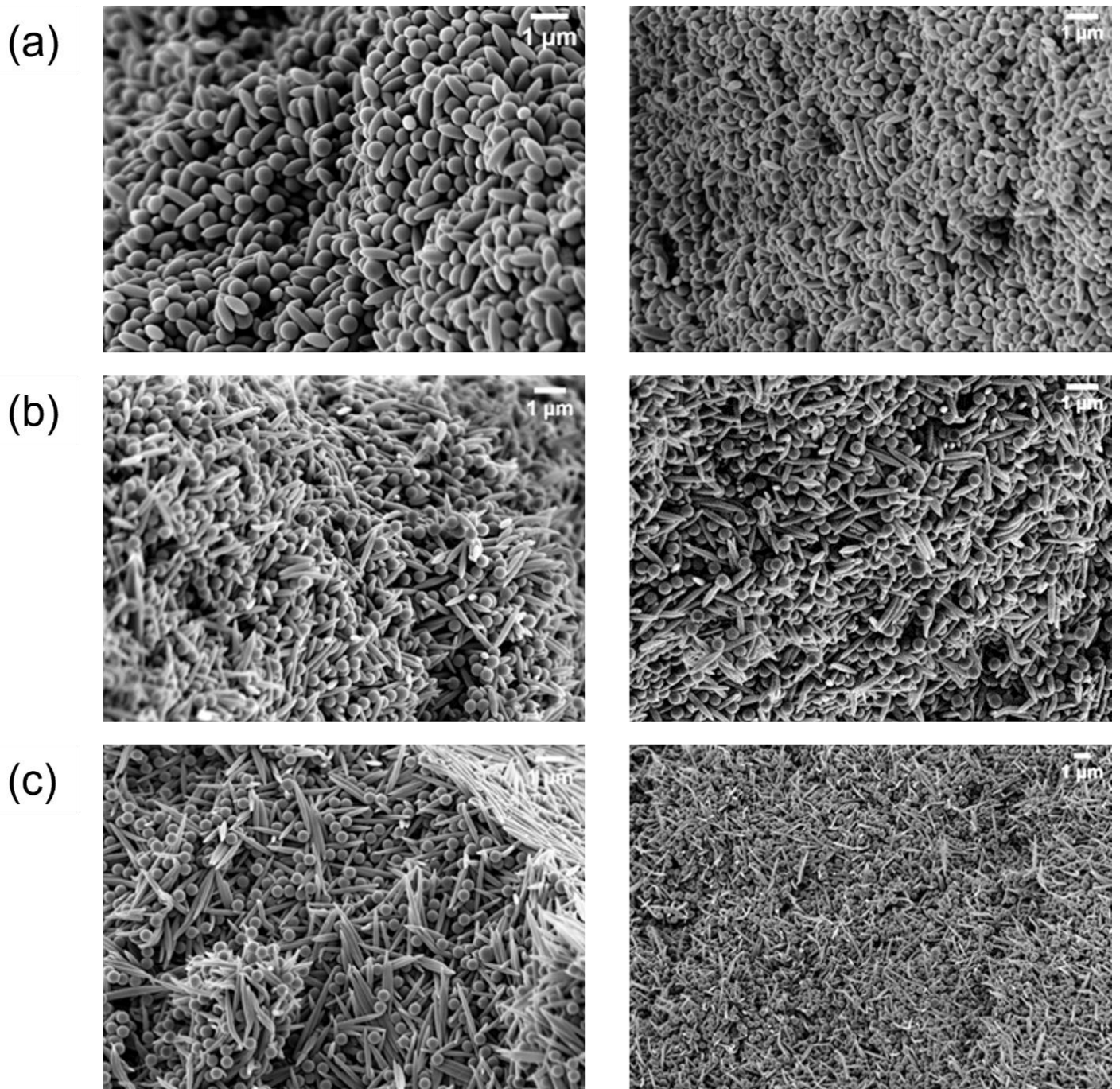


Fig. S14: The cross-section SEM images of supraparticles composed of sphere-ellipsoid mixtures with ellipsoids of $\lambda =$ (a) 4, (b) 6, and (c) 11. The left column represents evaporation at $40 \leq Pe_e \leq 50$ and $Pe_s = 10$ and the right column represents evaporation at $130 \leq Pe_e \leq 200$ and $30 \leq Pe_s \leq 50$.

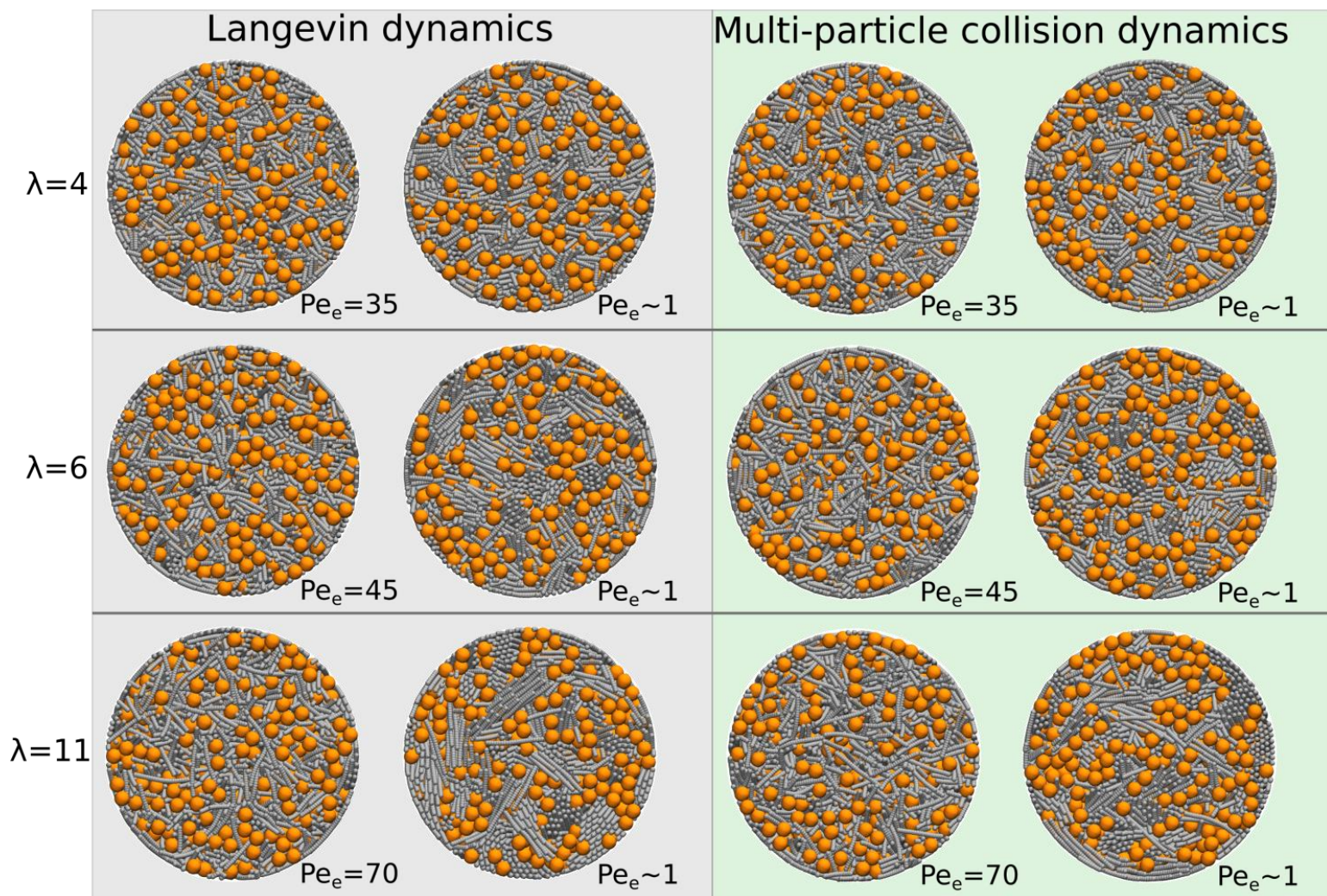


Fig. S15: Comparison of Langevin dynamics and multi-particle collision dynamics drying simulations.

$\lambda = 11$

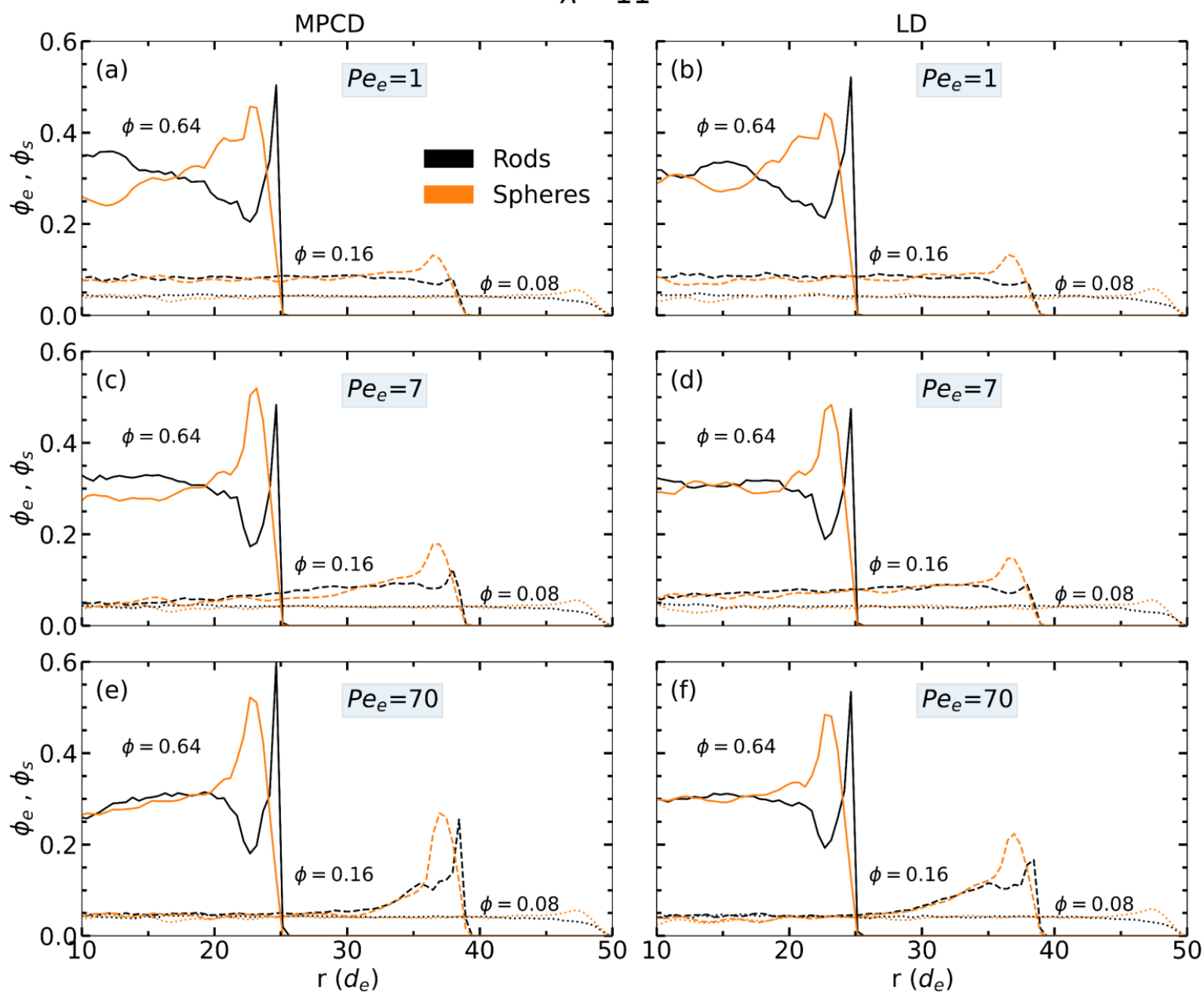


Fig. S16: Volume fraction profiles for rod ($\lambda = 11$) sphere mixture droplets with MPCD and LD methods.

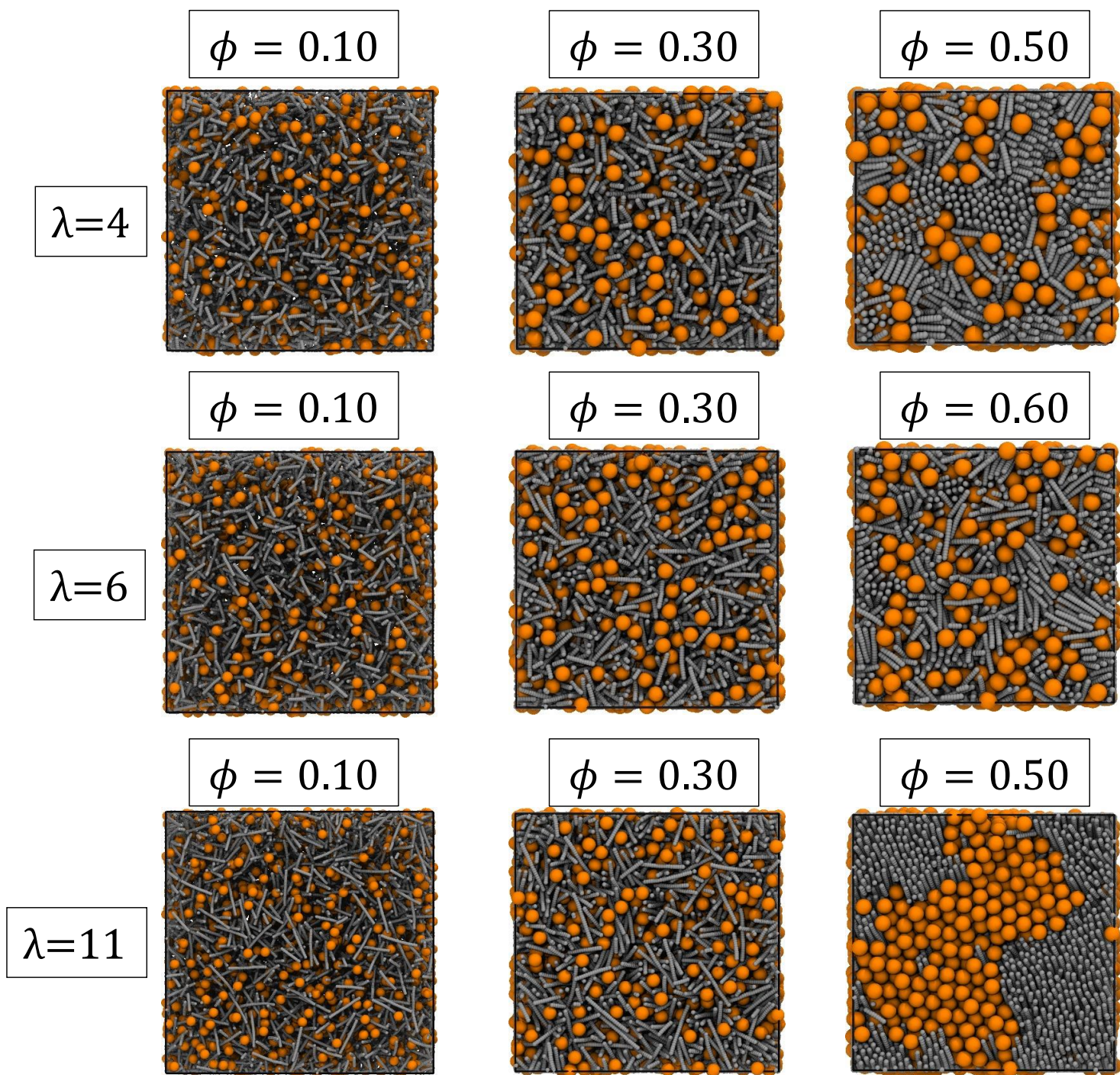


Fig. S17: Bulk simulations of sphere-rod mixtures of varying aspect ratios (rows) and varying packing fractions (columns).

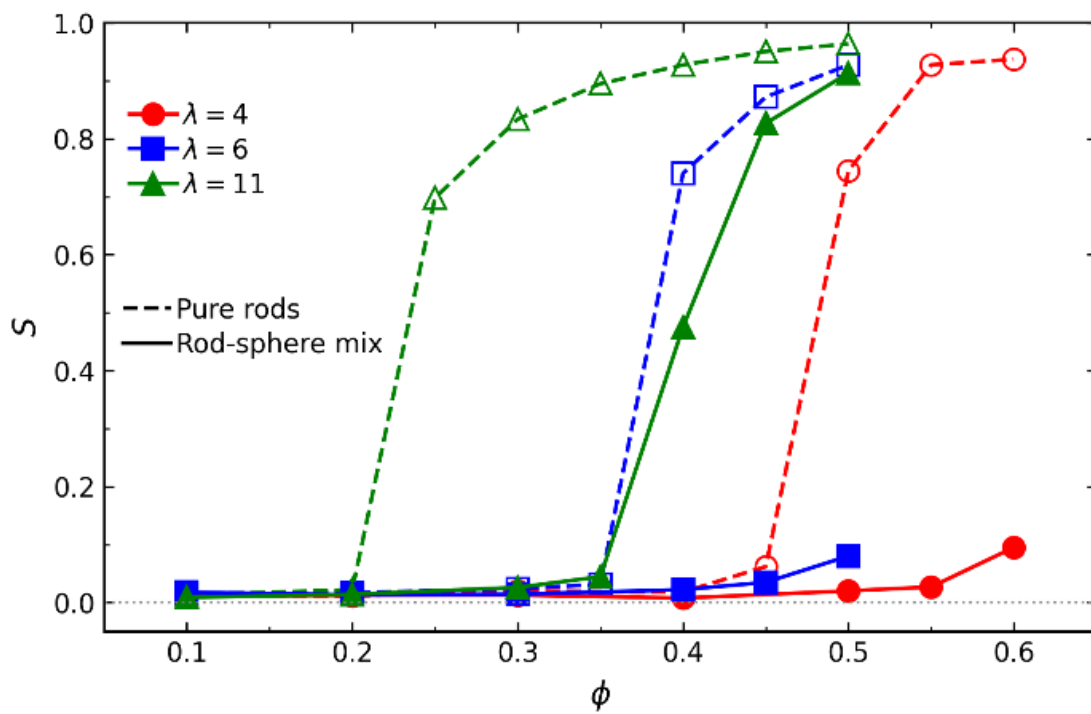


Figure S18: Global nematic ordering in bulk simulations of pure rods (dashed) and sphere-rod mixtures (solid)

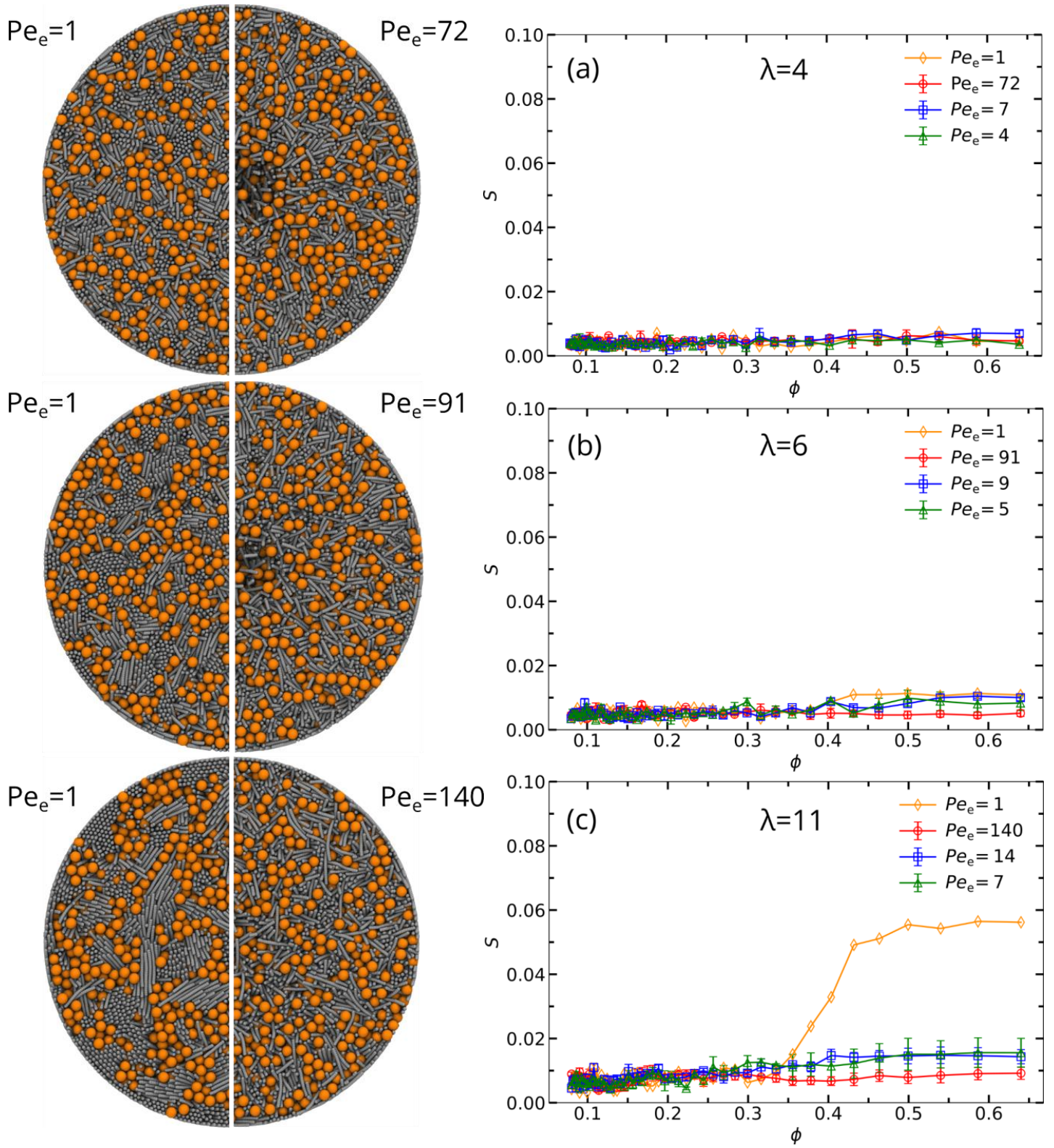


Figure S19: Global nematic ordering in droplets containing sphere-rod mixtures for (a) $\lambda = 4$, (b) $\lambda = 6$ and (c) $\lambda = 11$.

Summary and outlook

Advancements in particle synthesis techniques and recognition of the fact that particle shapes and interactions are key factors for the engineering of novel functional materials, has garnered significant interest in the scientific community over the last few decades. Nanoparticles of different shapes, such as cubes, rods, ellipsoids, tetrahedra, can now be synthesized with high precision and yield. Understanding the influence of shape on the nanoparticle dynamics and assembly is crucial for scientific and practical purposes. In this thesis, we investigated the dynamics and evaporation-driven assembly in colloidal suspensions using molecular dynamics simulations.

On the dynamics side, we first studied the transport properties – diffusion and sedimentation – in colloidal suspensions consisting of spherical particles. Colloidal suspension was described using a discrete particle model for the particles which were coupled with the multi-particle collision dynamics solvent (MPCD). In the discrete particle model, a single particle was represented as a mesh of point (vertex) particles that were connected by harmonic springs. We performed bulk simulations for a wide range of volume fractions and compared the MD+MPCD simulations with experimental measurements, theoretical predictions and Brownian dynamics simulations with free draining hydrodynamics (BD) and pairwise far-field hydrodynamics (RPY). In general, we found that the MPCD results were comparable with expectations from experimental measurements, theoretical predictions and RPY simulations. We found discrepancies in the short-time self-diffusion coefficients between MPCD and RPY simulations, which was likely due to partial coupling of the colloids with the MPCD solvent at short-times. At longer times, a proper coupling was achieved, resulting in expected volume fraction dependence of the self-diffusion and sedimentation coefficients. This indicated the presence of hydrodynamic interactions between colloidal particles in the MPCD simulations.

Taking advantage of the flexibility of the discrete particle model, we extended the scope of our study to investigate suspensions consisting of shape-anisotropic nanoparticles. We considered shapes such as cube, octahedron, tetrahedron, and spherocylinder. In line with our previous investigations, we performed bulk simulations for a range of volume fractions while ensuring to stay in the fluid phase for all the shapes. For the regular polyhedral shapes we found that shape had a clear influence on their transport properties, where we had fixed the edge length of the different polyhedra to aid comparison. At very low volume fractions, cubes and octahedra diffused slower than spheres, while tetrahedra diffused faster. This trend was consistent with expectations from a correlation based on sphericity of the different shapes and an approximation using spherical analogues with diameter equal to the

mean of circumscribing and inscribing sphere diameters. The diffusion and sedimentation coefficients showed varying volume fraction dependence, that was strongest for tetrahedra and weakest for spheres, with cubes and octahedra exhibiting intermediate behavior. The strong volume fraction dependence of the tetrahedra was attributed to the formation of pentagonal dipyramids at higher volume fractions.

For spherocylinders with small aspect ratios ($\lambda \leq 2$), we observed that the diffusion coefficient at low volume fractions aligned with the theoretical expectations, slowing with increasing aspect ratios. The volume fraction dependence of the transport properties deviated marginally in comparison to spheres, with significant deviations expected at higher aspect ratios, where it is known that the isotropic–nematic transition occurs at lower volume fractions.

On the assembly side, we probed the structure formation in supraparticles formed from the evaporation of colloidal droplets consisting of rod-like and/or spherical particles. The parameters of interest were the droplet evaporation rate and particle aspect ratios. We found that the orientational ordering and packing of the rod-like particles within the supraparticles was dependent on the evaporation rate and particle diffusion rate, which was characterized by the dimensionless Péclet number (Pe). At high Pe , we observed that particles tended to accumulate at the drying interface, resulting in random packing of rod-like particles inside the supraparticle. Experimental measurements indicated that random packing of elongated particles increased supraparticle porosity, which increased with aspect ratios of the elongated particles, suggesting applications in catalysis processes. On the other hand, at low Pe , rod-like particles could attain entropically favoured configurations, resulting in orientationally ordered clusters inside the supraparticles.

Supraparticles formed from rod–sphere mixtures exhibited a top layer rich in rods and a sphere-rich region just beneath it. This suggested that one could probably form supraparticles with a core–shell morphology by carefully tuning the aspect ratios of the rod-like particles and the sphere diameters. Similar to our previous observation, orientational ordering of the rod-like particles could be controlled through the evaporation rate.

Bibliography

- [1] Jean-Marie Lehn. “Supramolecular chemistry: Where from? Where to?” In: *Chemical Society Reviews* 46.9 (2017), pp. 2378–2379 (cit. on p. 1).
- [2] Sharon C Glotzer and Michael J Solomon. “Anisotropy of building blocks and their assembly into complex structures”. In: *Nature materials* 6.8 (2007), pp. 557–562 (cit. on p. 1).
- [3] M Baron. “Safe handling of nano materials and other advanced materials at workplaces”. In: *Project Number: F 2268* (2015), p. 52 (cit. on p. 1).
- [4] Yugang Sun and Younan Xia. “Shape-controlled synthesis of gold and silver nanoparticles”. In: *science* 298.5601 (2002), pp. 2176–2179 (cit. on p. 2).
- [5] Yi Wang, Jun Chen, Ruipeng Li, et al. “Controlled Self-Assembly of Gold Nanotetrahedra into Quasicrystals and Complex Periodic Supracrystals”. In: *Journal of the American Chemical Society* 145.32 (2023), pp. 17902–17911 (cit. on p. 2).
- [6] Sihai Chen, Zhong Lin Wang, John Ballato, Stephen H Foulger, and David L Carroll. “Monopod, bipod, tripod, and tetrapod gold nanocrystals”. In: *Journal of the American Chemical Society* 125.52 (2003), pp. 16186–16187 (cit. on p. 2).
- [7] Yu-Ying Yu, Ser-Sing Chang, Chien-Liang Lee, and CR Chris Wang. “Gold nanorods: electrochemical synthesis and optical properties”. In: *The Journal of Physical Chemistry B* 101.34 (1997), pp. 6661–6664 (cit. on p. 2).
- [8] Melis Yetkin, Yashraj M Wani, Kritika Kritika, et al. “Structure Formation in Supraparticles Composed of Spherical and Elongated Particles”. In: *Langmuir* 40.1 (2023), pp. 1096–1108 (cit. on pp. 2, 9, 21).
- [9] Ian Freestone, Nigel Meeks, Margaret Sax, and Catherine Higgitt. “The Lycurgus cup—a roman nanotechnology”. In: *Gold bulletin* 40 (2007), pp. 270–277 (cit. on p. 2).
- [10] Gregory J Higby. “Gold in medicine: a review of its use in the West before 1900”. In: *Gold bulletin* 15.4 (1982), pp. 130–140 (cit. on p. 2).
- [11] Robert Brown. “XXVII. A brief account of microscopical observations made in the months of June, July and August 1827, on the particles contained in the pollen of plants; and on the general existence of active molecules in organic and inorganic bodies”. In: *The philosophical magazine* 4.21 (1828), pp. 161–173 (cit. on p. 2).
- [12] Marc D Haw. “Colloidal suspensions, Brownian motion, molecular reality: a short history”. In: *Journal of physics: condensed matter* 14.33 (2002), p. 7769 (cit. on pp. 2, 3).
- [13] Gouy. “Note sur le mouvement brownien”. In: *J. Phys. Theor. Appl.* 7.1 (1888), pp. 561–564 (cit. on p. 3).
- [14] Jürgen Renn. “Einstein’s invention of Brownian motion”. In: *Annalen der Physik* 517 (2005), pp. 23–37 (cit. on p. 3).

- [15] Paul Langevin et al. “Sur la théorie du mouvement brownien”. In: *CR Acad. Sci. Paris* 146.530-533 (1908), p. 530 (cit. on p. 3).
- [16] Jean Perrin. “L’agitation moléculaire et le mouvement brownien”. In: *Comptes rendus* 146 (1908), pp. 967–970 (cit. on p. 3).
- [17] Jacob N Israelachvili. *Intermolecular and surface forces*. Academic press, 2011 (cit. on pp. 4–9).
- [18] Dixie J Goss and Ralph H Petrucci. *General chemistry principles & modern applications, petrucci, harwood, herring, madura: study guide*. pearson/prentice Hall, 2007 (cit. on p. 4).
- [19] Jan KG Dhont. *An introduction to dynamics of colloids*. Elsevier, 1996 (cit. on pp. 4, 7, 13–15).
- [20] Lawrie B Skinner, Congcong Huang, Daniel Schlesinger, et al. “Benchmark oxygen-oxygen pair-distribution function of ambient water from x-ray diffraction measurements with a wide Q-range”. In: *The Journal of chemical physics* 138.7 (2013) (cit. on p. 4).
- [21] Vicky V Mody, Rodney Siwale, Ajay Singh, and Hardik R Mody. “Introduction to metallic nanoparticles”. In: *Journal of Pharmacy and bioallied sciences* 2.4 (2010), pp. 282–289 (cit. on p. 5).
- [22] Aleksandra Zielińska, Filipa Carreiró, Ana M Oliveira, et al. “Polymeric nanoparticles: production, characterization, toxicology and ecotoxicology”. In: *Molecules* 25.16 (2020), p. 3731 (cit. on p. 5).
- [23] Emily DER Hyde, Ahmad Seyfaee, Frances Neville, and Roberto Moreno-Atanasio. “Colloidal silica particle synthesis and future industrial manufacturing pathways: a review”. In: *Industrial & Engineering Chemistry Research* 55.33 (2016), pp. 8891–8913 (cit. on p. 5).
- [24] Giuseppe Cavallaro, Rawil F Fakhrullin, and Pooria Pasbakhsh. *Clay nanoparticles: properties and applications*. Elsevier, 2020 (cit. on p. 5).
- [25] John D Weeks, David Chandler, and Hans C Andersen. “Role of repulsive forces in determining the equilibrium structure of simple liquids”. In: *The Journal of chemical physics* 54.12 (1971), pp. 5237–5247 (cit. on p. 5).
- [26] Hugo C Hamaker. “The London—van der Waals attraction between spherical particles”. In: *physica* 4.10 (1937), pp. 1058–1072 (cit. on p. 6).
- [27] Peter William Atkins, George Ratcliffe, Julio de Paula, and Mark Wormald. *Physical chemistry for the life sciences*. Oxford University Press, 2023 (cit. on p. 7).
- [28] Jacob Israelachvili and Richard Pashley. “The hydrophobic interaction is long range, decaying exponentially with distance”. In: *Nature* 300.5890 (1982), pp. 341–342 (cit. on p. 7).
- [29] Rico F Tabor, Chu Wu, Franz Grieser, Raymond R Dagastine, and Derek YC Chan. “Measurement of the hydrophobic force in a soft matter system”. In: *The journal of physical chemistry letters* 4.22 (2013), pp. 3872–3877 (cit. on p. 7).
- [30] LA Kohlstaedt, EC Sung, A Fujishige, and RD Cole. “Non-histone chromosomal protein HMG1 modulates the histone H1-induced condensation of DNA.” In: *Journal of Biological Chemistry* 262.2 (1987), pp. 524–526 (cit. on p. 8).
- [31] Wendong Liu, Michael Kappl, Werner Steffen, and Hans-Jürgen Butt. “Controlling supraparticle shape and structure by tuning colloidal interactions”. In: *Journal of Colloid and Interface Science* 607 (2022), pp. 1661–1670 (cit. on pp. 8, 9, 20, 21).

- [32]WB Russel, DA Saville, and WR Schowalter. “Colloidal dispersions cambridge univ”. In: *Press, Cambridge* (1989) (cit. on pp. 8, 17).
- [33]Arash Nikoubashman, Victoria E Lee, Chris Sosa, et al. “Directed assembly of soft colloids through rapid solvent exchange”. In: *ACS nano* 10.1 (2016), pp. 1425–1433 (cit. on p. 8).
- [34]Frank Smalenburg, Niels Boon, Maarten Kater, Marjolein Dijkstra, and René van Roij. “Phase diagrams of colloidal spheres with a constant zeta-potential”. In: *The Journal of chemical physics* 134.7 (2011) (cit. on p. 8).
- [35]Ana B Jódar-Reyes, Antonio Martín-Rodríguez, and Juan L Ortega-Vinuesa. “Effect of the ionic surfactant concentration on the stabilization/destabilization of polystyrene colloidal particles”. In: *Journal of colloid and interface science* 298.1 (2006), pp. 248–257 (cit. on p. 9).
- [36]C Bondy. “The creaming of rubber latex”. In: *Transactions of the Faraday Society* 35 (1939), pp. 1093–1108 (cit. on p. 9).
- [37]Sho Asakura and Fumio Oosawa. “On interaction between two bodies immersed in a solution of macromolecules”. In: *The Journal of chemical physics* 22.7 (1954), pp. 1255–1256 (cit. on p. 10).
- [38]Sho Asakura and Fumio Oosawa. “Interaction between particles suspended in solutions of macromolecules”. In: *Journal of polymer science* 33.126 (1958), pp. 183–192 (cit. on p. 10).
- [39]Miles Padgett and Roberto Di Leonardo. “Holographic optical tweezers and their relevance to lab on chip devices”. In: *Lab on a Chip* 11.7 (2011), pp. 1196–1205 (cit. on p. 14).
- [40]Michael P Allen and Dominic J Tildesley. *Computer simulation of liquids*. Oxford university press, 2017 (cit. on pp. 15, 24–26).
- [41]Jens Rotne and Stephen Prager. “Variational treatment of hydrodynamic interaction in polymers”. In: *The Journal of Chemical Physics* 50.11 (1969), pp. 4831–4837 (cit. on pp. 15, 25).
- [42]Hiromi Yamakawa. “Transport properties of polymer chains in dilute solution: hydrodynamic interaction”. In: *The Journal of Chemical Physics* 53.1 (1970), pp. 436–443 (cit. on pp. 15, 25).
- [43]John F Brady and Georges Bossis. “Stokesian dynamics”. In: *Annual review of fluid mechanics* 20.1 (1988), pp. 111–157 (cit. on p. 15).
- [44]Michael P Howard, Arash Nikoubashman, and Jeremy C Palmer. “Modeling hydrodynamic interactions in soft materials with multiparticle collision dynamics”. In: *Current Opinion in Chemical Engineering* 23 (2019), pp. 34–43 (cit. on pp. 15, 24–26, 28, 29).
- [45]Anatoly Malevanets and Raymond Kapral. “Mesoscopic model for solvent dynamics”. In: *The Journal of chemical physics* 110.17 (1999), pp. 8605–8613 (cit. on pp. 15, 24, 26, 27).
- [46]G Gompper, T Ihle, DM Kroll, and RG Winkler. “Multi-particle collision dynamics: A particle-based mesoscale simulation approach to the hydrodynamics of complex fluids”. In: *Advanced computer simulation approaches for soft matter sciences III* (2009), pp. 1–87 (cit. on pp. 15, 24–26).
- [47]Anthony JC Ladd and ROLF Verberg. “Lattice-Boltzmann simulations of particle-fluid suspensions”. In: *Journal of statistical physics* 104 (2001), pp. 1191–1251 (cit. on pp. 15, 24).

- [48]Guy G McNamara and Gianluigi Zanetti. “Use of the Boltzmann equation to simulate lattice-gas automata”. In: *Lattice Gas Methods For Partial Differential Equations*. CRC Press, 2019, pp. 289–296 (cit. on p. 15).
- [49]Yashraj M Wani, Penelope Grace Kovakas, Arash Nikoubashman, and Michael P Howard. “Diffusion and sedimentation in colloidal suspensions using multiparticle collision dynamics with a discrete particle model”. In: *The Journal of Chemical Physics* 156.2 (2022) (cit. on pp. 16, 25, 28, 29).
- [50]Yashraj M Wani, Penelope Grace Kovakas, Arash Nikoubashman, and Michael P Howard. “Mesoscale simulations of diffusion and sedimentation in shape-anisotropic nanoparticle suspensions”. In: *Soft Matter* (2024) (cit. on pp. 17, 29).
- [51]Patrice Bacchin, David Brutin, Anne Davaille, et al. “Drying colloidal systems: Laboratory models for a wide range of applications”. In: *The European Physical Journal E* 41 (2018), pp. 1–34 (cit. on p. 18).
- [52]Joseph L Keddie. “Film formation of latex”. In: *Materials Science and Engineering: R: Reports* 21.3 (1997), pp. 101–170 (cit. on p. 18).
- [53]Joseph Keddie and Alexander F Routh. *Fundamentals of latex film formation: processes and properties*. Springer Science & Business Media, 2010 (cit. on p. 18).
- [54]Paul Calvert. “Inkjet printing for materials and devices”. In: *Chemistry of materials* 13.10 (2001), pp. 3299–3305 (cit. on p. 18).
- [55]Emine Tekin, Patrick J Smith, and Ulrich S Schubert. “Inkjet printing as a deposition and patterning tool for polymers and inorganic particles”. In: *Soft matter* 4.4 (2008), pp. 703–713 (cit. on p. 18).
- [56]Katrin Burmester, Arne Pietsch, and Rudolf Eggers. “A basic investigation on instant coffee production by vacuum belt drying”. In: *Procedia Food Science* 1 (2011), pp. 1344–1352 (cit. on p. 18).
- [57]Robert D Deegan, Olgica Bakajin, Todd F Dupont, et al. “Capillary flow as the cause of ring stains from dried liquid drops”. In: *Nature* 389.6653 (1997), pp. 827–829 (cit. on p. 18).
- [58]Robert D Deegan, Olgica Bakajin, Todd F Dupont, et al. “Contact line deposits in an evaporating drop”. In: *Physical review E* 62.1 (2000), p. 756 (cit. on p. 18).
- [59]Robert D Deegan. “Pattern formation in drying drops”. In: *Physical review E* 61.1 (2000), p. 475 (cit. on p. 18).
- [60]Hua Hu and Ronald G Larson. “Marangoni effect reverses coffee-ring depositions”. In: *The Journal of Physical Chemistry B* 110.14 (2006), pp. 7090–7094 (cit. on p. 18).
- [61]Michael P Howard, Arash Nikoubashman, and Athanassios Z Panagiotopoulos. “Stratification dynamics in drying colloidal mixtures”. In: *Langmuir* 33.15 (2017), pp. 3685–3693 (cit. on pp. 18, 19).
- [62]Alexander F Routh and William B Zimmerman. “Distribution of particles during solvent evaporation from films”. In: *Chemical Engineering Science* 59.14 (2004), pp. 2961–2968 (cit. on pp. 18, 19).
- [63]Yuri Reyes and Yurko Duda. “Modeling of drying in films of colloidal particles”. In: *Langmuir* 21.15 (2005), pp. 7057–7060 (cit. on p. 18).

- [64] Yue Ma, HT Davis, and LE Scriven. “Microstructure development in drying latex coatings”. In: *Progress in Organic Coatings* 52.1 (2005), pp. 46–62 (cit. on p. 18).
- [65] RE Trueman, E Lago Domingues, SN Emmett, et al. “Autostratification in drying colloidal dispersions: experimental investigations”. In: *Langmuir* 28.7 (2012), pp. 3420–3428 (cit. on pp. 18, 19).
- [66] T Narita, P Hebraud, and F Lequeux. “Effects of the rate of evaporation and film thickness on nonuniform drying of film-forming concentrated colloidal suspensions”. In: *The European Physical Journal E* 17 (2005), pp. 69–76 (cit. on p. 18).
- [67] Michael P Howard, Arash Nikoubashman, and Athanassios Z Panagiotopoulos. “Stratification in drying polymer–polymer and colloid–polymer mixtures”. In: *Langmuir* 33.42 (2017), pp. 11390–11398 (cit. on pp. 18, 19).
- [68] Andrea Fortini, Ignacio Martín-Fabiani, Jennifer Lesage De La Haye, et al. “Dynamic stratification in drying films of colloidal mixtures”. In: *Physical review letters* 116.11 (2016), p. 118301 (cit. on p. 19).
- [69] Susanne Wintzheimer, Tim Granath, Maximilian Oppmann, et al. “Supraparticles: Functionality from uniform structural motifs”. In: *ACS nano* 12.6 (2018), pp. 5093–5120 (cit. on p. 19).
- [70] Wendong Liu, Jiarul Midya, Michael Kappl, Hans-Jürgen Butt, and Arash Nikoubashman. “Segregation in drying binary colloidal droplets”. In: *ACS nano* 13.5 (2019), pp. 4972–4979 (cit. on pp. 19–21).
- [71] Wendong Liu, Michael Kappl, and Hans-Jürgen Butt. “Tuning the porosity of supraparticles”. In: *ACS nano* 13.12 (2019), pp. 13949–13956 (cit. on pp. 19–21).
- [72] Xiao-Liang Fang, Cheng Chen, Ming-Shang Jin, et al. “Single-crystal-like hematite colloidal nanocrystal clusters: synthesis and applications in gas sensors, photocatalysis and water treatment”. In: *Journal of Materials Chemistry* 19.34 (2009), pp. 6154–6160 (cit. on p. 19).
- [73] Xiang Li, Nikunj Kumar Visaveliya, Lars Hafermann, et al. “Hierarchically structured particles for micro flow catalysis”. In: *Chemical Engineering Journal* 326 (2017), pp. 1058–1065 (cit. on p. 19).
- [74] Ke Hou, Jianyu Han, and Zhiyong Tang. “Formation of supraparticles and their application in catalysis”. In: *ACS Materials Letters* 2.1 (2019), pp. 95–106 (cit. on p. 19).
- [75] Nicolas Vogel, Stefanie Utech, Grant T England, et al. “Color from hierarchy: Diverse optical properties of micron-sized spherical colloidal assemblies”. In: *Proceedings of the National Academy of Sciences* 112.35 (2015), pp. 10845–10850 (cit. on p. 19).
- [76] Vinothan N Manoharan, Arnout Imhof, James D Thorne, and David J Pine. “Photonic crystals from emulsion templates”. In: *Advanced Materials* 13.6 (2001), pp. 447–450 (cit. on p. 19).
- [77] Maria Isabel Rial-Hermida, Nuno M Oliveira, Angel Concheiro, Carmen Alvarez-Lorenzo, and JF Mano. “Bioinspired superamphiphobic surfaces as a tool for polymer- and solvent-independent preparation of drug-loaded spherical particles”. In: *Acta Biomaterialia* 10.10 (2014), pp. 4314–4322 (cit. on p. 19).
- [78] Xiaolin Li, Meng Gu, Shenyang Hu, et al. “Mesoporous silicon sponge as an anti-pulverization structure for high-performance lithium-ion battery anodes”. In: *Nature communications* 5.1 (2014), p. 4105 (cit. on p. 19).

- [79]Reinhard Vehring, Willard R Foss, and David Lechuga-Ballesteros. “Particle formation in spray drying”. In: *Journal of aerosol science* 38.7 (2007), pp. 728–746 (cit. on p. 19).
- [80]DE Walton and CJ Mumford. “Spray dried products—characterization of particle morphology”. In: *Chemical Engineering Research and Design* 77.1 (1999), pp. 21–38 (cit. on p. 19).
- [81]Ali Hashmi, Yuhao Xu, Benjamin Coder, et al. “Leidenfrost levitation: beyond droplets”. In: *Scientific reports* 2.1 (2012), p. 797 (cit. on p. 19).
- [82]AD Dinsmore, Ming F Hsu, MG Nikolaidis, et al. “Colloidosomes: selectively permeable capsules composed of colloidal particles”. In: *Science* 298.5595 (2002), pp. 1006–1009 (cit. on p. 20).
- [83]Jishu Han, Xue Zhang, Yubing Zhou, et al. “Fabrication of CdTe nanoparticles-based superparticles for an improved detection of Cu 2+ and Ag+”. In: *Journal of Materials Chemistry* 22.6 (2012), pp. 2679–2686 (cit. on p. 20).
- [84]Zhe Liu, Yong Liu, Jinge Yang, et al. “Highly Efficient and Controlled Fabrication of Supraparticles by Leidenfrost Phenomenon”. In: *Langmuir* 38.30 (2022), pp. 9157–9165 (cit. on p. 20).
- [85]Michael Agthe, Tomás S Plivelic, Ana Labrador, Lennart Bergstrom, and German Salazar-Alvarez. “Following in real time the two-step assembly of nanoparticles into mesocrystals in levitating drops”. In: *Nano letters* 16.11 (2016), pp. 6838–6843 (cit. on p. 20).
- [86]Debasis Sen, Olivier Spalla, Olivier Taché, Patrick Haltebourg, and Antoine Thill. “Slow drying of a spray of nanoparticles dispersion. In situ SAXS investigation”. In: *Langmuir* 23.8 (2007), pp. 4296–4302 (cit. on p. 20).
- [87]Michael P Howard and Arash Nikoubashman. “Stratification of polymer mixtures in drying droplets: Hydrodynamics and diffusion”. In: *The Journal of Chemical Physics* 153.5 (2020) (cit. on pp. 20, 21).
- [88]Z Chua and S Seeger. “Superamphiphobic surfaces. Chem. 312”. In: *Soc. Rev* 43 (2014), pp. 2784–2798 (cit. on p. 21).
- [89]Hans-Jürgen Butt, Ciro Semperebon, Periklis Papadopoulos, et al. “Design principles for superamphiphobic surfaces”. In: *Soft Matter* 9.2 (2013), pp. 418–428 (cit. on p. 21).
- [90]Gianni Jacucci, Brooke W Longbottom, Christopher C Parkins, Stefan AF Bon, and Silvia Vignolini. “Anisotropic silica colloids for light scattering”. In: *Journal of Materials Chemistry C* 9.8 (2021), pp. 2695–2700 (cit. on p. 22).
- [91]Jessi ES van der Hoeven, Harith Gurunaryanan, Maarten Bransen, et al. “Silica-coated gold nanorod supraparticles: a tunable platform for surface enhanced Raman spectroscopy”. In: *Advanced Functional Materials* 32.27 (2022), p. 2200148 (cit. on p. 22).
- [92]Anatoly Malevanets and Raymond Kapral. “Solute molecular dynamics in a mesoscale solvent”. In: *The Journal of Chemical Physics* 112.16 (2000), pp. 7260–7269 (cit. on pp. 24, 27, 29).
- [93]Burkhard Dünweg and Anthony JC Ladd. “Lattice Boltzmann simulations of soft matter systems”. In: *Advanced computer simulation approaches for soft matter sciences III* (2009), pp. 89–166 (cit. on p. 24).
- [94]Donald L Ermak and J Andrew McCammon. “Brownian dynamics with hydrodynamic interactions”. In: *The Journal of chemical physics* 69.4 (1978), pp. 1352–1360 (cit. on p. 24).

- [95] Paweł J Zuk, E Wajnryb, KA Mizerski, and P Szymczak. “Rotne–Prager–Yamakawa approximation for different-sized particles in application to macromolecular bead models”. In: *Journal of Fluid Mechanics* 741 (2014), R5 (cit. on p. 25).
- [96] T Ihle and DM Kroll. “Stochastic rotation dynamics: A Galilean-invariant mesoscopic model for fluid flow”. In: *Physical Review E* 63.2 (2001), p. 020201 (cit. on p. 27).
- [97] Thomas Ihle and Daniel M Kroll. “Stochastic rotation dynamics. I. Formalism, Galilean invariance, and Green-Kubo relations”. In: *Physical Review E* 67.6 (2003), p. 066705 (cit. on p. 27).
- [98] JT Padding and AA Louis. “Hydrodynamic interactions and Brownian forces in colloidal suspensions: Coarse-graining over time and length scales”. In: *Physical Review E* 74.3 (2006), p. 031402 (cit. on pp. 27, 29).
- [99] Marisol Ripoll, K Mussawisade, RG Winkler, and G Gompper. “Dynamic regimes of fluids simulated by multiparticle-collision dynamics”. In: *Physical Review E* 72.1 (2005), p. 016701 (cit. on pp. 27, 28).
- [100] E Tüzel, Martin Strauss, Thomas Ihle, and Daniel M Kroll. “Transport coefficients for stochastic rotation dynamics in three dimensions”. In: *Physical Review E* 68.3 (2003), p. 036701 (cit. on p. 27).
- [101] N Kikuchi, CM Pooley, JF Ryder, and JM Yeomans. “Transport coefficients of a mesoscopic fluid dynamics model”. In: *The Journal of chemical physics* 119.12 (2003), pp. 6388–6395 (cit. on p. 27).
- [102] Antonio Lamura, Gerhard Gompper, Thomas Ihle, and DM Kroll. “Multi-particle collision dynamics: Flow around a circular and a square cylinder”. In: *Europhysics Letters* 56.3 (2001), p. 319 (cit. on p. 28).
- [103] K Mussawisade, M Ripoll, RG Winkler, and G Gompper. “Dynamics of polymers in a particle-based mesoscopic solvent”. In: *The Journal of chemical physics* 123.14 (2005) (cit. on p. 28).
- [104] Dan S Bolintineanu, Gary S Grest, Jeremy B Lechman, et al. “Particle dynamics modeling methods for colloid suspensions”. In: *Computational Particle Mechanics* 1 (2014), pp. 321–356 (cit. on p. 28).
- [105] Hiroshi Noguchi and Gerhard Gompper. “Dynamics of fluid vesicles in shear flow: Effect of membrane viscosity and thermal fluctuations”. In: *Physical Review E* 72.1 (2005), p. 011901 (cit. on p. 28).
- [106] G Batôt, Vincent Dahirel, Guillaume Mériguet, AA Louis, and Marie Jardat. “Dynamics of solutes with hydrodynamic interactions: Comparison between Brownian dynamics and stochastic rotation dynamics simulations”. In: *Physical Review E* 88.4 (2013), p. 043304 (cit. on p. 29).
- [107] Vincent Dahirel, Xudong Zhao, Baptiste Couet, Guillaume Batot, and Marie Jardat. “Hydrodynamic interactions between solutes in multiparticle collision dynamics”. In: *Physical Review E* 98.5 (2018), p. 053301 (cit. on p. 29).
- [108] Yasuhiro Inoue, Yu Chen, and Hirotada Ohashi. “Development of a simulation model for solid objects suspended in a fluctuating fluid”. In: *Journal of statistical physics* 107 (2002), pp. 85–100 (cit. on p. 29).

[109]Simón Poblete, Adam Wysocki, Gerhard Gompper, and Roland G Winkler. “Hydrodynamics of discrete-particle models of spherical colloids: A multiparticle collision dynamics simulation study”. In: *Physical Review E* 90.3 (2014), p. 033314 (cit. on p. 29).

Curriculum vitae

Personal Information

Name: **Yashraj Manish Wani**, M.Sc.
Nationality: Indian
Date of Birth: May 24, 1997
Place of Birth: Nashik
Current Address: Lucy-Hillebrand-Str. 4,
55128 Mainz
Email: ymanishw@uni-mainz.de



Education

- Nov 2020 – present **Ph.D. in Physics** at the *Institute of Physics, Johannes Gutenberg University of Mainz*.
Supervisor: Prof. Dr. Arash Nikoubashman
Thesis: “Dynamics and evaporation-driven assembly in colloidal suspensions consisting of shape-isotropic and shape-anisotropic particles.”
- Aug 2015 – May 2020 **B.S. – M.S. in Physics** at the *Indian Institute of Science Education and Research, Bhopal*.
Grade: 1,6 (German standard)
Master Thesis: “Dynamics of a semi-flexible polymer tethered at one end.”
Thesis Supervisor: Prof. Dr. Snigdha Thakur

Work Experience

- Nov 2020 – present Research assistant in Physics, *Johannes Gutenberg University of Mainz*

Scholarships and Awards

- Dec 2019 Council of Scientific and Industrial Research, National Eligibility Test for Junior Research Fellow
All India Rank – 202
- Aug 2015 – May 2020 INSPIRE (Innovation in Science Pursuit for Inspired Research) fellowship, Department of Science and Technology, India